FRICTIONAL EQUILIBRIUM POSTURES FOR ROBOTIC LOCOMOTION - COMPUTATION, GEOMETRIC CHARACTERIZATION, AND STABILITY ANALYSIS

YIZHAR OR

FRICTIONAL EQUILIBRIUM POSTURES FOR ROBOTIC LOCOMOTION - COMPUTATION, GEOMETRIC CHARACTERIZATION, AND STABILITY ANALYSIS

RESEARCH THESIS

SUBMITTED IN PARTIAL FULFILLMENT OF THE
REQUIREMENTS
FOR THE DEGREE OF DOCTOR OF PHILOSOPHY

YIZHAR OR

SUBMITTED TO THE SENATE OF THE TECHNION — ISRAEL INSTITUTE OF TECHNOLOGY
TAMMUZ, 5767 HAIFA JULY, 2007

THIS RESEARCH THESIS WAS SUPERVISED BY PROFESSOR ELON RIMON UNDER THE AUSPICES OF THE MECHANICAL ENGINEERING DEPARTMENT

ACKNOWLEDGMENT

First, I would like to express my sincere gratitude to Professor Elon Rimon for his support and dedicated guidance during all stages of this research.

Thanks to all members of the Center of Manufacturing Systems and Robotics at the Technion for their assistance and for manufacturing the experimental systems.

I would like to thanks the Dept. of Mechanical Engineering at the Technion, which was my second home during the last ten years.

Finally, I wish to thank my beloved family for their support and encouragement along the way.

THE GENEROUS FINANCIAL HELP OF THE TECHNION, THE NE'EMAN SCHOLARSHIP AND THE LEVZION SCHOLARSHIP IS GRATEFULLY ACKNOWLEDGED

This thesis is dedicated to my dear family with love.

Contents

List of Figures

List of Tables

Abstract

This thesis is concerned with computation and graphical characterization of robust and stable equilibrium postures suited for quasistatic multi-legged locomotion. Quasistatic locomotion consists of a sequence of equilibrium postures in which the robot supports itself stably against gravity while moving free limbs to new foothold positions. Automated planning for quasistatic legged locomotion requires tools for identification and computation of feasible equilibrium postures on rough and unstructured terrains. Such postures must be robust with respect to inertial forces generated by motion of the internal limbs, and should also possess dynamic stability with respect to position-and-velocity perturbations. Lumping the kinematic structure of the robot into a single rigid body with variable center of mass, the objective of this thesis is reduced to finding the region of center-of-mass locations achieving robust and stable equilibrium stances for a given set of frictional contacts, assuming Coulomb's friction model. The thesis formulates the center-of-mass region achieving feasible equilibrium and provides its geometric characterization, under a two-dimensional or three-dimensional gravitational field. The results are then generalized to computation of robust stances with respect to a given bounded set of disturbance forces and torques. Analyzing the system's dynamics under initial perturbations that may include contact separation, rolling or sliding, the thesis defines the new notion of

frictional stability. The dynamics of planar mechanical systems with frictional contacts is then formulated, using the concept of contact modes. Two fundamental phenomena of frictional dynamics, namely, dynamic ambiguity and dynamic inconsistency, are analyzed. The *strong equilibrium* criterion, which eliminates dynamic ambiguities is reviewed, and the novel *persistent equilibrium* criterion, which eliminates dynamic inconsistencies, is developed. These two criteria are formulated in terms of mass distribution and center-of-mass location, and are proven to be a key component in frictional stability, guaranteeing that a separated contact is recovering in finite time. The recovering of a separated contact involves a collision followed by an impact event, at which the dynamic solution is non-smooth. The dynamics of a planar rigid body undergoing sequential collisions at two contacts is formulated as a *hybrid dynamical system*, composed of phases of continuous dynamics interleaved by discrete impact events. Two types of dynamic solutions, the bouncing motion and the clattering motion, converging to re-establishment of one or two contacts, are analyzed. Using the technique of Poincaré map, the conditions for existence and stability of clattering motion are derived. The clattering stability condition depends on the coefficient of restitution, the mass distribution, and center-of-mass location. Finally, frictional stability is addressed, using the concept of completed dynamical system that concatenates the continuous phases of frictional dynamics with the phases of hybrid dynamics. The two components of persistent equilibrium and clattering stability are proven to be sufficient for frictional stability of planar two-contact stances. The theoretical analysis in this thesis is supported by graphical examples, experimental results, and numerical dynamic simulations.

List of Symbols

a_i : acceleration of the ith contact

$\mathcal{B}$: a rigid object in 2D or 3D

$\mathcal{C}_i$: the friction cone at the ith contact

f_i : the ith contact force

f_g : the gravitational force acting on $\mathcal{B}$

f_{ext} : the net external force acting on $\mathcal{B}$

g : the gravitational acceleration

$h_i(q)$: a smooth function representing the ith contact as a unilateral constraint

J : the 2×2 matrix of 90°-rotation in plane

$J_i(q)$: Jacobian matrix of the ith contact point

k : in chapters 2 to 4 is the number of contacts

k : in chapter 5 is the discrete-time index

m : the mass of $\mathcal{B}$

n_i : the unit vector normal to the ith contact

q : configuration of a mechanical system

$\dot{q}$: generalized velocity of a mechanical system

$\ddot{q}$: generalized acceleration of a mechanical system

$\mathcal{R}$: in Chapter 3 is the center-of-mass region of feasible equilibrium

$\widetilde{\mathcal{R}}$: in Chapter 3 is the horizontal projection of $\mathcal{R}$

$\mathcal{R}(\boldsymbol{w})$: in Chapter 2 is the feasible equilibrium region under an external wrench $\boldsymbol{w}$

s_i : in Chapter 3 is a unit vector tangent to the ith contact and perpendicular to t_i

t : the time variable

t_i : a unit vector tangent to the ith contact

t_k : in chapter 5 is the time of the kth collision

v_i : velocity of the ith contact

$\boldsymbol{x}$: location of $\mathcal{B}$'s center-of-mass

x_i : location of the ith contact point

$\boldsymbol{w}$: net wrench (i.e. force and torque) acting on $\mathcal{B}$'s center-of-mass, $\boldsymbol{w} = (f_{ext}, \tau_{ext})$

$\boldsymbol{w}_o$: the nominal gravitational wrench $(f_g, 0)$

θ : $\mathcal{B}$'s angle of orientation

τ_{ext} : the net external wrench acting on $\mathcal{B}$

μ : Coulomb's coefficient of friction

ρ : $\mathcal{B}$'s radius of gyration

Chapter 1

Introduction

Multi-legged robots capable of autonomous quasistatic locomotion are becoming progressively more sophisticated. Developers of legged robots strive to achieve stable locomotion on uneven terrains such as staircases [42], complex posture changes such as sitting and standing up [119], cargo lifting [74], and climbing [13, 59]. Possible applications of legged robots are, for example, surveillance of collapsed structures for survivors [107], inspection and testing of complex pipe systems [88], and maintenance of space stations or hazardous structures such as nuclear reactors [97], all requiring motion in congested, unstructured, and complex environments.

Quasistatic locomotion can be characterized as a series of postures in which the mechanism supports itself against gravity while moving its free limbs to new positions. For instance, the 3-legged robot shown in Figure 1.1 moves with a gait of 3-legged phases interleaved with 2-legged phases where it lifts a leg to a new position [93]. In order to achieve autonomous locomotion of such robots over uneven terrains, one needs basic tools for selecting postures that can passively support the mechanism against gravity

Figure 1.1: A 3-legged robot moving in a two-dimensional gravitational environment (the mechanism is supported by frictionless air bearings against the inclined plane).

while allowing motion of its free limbs according to task specification. On rough terrain, the robot must account for friction forces at its contacts with the environment, in order to achieve an equilibrium posture and generate the propulsion forces required for its motion. In order to resist the inertial wrenches (i.e. forces and torques) generated by motion of the internal limbs, the robot's posture should be *robust* with respect to a given neighborhood of external wrenches. Furthermore, a walking robot should be able to recover small position-and-velocity perturbations, which may cause contact separation, rolling or sliding at its footpads. Such perturbations can be caused by inaccuracies in the coordinated motion of internal limbs, as well as external disturbances such as wind or vibrations. Thus, the selected postures must also possess *dynamic stability* with respect to such perturbations. The goal of this research thesis is to provide the basic tools for computation and geometric characterization of dynamically stable equilibrium postures of a multi-legged robot on a rough frictional terrain, under a two-dimensional or three-dimensional gravitational field. The thesis uses a simplifying paradigm that lumps the complex kinematic structure of a robot into a single rigid body having the same contacts with the environment, and a variable center of mass. The key objective of this work is thus reduced as follows. Given a set

of frictional contacts, find the region of center-of-mass position achieving an equilibrium stance, which is robust with respect to disturbance wrenches, and dynamically stable with respect to position-and-velocity perturbations.

1.1 Literature Review

This section provides a survey of relevant works in the literature. The survey is divided into parts according to the different subjects treated in this thesis.

1.1.1 Quasistatic legged locomotion

In the field of quasistatic legged locomotion on rough terrains under the influence of gravity, some works conducted autonomous motion planning in the robot's full configuration space, e.g. [11, 13, 59]. In the reduced planning of center-of-mass and foothold location, a classical concept for characterization of feasible equilibrium stances is the *support polygon principle* [65], which states that the center-of mass must lie above the polygon spanned by the contacts. This principle was further extended for dynamic motion synthesis of humanoid robots with the concept of *zero moment point* (ZMP) [114]. This concept is widely used in current literature on humanoid robots, e.g. [42, 55, 113, 119]. However, the main limitation of the ZMP concept is that it assumes flat horizontal terrains. Recent attempts to generalize the ZMP concept to rough terrains appear in [35, 36]. Using a different approach, Bretl et al. [14] compute an adaptive approximation of the center-of-mass region for feasible equilibrium stances on frictional contacts in 3D. Their algorithm is based in iterative steps of solving convex optimization problems for checking the feasibility of a sampled center-of-mass locations. Finally, a milestone in robotic legged locomotion on

rough terrain is the six-legged biologically-inspired RHEX robot [96]. The actuation of the six legs of RHEX is tuned such that at each instant, a triplet of legs touch the ground, and generate a tripod stance. Thus, RHEX is capable of performing fast and dynamic motion, while the alternating tripods guarantee swinging between equilibrium stances. Note that most of the works mentioned above discuss the feasibility of static equilibrium, and do not consider dynamic stability.

1.1.2 Frictional grasping and manipulation

The problem of center-of-mass and foothold selection in order to achieve a frictional equilibrium stance is closely related with the problem of grasp planning, which was widely addressed in literature (see [10] for a thorough survey). Typical grasping systems assume full control of the contact forces. In these systems *force closure* [72] captures the fingers' ability to actively resist any external wrench acting on the grasped object [17, 56, 98, 118]. Multi-limb locomotion based on force closure is useful in tunnel-like environments where the mechanism can brace itself against opposing walls [33, 71, 94, 100]. However, legged locomotion on a terrain involves contacts that can typically balance only a neighborhood of wrenches about the gravitational force. Moreover, legged mechanisms are supported by *passive* contacts that can only react to applied wrenches. Legged locomotion is thus more related to passive grasping applications such as whole arm manipulation[1] [69, 75, 109, 110], fixturing [115, 120], and object recognition [54]. An especially relevant work by Erdmann et al. considers the feasible center-of-mass positions of objects held in frictional 2-contact stances by a palm manipulator [26]. Note, however, that a multi-legged mechanism can control

[1]In whole arm manipulation an object is manipulated by one or more articulated mechanisms which are allowed to establish multiple mid-link contacts with the manipulated object [10].

the gravitational wrench by varying its center-of-mass position. The latter possibility is analogous to pushing applications, where an object is manipulated in a planar environment by a pushing force [58, 62]. A graphical moment-labeling technique developed for these applications [18, 61] can be adapted to the 2D stances considered here. However, this method, which is limited to planar analysis, does not admit a natural extension to consider stance robustness with respect to external wrenches.

Under coulomb's friction model in three-dimensions, the frictional constraints become *quadratic*. Discussing frictional grasps in 3D, some works used polyhedral approximation of the friction cones [51, 90]. This approach enables formulation of equilibrium and grasp optimization as linear programs. Using the exact constraints, Bicchi [9] formulated the frictional force-closure test as a nonlinear differential equation. Han et. al. [38] formulated the exact frictional constraints as a linear matrix inequality (LMI) problem, for testing force-closure and optimizing actuator torques. While these methods are suitable for addressing a feasibility query or optimization of a scalar cost function, they have no generalization for computing the feasible center-of-mass region.

1.1.3 Dynamic stability of frictional equilibrium postures

Classical stability definitions for equilibrium points of a dynamical system are based on considering a small perturbation in the system's state (i.e. position and velocity) about equilibrium, and analyzing the trajectory of the dynamical system in response to this perturbation (e.g. Lyapunov stability, [48, 52]). In the robotics literature, some works analyzed the stability of robotic systems with multiple contacts in the context of grasping. In [27, 73] the stability of force closure grasps is analyzed, under the assumption that the contact forces are actively controlled. In [44, 99, 101], the stability of force-closure grasps with passive fingers is considered, by modeling

the natural compliance at the contacts, and accounting for joints' stiffness. This approach is further extended in [92], which uses the joints' control law to induce linear contact compliance, and computes stable equilibrium postures of a legged robot in two-dimensional gravitational field. However, all the works mentioned above analyze stability only with respect to perturbations in which all contacts are maintained fixed (or rolling), and disregarded perturbations in which the contacts are sliding or separating. Mason et al. [64] analyzed dynamic stability of frictionless equilibrium stances on non-flat terrains in 2D and 3D, while accounting for all possible perturbations. In their analysis, they checked conditions for local minimum of gravitational potential energy on the stratified set of all non-penetrating configurations in configuration space. However, since frictional equilibrium postures are generally not associated with local minima of an obvious potential function, their method cannot be extended to the frictional case. Thus, a key objective of this thesis is to analyze the stability of frictional equilibrium postures with respect to all possible perturbations, including contact separation, rolling or sliding, under the rigid body paradigm, assuming that the contact forces are passively generated by frictional contact constraints. While initial progress toward stability analysis is reported for specific scenarios [29, 40, 87, 60], a general stability theory in frictional multi-contact settings is still a challenging open problem.

1.1.4 Dynamics under frictional contacts

Stability analysis of frictional equilibrium postures requires investigation of the system's dynamics in response to a position-and-velocity perturbation. The dynamics of mechanical systems with frictional contacts under Coulomb's friction model was

widely investigated in robotics literature, for applications such as dynamic simulations [105] and assembly planning [7]. The first to identify some paradoxical results related to the dynamics under rigid body paradigm and Coulomb's friction model was Painlevé [83], with his famous sliding rod example. In this example, which was given some geometrical interpretations in [63], a thin rod is sliding on a frictional plane. For some certain choices of the rod's physical parameters and geometry, there exist initial conditions under which the instantaneous solution of the rod's constrained dynamics is inconsistent with the assumptions of the model. This paradoxical result has been recently resolved by a solution of impulsive forces, using the concept of *tangential impact* [8, 117], (or "impact without collision" [16, 28]), in which the contact force becomes impulsive, causing a discontinuous velocity jump.

Another closely related phenomenon of frictional dynamics is the *dynamic jamming*, which was first analyzed by Dupont and Yamajako [24]. In a dynamic jamming scenario, a planar mechanical system with sliding contacts undergoes a singular event at which the contact forces and sliding accelerations become unbounded in finite time, and the sliding dynamics' solution becomes inconsistent. After the jamming event, a tangential impact event occurs, causing an abrupt halt of sliding, followed by contact separation. This scenario, which is predicted by the tangential impact theory, was recently verified experimentally by Meltz, Or and Rimon [67] on an experimental system mimicking Painlevé's rod.

The dynamics of planar mechanical system with frictional contacts admits a special structure, which is governed by the system's *contact modes* [91]. The instantaneous frictional dynamics can be formulated as a *linear complementarity problem* [4, 57], which accounts for all contact modes in a unified framework. This formulation enables investigation of the conditions for existence and uniqueness of solution [86]. While

the problem of solution's inexistence can be resolved by impulsive solutions [105] or tangential impacts [28, 117], the problem of *dynamic ambiguity* [25, 91], at which the instantaneous dynamics has multiple solutions, is indeterminable. Some attempts to address this problem are conducted in [23, 53], where the rigid body assumption and Coulomb's friction model are relaxed, and a contact compliance model is used to predict the dynamic response and resolve the ambiguity. However, this approach is not only computationally intensive, but the mechanics of compliance in the presence of friction is still an open problem investigated in the solid mechanics literature [50]. In order to avoid the problematic cases of frictional dynamic ambiguity under the rigid-body paradigm, Pang and Trinkle [85] introduced the notion of *strong stability criterion*, which requires that the only consistent dynamic solution is static equilibrium. This principle of elimination dynamic ambiguity was used in applications of sensorless part insertion [6], manipulation tasks involving frictional contacts [7], and motion planning for robotic climbing [33]. Note that despite its name, strong stability criterion has no obvious relation to dynamic stability, and thus in this thesis it is called the *strong equilibrium criterion*.

1.1.5 Impact mechanics and hybrid dynamical systems

When considering the dynamics of mechanical systems with contacts in response to perturbations that involve contact separation, one must account for the *impact* occurring when a separated contact is recovered. The subject of rigid body collisions was widely explored in the literature, see, for example the textbooks [108] and [16] with the references therein. Many models were proposed for rigid body impact under Coulomb's friction, e.g. [12, 21, 117]. The reader is referred to [16, 106] and to the Ph.D. thesis of Chaterjee [20] for a thorough review and comparison of frictional

impact models in 2D and 3D.

A mechanical system undergoing a sequence of impact events are a special subclass of *hybrid dynamical systems*, which are systems composed of phases of continuous dynamics interleaved by discrete events of "switching" or discontinuous jumps [37, 112]. A classical technique for analyzing the dynamics of such systems is the *Poincaré map* [34, 70]. This technique is based on sampling the dynamic solution of the hybrid system at the times of impacts, thus reducing the problem to analysis of discrete-time dynamical systems. Wang [116] used Poincaré map to analyze the stability of a single contact under sequential frictionless impacts. Goyal et al. [30, 31] analyzed the dynamics of clattering of a horizontal rod undergoing collisions at its two endpoints, under the simplifying assumption of negligible gravity.

A key feature in hybrid dynamical system is the *Zeno solution*, which is a solution that includes an infinite number of switches (or impact events) in finite time [41, 102, 112], as in the classical example of a bouncing ball [2, 121]. While the hybrid system fails to predict the dynamic solution beyond the Zeno time, Ames et al. proposed the concept of *completed dynamical system* [3] for mechanical systems under unilateral constraints. This concept suggests that at the Zeno point the system switches to a holonomically constrained dynamical system. Using this concept, the dynamic response to contact separation can be analyzed beyond the Zeno point associated with contact re-establishment, enabling characterization of dynamic stability in a physically meaningful way.

1.2 Summary of Contributions

This section outlines the structure of this thesis and summarizes the main contribution of each chapter.

Chapter 2 considers planar frictional stances, and discusses the computation of the *feasible equilibrium region*, denoted $\mathcal{R}$. The feasible equilibrium region for a given set of contacts is the region of center-of-mass locations for which equilibrium can be generated by the contact forces under Coulomb's friction model. The section shows that $\mathcal{R}$ is a vertical strip whose boundaries can be computed by solving two *linear programming* problems. The section also provides a graphical construction of $\mathcal{R}$ for two contacts, and gives an efficient geometric algorithm that computes $\mathcal{R}$ for multiple contact stances. Next, the results are extended to computation of the *robust equilibrium region*, which guarantees feasible equilibrium under any external wrench within a given bounded neighborhood of the nominal gravitational wrench. Finally, the theoretical results are validated by experiments that test the robustness of a two-legged planar mechanism on a frictional terrain.

Chapter 3 is concerned with computation of the feasible equilibrium region $\mathcal{R}$ for frictional stances in three dimensions. Some fundamental properties of $\mathcal{R}$ are established, along with its relations with the classical *support polygon principle*, which states that the center-of-mass must lie within the vertical prism spanned by the contacts in order to maintain feasible equilibrium. Focusing on three-contact stances, the computation of $\mathcal{R}$, which is essentially nonlinear due to the quadratic nature of Coulomb's friction law in 3D, is then addressed by two different approaches. The first approach formulates $\mathcal{R}$ as a projection of a five-dimensional convex region in the composite space of contact forces and center-of-mass location onto a two-dimensional

plane. Replacing the quadratic friction cones with polyhedrons, $\mathcal{R}$ can then be approximated to any desired accuracy by standard methods for projection of polyhedral sets onto lower-dimensional subspaces. The second approach formulates $\mathcal{R}$ as an intersection of a six-dimensional convex cone and a two-dimensional affine plane in wrench space, which is the composite space of net forces and torques. Using techniques of differential geometry, The exact boundary cells of $\mathcal{R}$ are then formulated, and their geometric characterization is obtained by methods of *line geometry*. Next, the effect of changes in the coefficient of friction on the topological structure of $\mathcal{R}$ is investigated. The theoretical results are then validated with an experimental setup of a three-legged mechanism with a variable center-of-mass. Finally, the chapter concludes by sketching the generalizations to multiple contacts and to consider stance robustness.

Chapter 4 defines the notion of *frictional stability* of equilibrium stances with respect to position-and-velocity perturbations. The dynamics of planar mechanical systems with frictional contacts is formulated using the concept of *contact modes*. Three phenomena which are unique to this kind of dynamics are dynamic ambiguity, dynamic inconsistency and dynamic jamming. The chapter analyzes these phenomena in terms of center-of-mass location and mass distribution. The concept of *strong equilibrium*, which eliminates dynamic ambiguities is then reviewed. It is then shown that strong equilibrium is a necessary condition for frictional stability. Next, the chapter defines a new notion of *persistent equilibrium*, which guarantees that the dynamic response avoids dynamic inconsistency and dynamic jamming scenarios, and results in recovering of separated contacts in finite time. Finally, the chapter concludes by sketching the generalizations to three dimensions, and to robustness of strong and persistent equilibrium.

Chapter 5 analyzes the dynamics of a planar rigid body undergoing sequential collisions at the contacts. The non-smooth *impact* event, occurring when a separated contact recovers, is formulated under the rigid body assumption, using the *coefficient of normal restitution*. The dynamical system is then formulated as a *hybrid dynamical system*, composed of phases of continuous dynamics interleaved by discrete impact events. Using the symmetric horizontal rod example, two different modes of motion, namely, the bouncing motion and the clattering motion, are analyzed. These motions results in converging to a Zeno solution associated with re-establishment of one or two contacts. Next, the region initial conditions leading to bouncing motion on a single contact is formulated. Using the technique of *Poincaré map*, the conditions for existence and stability of clattering motion are derived. The clattering stability condition depends on the coefficient of restitution and the rod's mass distribution. Finally, the results are extended to general two-stances of a planar rigid body with variable mass distribution and center-of-mass location.

Chapter 6 combines the results of all previous chapters, and presents sufficient conditions for frictional stability of two-contact equilibrium stances of a planar rigid body. The chapter also provides a procedure for computation of the center-of-mass region achieving stable equilibrium stances on a given terrain, and demonstrates with graphical examples. Finally, Chapter 7 concludes by discussing limitations of the results in this thesis, and listing some possible directions of future research.

Chapter 2

Robust Equilibrium Stances in 2D

This chapter focuses on planar mechanisms supported by frictional contacts in a two-dimensional gravitational environment. As a first step, we lump the complex kinematic structure of the mechanism into a single rigid body $\mathcal{B}$ having the same contacts with the environment and a variable center of mass. The feasible equilibrium postures associated with a given set of contacts and the nominal gravitational wrench correspond to center-of-mass locations of $\mathcal{B}$ that guarantee a feasible equilibrium stance for the same contacts. However, the mechanism is additionally subjected to inertial forces generated by its moving parts. We lump these forces into a neighborhood of disturbance wrenches (i.e. forces and torques) centered at the nominal gravitational wrench. Under this reduction, a stance of $\mathcal{B}$ is *robust* if the contacts can passively resist the entire wrench neighborhood. Based on this notion of robustness our objective is as follows. Given a k-contact stance of $\mathcal{B}$ and a neighborhood of disturbance wrenches, we wish to identify the *robust equilibrium region* defined as all center-of-mass locations of $\mathcal{B}$ at which the contacts can passively resist the wrench neighborhood.

The structure and contributions of the chapter are as follows. First, it considers center-of-mass positions that give a feasible equilibrium of $\mathcal{B}$ under the influence of a single external wrench. Section 2.1 formulates this region as a linear programming problem. Section 2.2 provides its graphical characterization and a potentially faster line-sweep algorithm for its computation. The main result is that the feasible equilibrium region of a general k-contact stance is an *infinite strip* whose position and orientation is determined by the contacts and the external wrench acting on $\mathcal{B}$. Next, this result is generalized to neighborhoods of disturbance wrenches. Section 2.3 formulates the robust equilibrium region as a linear programming problem and provides its graphical characterization. The main result in this section is that the robust equilibrium region of a general k-contact stance is a *parallelogram* whose shape and size is determined by the contacts and the wrench neighborhood. Section 2.4 reports on experiments validating the analytical equilibrium criterion on a two-legged prototype.

2.1 The Feasible Equilibrium Region

We now introduce basic terminology and define the feasible equilibrium region of a stance. Then we formulate the computation of the feasible equilibrium region as a linear programming problem, and draw two properties useful for its graphical characterization.

2.1.1 Basic terminology

Let $\mathcal{B}$ be a planar rigid object with a variable center of mass, which is supported by k frictional point contacts in a two-dimensional gravitational environment. The

gravitational force acting at $\mathcal{B}$'s center of mass, denoted f_g, defines the vertical downward direction. The environment is assigned a fixed world frame aligned with the vertical direction, and $\mathcal{B}$ is assigned a body frame with origin at its center of mass. The position of $\mathcal{B}$'s center of mass in the world frame is denoted x. The contact points are denoted $x_1 \dots x_k$ (all expressed in the fixed world frame), and the contact forces acting on $\mathcal{B}$ are denoted $f_1 \dots f_k$. Using this notation, the torque generated by f_i about $\mathcal{B}$'s center of mass is the scalar $\tau_i = (x_i - x)^T J^T f_i$, where $J = \begin{bmatrix} 0 & -1 \\ 1 & 0 \end{bmatrix}$. Assuming Coulomb's friction law, each force f_i must lie in a *friction cone*, denoted $\mathcal{C}_i$, in order to avoid sliding. Let f_i^n and f_i^t denote the normal and tangential components of f_i. Then $\mathcal{C}_i = \{f_i : |f_i^t| \leq \mu f_i^n,\ f_i^n \geq 0\}$ where μ is the coefficient of friction. We also need the following equivalent terminology for $\mathcal{C}_i$. Let C_i^l and C_i^r denote unit vectors along the left and right edges of $\mathcal{C}_i$ (Figure 2.1(a)). Then the ith friction cone is given by $\mathcal{C}_i = \{f_i^l C_i^l + f_i^r C_i^r : f_i^l, f_i^r \geq 0\}$. The object $\mathcal{B}$ is additionally subjected to a disturbance wrench $(f_d, \tau_d) \in I\!R^2 \times I\!R$, where (f_d, τ_d) is expressed with respect to $\mathcal{B}$'s center of mass. Let $\boldsymbol{w} = (f_{ext}, \tau_{ext}) \in I\!R^2 \times I\!R$ denote the net external wrench acting on $\mathcal{B}$, then $f_{ext} = f_g + f_d$ such that $\|f_d\| \ll \|f_g\|$. Since f_g generates no torque about x, we have that $\tau_{ext} = \tau_d$.

The equilibrium condition is as follows. Let G_f and G_τ denote the matrices associated with the forces and torques at the contacts:

$$\begin{aligned} G_f &= \begin{bmatrix} C_1^l & C_1^r & \cdots & C_k^l & C_k^r \end{bmatrix}_{2\times 2k} \\ G_\tau &= -\begin{bmatrix} x_1^T J C_1^l & x_1^T J C_1^r \cdots x_k^T J C_k^l & x_k^T J C_k^r \end{bmatrix}_{1\times 2k}. \end{aligned}$$

Let $\boldsymbol{f} = \begin{pmatrix} f_1^l & f_1^r \cdots f_k^l & f_k^r \end{pmatrix}$ denote the $2k$-vector of normal and tangential contacts

force components. Then the equilibrium condition is given by

$$\begin{bmatrix} G_f \\ G_\tau \end{bmatrix} \boldsymbol{f} = - \begin{pmatrix} f_{ext} \\ \tau(x) \end{pmatrix} \text{ and } \boldsymbol{f} \geq \vec{0}, \tag{2.1}$$

where $\tau(x) = x^T J^T f_{ext} + \tau_{ext}$ is the net torque generated by $\boldsymbol{w} = (f_{ext}, \tau_{ext})$ about the world frame origin. Note that the contact forces are statically indeterminate for $k \geq 2$ contacts. We can now formally define the feasible equilibrium region.

Definition 1 *Given a set of k frictional contacts and an external wrench $\boldsymbol{w}$ acting on $\mathcal{B}$, the* **feasible equilibrium region** *associated with $\boldsymbol{w}$, denoted $\mathcal{R}(\boldsymbol{w})$, is the set of $\mathcal{B}$'s center-of-mass locations for which there exist contact forces $f_i \in \mathcal{C}_i$ $(i = 1 \ldots k)$ satisfying the equilibrium condition* (2.1).

2.1.2 Computation of the feasible equilibrium region

We show that the feasible equilibrium region is an infinite strip computable as a linear programming problem. As noted by several authors [13, 64], the equilibrium formulation (2.1) can be interpreted as a collection of linear inequalities in the composite $(\boldsymbol{f}, x)$ space. The following key theorem characterizes the feasible equilibrium region as a pair of linear programs.

Theorem 1 *Let $\mathcal{B}$ be supported by $k \geq 2$ frictional contacts in a two-dimensional gravitational field, and be subjected to a net external wrench $\boldsymbol{w} = (f_{ext}, \tau_{ext})$. If the feasible equilibrium region $\mathcal{R}(\boldsymbol{w})$ is nonempty, it is generically an* ***infinite strip*** *parallel to f_{ext} given by*

$$\mathcal{R}(\boldsymbol{w}) = \left\{ x \in \mathbb{R}^2 : \tau_{min} \leq x^T J^T f_{ext} + \tau_{ext} \leq \tau_{max} \right\}, \tag{2.2}$$

where τ_{min} and τ_{max} are obtained by solving the linear programming problems:

$$\begin{array}{ll} \tau_{min} = min\{-G_\tau \boldsymbol{f}\} & \tau_{max} = max(-G_\tau \boldsymbol{f}) \\ s.t. & s.t. \\ G_f \boldsymbol{f} = -f_{ext} & G_f \boldsymbol{f} = -f_{ext} \\ \boldsymbol{f} \geq 0 & \boldsymbol{f} \geq 0 \end{array} \tag{2.3}$$

Proof: The k contacts and external wrench are fixed. Hence the equilibrium and friction constraints take place in a $(2k+1)$-dimensional space whose coordinates are $(\boldsymbol{f}, \tau)$, where τ is the net torque acting on $\mathcal{B}$ with respect to a fixed world frame. Since the constraints in (2.1) are linear in $\boldsymbol{f}$ and τ, they form a convex polytope in $I\!R^{2k+1}$. For $k \geq 2$ contacts the projection of the $(\boldsymbol{f}, \tau)$-polytope onto the τ-axis is an interval $[\tau_{min}, \tau_{max}]$. Once the interval is computed, its pre-image under the linear mapping $\tau(x) = x^T J^T f_{ext} + \tau_{ext}$ yields an infinite strip parallel to f_{ext} of allowed center-of-mass locations. The projection of the polytope onto the τ-axis is equivalent to the following pair of linear programs in $\boldsymbol{f}$-space. According to (2.1), $\tau = -G_\tau \boldsymbol{f}$. Hence the extreme values of τ over the $(\boldsymbol{f}, \tau)$-polytope correspond to the minimum and maximum of $-G_\tau \boldsymbol{f}$ over the $\boldsymbol{f}$-polytope: $\{\boldsymbol{f} : G_f \boldsymbol{f} = -f_{ext}, \boldsymbol{f} \geq \vec{0}\}$. These extreme values are τ_{min} and τ_{max} in the linear programs of the theorem. $\square$

Let us make three comments on the theorem. First, the interval $[\tau_{min}, \tau_{max}]$ captures the range of torques that can be resisted by contact reaction forces satisfying force equilibrium and friction constraints. The feasible equilibrium strip can therefore be written as $\mathcal{R}(\boldsymbol{w}) = \{x : \tau_{min} \leq \tau(x) \leq \tau_{max}\}$. Second, in certain situations τ_{min} and/or τ_{max} may not exist, either when the linear problem is infeasible, or when it is unbounded. In the first case, $\mathcal{R}(\boldsymbol{w})$ is empty, while in the latter case ($\mathcal{R}(\boldsymbol{w})$ spans a halfplane, or the entire plane, as demonstrated in the example below. Third, for a single contact $\mathcal{R}(\boldsymbol{w})$ is a line parallel to f_{ext} and passing through the contact. The

strip $\mathcal{R}(\boldsymbol{w})$ associated with $k \geq 2$ contacts degenerates to such a line in the special case where all friction cones point to the same side of f_{ext}, such that one friction cone edge is aligned with f_{ext}.

Example 1. Figure 2.1(a) shows the region $\mathcal{R}(\boldsymbol{w})$ for two contacts with $\mu = 0.3$, using the nominal gravitational wrench $\boldsymbol{w} = (f_g, 0)$. Note that $\mathcal{R}(\boldsymbol{w})$ is a vertical strip spanned by the polygon $\mathcal{C}_1 \cap \mathcal{C}_2$. This observation is part of the full graphical characterization discussed below. Figure 2.1(b) shows the same stance with $\mu = 2.0$, using the nominal gravitational wrench $\boldsymbol{w} = (f_g, 0)$. In this case τ_{min} and τ_{max} are unbounded and $\mathcal{R}(\boldsymbol{w})$ spans the entire plane. Note that in this case the line segment connecting x_1 and x_2 is contained in the friction cones $\mathcal{C}_1$ and $\mathcal{C}_2$, thus satisfying Nguyen's frictional force closure condition [72]. In general, $\mathcal{R}(\boldsymbol{w}_0)$ is bounded when the friction cones are *upward pointing*, in the sense that $f_i \cdot f_g \leq 0$ for all $f_i \in \mathcal{C}_i$ $(i = 1, 2)$. Indeed, both friction cones are upward pointing in Figure 2.1(a), while none is upward pointing in Figure 2.1(b).

2.1.3 Properties of the feasible equilibrium region

We now describe two structural properties of $\mathcal{R}(\boldsymbol{w})$. The first property will be the basis for the graphical characterization and is stated in the following proposition.

Proposition 2.1.1 *Let $\mathcal{B}$ be supported by k frictional contacts in a two-dimensional gravitational environment, and be subjected to an external wrench $\boldsymbol{w} = (f_{ext}, \tau_{ext})$. Then $\mathcal{R}(\boldsymbol{w})$ is the convex hull of the pairwise feasible equilibrium regions,*

$$\mathcal{R}(\boldsymbol{w}) = \mathsf{conv}\{\mathcal{R}_{ij}(\boldsymbol{w}) \ , \ 1 \leq i, j \leq k\},$$

where $\mathcal{R}_{ij}(\boldsymbol{w})$ is the feasible equilibrium region associated with two contacts x_i and x_j, and conv *denotes convex hull.*

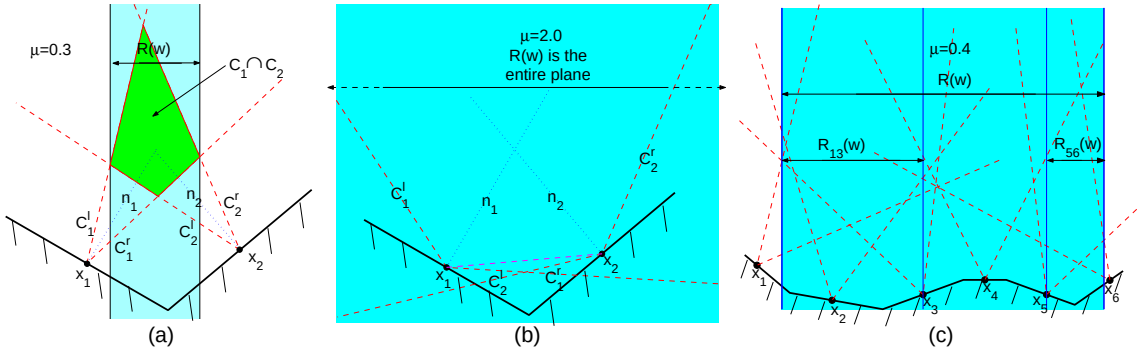

Figure 2.1: The feasible equilibrium region $\mathcal{R}(\boldsymbol{w})$ for (a)-(b) two contacts, and (c) six contacts.

A proof of the proposition appears in Appendix A.

This proposition asserts that $\mathcal{R}(\boldsymbol{w})$ can be computed in terms of the equilibrium strips generated by all pairs of contacts. Since these strips are all parallel to f_{ext}, their convex hull is simply the strip bounded by the leftmost and rightmost edges of the pairwise strips. A second notable property is that $\mathcal{R}(\boldsymbol{w})$ is completely determined by at most *four* out of the k contacts. This observation is stated in the following corollary.

Corollary 2.1.2 *Let $\mathcal{B}$ be supported by $k \geq 4$ frictional contacts in a two-dimensional gravitational environment, and be subjected to an external wrench $\boldsymbol{w} = (f_{ext}, \tau_{ext})$. Let $\mathcal{R}(\boldsymbol{w})$ be the feasible equilibrium region associated with $\boldsymbol{w}$. Then there exist at least $k-4$ contacts that can be removed without affecting $\mathcal{R}(\boldsymbol{w})$.*

A proof of the corollary also appears in Appendix A. Note that the remaining contacts are non-essential only for the purpose of determining the feasible equilibrium region. These contacts may prove important for other purposes, such as contact force minimization over the center-of-mass locations.

Example 2: Figure 2.1(c) shows the region $\mathcal{R}(\boldsymbol{w})$ for six contacts with $\mu = 0.4$, using the nominal gravitational wrench $\boldsymbol{w} = (f_g, 0)$. Computing the vertical strips $\mathcal{R}_{ij}(\boldsymbol{w})$ associated with all possible pairs of contacts, one can see that the leftmost edge is associated with $\mathcal{R}_{13}$ while the rightmost edge is associated with $\mathcal{R}_{56}$. The feasible equilibrium region associated with all six contacts is simply the vertical strip bounded by the leftmost and rightmost edges. Moreover, the four contacts x_1, x_3, x_5, x_6 completely determine $\mathcal{R}(\boldsymbol{w})$.

2.2 Graphical Characterization of Feasible Equilibrium Region

The k-contact feasible equilibrium region is the convex hull of the pairwise feasible equilibrium strips (Proposition 2.1.1). Hence we focus on the graphical characterization of the individual 2-contact equilibrium strips, with the understanding that the convex hull of the pairwise strips is a strip bounded by their leftmost and rightmost edges.

First consider the 2-contact equilibrium strip associated with the nominal gravitational wrench $\boldsymbol{w}_0 = (f_g, 0)$. In this case $\mathcal{R}(\boldsymbol{w}_0)$ is a vertical strip that can be obtained by union and intersection of *five* strips, each having a distinct geometric interpretation. The five strips are as follows. Let $\mathcal{C}_i^-$ denote the negative reflection of the friction cone $\mathcal{C}_i$ about its base point x_i. Let S_0^{++} denote the infinite vertical strip spanned by the polygon $\mathcal{C}_1 \cap \mathcal{C}_2$. Similarly, let S_0^{+-}, S_0^{-+}, and S_0^{--} denote the infinite vertical strips spanned by the polygons $\mathcal{C}_1^+ \cap \mathcal{C}_2^-$, $\mathcal{C}_1^- \cap \mathcal{C}_2^+$, and $\mathcal{C}_1^- \cap \mathcal{C}_2^-$. Note that some of these polygons and their associated strips may be empty. The fifth strip, denoted Π_0, is the infinite vertical strip bounded by the contacts x_1 and x_2. The

graphical construction of $\mathcal{R}(\boldsymbol{w}_0)$ is summarized in the following lemma.

Lemma 2.2.1 *Let $\mathcal{B}$ be supported by two frictional contacts in a two-dimensional gravitational environment, and be subjected to a nominal gravitational wrench $\boldsymbol{w}_0 = (f_g, 0)$. Then the feasible equilibrium region $\mathcal{R}(\boldsymbol{w}_0)$ is an infinite vertical strip given by*

$$\mathcal{R}(\boldsymbol{w}_0) = \big((S_0^{++} \cup S_0^{--}) \cap \Pi_0\big) \cup \big((S_0^{+-} \cup S_0^{-+}) \cap \bar{\Pi}_0\big), \tag{2.4}$$

where $\bar{\Pi}_0$ is the complement of Π_0 in $I\!R^2$.

Proof: There are three external forces acting on $\mathcal{B}$: the gravitational force f_g acing at x, and the contact forces f_1 and f_2 acting at x_1 and x_2. The net moment generated by these forces must vanish at an equilibrium. It can be verified that the vanishing of the net moment implies that the three force lines intersect at a common point denoted z (in the special case where all forces are parallel, z lies at infinity). Since each f_i must lie in its friction cone $\mathcal{C}_i$, the point z must lie in the intersection of the double-cones $\mathcal{C}_1 \cup \mathcal{C}_1^-$ and $\mathcal{C}_2 \cup \mathcal{C}_2^-$. The line of f_g passes through both x and z. Hence concurrency of the three force lines implies that x must lie in one of the infinite vertical strips spanned by the intersection $(\mathcal{C}_1 \cup \mathcal{C}_1^-) \cap (\mathcal{C}_2 \cup \mathcal{C}_2^-)$. These are precisely the four strips S_0^{++}, S_0^{+-}, S_0^{-+}, and S_0^{--} (Figure 2.2(a)-(b)).

Next consider the force equation $f_1 + f_2 + f_g = 0$. Note that even though the concurrency point z can lie in the double-cone $\mathcal{C}_i \cup \mathcal{C}_i^-$, the contact force f_i can lie only in the positive cone $\mathcal{C}_i$ for $i = 1, 2$. Let u_i be a unit vector from x_i to z $(i = 1, 2)$. There are four cases to consider depending on the location of the concurrency point z. First consider the case where $z \in \mathcal{C}_1 \cap \mathcal{C}_2$. In this case $u_1 \in \mathcal{C}_1$ and $u_2 \in \mathcal{C}_2$. Hence each f_i can be written as $f_i = \alpha_i u_i$ for some $\alpha_i \geq 0$. Let $f_g^\perp = J f_g$ denote the horizontal direction. Multiplying the equation $f_1 + f_2 + f_g = 0$ by $f_g^\perp$ gives:

$\alpha_1(u_1 \cdot f_g^\perp) + \alpha_2(u_2 \cdot f_g^\perp) = 0$. Since $\alpha_i \geq 0$, we conclude that $u_1 \cdot f_g^\perp$ and $u_2 \cdot f_g^\perp$ must have opposite signs. The graphical interpretation of this fact is that z must lie *inside* the vertical strip Π_0 bounded by x_1 and x_2. Since x and z lie on a common vertical line, x must lie in the intersection $S_0^{++} \cap \Pi_0$ (Figure 2.2(c)). Next consider the case where $z \in \mathcal{C}_1 \cap \mathcal{C}_2^-$. In this case $u_1 \in \mathcal{C}_1$ while $u_2 \in \mathcal{C}_2^-$. Hence $f_i = \alpha_i u_i$ such that $\alpha_1 \geq 0$ and $\alpha_2 \leq 0$. The equation $\alpha_1(u_1 \cdot f_g^\perp) + \alpha_2(u_2 \cdot f_g^\perp) = 0$ now implies that $u_1 \cdot f_g^\perp$ and $u_2 \cdot f_g^\perp$ must have the same sign. The graphical interpretation of this fact is that z must lie *outside* the vertical strip Π_0. Thus, x lies in the intersection $S_0^{+-} \cap \bar{\Pi}_0$. By applying similar arguments to the remaining two cases where $z \in \mathcal{C}_1^- \cap \mathcal{C}_2^-$ and $z \in \mathcal{C}_1^- \cap \mathcal{C}_2$, formula (2.4) is obtained. $\square$

Note that the five vertical strips comprising $\mathcal{R}(\boldsymbol{w}_0)$ always form a *single connected strip* (Theorem 1). The graphical characterization of $\mathcal{R}(\boldsymbol{w}_0)$ also captures the situations where $\mathcal{R}(\boldsymbol{w}_0)$ is unbounded, as in the example of Figure 2.1(b). The graphical characterization is consistent with the analysis provided in [15] for 3-legged climbing, and with the characterization given in [26] for object manipulation under the influence of gravity. It is also worth discussing the *moment labelling* technique developed for pushing applications in planar environments [18, 61]. This technique depicts the net reaction wrench generated by k frictional contacts in terms of signed polygons P_- and P_+. All lines passing between the two polygons in a direction determined by their sign are possible reaction wrenches. In particular, $\mathcal{R}(\boldsymbol{w}_0)$ is the vertical strip bounded by P_- and P_+. Moment labelling can thus provide an alternative to our graphical technique of taking the convex hull of pairwise strips.

Example 3: Consider formula (2.4) for the special case where the two contacts lie on a common terrain segment. If the two friction cones contain the upward vertical

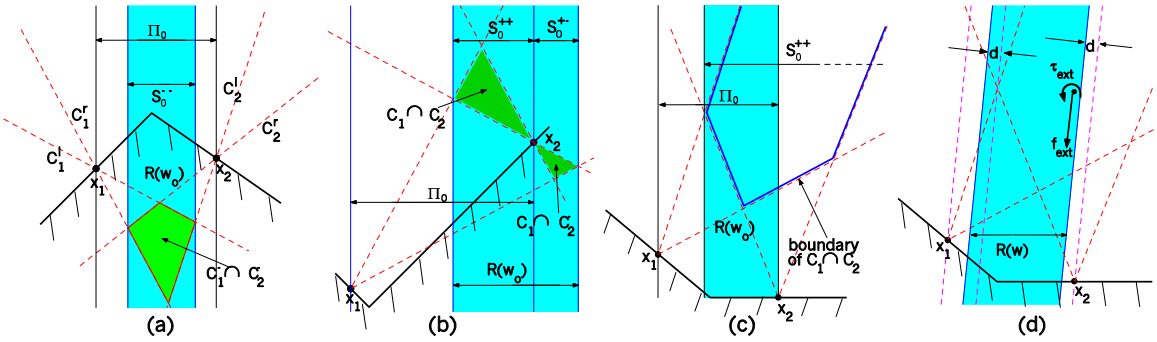

Figure 2.2: Graphical characterization of $\mathcal{R}(\boldsymbol{w})$ in four cases: (a) $\mathcal{R}(\boldsymbol{w}_0) = S^{--} \cap \Pi$, (b) $\mathcal{R}(\boldsymbol{w}_0) = S^{++} \cup S^{+-}$, (c) $\mathcal{R}(\boldsymbol{w}_0) = S_1^{++} \cap \Pi$, (d) $\mathcal{R}(\boldsymbol{w})$ for a general wrench $\boldsymbol{w} = (f_{ext}, \tau_{ext})$.

direction, $S_0^{++} = S_0^{--} = I\!R^2$ and $S_0^{+-} = S_0^{-+} = \emptyset$. In this case $\mathcal{R}(\boldsymbol{w}_0) = \Pi_0$. This special case still holds true when the two contacts lie on disjoint pieces of the line segment joining the contacts.

Consider now the graphical characterization of the 2-contact feasible equilibrium strip for a general external wrench $\boldsymbol{w} = (f_{ext}, \tau_{ext})$. When $\tau_{ext} = 0$ the net force $f_{ext} = f_g + f_d$ acts along a line passing through $\mathcal{B}$'s center of mass, but now the line is rotated with respect to the vertical direction. In this case the feasible equilibrium region is constructed by the same procedure described above, except that now the five vertical strips are rotated as to match the direction of f_{ext}. When $\tau_{ext} \neq 0$, the wrench $\boldsymbol{w}$ is equivalent to a pure force f_{ext} acting on $\mathcal{B}$ along a line having a perpendicular offset d from x, where $d = \tau_{ext}/\|f_{ext}\|$. Hence the five strips are rotated and parallel shifted by $-d$ as shown in Figure 2.2(d). The following lemma summarizes the construction of the general 2-contact feasible equilibrium strip.

Lemma 2.2.2 *Let $\mathcal{B}$ be supported by two frictional contacts in a two-dimensional gravitational environment, and be subjected a net external wrench $\boldsymbol{w} = (f_{ext}, \tau_{ext})$.*

Let $S^{++}, S^{+-}, S^{-+}, S^{--}$ *be the strips spanned by the polygons* $\mathcal{C}_1 \cap \mathcal{C}_2, \mathcal{C}_1^+ \cap \mathcal{C}_2^-, \mathcal{C}_1^- \cap \mathcal{C}_2^+, \mathcal{C}_1^- \cap \mathcal{C}_2^-$*, and let* Π *be the strip bounded by* x_1 *and* x_2*, such that the five strips are parallel to* f_{ext} *and parallel shifted by* $-\tau_{ext}/\|f_{ext}\|$*. Then the feasible equilibrium region* $\mathcal{R}(\boldsymbol{w})$ *is an infinite strip parallel to* f_{ext} *given by*

$$\mathcal{R}(\boldsymbol{w}) = \left((S^{++} \cup S^{--}) \cap \Pi\right) \cup \left((S^{+-} \cup S^{-+}) \cap \bar{\Pi}\right),$$

where $\bar{\Pi}$ *is the complement of* Π *in* $\mathbb{R}^2$*.*

Line sweep algorithm for computing $\mathcal{R}(\boldsymbol{w})$. The feasible equilibrium strip of a k-contact stance can be computed as the convex hull of all pairwise strips in $O(k^2)$ steps. We describe in Appendix B a more sophisticated line-sweep algorithm that computes $\mathcal{R}(\boldsymbol{w})$ in practically $O(k)$ steps. The main steps of the algorithm for the case of $\boldsymbol{w}_0 = (f_g, 0)$ are as follows. The algorithm stores the $2k$ directed lines aligned with the friction cones' edges in lists $\mathcal{L}_1$ and $\mathcal{L}_2$. The list $\mathcal{L}_1$ contains the lines pointing to the *left* of the upward vertical direction, while $\mathcal{L}_2$ contains the lines pointing to the *right* of the upward vertical direction. The set of intersection points of left-pointing lines with right-pointing lines is denoted $\mathcal{S}$. A key fact is that the edges of $\mathcal{R}(\boldsymbol{w}_0)$ are vertical lines passing through the leftmost and rightmost points of $\mathcal{S}$. Let us next consider the computation of the right edge of $\mathcal{R}(\boldsymbol{w}_0)$ or, equivalently, the rightmost point of $\mathcal{S}$. The algorithm computes in $O(k)$ steps a line $l'(0)$ on the right side of $\mathcal{S}$. The algorithm also selects a suitable initial point of $\mathcal{S}$, and defines the vertical line through this point as the initial sweep line $l(0)$. At the ith iteration the algorithm selects a vertical line at the middle of the strip bounded by $l(i)$ and $l'(i)$. Then it checks whether the middle line lies to the right of $\mathcal{S}$. If it does, the middle line becomes $l'(i+1)$ and $l(i+1)$ moves to a new point of $\mathcal{S}$ on the right side of $l(i)$. Otherwise $l'(i+1) = l'(i)$, and $l(i+1)$ moves to a point of $\mathcal{S}$ which lies on the middle-line's right

side. The algorithm next inspects the intersection pattern of the lines of $\mathcal{L}_1$ and $\mathcal{L}_2$ with $l(i+1)$, and removes from these lists lines that do not affect the points of $\mathcal{S}$ on the right side of $l(i+1)$. The iterations repeat until $\mathcal{L}_1$ and $\mathcal{L}_2$ become simultaneously empty. At this stage $l(i+1)$ has reached the rightmost point of $\mathcal{S}$ and the algorithm terminates.

The computational complexity of the algorithm is as follows. As discussed in the appendix, at least one line is removed from $\mathcal{L}_1$ or $\mathcal{L}_2$ in each iteration. Hence there are $O(k)$ iterations. The number of iterations is also bounded by the binary bisection to $\log(\Delta/\delta)$, where Δ is the initial search width and δ is the minimal search width. Since each iteration takes $O(k)$ steps, the total run-time is $k \cdot \min\{k, \log(\Delta/\delta)\}$. In practical settings $\log(\Delta/\delta)$ is a small constant, and the algorithm runs in $O(k)$ steps. An execution example of the algorithm on a 6-contact stance is provided in the appendix.

2.3 The Robust Equilibrium Region

So far we focused on the feasible equilibrium region of a k-contact stance associated with a specific external wrench. In this section we consider the robust equilibrium region associated with neighborhoods of external wrenches. The wrench neighborhoods represent inertial forces generated by moving limbs of the mechanism, but can also represent environmental disturbances as well as positioning inaccuracies. First we introduce a convenient parameterization for wrench neighborhoods and define the robust equilibrium region. Then we formulate the computation of the robust equilibrium region as a linear programming problem, and finally discuss its graphical construction.

2.3.1 Parametrization of the wrench neighborhood $\mathcal{W}$

The wrench parametrization is based on the following homogeneity property. If $\boldsymbol{f}$ is the $2k$-vector of reaction forces satisfying the equilibrium condition (2.1) for $\boldsymbol{w}_{ext}$, then $s\boldsymbol{f}$ satisfies (2.1) for $s\boldsymbol{w}_{ext}$ where s is a positive scalar. Let (f_x, f_y) denote the horizontal and vertical coordinates of f_{ext}. Since $f_{ext} = f_g + f_d$ such that f_g is vertical and $\|f_d\| \ll \|f_g\|$, we may assume that $f_y \neq 0$. Thus we define *homogeneous coordinates* for wrench space as (p, q), where $p \triangleq f_x/f_y$ and $q \triangleq \tau_{ext}/f_y$. The (p, q) coordinates can be interpreted as follows. The nominal gravitational wrench, $\boldsymbol{w}_o = (f_g, 0)$, corresponds to $(p, q) = (0, 0)$. Any other wrench $\boldsymbol{w} = (f_{ext}, \tau_{ext}) \in I\!R^2 \times I\!R$ can be represented by its magnitude and an oriented line of action. The wrench's line of action is oriented along f_{ext}, and the horizontal distance of this line from $\mathcal{B}$'s center-of-mass is τ_{ext}/f_y. Hence p represents the orientation of the wrench's line of action, and q represents its horizontal distance from $\mathcal{B}$'s center of mass at x. Using (p, q), we assume that $\mathcal{W}$ is a *rectangular neighborhood* given by $\mathcal{W} = \{(p, q) : \kappa_1 \leq p \leq \kappa_2, \nu_1 \leq q \leq \nu_2\}$, where κ_i and ν_i are given constants for $i = 1, 2$. Note that $\mathcal{W}$ is specified relative to the gravitational wrench in a way which is independent of the choice of world and body frames. The definition of the robust equilibrium region associated with $\mathcal{W}$ is as follows.

Definition 2 *Given a k-contact stance and a neighborhood $\mathcal{W}$ of external wrenches acting on $\mathcal{B}$, the* **robust equilibrium region** *of $\mathcal{W}$, denoted $\mathcal{R}(\mathcal{W})$, is the set of $\mathcal{B}$'s center-of-mass locations at which all wrenches of $\mathcal{W}$ possess feasible contact forces $f_i \in \mathcal{C}_i$ $(i = 1 \ldots k)$ satisfying the equilibrium equation* (2.1).

The robust equilibrium region can be equivalently defined as the intersection of the feasible equilibrium strips associated with the individual wrenches in $\mathcal{W}$ i.e., $\mathcal{R}(\mathcal{W}) =$

$\cap_{\boldsymbol{w}\in\mathcal{W}}\mathcal{R}(\boldsymbol{w})$.

2.3.2 Computation of the robust equilibrium region

We now show how to compute the robust equilibrium region as a linear programming problem. In order to obtain the (p, q) version of the equilibrium condition (2.1), we divide both sides of (2.1) by $f_y \neq 0$ and obtain the equivalent equilibrium condition:

$$\begin{bmatrix} G_f \\ G_\tau \end{bmatrix} \boldsymbol{f} = - \begin{pmatrix} p \\ 1 \\ \tau(x) \end{pmatrix}, \tag{2.5}$$

where $\boldsymbol{f} \geq \vec{0}$ and $\tau(x) = x^T J^T \begin{pmatrix} p \\ 1 \end{pmatrix} + q$. The following theorem characterizes the robust equilibrium region as a linear programming problem.

Theorem 2 *Let $\mathcal{B}$ be supported by k frictional contacts in a two-dimensional gravitational environment, and be subjected to a neighborhood $\mathcal{W} = [\kappa_1, \kappa_2] \times [\nu_1, \nu_2]$ of disturbance wrenches. Then the robust equilibrium region of $\mathcal{W}$ is a* **finite parallelogram** *given by*

$$\begin{aligned} \mathcal{R}(\mathcal{W}) = \ & \big\{ x \in I\!R^2 : \tau_{1,min} - \nu_1 \leq x^T J^T f^1_{ext} \leq \tau_{1,max} - \nu_2 \\ & \qquad \text{and} \ \ \tau_{2,min} - \nu_1 \leq x^T J^T f^2_{ext} \leq \tau_{2,max} - \nu_2 \big\}, \end{aligned}$$

where $f^i_{ext} = (\kappa_i, 1)$ for $i = 1, 2$, and $\tau_{i,min}, \tau_{i,max}$ are obtained by solving the linear programming problems:

$$\begin{array}{ll} \tau_{i,min} = min\{-G_\tau \boldsymbol{f}\} & \tau_{i,max} = max(-G_\tau \boldsymbol{f}) \\ s.t. & s.t. \\ G_f \boldsymbol{f} = -f^i_{ext} & G_f \boldsymbol{f} = -f^i_{ext} \\ \boldsymbol{f} \geq 0 & \boldsymbol{f} \geq 0 \end{array} \qquad \text{for } i = 1, 2. \tag{2.6}$$

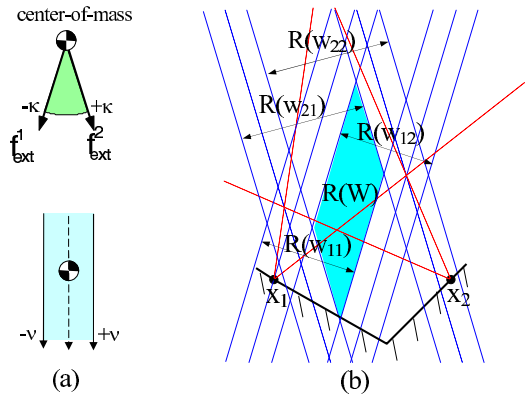

Figure 2.3: (a) Depiction of the wrench neighborhood $\mathcal{W} = [-\kappa, \kappa] \times [-\nu, \nu]$. (b) The robust equilibrium region is the parallelogram $\mathcal{R}(\mathcal{W})$.

The Proof of this theorem appears in Appendix A.

The theorem can be easily extended to wrench neighborhoods $\mathcal{W}$ specified as convex polygons in the (p, q) plane. In this case $\mathcal{R}(\mathcal{W})$ is the intersection of the feasible equilibrium strips associated with the external wrenches parametrized by the vertices of $\mathcal{W}$. The theorem specifies a graphical construction of $\mathcal{R}(\mathcal{W})$ as a parallelogram obtained by intersecting the feasible equilibrium strips associated with the vertices of $\mathcal{W}$. This construction is illustrated in the following example.

Example 3: Consider the 2-contact stance shown in Figure 2.3(b), where the coefficient of friction is $\mu = 0.4$. We selected a rectangular wrench neighborhood $\mathcal{W} = [-\kappa, \kappa] \times [-\nu, \nu]$ with $\kappa = 0.3$ and $\nu = \|x_2 - x_1\|/8$. The neighborhood $\mathcal{W}$ is depicted in Figure 2.3(a) as a sector of force-directions representing the interval $[-\kappa, \kappa]$, and a strip of force-lines representing the interval $[-\nu, \nu]$. Figure 2.3(b) shows the strips $\mathcal{R}(\boldsymbol{w}_{ij})$ associated with the vertices of $\mathcal{W}$, where each strip is constructed graphically using Lemma 2.2.2. The robust equilibrium region is the shaded parallelogram obtained by intersecting the four strips.

The example illustrates an important property of the robust equilibrium region. *No matter how small is the wrench neighborhood $\mathcal{W}$, it always imposes an upper limit on the height of $\mathcal{B}$'s center-of-mass locations.* In other words, as the height of $\mathcal{B}$'s center of mass above the contacts increases, the neighborhood $\mathcal{W}$ must shrink so that $\mathcal{B}$'s center of mass would remain in the robust equilibrium region.

Line sweep algorithm for computing $\mathcal{R}(\mathcal{W})$. In principle one can invoke the line-sweep algorithm of the previous section for each vertex of $\mathcal{W}$, then intersect the resulting strips. But a more efficient use of the line-sweep algorithm is as follows. The neighborhood $\mathcal{W}=[-\kappa,\kappa]\times[-\nu,\nu]$ crosses the p-axis at $(\kappa_1, 0)$ and $(\kappa_2, 0)$. These points represent zero-torque wrenches with f_{ext} at the extreme orientations κ_1 and κ_2. By invoking the line-sweep algorithm at these two points rather than at the four vertices, one obtains two feasible equilibrium strips that can be processed as follows. The bounding lines of the two strips are parallel shifted by $-\tau_{ext}/\|f_{ext}\|$, using the values (f_{ext}, τ_{ext}) at the vertices of $\mathcal{W}$. This gives two narrower strips, and their intersection is precisely $\mathcal{R}(\mathcal{W})$.

2.4 Experimental Results

We describe preliminary experiments that measure the static response of a two-legged prototype to disturbance forces. The goal of these experiments is to validate the stance equilibrium criteria for an object supported by frictional contacts against gravity and subjected to disturbance forces. The experimental system shown in Figure 2.4 consists of a two-legged prototype made of Aluminium. The center-of-mass position can be freely changed by sliding a heavy weight on a bar mounted on a rotational joint. However, the experiments focus on the response to varying disturbance forces

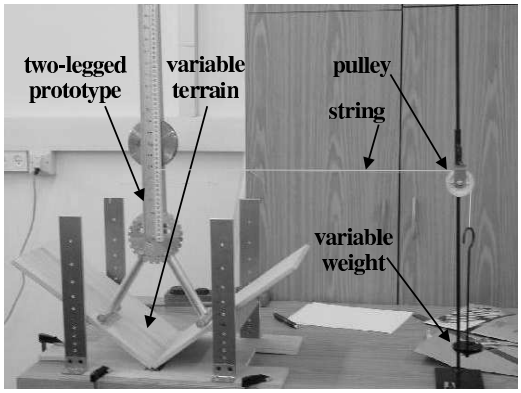

Figure 2.4: Experimental setup of a two-legged prototype.

under a fixed center-of-mass position. The mechanism is placed on a terrain made of two rigid segments with adjustable slopes. The segments in the experiments form a symmetric v-shaped terrain with fixed slopes of $\alpha = 26.7°$. The contacts are placed at equal heights on the two segments, at a horizontal distance $l = 237$ mm from each other. A horizontal force f_d is applied on the mechanism by a variable weight hung on a string attached through a pulley to the mechanism's central bar. The magnitude of f_d is then gradually increased until it reaches a critical value at which the contacts break, roll, or slip. The critical force is recorded, and the process is repeated for different heights of f_d's application point. Note that the measurements span a neighborhood about the origin in the (p, q) parametrization of the previous section: the variation of f_d's magnitude varies the orientation parameter p, and the variation of f_d's height varies the torque parameter q. As a preliminary step, the coefficient of friction was experimentally determined to be $\mu = 0.25$ with a standard deviation of $\pm 6.5\%$.

Let us first analyze the mechanism's response to varying disturbance forces. Let h denote the height of f_d's application point above the contacts. The disturbance

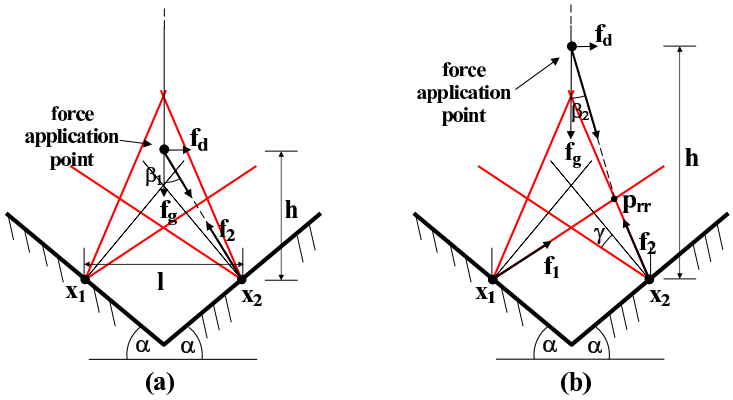

Figure 2.5: Graphical characterization of critical disturbance force: (a) $\|f_d\| = mg\tan(\beta_1)$, and (b) $\|f_d\| = mg\tan(\beta_2)$.

force has variable magnitude and application point height. The gravitational force has a constant magnitude mg, where $m = 2.4$ kg and g is the gravity constant. The net external force, $f_{ext} = f_g + f_d$, acts through the string attachment point at an angle $\beta = \tan^{-1}(\|f_d\|/mg)$ with respect to the vertical direction. The contact reaction forces are statically indeterminate in this setup, but critical events where an equilibrium ceases to be feasible can be determined as follows. Consider the case where f_d is directed to the right. In this case two critical events can occur. The first event occurs when the line of f_{ext} passes through x_2 (Figure 2.5(a)). In this case the contact reaction force at x_1 vanishes, resulting in contact breakage at x_1 and rolling about x_2. The corresponding critical force angle is $\beta_1 = \tan^{-1}(l/2h)$. The second event occurs when the line of f_{ext} passes through the intersection point of the friction cones' right edges (p_{rr} in Figure 2.5(b)). In this case both contacts start sliding to the *left,* and the contact reaction forces lie on the friction cones' right edges. The corresponding critical force angle is $\beta_2 = \tan^{-1}\left(l\sin 2\gamma/(2h\sin 2\gamma - l\cos 2\alpha - l\cos 2\gamma)\right)$, where $\gamma = \tan^{-1}(\mu) = 13.8°$. The critical disturbance force associated with contact breakage or sliding has magnitude $\|f_d\| = mg\tan(\beta)$ where $\beta = \min\{\beta_1, \beta_2\}$. The

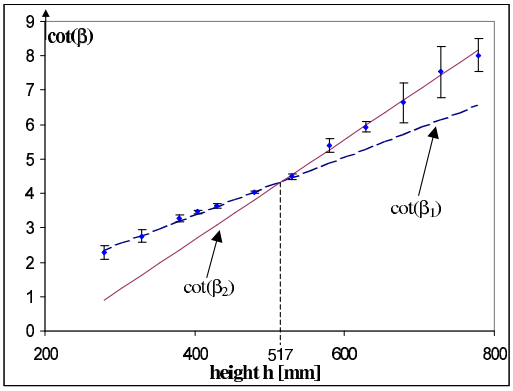

Figure 2.6: Experimental (dots) and theoretical (solid and dashed lines) results of $\cot(\beta)$ as a function of h. The bars represent two standard deviations.

event dominating $\min\{\beta_1, \beta_2\}$ can be determined as a function of f_d's application point as follows. When f_d's application point lies inside the polygon $\mathcal{C}_1 \cap \mathcal{C}_2$ as in Figure 2.5(a), $\beta_1 < \beta_2$ and the mechanism starts rolling about x_2. When f_d's application point lies above $\mathcal{C}_1 \cap \mathcal{C}_2$ as in Figure 2.5(b), $\beta_2 < \beta_1$ and the mechanism starts sliding at both contacts.

The experimental results are presented in Figure 2.6. For each force application height five experiments were conducted, and the average critical $\|f_d\|$ was measured with its corresponding angle β. In order to present a linear relationship, we plot $\cot(\beta)$ as a function of h. The dashed and solid lines are $\cot(\beta_1)$ and $\cot(\beta_2)$, computed analytically as a function of h. Since $\beta = \min\{\beta_1, \beta_2\}$, the experimental results were expected to follow the line of $\cot(\beta_1)$ for $h < h_0$, then follow the line of $\cot(\beta_2)$ for $h > h_0$. The height h_0 occurs when f_d's application point lies at the top of the polygon $\mathcal{C}_1 \cap \mathcal{C}_2$, given by $h_0 = l \cot(\alpha - \gamma)/2 = 517$ mm. The experimental results are marked as dots with error bars of two standard deviations. One can see a close matching of the predicted behavior with the experimental results. The close matching validates the criteria employed in the construction of the robust equilibrium region.

The experiments also indicate that feasible equilibrium stances are generated by the mechanism without any dynamic ambiguity. This topic is further discussed in [77].

More extensive experiments with a 3-legged robot are currently under preparation (see Figure 1.1). In these experiments the robot either supports itself on three legs while adjusting its center of mass position, or it supports itself on two legs while lifting a third leg to a new position. Both phases involve inertial forces generated by moving parts of the mechanism. These forces act as disturbances on the contacts, and the experiments will verify that selection of robust postures allows the contacts to passively resist these disturbance forces.

Chapter 3

Frictional Equilibrium Stances in 3D

This chapter is concerned with computation and graphical characterization of equilibrium postures for mechanisms supported by frictional point-contacts in a three-dimensional gravitational field. For a given set of contacts, this problem is reduced to the computation of the center-of-mass feasible region $\mathcal{R}$, that maintains equilibrium stances while satisfying the frictional constraints.

The main contributions of this chapter are as follows. First, it provides three different approaches for implicit formulations of $\mathcal{R}$, and shows that these formulations are essentially nonlinear due to the quadratic nature of frictional constraints in 3D. Second, it provides an exact formulation for the boundary of $\mathcal{R}$ for three contacts. Third, it gives a geometric interpretation for the boundary of $\mathcal{R}$, describes its topological structure, and discusses its relation with the famous *support polygon principle*. Finally, this chapter shows experimental results for a 3-legged prototype supported on frictional terrain, that validate the theoretical computation.

The structure of this chapter is as follows. The next section formulates the equilibrium condition, defines the feasible center-of-mass region $\mathcal{R}$, and reviews some of its fundamental properties. Section 3.2 reviews the *support polygon principle*, and discusses its relation with the feasible region $\mathcal{R}$ for 3-legged stances. Section 3.3 formulates $\mathcal{R}$ as a projection of a five-dimensional convex set onto a two-dimensional plane. Replacing the quadratic friction cones with polyhedrons, this problem can is approximated to arbitrary accuracy by standard methods for a projecting of polyhedral sets onto lower-dimensional subspaces. Section 3.4 formulates $\mathcal{R}$ as an intersection of a six-dimensional convex cone and a two-dimensional affine plane in wrench space. Using techniques of differential geometry, The exact boundary cells of $\mathcal{R}$ are then formulated, and graphical examples are provided. Section 3.5 provides geometric interpretations for the boundary of $\mathcal{R}$, and shows how its topological structure is affected by changing the coefficient of friction μ. Section 3.6 presents experimental results. Finally, the closing section discusses future extensions of the results to multiple contacts, and to stance robustness with respect to disturbance forces and torques.

3.1 Definition of Equilibrium Stances in 3D

We now define basic terminology and formulate the equilibrium condition in 3D. Then we define the feasible region of center-of-mass locations achieving equilibrium stances, and review some of its basic properties. Let a solid object $\mathcal{B}$ be supported by k frictional contacts under gravity. Let x_i be the position of the ith contact, and

let f_i be the ith contact reaction force. The static equilibrium condition is given by

$$\sum_{i=1}^{k} \begin{pmatrix} I \\ [x_i \times] \end{pmatrix} f_i = - \begin{pmatrix} I \\ \boldsymbol{x} \times \end{pmatrix} f_g \tag{3.1}$$

where x_i is the position of the ith contact, $\boldsymbol{x}$ is the position of $\mathcal{B}$'s center-of-mass, f_i is the ith contact reaction force, f_g is the gravitational force acting at $\boldsymbol{x}$, I is the 3×3 identity matrix, and $[a\times]$ is the cross-matrix satisfying $[a\times]v = a \times v$ for all $v \in I\!R^3$. Note that for any $k \geq 3$ the static solution for f_i is generically indeterminate of degree $3k - 6$. However, assuming point-contact with Coulomb's friction model, the contact forces f_i must lie in their respective friction cones $\mathcal{C}_i$, defined as

$$\mathcal{C}_i = \{f_i : f_i \cdot n_i \geq 0 \text{ and } (f_i \cdot s_i)^2 + (f_i \cdot t_i)^2 \leq (\mu f_i \cdot n_i)^2\}, \tag{3.2}$$

where μ is the coefficient of friction, n_i is the outward unit normal at x_i, and s_i, t_i are unit tangents at x_i, such that (s_i, t_i, n_i) is a right-handed frame. The friction constraints can also be written as the following linear and quadratic inequalities;

$$\begin{aligned} \mathcal{C}_i &= \{f_i : f_i \cdot n_i \geq 0 \text{ and } f_i^T B_i f_i \leq 0\}, \text{ where} \\ B_i &= [s_i \;\; t_i \;\; n_i] \cdot \mathsf{diag}(1, 1, -\mu^2) \cdot [s_i \;\; t_i \;\; n_i]^T. \end{aligned} \tag{3.3}$$

We assume that the coefficient of friction μ at all contacts is known. A 3D stance is defined by the contact points x_i and the center-of-mass position $\boldsymbol{x}$. For a given set of contacts $x_1 \ldots x_k$, the 3D feasible equilibrium region ,denoted $\mathcal{R}$, is all center-of-mass locations for which there exist contact reaction forces $f_i \in \mathcal{C}_i$ that satisfy the static equilibrium condition (3.1). The goal of this chapter is to compute the feasible region $\mathcal{R}$ for any given set of contacts. First, we review some fundamental properties of $\mathcal{R}$, summarized in the following proposition.

Proposition 3.1.1 ([81]) *Let a solid object $\mathcal{B}$ be supported by k frictional contacts against gravity in three-dimensions. If the feasible equilibrium region $\mathcal{R}$ is nonempty, it is an infinite vertical prism. This prism is a single connected set and its cross-section is convex. Furthermore, its dimension for k contacts is generically* $\min\{3, k\}$.

It is worth noting that for a single contact $\mathcal{R}$ is a vertical line through the contact, and for two contacts it is a vertical strip in the plane passing through the contacts. For $k \geq 3$ contacts $\mathcal{R}$ is a vertical prism whose position has no obvious relation to the position of the contacts. However, in the special case where all friction cones contain the upward vertical direction, the prism $\mathcal{R}$ contains the contacts. This special case is related to the familiar support polygon principle, discussed in the next section. Note, too, that for $k \geq 3$ contacts, a special case occurs when all contacts are aligned along a common spatial line. In this non-generic case, $\mathcal{R}$ degenerates to a two-dimensional strip that lies within the vertical plane passing through the contacts.

The problem of computing the prism $\mathcal{R}$ is thus reduced to computing its horizontal cross-section, denoted $\widetilde{\mathcal{R}}$, in $\mathbb{R}^2$. Since $k = 3$ is the smallest number of contacts for which $\mathcal{R}$ is fully three-dimensional, this chapter focuses on the computation of $\widetilde{\mathcal{R}}$ for 3-contact stances, while in the concluding section we discuss the extension to multiple contacts.

3.2 Relation to The Support Polygon Principle

The support polygon principle (known as the tripod rule in 3-legged cases) appears in the early quasi-static locomotion literature as a posture stability criterion over flat horizontal terrains [65]. This principle states that $\mathcal{B}$'s center-of-mass must lie in a vertical prism, denoted Π, which is spanned by the contacts. The support

polygon, denoted $\widetilde{\Pi}$, is defined as the horizontal projection of Π. In the following, we show that *for non-flat frictional terrains, the support polygon principle may yield unstable stances.* We test the support polygon principle for 3-legged stances on general frictional terrains, and characterize the stances for which Π gives the exact feasible region $\mathcal{R}$. We also characterize the stances for which either $\mathcal{R} \subset \Pi$ or $\Pi \subset \mathcal{R}$.

We will use the following definitions. First, $\boldsymbol{e} = (0\ 0\ 1)$ denotes the upward vertical direction. A contact x_i is defined as *quasi-flat* if $\boldsymbol{e} \in \mathcal{C}_i$. A stance is defined as *quasi-flat* if all its contacts are quasi-flat (Figure 3.1(a)). Second, the *base plane* $\mathcal{B}_o$ denotes the plane passing through the three contact points in $\mathbb{R}^3$, and n_o denotes the normal to $\mathcal{B}_o$, chosen such that $\boldsymbol{e} \cdot n_o \geq 0$. A 3-legged stance is defined as *tame* if $\boldsymbol{e} \cdot n_o > 0$ and all forces $f_i \in \mathcal{C}_i$ satisfy $f_i \cdot n_o > 0$ for $i = 1, 2, 3$. The following theorem determines the relation between $\mathcal{R}$ and Π.

Theorem 3 *Let a solid object $\mathcal{B}$ be supported in a 3-legged stance on frictional contacts against gravity in three-dimensions. Let $\mathcal{R}$ denote the feasible equilibrium region, and let Π denote the vertical prism spanned by the contacts. Then:*

1. *For quasi-flat stances,* $\Pi \subseteq \mathcal{R}$

2. *For tame stances,* $\Pi \supseteq \mathcal{R}$.

Proof sketch: The proof of part 1 is trivial and uses the convexity of $\mathcal{R}$. The proof of part 2 is based on the following argument. Let l_{ij} denote the line passing through two contacts x_i and x_j, and let x_k denote the third contact. It can be shown that for a tame equilibrium stance, any contact force $f_k \in \mathcal{C}_k$ at x_k generates a torque about l_{ij} whose sign opposes the torque about l_{ij} generated by the gravitational force f_g acting at x_k. This implies that the center-of-mass $\boldsymbol{x}$ must lie in a halfspace bounded

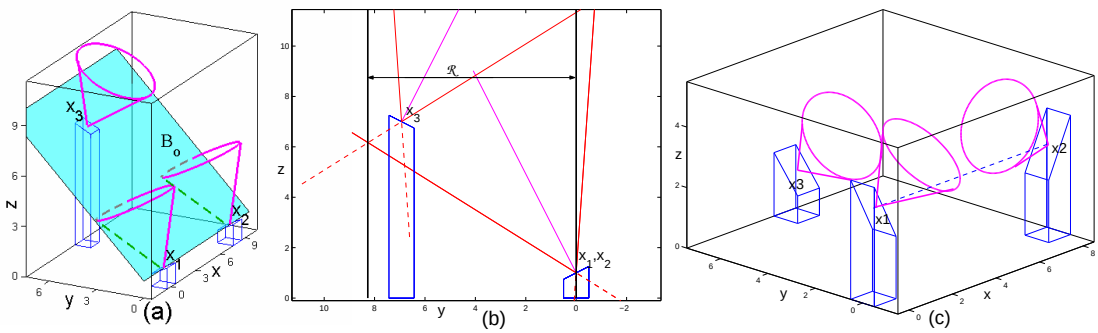

Figure 3.1: (a) A 3-legged non-tame stance and (b) its projection onto yz symmetry plane, together with the projected $\mathcal{R}$. (c) A 3-legged force-closure stance.

by the vertical plane passing through x_i and x_j in order to maintain equilibrium. The detailed proof appears in Appendix A. □

Examples: We start with two examples of non-tame stances where $\Pi \subset \mathcal{R}$. Figure 3.1(a) shows a non-tame but quasi-flat stance with $\mu = 0.5$. Figure 3.1(b) shows the projection of the feasible equilibrium region $\mathcal{R}$ onto the yz plane for this stance. Due to symmetry, this projection can be computed using planar methods developed in [80], while considering the yz-projection of the friction cones. It is clearly seen that the left bound of $\mathcal{R}$ exceeds the support polygon. Note the fact that the contacts x_1, x_2 lie within the yz- projection of the friction cone $\mathcal{C}_3$, which violates the condition for a tame stance. This situation is common in vertical climbing applications [13] . Figure 3.1(c) shows a non-tame non-quasi-flat stance with $\mu = 0.5$. Notice that the spatial line segment connecting x_1 and x_2 (dashed) is fully contained in $\mathcal{C}_1$ and $\mathcal{C}_2$, and intersects $\mathcal{C}_3$. In this situation the three contacts establish 3D force closure [72]. Therefore, the contacts can resist any gravitational load, and the feasible region is the entire space $\mathcal{R} = I\!R^3$. This situation is common in grasping or fixturing applications .

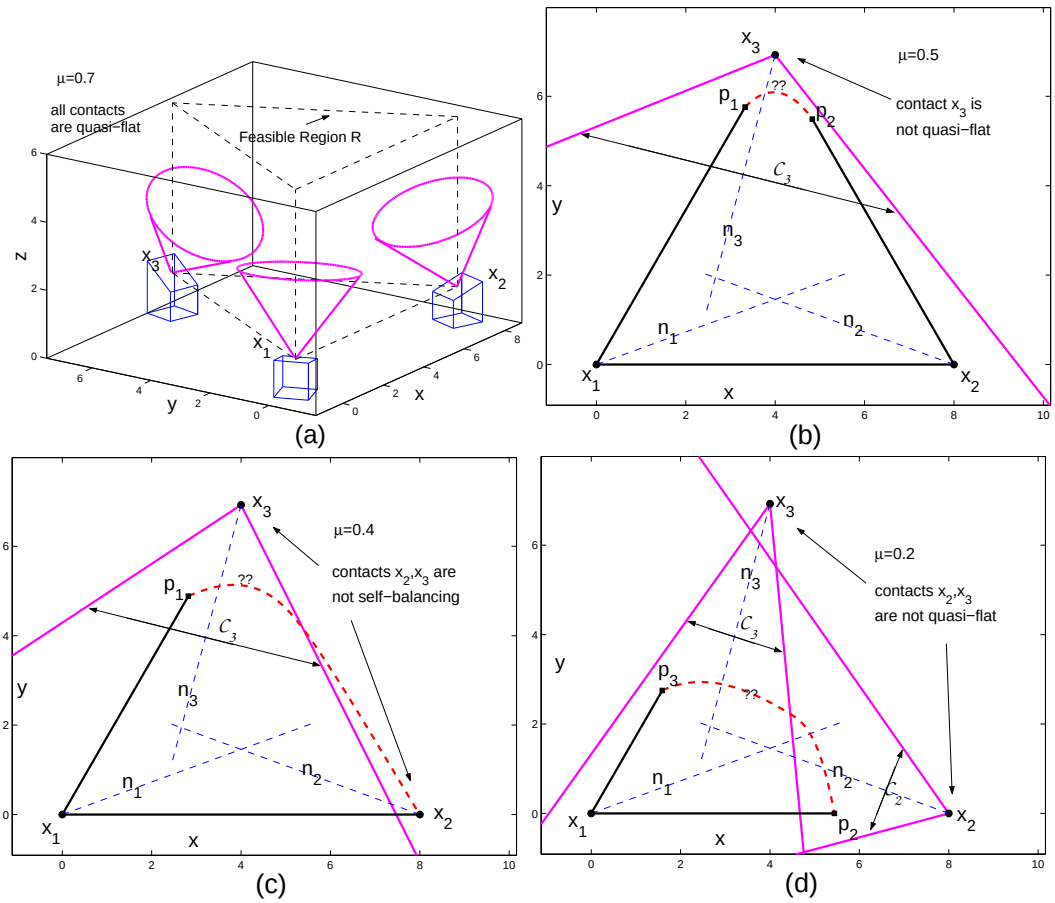

Figure 3.2: (a) A 3-legged tame stance for $\mu = 0.7$, and its horizontal projections for (b) $\mu = 0.5$, (c) $\mu = 0.4$, and (d) $\mu = 0.2$.

In the rest of this chapter we focus on tame stances, for which $\mathcal{R} \subseteq \Pi$. On nearly-horizontal terrains where the coefficient of friction μ is sufficiently large, all contacts are quasi-flat. In this case, theorem 3 implies that $\mathcal{R} = \Pi$, and the classical support polygon principle holds true. However, when the contact normals are more inclined and μ is smaller, the support polygon is an over approximation of the feasible region $\mathcal{R}$, as shown in the following example.

Figure 3.2(a) shows a 3-contact tame stance with coefficient of friction $\mu = 0.7$. In this case, all contacts are quasi-flat, hence the feasible region $\mathcal{R}$ is precisely the prism Π. However, decreasing of μ significantly changes the properties of $\mathcal{R}$ and its horizontal cross-section $\widetilde{\mathcal{R}}$. Figure 3.2(b) shows a top view of the same 3-contact stance, with $\mu = 0.5$. Let $\tilde{x}_i$ and $\tilde{\mathcal{C}}_i$ denote the horizontal projections of the contacts x_i and the friction cones $\mathcal{C}_i$ (for convenience, the symbol '$\sim$' is omitted in the labelling inside the figures). Note that in this case the contacts x_1 and x_2 are quasi-flat, while x_3 is not. Therefore, the horizontal projections $\tilde{\mathcal{C}}_1$ and $\tilde{\mathcal{C}}_2$ span the entire plane, while $\tilde{\mathcal{C}}_3$ is a planar sector. Since $x_1, x_2 \in \mathcal{R}$, the whole line segment $\tilde{x}_1 - \tilde{x}_2$ lies on the boundary of $\widetilde{\mathcal{R}}$. However, $x_3 \notin \mathcal{R}$, hence only parts of the segments $\tilde{x}_1 - \tilde{x}_3$ and $\tilde{x}_2 - \tilde{x}_3$ lie on the boundary of $\widetilde{\mathcal{R}}$, ending at the points $\tilde{p}_1$ and $\tilde{p}_2$. The line segment $\tilde{x}_i - \tilde{p}_i$ for $i = 1, 2$ is a horizontal projection of a planar vertical strip, which is precisely the feasible equilibrium region associated with two active contacts at x_i and x_3. This vertical strip can be computed by applying the planar methods shown in [80] while the contact forces are restricted to lie within the vertical plane passing through x_i and x_3. Note that *there is an unknown missing part in the boundary of* $\widetilde{\mathcal{R}}$, between $\tilde{p}_1$ and $\tilde{p}_2$. Note, too, that due to the convexity of $\widetilde{\mathcal{R}}$, the line segment $\tilde{p}_1 - \tilde{p}_2$ is contained in $\widetilde{\mathcal{R}}$, and can be used as a conservative approximation for this missing boundary.

Figure 3.2(c) shows the horizontal projection of contact normals and friction cones for $\mu = 0.4$. Notice that since the projected cone $\tilde{\mathcal{C}}_3$ does not contain $\tilde{x}_2$, contacts x_2 and x_3 alone cannot balance any gravitational load, and the segment $\tilde{x}_2 - \tilde{x}_3$ does not contribute any part to the boundary of $\widetilde{\mathcal{R}}$. As before, contacts x_1 and x_3 contribute the segment $\tilde{x}_1 - \tilde{p}_1$, and there is an unknown missing part between $\tilde{p}_1$ and $\tilde{x}_2$.
Figure 3.2(d) shows the horizontal projection of contact normals and friction cones for $\mu = 0.2$. The contacts x_2 and x_3 are not quasi-flat, but x_1 is still quasi-flat and $\tilde{x}_1$ is contained in $\tilde{\mathcal{C}}_2$ and $\tilde{\mathcal{C}}_2$. Therefore, the boundary of $\widetilde{\mathcal{R}}$ now consists of the segments $\tilde{x}_1 - \tilde{p}_3$ and $\tilde{x}_1 - \tilde{p}_2$, together with a missing unknown part connecting $\tilde{p}_2$ and $\tilde{p}_3$.
In these examples the support polygon principle is obviously an *over-approximation* of the feasible region $\mathcal{R}$. Therefore, it is unsafe to apply this principle for non-flat terrains with low friction. The objective of the next sections is to compute the exact feasible region $\mathcal{R}$ on non-flat frictional terrain. In particular, we compute the boundaries of the horizontal cross-section $\widetilde{\mathcal{R}}$ associated with three contact forces, which cannot be computed by planar methods. We use three different approaches to derive implicit formulations for $\mathcal{R}$.

3.3 Formulation of the Feasible Region Using Projection

This section formulates the feasible region $\mathcal{R}$ for three-contact stances as a projection of a nonlinear convex region in a five-dimensional space. First, we rewrite the static equilibrium condition (3.1) in matrix form. Define $\boldsymbol{f} = (f_1, f_2, f_3) \in \mathbb{R}^9$ as the combined forces vector. The equilibrium condition (3.1) can be rewritten in matrix form as

$$G\boldsymbol{f} = T\tilde{x} + u_o,$$

$$\text{where } G = \begin{pmatrix} I & I & I \\ [x_1\times] & [x_2\times] & [x_3\times] \end{pmatrix}, T = \begin{pmatrix} 0_{3\times 2} \\ EJ^T \end{pmatrix} \quad , \quad u_o = \begin{pmatrix} -f_g \\ \vec{0} \end{pmatrix}, \tag{3.4}$$

and $\tilde{x}$ is the horizontal projection of the center-of-mass location. The static response is indeterminate of degree 3. Therefore, the static forces f_i can be expressed by $\boldsymbol{\eta} \in I\!R^3$ and $\tilde{\boldsymbol{x}} \in I\!R^2$, as

$$\boldsymbol{f} = M_\eta \boldsymbol{\eta} + M_x \tilde{\boldsymbol{x}} + \boldsymbol{\eta}_o, \tag{3.5}$$

where $M_\eta \in I\!R^{9\times 3}$ is a matrix whose columns span the nullspace of G, $M_x = G^\dagger T$ and $\boldsymbol{\eta}_o = G^\dagger u_o$, where $G^\dagger \in I\!R^{9\times 6}$ is a left pseudo-inverse of G. The pair $(\tilde{\boldsymbol{x}}, \boldsymbol{\eta})$ parametrizes all center-of-mass locations and contact forces satisfying the equilibrium condition (3.4). The frictional constraints (3.3) can be rewritten as:

$$\boldsymbol{f} \cdot \bar{n}_i \geq 0 \quad , \quad \boldsymbol{f}^T \bar{B}_i \boldsymbol{f} \geq 0 \quad , \quad i = 1, 2, 3, \tag{3.6}$$

where $\bar{n}_i$ and $\bar{B}_i$ are n_i and B_i properly augmented in a column vector and a block-diagonal matrix respectively. Substituting the expression for $\boldsymbol{f}$ in (3.5) into the inequality constraints (3.6), gives six inequalities in $(\tilde{\boldsymbol{x}}, \boldsymbol{\eta})$. These inequalities define a feasible region $\mathcal{E}$ in $(\tilde{\boldsymbol{x}}, \boldsymbol{\eta})$ space:

$$\begin{aligned} \mathcal{E} = \{(\tilde{\boldsymbol{x}}, \boldsymbol{\eta}) : \quad & \bar{n}_i \cdot (M_\eta \boldsymbol{\eta} + M_x \tilde{\boldsymbol{x}} + \boldsymbol{\eta}_o) \geq 0, \text{ and} \\ & (M_\eta \boldsymbol{\eta} + M_x \tilde{\boldsymbol{x}} + \boldsymbol{\eta}_o)^T \bar{B}_i (M_\eta \boldsymbol{\eta} + M_x \tilde{\boldsymbol{x}} + \boldsymbol{\eta}_o) \geq 0, \\ & \text{for } i = 1, 2, 3\}. \end{aligned} \tag{3.7}$$

It can be shown that $\mathcal{E}$ is a convex region, and that for tame stances it is also bounded. A key observation is that the cross-section $\widetilde{\mathcal{R}}$ of the center-of-mass feasible region is precisely the projection of $\mathcal{E}$ onto the $\tilde{\boldsymbol{x}}$-plane. In the following we provide an implicit formulation for the exact boundary of $\widetilde{\mathcal{R}}$, which cannot be practically implemented

for explicit computation. Then we show that when replacing the quadratic friction cones with circumscribed polyhedra, the projection approach naturally leads to an efficient polygonal approximation of $\widetilde{\mathcal{R}}$.

3.3.1 Exact formulation

We now characterize the the boundary curves of $\widetilde{\mathcal{R}}$, and express them as solutions of systems of quadratic polynomials in $(\tilde{\boldsymbol{x}}, \boldsymbol{\eta})$. The boundary curves of $\widetilde{\mathcal{R}}$ are projection of *silhouette curves* of $\mathcal{E}$. The following theorem which characterizes the silhouette curves, is an adaptation of standard results to our purposes (e.g. [19, p. 102]).

Theorem 4 (Silhouette Theorem) *Let $\Pi : I\!R^5 \to I\!R^2$ be the coordinate projection $\Pi(\tilde{\boldsymbol{x}}, \boldsymbol{\eta}) = \tilde{\boldsymbol{x}}$. Let $\mathcal{E} = \{(\tilde{\boldsymbol{x}}, \boldsymbol{\eta}) \in I\!R^5 : \Psi_1(\tilde{\boldsymbol{x}}, \boldsymbol{\eta}) \leq 0, \ldots, \Psi_6(\tilde{\boldsymbol{x}}, \boldsymbol{\eta}) \leq 0\}$. Then $\Pi(\mathcal{E})$ is a two-dimensional region bounded by the projection of the silhouette curves of $\mathcal{E}$, consisting of critical points of Π on the boundary of $\mathcal{E}$. Moreover, the silhouette curves consist of points $(\tilde{\boldsymbol{x}}, \boldsymbol{\eta}) \in \mathcal{E}$ on which the gradients $\{\nabla_\eta \Psi_{i_1}(\tilde{\boldsymbol{x}}, \boldsymbol{\eta}), \ldots, \nabla_\eta \Psi_{i_n}(\tilde{\boldsymbol{x}}, \boldsymbol{\eta})\}$ positively span the zero vector, where $\Psi_{i_1}, \ldots, \Psi_{i_n}$ are the constraints that vanish at $(\tilde{\boldsymbol{x}}, \boldsymbol{\eta})$.*

We now provide a characterization of the silhouette curves of $\mathcal{E}$ by using the Silhouette Theorem. Note that the set defined by $\bar{n}_i \cdot (M_\eta \boldsymbol{\eta} + M_x \tilde{\boldsymbol{x}} + \boldsymbol{\eta}_o) = 0$ for some $i \in \{1, 2, 3\}$, if nonempty, is a line in $(\tilde{\boldsymbol{x}}, \boldsymbol{\eta})$ space, and is automatically a silhouette curve of $\mathcal{E}$. Therefore we focus on silhouette curves associated with contact forces that are all active, hence all contact forces satisfy $n_i \cdot f_i > 0$ for $i = 1 \ldots k$, and all the linear constraints in (3.6) do not vanish. Let us define the $\Psi_i = (M_\eta \boldsymbol{\eta} + M_x \tilde{\boldsymbol{x}} + \boldsymbol{\eta}_o)^T \bar{B}_i (M_\eta \boldsymbol{\eta} + M_x \tilde{\boldsymbol{x}} + \boldsymbol{\eta}_o)$ for $i = 1, 2, 3$. The gradient of Ψ_i is given by $\nabla_\eta \Psi_i = 2\bar{B}_i (M_\eta \boldsymbol{\eta} + M_x \tilde{\boldsymbol{x}} + \boldsymbol{\eta}_o)$.

Note that $\nabla_\eta \Psi_i$ is linear in $(\boldsymbol{x}, \boldsymbol{\eta})$. The silhouette curves can be now classified as type-1 to type-3 curves, where type-n curves consist of points $(\tilde{\boldsymbol{x}}, \boldsymbol{\eta}) \in \partial\mathcal{E}$ for which n of the quadratic forms $\Psi_i(\tilde{\boldsymbol{x}}, \boldsymbol{\eta})$ vanish.

Type-1 curves lie within a four-dimensional submanifold of $I\!R^5$ defined by $\{(\tilde{\boldsymbol{x}}, \boldsymbol{\eta}) : \Psi_i(\tilde{\boldsymbol{x}}, \boldsymbol{\eta}) = 0$, for some $i \in \{1, 2, 3\}\}$. The silhouette condition implies that $\nabla_\eta \Psi_i = \vec{0}$. Therefore, the type-1 silhouette curves are defined as the solution set of a system of three linear equations and one quadratic equation in five unknowns. These curves can be formulated explicitly as a solution of a quadratic equation in $(\tilde{\boldsymbol{x}}, \boldsymbol{\eta})$. In the next section we show that for our problem, type-1 silhouette curves do not generically exist.

Type-2 curves lie within a 3-dimensional submanifold of $I\!R^5$ defined by $\{(\tilde{\boldsymbol{x}}, \boldsymbol{\eta}) : \Psi_{i_1}(\tilde{\boldsymbol{x}}, \boldsymbol{\eta}) = 0$ and $\Psi_{i_1}(\tilde{\boldsymbol{x}}, \boldsymbol{\eta}) = 0\}$, where $i_1, i_2 \in \{1, 2, 3\}$. The silhouette condition implies that the matrix $M_2(\tilde{\boldsymbol{x}}, \boldsymbol{\eta}) = [\nabla_\eta \Psi_{i_1} \ \nabla_\eta \Psi_{i_2}]$ must be rank-deficient. This implies that two determinants of 2×2 sub-matrices of $M_2(\tilde{\boldsymbol{x}}, \boldsymbol{\eta})$ must vanish. Therefore, the type-2 silhouette curves associated with the indices i_1, i_2 are defined as the intersection of two quadratic hypersurfaces $\Psi_{i_1} = 0$, $\Psi_{i_2} = 0$, and two determinants of square sub-matrices of M_2, which are also quadratic in $(\tilde{\boldsymbol{x}}, \boldsymbol{\eta})$. This amounts to solving a set of four polynomial equations in five unknowns, which results in a one-dimensional solution set.

Type-3 curves lie within a two-dimensional submanifold of $I\!R^5$ defined by $\{(\tilde{\boldsymbol{x}}, \boldsymbol{\eta}) : \Psi_i(\tilde{\boldsymbol{x}}, \boldsymbol{\eta}) = 0$, $i = 1, 2, 3$. The silhouette condition implies that the matrix $M_3(\tilde{\boldsymbol{x}}, \boldsymbol{\eta}) = [\nabla_\eta \Psi_1 \ \nabla_\eta \Psi_2 \ \nabla_\eta \Psi_3]$ must be rank-deficient. This condition gives an additional equation which is in $(\tilde{\boldsymbol{x}}, \boldsymbol{\eta})$. Thus, type-3 silhouette curves are the one-dimensional solution set of a system of three quadratic equations and a cubic equation in five unknowns. The total degree of this system is 24, while the total degree of type-2 curves is 16.

Note that some parts of the solution sets must be discarded, because they do not satisfy the condition of *positive* span. For a given solution $(\tilde{\boldsymbol{x}}, \boldsymbol{\eta})$, checking the positive span condition can be done by solving a simple linear program. The projection of all the silhouette curves onto $\tilde{x}$-plane results in a planar arrangement of candidate boundary curves. Finally, the actual boundary consists of the "outmost" curves, and can by simply taking the convex hull of all curves.

The projection approach provides implicit formulation of all candidate boundary curves, for three of frictional contacts (see [79] for generalization to k contacts). Each boundary curve is formulated as solution of a system of four polynomial equations in $(\tilde{\boldsymbol{x}}, \boldsymbol{\eta})$. The total degree of each polynomial system is less than or equal to 24. However, applying standard elimination methods [95] for eliminating $\boldsymbol{\eta}$ and obtaining a single polynomial in $\tilde{\boldsymbol{x}}$, results in a highly redundant polynomial of degree higher than 1000. Therefore, this formulation is essentially impractical for exact computation of $\widetilde{\mathcal{R}}$. Nevertheless, we now show that the projection approach naturally leads to an efficient polygonal approximation of $\widetilde{\mathcal{R}}$, when the quadratic friction cones are replaced with circumscribed polyhedra

3.3.2 Approximate computation

We now present an approximate solution using polyhedral approximation of the quadratic frictional constraints, and applying an efficient algorithm for projection of a high-dimensional convex polytope onto a lower dimensional space. First, we formulate the approximation of friction cones by n-sided polyhedra. Then we represent the approximate linear constraint in the equilibrium space and derive the approximate feasible region $\mathcal{E}'$. Computing the approximation for $\widetilde{\mathcal{R}}$ is thus reduced to projection of a five-dimensional convex polytope onto a plane, which can be implemented by

efficient algorithms.

The exact friction cone in 3D can be approximated by an inscribed n-sided polyhedron, such that the quadratic constraint (3.2) is replaced with n linear constraints. The approximate polyhedron $\mathcal{C}'_i$ is defined by

$$\begin{aligned}\mathcal{C}'_i = \{f_i : &(\sin\theta_{j+1} - \sin\theta_j)(f_i \cdot s_i) \\ &+(\cos\theta_j - \cos\theta_{j+1})(f_i \cdot t_i) \leq \beta(f_i \cdot n_i)\ ,\ j = 1 \ldots n\},\end{aligned} \tag{3.8}$$

where $\theta_j = \frac{2\pi j}{n}$, $\beta = \mu \sin\left(\frac{2\pi}{n}\right)$. The linear constraints can be written in matrix form as $A_i f_i \leq 0$, where

$$A_i = \begin{pmatrix} \sin\theta_2 - \sin\theta_1 & \cos\theta_1 - \cos\theta_2 & -\beta \\ \vdots & \vdots & \vdots \\ \sin\theta_{n+1} - \sin\theta_n & \cos\theta_n - \cos\theta_{n+1} & -\beta \end{pmatrix} \begin{pmatrix} s_i & t_i & n_i \end{pmatrix}^T .$$

Using the equilibrium space parametrization (3.5), the approximated feasible region in $(\tilde{\boldsymbol{x}}, \boldsymbol{\eta})$ space is the convex polytope defined by

$$\mathcal{E}' = \{(\tilde{\boldsymbol{x}}, \boldsymbol{\eta}) : \ \ \bar{A}_i(M_\eta \boldsymbol{\eta} + M_x \tilde{\boldsymbol{x}} + \boldsymbol{\eta}_o) \leq 0,\ \text{, for } i = 1 \ldots k\} \tag{3.9}$$

Where $\bar{A}_i$ is a proper augmentation of A_i in a block-diagonal matrix of dimensions $3n \times 9$. The approximation of $\widetilde{\mathcal{R}}$ now reduces to computation of the convex polygon $\widetilde{\mathcal{R}}'$ obtained by projecting $\mathcal{E}'$ onto $\tilde{\boldsymbol{x}}$-plane. This is a classical problem, which is widely explored in computational geometry literature (e.g. [43, 47]). In the following graphical examples, we implement a variant of the efficient contour-tracking algorithm proposed by Ponce et al. [90] for projection of a high-dimensional convex polytope onto a lower dimensional space, in the context of grasp planning. According to the analysis in [90], the algorithm solves a sequence of linear programs, and runs in $O(nt)$ time, where t is the number of edges in the resulting polygon. The resulting

projected is a polygonal region $\widetilde{\mathcal{R}}'$, which is inscribed within $\widetilde{\mathcal{R}}$, and thus can be used as a conservative approximation. Moreover, one can use circumscribing polyhedra instead of inscribed polyhedra for approximating the friction cones, by simply replacing μ by $\mu/\cos(\pi/n)$ in (3.8). The resulting projection is polygonal region $\widetilde{\mathcal{R}}''$, which is circumscribing $\widetilde{\mathcal{R}}$, and thus can be used as a outer approximation. These two approximation can be made arbitrarily accurate by increasing the number of facets n, for the cost of growing computational complexity.

Graphical example:

Consider the three-contact stance with the same contact arrangement of Fig. 3.2. Using the approximate projection method, Figs. 3.3a,b,c shows the inscribed and circumscribing polygonal approximations $\mathcal{R}'$ (shaded region) and $\mathcal{R}''$ (dashed line), for coefficient of friction 0.5, 0.4, and 0.2, respectively. Recall that the points p_i on the edges of the support polygon in Fig. 3.2 were computed using planar methods for two nonzero contact forces. Note, however, that not all of these points are contained in the conservative approximations $\widetilde{\mathcal{R}}'$. Note, too, that $\widetilde{\mathcal{R}}'$ depends strongly on the choice of the tangent unit vectors s_i, t_i, which affects the rotation angle of the inscribed polyhedron $\mathcal{C}_i'$ about n_i.

3.4 Formulating the Feasible Region in Wrench Space

This section presents a novel method for computing the feasible equilibrium region. In this method $\widetilde{\mathcal{R}}$ is formulated as an intersection of a six-dimensional nonlinear cone and an affine two-dimensional subspace in wrench space. Let *wrench space* have force-and-torque coordinates $(f, \tau) \in \mathbb{R}^6$. As $\mathcal{B}$'s center of mass varies in physical space,

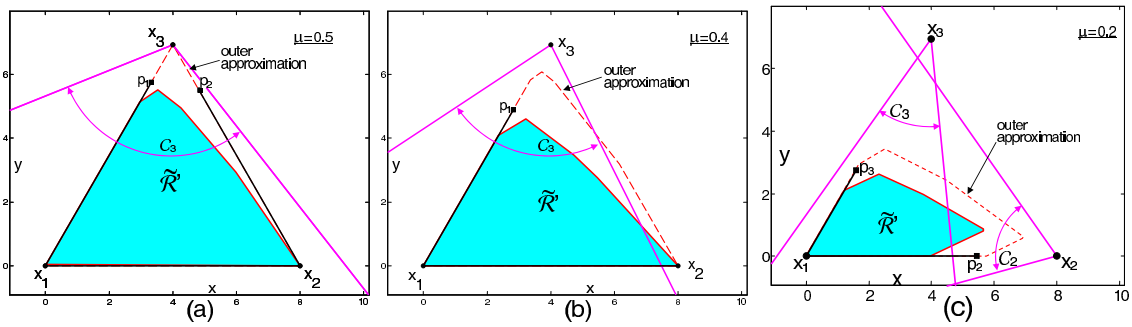

Figure 3.3: Polyhedral approximation of $\widetilde{\mathcal{R}}$ for a 3-contact stance with (a)$\mu = 0.5$, (b)$\mu = 0.4$, (c)$\mu = 0.4$.

the gravitational wrench on the right side of (3.1) spans a two-dimensional affine subspace in wrench space (the component of $\boldsymbol{x}$ along $\boldsymbol{e}$ is mapped to zero). Let L denote this subspace. On the other hand, as the contact forces vary in their friction cones, their net reaction wrench on the left side of (3.1) spans a cone in wrench space. Let N denote this cone. The intersection $N \cap L$ is generically a two-dimensional region in wrench space. This region contains all net wrenches that can be generated by the contact forces, and balance the wrench of gravitational force acting at $\boldsymbol{x}$. Any wrench $(f, \tau) \in N \cap L$ is associated with a single center-of-mass horizontal position $\tilde{\boldsymbol{x}}$, via the linear mapping $\tau = \boldsymbol{x} \times f_g$. Therefore, the horizontal cross section $\widetilde{\mathcal{R}}$ is fully determined by the region $N \cap L$ in wrench space. Since $\widetilde{\mathcal{R}}$ is convex, $N \cap L$ is also convex, thus the problem reduces to computation of its one-dimensional boundary. This computation is conducted in three stages, as follows. First, we characterize the *equilibrium contact forces*, which are contact forces generating wrenches that lie on the affine subspace L. Then we characterize *critical contact forces*, which are contact forces generating wrenches that lie on the five-dimensional boundary the wrench cone N. Finally we compute the *critical equilibrium contact forces*, generating wrenches that lie on the boundary of the intersection $N \cap L$, and formulate the boundary

curves of $\widetilde{\mathcal{R}}$. The results are demonstrated on the same graphical example presented in section 3.2.

3.4.1 Characterizing equilibrium contact forces

We now characterize the contact forces generating wrenches that lie on the affine subspace L. Such contact forces balance the gravitational force f_g, and generate zero torque about the vertical axis. The characterization of such contact forces is given in the following lemma.

Lemma 3.4.1 *Given a 3-legged tame stance with contacts at x_1, x_2, x_3, the contact forces f_1, f_2, f_3 generate a wrench that lies on L if and only if they satisfy the following conditions:*

1. A single nonzero contact force f_i generates a wrench that lies on L if and only if $f_i = -f_g$.

2. Two nonzero contact forces f_i and f_j generate a wrench that lies on L if and only if they lie in the vertical plane that passes through the contacts x_i and x_j, and satisfy $f_i + f_j = -f_g$.

3. Three nonzero contact forces f_1, f_2, f_3 associated with L if and only if they satisfy

$$\begin{aligned} &f_1 + f_2 + f_3 = -f_g, \text{ and } \det[H_1 f_1 \; H_2 f_2 \; H_3 f_3] = 0, \\ &\text{where } H_i = \begin{pmatrix} E^T \\ \boldsymbol{e}^T [x_i \times] \end{pmatrix} \text{ for } i = 1, 2, 3. \end{aligned} \tag{3.10}$$

Proof: The cases of one or two nonzero contact forces can be verified by inspection. In the case of three nonzero contact forces, in order to generate equilibrium, they must balance f_g. Moreover, they must generate zero torque about the vertical axis.

Therefore, the horizontal projections of the contact forces must intersect at a single point. These two conditions are formulated in (3.10). $\square$

3.4.2 Characterizing critical contact forces

We now characterize the contact forces generating wrenches that lie on the boundary of the cone N. The cone N consists of all wrenches generated by contact forces that satisfy the frictional constraints, and can be formulated as

$$N = \{w = \sum_{i=1}^{3} \begin{pmatrix} f_i \\ x_i \times f_i \end{pmatrix} \ , \ f_i \in \mathcal{C}_i\}. \tag{3.11}$$

This cone is generically six-dimensional, and our goal is to compute the contact forces f_i generating wrenches that lie on its five-dimensional boundary. As a preliminary step, let us define some additional notations. Recall that the base plane $\mathcal{B}_o$ was defined as the plane passing through the contacts, and that n_o denotes the normal to $\mathcal{B}_o$. Let s_o and t_o denote two orthogonal unit vectors in $\mathcal{B}_o$, such that (s_o, t_o, n_o) is a right-handed frame. Finally, let $E_o = I - n_o n_o^T$ denote the matrix that projects vectors in $I\!R^3$ onto $\mathcal{B}_o$, and define $R_{90} = I + [n_o \times]$ as the 90°-rotation matrix about n_o. Each nonzero contact force f_i that lies on the boundary of its friction cone can be parametrized by the pair $(c_i, \phi_i) \in I\!R^+ \times [0, 2\pi)$ as

$$f_i = c_i u_i(\phi_i), \text{ where } u_i(\phi_i) = \mu \cos(\phi_i) s_i + \mu \sin(\phi_i) t_i + n_i. \tag{3.12}$$

Let $\mathcal{B}_i(\phi_i)$ denote the plane tangent to the boundary of $\mathcal{C}_i$ that contains $u_i(\phi_i)$, and let l_{i0} denote the line of intersection between the tangent plane $\mathcal{B}_i(\phi_i)$ and the base plane $\mathcal{B}_o$. Finally, define $M_i = I - (1+\mu^2) n_i n_i^T$. It can then be verified that $M_i u_i(\phi_i)$ is normal to $\mathcal{B}_i(\phi_i)$, and that the vector $l_i = R_{90} E_o M_i u_i(\phi_i)$ is parallel to l_{i0}.

The following lemma formulates three different types of critical contact forces associated with five-dimensional boundary cells of N, and provides their geometric interpretation.

Lemma 3.4.2 *Given a 3-legged tame stance with contacts at x_1, x_2, x_3 and their friction cones $\mathcal{C}_1, \mathcal{C}_2, \mathcal{C}_3$, there are three types of critical contact forces. The critical forces are associated with three different types of five-dimensional boundary cells of the wrench cone N, and are formulated as follows:*

1. *Type-1 critical contact forces consist of one zero force and two nonzero forces varying freely within their friction cones.*

2. *Type-2 critical contact forces consist of one nonzero force f_1 varying freely within its friction cone $\mathcal{C}_1$, and two nonzero forces lying on the boundaries of their friction cones. The two forces f_2 and f_3 have fixed directions, and are parametrized by $f_2 = c_2 u_2(\phi_2^*), f_3 = c_3 u_3(\phi_3^*)$ (the contacts' indices may be arbitrarily permuted). The fixed directions $u_2(\phi_2^*)$ and $u_3(\phi_3^*)$ are determined such that the lines l_{20} and l_{30} pass through the contact point x_1. This condition is formulated as follows:*

$$n_o^T[(x_i - x_1)\times]l_i(\phi_i^*) = 0 \quad , i = 2, 3. \tag{3.13}$$

3. *Type-3 critical contact forces are three nonzero forces lying on the boundaries of their friction cones, and parametrized by $f_i = c_i u_i(\phi_i), i = 1, 2, 3$. The forces are directed such that the three lines l_{i0} all intersect at a common point. This*

condition is formulated as follows:

$$\begin{aligned}
&\det(\mathcal{M}) = 0, \\
&\textit{where } \mathcal{M} = [E_1 l_1(\phi_1) \;\; E_2 l_2(\phi_2) \;\; E_3 l_3(\phi_3)] = 0, \\
&E_i = \begin{pmatrix} s_o^T \\ t_o^T \\ n_o^T [x_i \times] \end{pmatrix}, \textit{ and } l_i(\phi_i) = R_{90} M_i u_i(\phi_i) \;\; , i = 1, 2, 3.
\end{aligned} \tag{3.14}$$

Proof sketch: The outline of the proof is as follows. For each type, we choose a set ψ of m parameters that parametrize the contact forces. A force f_i that lies in the interior of its friction cone is parametrized by its three components in $I\!R^3$, while nonzero force f_i that lies on the boundary of $\mathcal{C}_i$ is parametrized by the pair (c_i, ϕ_i) as shown in (3.12). Composing this parametrization with (3.11) defines a map $\chi : I\!R^m \to N$. A necessary condition for a wrench w to lie on a five-dimensional boundary cell of N, is that it is an image of a critical point of χ, on which the $6 \times m$ Jacobian matrix $\frac{\partial \chi}{\partial \psi}$ has a rank of 5. In the rest of the proof, which appears in Appendix A, we explicitly formulate the Jacobian matrix for each type, and derive the condition for its rank deficiency. □

3.4.3 Computing the boundary curves

We now complete the computation of the boundary curves of $\widetilde{\mathcal{R}}$. The *equilibrium forces* generating wrenches that lie on the affine subspace L are formulated in Lemma 3.4.1. The *critical forces* generating wrenches that lie on the boundary of the wrench cone N are formulated in Lemma 3.4.2. Combining these two conditions together gives rise to *critical equilibrium forces*, generating wrenches that lie on candidate boundary curves of the intersection $N \cap L$. Recall that $\tilde{\boldsymbol{x}} = E^T \boldsymbol{x}$ denotes the center-of-mass horizontal projection. Using the equilibrium condition (3.1), the candidate

boundary curves of $\widetilde{\mathcal{R}}$ can be obtained from the critical equilibrium forces f_1, f_2, f_3 via the linear mapping

$$\tilde{\boldsymbol{x}} = J^T E^T \sum_{i=1}^{3} [x_i \times] f_i.$$

The formulation of candidate boundary curves of $\widetilde{\mathcal{R}}$ is summarized in the following corollary.

Corollary 3.4.3 *Let a solid object $\mathcal{B}$ be supported by 3 frictional contacts against gravity in a tame stance. Then the feasible equilibrium region $\mathcal{R}$ is a vertical prism with a horizontal cross-section $\widetilde{\mathcal{R}}$, whose candidate boundary curves are of the three types listed below.*

1. *Type-1 boundary curves occur when the horizontal projection of two friction cones $\tilde{\mathcal{C}}_i$ and $\tilde{\mathcal{C}}_j$ contain the edge $\tilde{x}_i - \tilde{x}_j$ of the support polygon. In such cases, type-1 boundary curve is a line segment lying on the edge $\tilde{x}_i - \tilde{x}_j$. The endpoints of this segment can be computed by using the planar methods described in [80] for computation of the planar vertical strip associated with two nonzero contact forces f_i and f_j that are restricted to a common vertical plane.*

2. *Type-2 candidate boundary curves are straight line segments parametrized by*

$s \in [0,1]$ *as*

$\tilde{\boldsymbol{x}} = J^T E^T \sum_{i=1}^{3} [x_i \times] f_i(s)$,

and s *is additionally restricted such that* $f_i(s) \in \mathcal{C}_i$ *for* $i = 1,2,3$, *where*

$f_1(s) = s c_1^a u_1(\phi_1^a) + (1-s) c_1^b u_1(\phi_1^b)$,

$f_i(s) = (s c_i^a + (1-s) c_i^b) u_i(\phi_i^*)$, *for* $i = 2,3$,

$u_i(\phi_i) = \mu \cos(\phi_i) s_i + \mu \sin(\phi_i) t_i + n_i$,

c_i^a *are solutions of the linear system* $c_1^a u_1(\phi_1^a) + c_2^a u_2(\phi_2^*) + c_3^a u_3(\phi_3^*) = -f_g$,

c_i^b *are solutions of the linear system* $c_1^b u_1(\phi_1^b) + c_2^b u_2(\phi_2^*) + c_3^b u_3(\phi_3^*) = -f_g$,

ϕ_2^* *and* ϕ_3^* *are solutions of (3.13), and* ϕ_1^a, ϕ_1^b *are the two solutions for* ϕ_1 *in the equation*

$\det \begin{bmatrix} H_1 u_1(\phi_1) & H_2 u_2(\phi_2^*) & H_3 u_3(\phi_3^*) \end{bmatrix} = 0$, *where* H_i *are defined in (3.10),*

and the contacts' indices can be arbitrarily permuted.

(3.15)

3. *Type-3 candidate boundary curves are formulated as*

$\tilde{\boldsymbol{x}} = J^T E^T \sum_{i=1}^{3} c_i [x_i \times] u_i(\phi_i)$, *where*

c_i *are solutions of* $c_1 u_1(\phi_1) + c_2 u_2(\phi_2) + c_3 u_3(\phi_3) = -f_g$,

$u_i(\phi_i) = \mu \cos(\phi_i) s_i + \mu \sin(\phi_i) t_i + n_i$,

and ϕ_1, ϕ_2, ϕ_3 *are the one-dimensional solution set of the equations*

$\det \begin{bmatrix} H_1 u_1(\phi_1) & H_2 u_2(\phi_2) & H_3 u_3(\phi_3) \end{bmatrix} = 0$, *and* $\det \begin{bmatrix} E_1 l_1(\phi_1) & E_2 l_2(\phi_2) & E_3 l_3(\phi_3) \end{bmatrix} = 0$

, *such that* $c_i > 0$, *where* H_i *are defined in (3.10), and* $E_i, l_i(\phi_i)$ *are defined in (3.14).*

(3.16)

Graphical Examples: Figures 3.4(a)-(d) show the horizontal cross section $\widetilde{\mathcal{R}}$ (shaded region) for different values of μ in the contact arrangement of Figure 2(a). The boundary of $\widetilde{\mathcal{R}}$ consists of type-1 line segments (thick lines), type-2 line segments (dashed lines), and type-3 curves (solid). Figures 3.4(a),(b),(c) correspond to $\mu =$

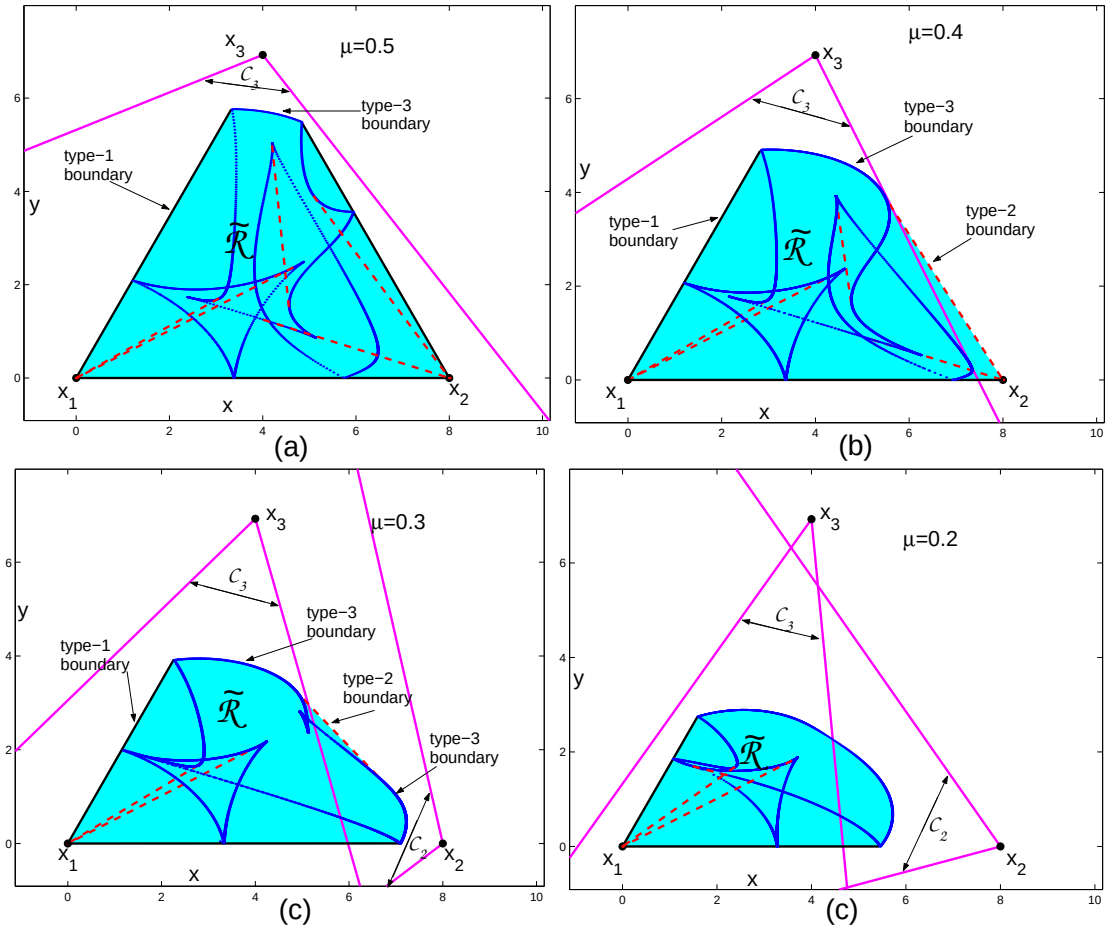

Figure 3.4: The horizontal cross section $\widetilde{\mathcal{R}}$ of the feasible region (shaded) for the 3-legged tame stance of Figure 3.2(a), with (a)$\mu = 0.5$ (b) $\mu = 0.4$, (c) $\mu = 0.3$, and (d) $\mu = 0.2$.

$0.5, 0.4, 0.2$, and resolve the missing gaps shown in Figures 3.2(b),(c),(d) respectively. Figure 3.4(d) shows $\widetilde{\mathcal{R}}$ for $\mu = 0.1$. Note that in this case no gravitational load can be balanced by less than three active contacts. Therefore, $\mathcal{R}$ lies strictly inside Π, and the boundary of $\widetilde{\mathcal{R}}$ consists only of type-2 and type-3 boundary curves.

We now make two comments about computational aspects of the results. First, note that the computation of the candidate boundary curves results in a planar arrangement, where only a part of the curves contributes to the actual boundary of $\widetilde{\mathcal{R}}$. In order to complete the computation of $\widetilde{\mathcal{R}}$, one must compute the convex hull of all

the candidate boundary curves. The reader is referred to [5],[49] for details about computing convex hull of parametric and algebraic curves.

Second, note that type-1 and type-2 boundary curves are easy to compute in closed-form. However, for computing type-3 boundary curves, one needs to find the one-dimensional solution set of two nonlinear equations in (ϕ_1, ϕ_2, ϕ_3), which do not have a closed-form formulation. In Appendix C we define the variables $\beta_i = \tan(\phi_i/2)$ and apply dialytic elimination methods [95] on the two equations in (3.14) to obtain a single polynomial of degree 16 in (β_1, β_2), where each unknown appears in degree 8. This equation can be solved numerically by searching the values of β_1 on a discrete grid, finding the real roots of an eight-degree polynomial for β_2 numerically, and then solving a quadratic equation for the eliminated β_3. A different approach for computing type-3 boundary curves is to choose a sample point (ϕ_1, ϕ_2, ϕ_3) that solves (3.14), and track the solution curve numerically by marching along its tangent vector, until the curve is closed. The main drawback of this method is that it results in a single closed curve, while the full solution set may consist of several disjoint closed curves. Choosing a suitable set of sample points that will guarantee that *all* the solution curves are found is still a challenging problem. A possible solution for this problem is using a line-sweep algorithm, and choosing the set of sample points where the solution curve is parallel to the sweep line, as done by Ponce. et. al. [89] in the context of planar grasp planning for curved objects. In our case, however, finding these special sample points requires solving a system of two polynomials of degree 16 and 15 in two unknowns, which can be done by applying homotopy continuation methods [111]. In this paper we choose to focus on the geometrical intuition, rather than on these computational issues.

3.5 Graphical Characterization of The Feasible Equilibrium Region

In this section we provide physical intuition and a graphical characterization of the boundary of $\widetilde{\mathcal{R}}$. First, we give a physical characterization to each of the three types of boundary curves. Next, we discuss the relation between the line geometry and the computation of critical contact forces. Finally, we describe the effect of changing the coefficient of friction μ on the topological structure of the boundary of $\widetilde{\mathcal{R}}$, and demonstrate the results on graphical examples.

3.5.1 Physical characterization of boundary curves

When the center-of-mass $\boldsymbol{x}$ is located on the boundary of $\mathcal{R}$, the reaction forces that generate equilibrium are also consistent with the onset of a non-static contact mode, at which the mechanism quasistatically starts to move. Each type of boundary curve corresponds to the onset of a different non-static contact mode. type-1 boundary curves, which lie on edges of the support polygon $\tilde{\mathcal{S}}$, are associated with two nonzero contact forces lying within their friction cones, while the third contact force is zero. Therefore, these curves correspond to tipping-over motion of the mechanism, involving pure rolling about two contacts and contact breakage at the third contact. type-2 boundary curves are associated with two contact forces lying on the boundaries of their friction cones, while the third contact force lies within its friction cone. Therefore, these curves correspond to onset of sliding on two contacts and pure rolling about the third contact. type-3 boundary curves are associated with three nonzero contact forces lying on boundary of their friction cones. Therefore, these curves correspond to onset of simultaneous sliding at all three contacts.

3.5.2 Relation to line geometry

We now revisit the graphical characterization of type-3 critical forces and discuss its close relation to line geometry. Line geometry is used to describe geometric relations between lines in space. We now overview few basic definitions from line geometry, which are relevant to our problem. The reader is referred to [22],[32],[45] for a deeper presentation of line geometry and its application to spatial geometry. One of the most fundamental definitions in line geometry is the *plücker coordinates of a line*, defined as follows. given a line in space that passes through a point q and directed along the unit vector u, its plücker coordinates are the pair $(u, q \times u)$, which can be interpreted as a vector in $\mathbb{R}^6$. A set of spatial lines is called *linearly dependent*, if the plücker coordinates of these lines are linearly dependent in $\mathbb{R}^6$. A set of lines is said to be of dimension d, if its associated plücker coordinates span a d-dimensional linear subspace of $\mathbb{R}^6$. Finally, a *flat pencil centered at* q is the set spanned by a pair of independent lines which intersect at a point $q \in \mathbb{R}^3$. The most important key feature of line geometry is a systematic classification and graphical characterization of all possible d-dimensional sets of n lines in space, where $d \leq \min\{n, 6\}$. This feature is frequently applied in the field of robot kinematics for identifying singular configurations of parallel robots, for example in [39],[68]. We now show that the same analysis can be applied in our problem for computing type-3 critical forces. Note that the columns of the 6×6 Jacobian matrix in (A.2) are plücker coordinates of six lines in space. Note, too, that each pair of lines form a flat pencil centered at a contact point x_i. Therefore, the problem of characterizing type-3 critical forces reduces to the problem of identifying when a set of six lines consisting of three flat pencils is linearly dependent. This problem was already considered in the robotics literature by Simaan and Shoham [103], for singularity analysis of a class of parallel robots

with six degrees-of-freedom. In their work, they identified three types of singularity, denoted $S1, S2$, and S3. The characterization of $S1$ singularity is that the three planes spanned by the three flat pencils intersect the base plane $\mathcal{B}_o$ at a common point. In this case, the six lines span a five-dimensional set, called *general linear complex.* Note that this is exactly the condition stated here in Lemma 3.4.2 and formulated in (3.14). The characterization of $S2$ singularity is that the three center points x_i of the three flat pencil all lie on a common line in space. In this case, the six lines span a five-dimensional set called *special linear complex..* Note that this the special case where the three contacts lie along a common spatial line, and the feasible region $\widetilde{\mathcal{R}}$ degenerates to a planar strip.[1] The characterization of $S3$ singularity is that the three flat pencils intersects at a common line that lies in the base plane $\mathcal{B}_o$. In this case, the six lines span a special four-dimensional set called *degenerate linear congruence.* It can be shown that this special case, which is *not* captured by (3.14) in our work, violates the conditions for a tame stance.

3.5.3 Characterizing changes in the boundary of $\widetilde{\mathcal{R}}$

We now describe the effect of changing the coefficient of friction μ on the topological structure of the boundary of $\widetilde{\mathcal{R}}$. Starting with a coefficient of friction μ which is sufficiently high, all contacts are quasi-flat, hence the boundary of $\widetilde{\mathcal{R}}$ are precisely the edges of the support polygon $\tilde{\mathcal{S}}$ (note that we assume a tame stance). While μ gradually decreases, $\widetilde{\mathcal{R}}$ continuously shrinks, and its boundary undergoes topological changes. Each topological change is associated with a critical value of μ. There are four types of critical values of μ, each associated with a different event of topological

[1] In fact, there is another possible case of special linear complex, where the three flat pencils intersect at a common line. However, this case is also captured by (3.14).

change in the boundary of $\widetilde{\mathcal{R}}$. The four types of critical events are characterized and formulated in the following proposition.

Proposition 3.5.1 *Let a solid object $\mathcal{B}$ be supported by 3 frictional contacts against gravity in a tame stance. Given the contacts x_i and the contact normals n_i, when the coefficient of friction μ is continuously decreased, there is a finite set of critical values of μ, corresponding to four types of critical events, listed as follows.*

1. *Type-A critical event occurs when the boundary of a friction cone $\mathcal{C}_i$ contains the upward vertical direction $\boldsymbol{e}$. The corresponding critical value of μ is $\mu_A^* = \tan(\cos^{-1}(n_i \cdot \boldsymbol{e}))$. For $\mu > \mu_A^*$, $\tilde{x}_i$ lies on the boundary of $\widetilde{\mathcal{R}}$. For $\mu < \mu_A^*$, $\tilde{x}_i$ is no longer contained in $\widetilde{\mathcal{R}}$, and a new piece of type-3 boundary curves evolves on the boundary of $\widetilde{\mathcal{R}}$, connecting the endpoints of the two type-1 line segments adjacent to $\tilde{x}_i$.*

2. *Type-B critical event occurs when a projected contact $\tilde{x}_i$ lies on an edge of a projected friction cone $\tilde{\mathcal{C}}_j$, while $\tilde{\mathcal{C}}_i$ contains $\tilde{x}_j$. The corresponding critical value of μ, denoted μ_B^*, is a solution for μ in the system of two equations in the unknowns (μ, ϕ_i), given by*

$$\begin{aligned} &\boldsymbol{e} \cdot (\cos(\phi_i) s_i + \sin(\phi_i) t_i - \mu n_i) = 0 \\ &(\tilde{x}_j - \tilde{x}_i) \cdot JE(\mu \cos(\phi_i) s_i + \mu \sin(\phi_i) t_i + n_i) = 0. \end{aligned}$$

   For $\mu > \mu_B^*$, a line segment along the edge $\tilde{x}_i - \tilde{x}_j$ lies on the boundary of $\widetilde{\mathcal{R}}$. For $\mu < \mu_B^*$, the edge $\tilde{x}_i - \tilde{x}_j$ is not contained in $\widetilde{\mathcal{R}}$, and is replaced with a type-2 boundary line.

3. *Type-C critical event occurs when there exists a triplet of equilibrium forces (f_i, f_j, f_k) lying on the boundaries of $\mathcal{C}_i, \mathcal{C}_j, \mathcal{C}_k$ respectively, with the corresponding tangent planes $\mathcal{B}_i, \mathcal{B}_j, \mathcal{B}_k$, that satisfy the following conditions. First, $\mathcal{B}_i$*

and $\mathcal{B}_j$ pass through x_k. Second, $\mathcal{B}_k$ contains the vertical direction $\boldsymbol{e}$. Using the parametrization $f_l = u_l(\mu, \phi_l) = \mu\cos(\phi_l)s_l + \mu\sin(\phi_l)t_l + n_l$ for $l = i, j, k$, the corresponding critical value of μ, denoted μ_C^*, is a solution for μ in the system of four equations in the unknowns $(\mu, \phi_i, \phi_j, \phi_k)$, given by

$$\boldsymbol{e} \cdot M_k u_k(\mu, \phi_k) = 0$$

$$n_o^T[(x_i - x_k)\times]R_{90}E_o M_i u_i(\mu, \phi_i) = 0$$

$$n_o^T[(x_i - x_k)\times]R_{90}E_o M_j u_j(\mu, \phi_j) = 0$$

$$\det[H_i u_i(\mu, \phi_i)\ H_j u_j(\mu, \phi_j)\ H_k u_k(\mu, \phi_k)] = 0.$$

For $\mu = \mu_C^*$, a candidate boundary curve of type-2 degenerates to a single point, connecting two type-3 candidate boundary curve. For $\mu < \mu_C^*$ this point either grows into a piece of type-2 candidate boundary curve, or it vanishes, merging two adjacent type-3 candidate boundary curve into a single curve.

4. *Type-D critical event occurs when the intersection region of the three projected friction cones $\tilde{\mathcal{C}}_1, \tilde{\mathcal{C}}_2, \tilde{\mathcal{C}}_3$ degenerates to a single point. The corresponding critical value of μ, denoted μ_D^*, is a solution for μ in the system of four equations in the unknowns $(\mu, \phi_1, \phi_2, \phi_3)$, given by*

$$\boldsymbol{e} \cdot M_i u_i(\mu, \phi_i) = 0 \text{ for } i = 1, 2, 3$$

$$\det[H_1 u_1(\mu, \phi_1)\ H_2 u_2(\mu, \phi_2)\ H_3 u_3(\mu, \phi_3)] = 0.$$

The horizontal cross-section $\widetilde{\mathcal{R}}$ degenerates to a single point for $\mu = \mu_D^*$, and becomes empty[2] for $\mu = \mu_D^*$.

Graphical Examples: We now demonstrate the evolution of the boundary of $\widetilde{\mathcal{R}}$ on the graphical example of Figure 4(a)-(d), based on the contact arrangement depicted

[2]Excpet for the non-generic cases where a contact normal is purely vertical, or two contact normals lie on a common vertical plane, or the three contact normals all intersect a common vertical line, where the region $\widetilde{\mathcal{R}}$ is non-empty even for the frictionless case $\mu = 0$ [64].

in Figure 2(a). For $\mu = 0.7$, all contacts are quasi-flat, hence $\widetilde{\mathcal{R}}$ is precisely the support polygon $\tilde{\mathcal{S}}$. When μ gradually decreases, a critical event of type-A occurs for $\mu = 0.6745$, at which $\boldsymbol{e}$ lies on the boundary of $\mathcal{C}_3$. Figure 4(a) shows $\widetilde{\mathcal{R}}$ for $\mu = 0.5$, where $\tilde{x}_3$ is not contained in $\widetilde{\mathcal{R}}$, and a piece of a type-3 boundary curve evolves on the boundary of $\widetilde{\mathcal{R}}$, connecting the endpoints of the two type-1 line segments adjacent to $\tilde{x}_3$. When μ is further decreased, a critical event of type-B occurs for $\mu = 0.4305$, at which $\tilde{x}_2$ lies on an edge of a projected friction cone $\tilde{\mathcal{C}}_3$. Figure 4(b) shows $\widetilde{\mathcal{R}}$ for $\mu = 0.4$, where the edge $\tilde{x}_2$–$\tilde{x}_3$ is not contained in $\widetilde{\mathcal{R}}$, and is replaced by a type-2 curve on the boundary of $\widetilde{\mathcal{R}}$. When μ is further decreased, another critical event of type-A occurs for $\mu = 0.3639$, at which $\boldsymbol{e}$ lies on the boundary of $\mathcal{C}_2$. Figure 4(c) shows $\widetilde{\mathcal{R}}$ for $\mu = 0.3$, where $\tilde{x}_2$ is not contained in $\widetilde{\mathcal{R}}$, and a piece of a type-3 boundary curve evolves on the boundary of $\widetilde{\mathcal{R}}$, connecting a type-1 and a type-2 boundary curves. When μ is further decreased, a critical event of type-C occurs for $\mu = 0.2196$, at which a type-2 boundary curve of $\widetilde{\mathcal{R}}$ degenerates into a point. Figure 4(d) shows $\widetilde{\mathcal{R}}$ for $\mu = 0.2$, where this type-2 boundary curve vanishes, and two adjacent pieces of type-3 boundary curves merge into one piece on the boundary of $\widetilde{\mathcal{R}}$. When μ is further decreased towards zero while passing other critical events of types A,B,and C, $\widetilde{\mathcal{R}}$ gradually shrinks, until a type-D critical event occurs for $\mu = 0.0243$, at which $\widetilde{\mathcal{R}}$ degenerates to a point. For $\mu < 0.0243$, the region $\widetilde{\mathcal{R}}$ is empty.

3.6 Experimental Results

This section describes preliminary experiments that measure the feasible equilibrium region of a three-legged prototype supported by a frictional terrain. The experimental system, shown in Figure 3.5, consists of a three-legged mechanism made of

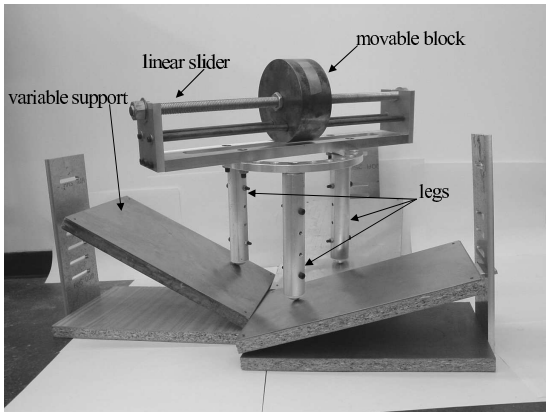

(a)

Figure 3.5: Experimental setup of a two-legged prototype.

Aluminium. The mechanism consists of an annular frame and three prismatic legs with spherical footpads, making point contacts with three Aluminium plates. A heavy steel cylinder moves along a horizontal linear slider, which is mounted on top of the annular frame. The three supporting plates maintain fixed position and adjustable slopes, such that the contact normals can be varied. The dimensions of the mechanisms are as follows. The diameter of the annular frame is 212 mm. The nominal length of the legs is 180 mm, and the length of the linear slider is 430 mm. The total weight of the mechanism is 7.9 Kg, while the movable cylinder weighs 4.2 Kg.

After placing the mechanism on the supporting plates, the heavy cylinder is moved continuously along the slider, thus varying the center-of-mass along a straight line. The center-of-mass is moved until reaching the boundary of the feasible equilibrium region, where a critical event of contact breakage or slippage is observed. The critical center-of-mass position is then recorded, and the process is repeated with the linear slider mounted in different angles on the horizontal plane. The slider's angles eventually span the whole 360° range with resolution of 15°. This enables mapping of discrete points on the boundary of $\widetilde{\mathcal{R}}$, and comparing these points with the theoretical

results for a given contact arrangement.

The contact points are positioned at equal heights, making an equilateral triangle in a horizontal plane, with edge lengths of 165 mm. The supporting plates at x_1 and x_2 are horizontal, such that n_1 and n_2 are purely vertical. The support at x_3 is rotated such that n_3 makes a 30° angle with the vertical upward direction, and its horizontal projection makes a 20° angle with the bisector of the equilateral triangle in a horizontal plane. As a preliminary step, the coefficient of friction was determined to be $\bar{\mu} = 0.26$ with a standard deviation of $\sigma = \pm 13.2\%$. Figure 3.6(a) shows a top view of the contacts and the horizontal projection of the friction cone $\mathcal{C}_3$ for the given contact arrangement (since x_1 and x_2 are flat, the horizontal projection of $\mathcal{C}_1$ and $\mathcal{C}_2$ span the entire plane). The theoretical region $\widetilde{\mathcal{R}}$, computed for with $\mu = \bar{\mu}$, appears as a shaded region. Note that the boundary of $\widetilde{\mathcal{R}}$ consists of curves of all three types. Hence one expects three qualitatively distinct critical events in the experiment. In the experiment, the boundary of $\widetilde{\mathcal{R}}$ is mapped by discrete points, all lying along rays that emanate from the geometric center of the equilateral triangle formed by the contacts. For each angle of the linear slider, ten measurements were recorded. Figure 3.6(b) shows the experimentally measured center-of-mass critical positions, together with the theoretical results. The experimental measurements are marked by '$\times$', while the theoretical boundaries of $\widetilde{\mathcal{R}}$ for $\mu = \bar{\mu} + \sigma$ and for $\mu = \bar{\mu} - \sigma$ appear as solid and dashed lines.

We now briefly discuss the results and provide some insights gained from the experiments. First, note that the measurements associated with the type-1 boundary of $\widetilde{\mathcal{R}}$ have a very small variance and match closely with the theoretical boundary lines, except for measurements near x_1 and x_2. However, the measurements associated with the type-2 and type-3 boundaries of $\widetilde{\mathcal{R}}$ have a much larger variance. Yet all of these

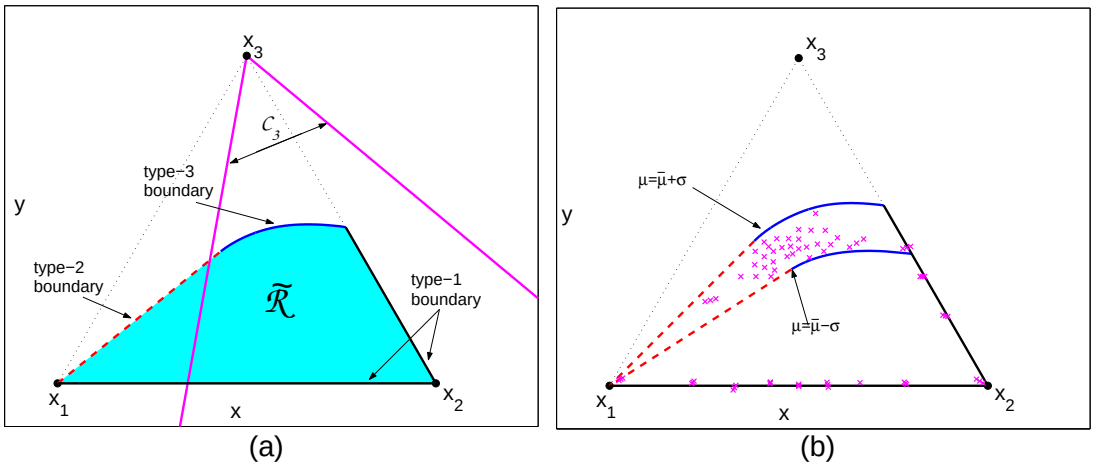

Figure 3.6: (a) Theoretical computation of $\widetilde{\mathcal{R}}$ (shaded region) for $\mu = \bar{\mu}$ (b) Experimental measurements of critical center of mass positions ('×') compared with the theoretical boundaries of $\widetilde{\mathcal{R}}$ for $\mu = \bar{\mu} \pm \sigma$ (solid and dashed curves).

points fall within the region computed theoretically for the range $\bar{\mu} \pm \sigma$. Thus the theoretical model of point contact with friction is validated. The reason for the difference in the variances is that type-1 boundaries are associated with pure rolling about two contacts and breaking the third contact. Hence the corresponding center-of-mass position depends only on geometry of the contacts arrangement. These boundaries can be easily obtained experimentally, except for measurements near x_1 and x_2 associated with pure rolling about a single contact, which is a highly sensitive scenario. On the other hand, type-2 and type-3 boundaries are associated with sliding at two or three contacts. The corresponding center-of-mass position is highly dependent on the coefficient of friction μ, whose value is determined experimentally, and is subject to large deviations. A possible explanation for the large deviations obtained in measuring μ is the fact that spherical footpads generate point contact with the supports, which is highly sensitive to surface irregularities. A possible solution to this problem can be "flattening" of the footpads to distribute the contact over patches of small area.

However, in this case the hard-finger contact model should be replaced by a soft-finger contact model, which includes torques about the contact normals. An additional interesting result of the experiment is that the critical event of rolling, associated with type-1 boundary, was clearly and distinguishably observed in the experiment. The two other critical events of sliding at two contacts while rolling at a third contact and of sliding a all three contacts, could be easily distinguished from pure rolling. However, in some cases, they could not be visually distinguished between themselves. Therefore, for a complete experimental validation of the onset of all three non-static contact modes predicted by the theory, one might need to use contact sensors or fast cameras to track the instantaneous motion of the mechanism during sliding.

3.7 Additional Extensions

In this chapter we have formulated the center-of-mass feasible equilibrium region for three frictional contacts as an intersection of a convex cone and a hyperplane in the six-dimensional wrench space. Using this formulation, we have derived a classification and closed-form expressions of the candidate boundary curves of the feasible equilibrium region. We provided a geometric characterization of the boundary curves, and classified the topological changes in the boundary as a function of the coefficient of friction μ. The theoretical computation was illustrated with graphical examples, and validated by experimental results.

We now consider now some possible generalizations of this work. First consider a stance with a general number of contacts. In such stances, the support polygon $\widetilde{\Pi}$ is the convex hull of the projected contacts $\tilde{x}_1 \dots \tilde{x}_k$. One first needs to extend the notion of tame stances to multiple contacts. A k-contact stance is *tame* if for any edge

$\tilde{x}_i - \tilde{x}_j$ of the support polygon $\widetilde{\Pi}$, all possible torques generated by the contact forces about the line $\tilde{x}_i - \tilde{x}_j$ have the same sign. Using this definition, Theorem 3 generalizes. Namely, it can be shown that for a k-contact tame stance, $\mathcal{R}$ is bounded, and satisfies $\mathcal{R} \subseteq \Pi$. Furthermore, it can be shown that all boundaries of $\mathcal{R}$ are associated with no more than *three* nonzero critical contact forces. Hence for k-contact tame stances, the feasible region $\mathcal{R}$ is the *convex hull* of all the feasible regions $\mathcal{R}_{i,j,k}$, associated with all possible triplets of contacts (x_i, x_j, x_k).

A second important extension is the investigation of *non-tame stances.* In such cases the feasible equilibrium region can exceed the support polygon prism Π, and may even span the whole space [82]. More interestingly, in some cases $\widetilde{\mathcal{R}}$ can become unbounded in certain directions. Furthermore, a deeper look at the analysis in section 3.4 suggests that in such cases a new type of boundary curve may evolve. In this view, the analysis of the effects of changes in μ on the boundary of $\widetilde{\mathcal{R}}$ can be extended to account for $\mu \in [0, \infty]$. In the case when μ is sufficiently large $\widetilde{\mathcal{R}}$ may be unbounded. While μ gradually decreases, $\widetilde{\mathcal{R}}$ shrinks toward the support polygon $\widetilde{\Pi}$, and then keeps on shrinking within $\widetilde{\Pi}$ until it becomes empty.

Finally, the feasible equilibrium region was computed while considering a single gravitational load. However, in practice one must consider stances which are *robust* with respect to a neighborhood of disturbance wrenches surrounding the nominal gravitational wrench. Thus, the notion of stance robustness, defined in Chapter 2 requires generalization to the 3D case. We now briefly sketch such a generalization. Let $\boldsymbol{w}_{ext} = (f_{ext}, \tau_{ext}) = (f_x, f_y, f_z, \tau_x, \tau_y, \tau_z)$ denote an external wrench acting on $\mathcal{B}$. The feasible equilibrium region associated with $\boldsymbol{w}_{ext}$ is an infinite prism parallel to f_{ext}, whose cross-section can be computed by intersecting the wrench cone N with an appropriate affine subspace corresponding to $\boldsymbol{w}_{ext}$. Let $\mathcal{W}$ be a convex and

bounded neighborhood of wrenches, with the nominal gravitational wrench $\boldsymbol{w}_0 = (f_g, \vec{0})$ lying within its interior. Assume that $\mathcal{W}$ is a polyhedral set spanned by the vertices $\boldsymbol{w}_1 \ldots \boldsymbol{w}_m$. Let $\mathcal{R}_i$ denote the feasible equilibrium region associated with an individual wrench $\boldsymbol{w}_i$ for $i = 1 \ldots m$. Generalizing the result of Theorem 2, it can be shown that the region obtained by intersecting the individual feasible regions $\mathcal{R}_i$ is *robust*, in the sense that the contacts can resist any external wrench in $\mathcal{W}$ with the center-of-mass lying within this region.

The wrench parametrization and some graphical constructions from chapter 2 can also be generalized to the 3D case, as follows. Since the equilibrium condition is homogenous in $\boldsymbol{w}_{ext}$, we scale it by the f_z components and define the homogenous wrench coordinates $p_x = f_x/f_z$, $p_y = f_y/f_z$ and $q_x = \tau_x/f_z$, $q_y = \tau_y/f_z$, $q_z = \tau_z/f_z$. Note that the wrench parametrized by zero corresponds to $\boldsymbol{w}_0$. Consider now a symmetric rectangular wrench set $\mathcal{W}$, defined by $p_x \in [-\kappa_x, \kappa_x]$, $p_y \in [-\kappa_y, \kappa_y]$, $q_x \in [-\nu_x, \nu_x]$, $q_y \in [-\nu_y, \nu_y]$, $p_z \in [-\nu_z, \nu_z]$. The robust equilibrium region associated with the wrench neighborhood $\mathcal{W}$ can be constructed as follows. First, compute the eight prismatic regions corresponding to wrenches parametrized by $p_x = \pm\kappa_x, p_y = \pm\kappa_y, q_z = \pm\nu_z, q_x = q_y = 0$, and construct their intersection. Then robust equilibrium region can now be obtained from the intersection region by inward shifting its boundary by offset ν_x in the x direction and nu_y in the y direction.

Chapter 4

Continuous Dynamics of Planar Mechanical Contact Systems

This chapter analyzes the dynamics of planar mechanical systems with frictional contacts. The main objective of this chapter is to discuss the dynamic stability of frictional equilibrium postures, based on the system's dynamics and its response to small position-and-velocity perturbations. The structure of this chapter is as follows. Section 4.1 formulates the dynamics of planar mechanical systems with frictional contacts, which are a subclass of constrained dynamical systems, and introduces the notion of the system's *contact modes*, which determine the dynamic response of the system. Section defines the notion of *frictional stability*, and discusses its relationship with classical definitions of dynamic stability. Focusing on the reduced model of a single rigid body with variable center-of-mass, Section 4.3 enumerates all the possible contact modes, and formulates the conditions for their feasibility, It is then shown that the dynamic solution may suffer from special difficulties which are unique to this kind of dynamical systems, such as indeterminacy, inconsistency, and

dynamic jamming. Section 4.4 introduces the *strong equilibrium condition*, which eliminates all the dynamic indeterminacies, and shows that strong equilibrium is a necessary condition for frictional stability. Section 4.4 introduces the *persistent equilibrium condition*, which eliminates all the dynamic inconsistencies, and shows that under persistent equilibrium condition, the dynamic response is guaranteed to have a separated contact recovered a sliding contact fixed in finite time. Finally, Section 4.6 sketches some possible generalizations of the analysis.

4.1 Formulation of Frictional Dynamics and Contact Modes

This section formulates the dynamics of planar mechanical systems with frictional contacts. The dynamic solution of such systems depends on the instantaneous interaction at the contacts, namely the *contact mode* of the system. Let Q denote the n-dimensional configuration space of a mechanical system, and let $(q, \dot{q})$ denote the dynamical system's state, composed of the system's configuration and velocity. The system is subject to k frictional contacts. Recall that x_i denotes the i-th contact point, and that t_i, n_i denote the tangent and normal unit vectors at x_i for $i = 1 \dots m$. It is assumed that the terrain is *piecewise linear*, and hence t_i, n_i are constant in the vicinity of the contact x_i for $i = 1 \dots k$. The dynamics of the system is governed by its *equation of motion*, given by

$$M(q)\ddot{q} + B(q, \dot{q}) + G(q) = \sum_{i=1}^{k} J_i^T(q) f_i. \tag{4.1}$$

The matrix $M(q)$ is denoted the system's matrix of inertia. $B(q, \dot{q})$ is a vector of velocity-dependent generalized forces, and $G(q)$ is the vector of gravitational terms.

On the right hand side of (4.1), $f_i \in I\!R^2$ is the contact force at the i-th contact, and $J_i(q)$ is the Jacobian matrix satisfying $v_i = J_i(q)\dot{q}$, where $v_i \in I\!R^2$ is the instantaneous velocity of $\mathcal{B}$ at the i-th contact point. The derivation of these equations of motion is discussed in many classical books of mechanics, e.g. [66], and of robot dynamics, e.g. [104]. The dynamic solution $q(t)$ for given initial conditions is obtained by integrating the equation of motion (4.1) for a time interval. At a given instant of time, q and $\dot{q}$ are known, and one needs to solve (4.1) for the acceleration $\ddot{q}$. Note that in addition to $\ddot{q}$, the instantaneous contact forces f_i are also unknown in (4.1). Therefore, additional information must be used in order to obtain an instantaneous dynamic solution for $\ddot{q}$ and f_i. This missing information is the *contact mode* of the system, which imposes constraints on the contact force f_i and the velocity v_i at each contact. Table 4.1 lists the four possible contact modes for a single contact at x_i, which are denoted S,F,R, and L, corresponding to contact separation, fixed (or rolling) contact, right-sliding contact and left-sliding contact, respectively. A contact mode of a system with m contacts is encoded by a word of m letters from the alphabet $\{S, F, R, L\}$. For example, the contact mode SR of a two-contact system means that the contact x_1 is instantaneously separating, while the contact x_2 is sliding to the right. Each contact mode is associated with linear equality and inequality constraints on the contact force f_i and on the velocity at the contact v_i. Choosing a contact mode imposes two scalar equality constraints for each contact. Assuming that a contact mode is maintained for a finite time interval, each equality constraint on v_i can be differentiated with respect to time, to obtain a similar constraint on the acceleration at the contact, denoted a_i. Using the relation $a_i = J_i(q)\ddot{q} + \dot{J}_i(q)\dot{q}$ yields an equality constraint which is affine in $\ddot{q}$. Augmenting the equation of motion (4.1) with the $2m$ equality constraints associated with a given contact mode, one obtains a square linear system in the unknowns $\ddot{q}$

contact mode	physical meaning	kinematic constraints	force constraints
S	Separation	$v_i \cdot n_i > 0$	$f_i = \vec{0}$
F	Fixed	$v_i = \vec{0}$	$\lvert f_i \cdot t_i \rvert \leq \mu(f_i \cdot n_i)$
R	Right sliding	$v_i \cdot n_i = 0$ $v_i \cdot t_i > 0$	$f_i \cdot t_i = -\mu(f_i \cdot n_i)$ $f_i \cdot n_i \geq 0$
L	Left sliding	$v_i \cdot n_i = 0$ $v_i \cdot t_i < 0$	$f_i \cdot t_i = \mu(f_i \cdot n_i)$ $f_i \cdot n_i \geq 0$

Table 4.1: The possible contact modes at a single frictional contact.

and f_i , $i = 1 \ldots m$. This system is generically full rank, and gives a unique solution for the instantaneous dynamics associated with the given contact mode. However, since each contact mode is also associated with inequality constraints, the dynamic solution should then be assigned into these inequalities to check if the chosen contact mode is *consistent*. Note that since at a given instant the velocities v_i are known, the kinematic inequalities associated with v_i can be checked directly without solving the dynamics. Thus, kinematically inconsistent contact modes can be ruled out in advance. However, in the special case where the system is at rest, $v_i = \vec{0}$ for all i, and the kinematic inequality constraints are trivially satisfied as equalities. In this case, one needs to differentiate these inequalities with respect to time or, equivalently, replace v_i with its corresponding acceleration a_i. The consistency of a contact mode is then checked by assigning the dynamic solution for a_i into the kinematic inequalities, and assigning the solution for f_i into the force inequalities.

Summarizing the procedure described above, in order to find the instantaneous dynamic solution of a planar mechanical system with frictional contacts, one needs to conduct the following steps. First, given the system's current state $(q, \dot{q})$, compute the velocities v_i at each contact. Second, enumerate all candidate contact modes which are consistent with these velocities (i.e. satisfy the kinematic constraints). For

each of the candidate contact modes, compute the associated instantaneous dynamic solution, and substitute into the contact mode's inequalities to check if it is consistent. Finally, pick a contact mode which is consistent, and its associated dynamic solution. This solution can then be used to integrate (4.1) and compute the system's trajectory $q(t)$ until this contact mode becomes inconsistent.

Given this procedure, one can compute the dynamic solution under given initial conditions. This motivates the discussion of dynamic stability of equilibrium postures which appears in the next section. Stability analysis is based on considering the system's dynamics in response to small perturbation about an equilibrium configuration.

A fundamental problem of planar mechanical system with frictional contact is that in some cases this procedure fails to provide a dynamic solution. One such case is *frictional inconsistency*, in which no contact mode is consistent. The second case is *frictional indeterminacy*, in which two or more contact modes are simultaneously consistent. The next section demonstrates these abnormal phenomena for the reduced model of a planar rigid body with variable center-of-mass, and discusses their influence on stability of frictional equilibrium postures.

4.2 Definition of Frictional Stability in Mechanical Contact Systems

This section discusses the dynamic stability of frictional equilibrium postures, and introduces the definition of frictional stability for equilibrium postures of planar mechanical systems with frictional contacts. The definition is based on analyzing the of dynamic solution of a mechanical system under small position-and velocity perturbation about a frictional equilibrium posture. The dynamic solution of frictional

systems was partially defined in the previous section, and its complete definition will be given in Chapter 5. Thus, this chapter analyze only one of two components of frictional stability.

Classical definitions of local stability of equilibrium points of a dynamical system are based on considering a small perturbation in the system's state (i.e. position and velocity) about an equilibrium point, and analyzing the trajectory of the dynamical system in response to this perturbation (e.g. Lyapunov stability in [48, 52]). An equilibrium point is *locally stable*, if for any arbitrarily small state-perturbation, the trajectory of the dynamical system stays within a small bounded neighborhood of the original equilibrium state. A locally stable equilibrium point is also *asymptotically stable* if for any arbitrarily small state perturbation, the trajectory of the dynamical system converges asymptotically to the original equilibrium state.

In the robotics literature, some works analyzed the stability of robotic systems with multiple contacts, in the context of grasping. In [73],[27] the stability of force closure grasps is analyzed, under the assumption that the contact forces are actively controlled. In [101], the stability of grasping with passive fingers is considered, by modelling the natural compliance at the contacts, and [44] also accounts for joints' stiffness. However, all the works mentioned above considered only perturbations in which all contacts are maintained fixed (or rolling), and disregarded perturbations in which the contacts are sliding or separating. In this work we want to analyze the stability of equilibrium postures with respect to all possible perturbations, including contact separation, rolling or sliding, under the rigid body paradigm, assuming that the contact forces are passively generated by frictional contact constraints. The following example illustrates the problematic nature of our desired stability properties. Consider a planar rigid body supported by two frictional contacts in gravitational

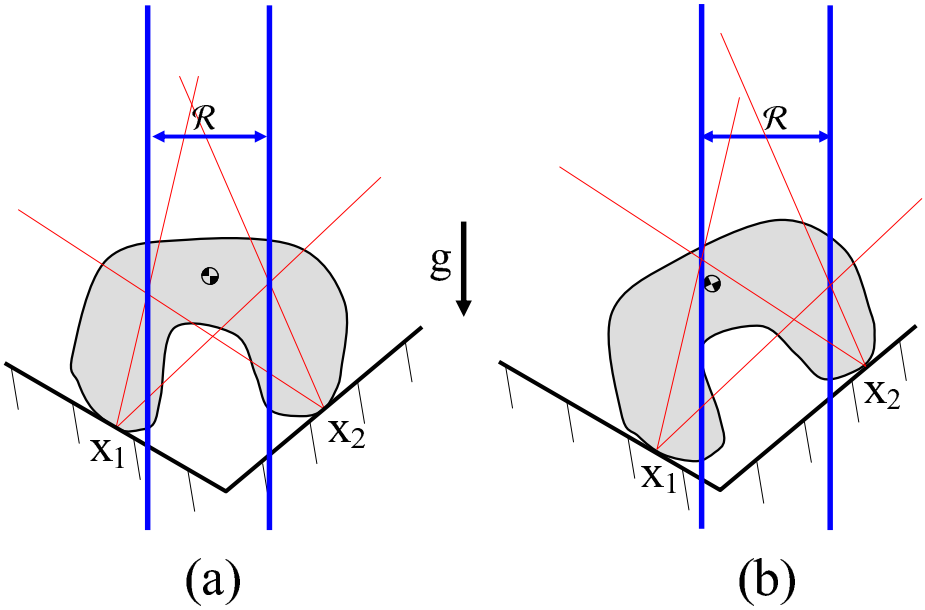

Figure 4.1: (a) A frictional equilibrium stance (b) A perturbed stance that still maintains feasible equilibrium.

field. Figure 4.1a depicts the rigid body, the contacts, and the feasible equilibrium region for the center-of-mass. Consider a perturbation in which the body is slightly rotated while both contacts slide to the right, and left at rest in the new posture. Figure 4.1b shows the rigid body after this perturbation. Note that under this perturbation, the center-of-mass has been shifted, but it still lies within the feasible equilibrium region. Therefore, the perturbed configuration is also a frictional equilibrium posture, and the body may stay in the new posture, rather than converging back to the original one. This example demonstrates the key observation that *frictional equilibrium postures are never asymptotically stable*, and might be neutrally stable with respect to a set of contact-preserving perturbations. On the other hand, the definition of locally stability is insufficient, since we would like to ensure that that the perturbed system

converges back to an equilibrium point, while all contacts are re-established. The observations above motivates the introduction of the new definition of frictional stability. Since the definition uses the notion of small neighborhood of an equilibrium postures, we assume that q is a set of local coordinates parametrizing a small neighborhood of q_0 in configuration space. Thus, we treat both q and $\dot{q}$ as elements in $I\!R^n$, and use the Euclidean norm $\|\cdot\|$ to define small neighborhoods of equilibrium postures as follows. Let q_0 be an equilibrium posture of a mechanical system. Define an ϵ-neighborhood of the equilibrium state as $N_\epsilon = \{(q, \dot{q}) : \quad \|q - q_0\| < \epsilon$, and $\|\dot{q}\| < \epsilon\}$. Using this notion of small neighborhoods, the definition of frictional stability of equilibrium posture is as follows.

Definition 3 *Consider a planar mechanical system with k frictional contacts. A frictional equilibrium posture q_0 of the system possesses* frictional stability *if for any arbitrarily small $\delta > 0$, there exists sufficiently small $\epsilon > 0$, such that for any non-penetrating state-perturbation $(q(0), \dot{q}(0)) \in N_\epsilon$, the trajectory of the dynamical system $q(t), \dot{q}(t))$ converges to an equilibrium posture such that all k contacts are re-established, while staying within the neighborhood N_δ of the original equilibrium posture.*

4.3 Dynamics of Perturbed Equilibrium Stances of a Planar Rigid Body

This section uses the concepts derived in section 4.1 to analyze the dynamics of frictional two-contact equilibrium stances in 2D under small perturbations. We use the simplifying paradigm that lumps all the kinematics into a single rigid body $\mathcal{B}$ with

contact mode	physical meaning	kinematic constraints	force constraints
S	Separation	$a_i \cdot n_i \geq 0$	$f_i^l = f_i^r = 0$
F	Fixed	$a_i = \vec{0}$	$f_i^l, f_i^r \geq 0$
R	Right sliding	$a_i \cdot n_i = 0$ $a_i \cdot t_i \geq 0$	$f_i^r = 0$ $f_i^l \geq 0$
L	Left sliding	$a_i \cdot n_i = 0$ $a_i \cdot t_i \leq 0$	$f_i^l = 0$ $f_i^r \geq 0$

Table 4.2: Contact modes at a zero-velocity state.

fixed contacts and a variable center-of-mass. Using the dynamic solution associated with a non-static contact mode, its inequality constraints define a *feasibility region* of center-of-mass positions for which this contact mode is consistent. Using the feasibility regions of all contact modes, the phenomena of frictional indeterminacy and inconsistency are demonstrated.

First, let us reformulate the contact modes constraint as follows. Recall that C_i^l and C_i^r denote unit vectors along the left and right edges of the friction cone $\mathcal{C}_i$ for $i = 1, 2$. Each contact force within its friction cone can be decomposed as $f_i = f_i^l C_i^l + f_i^r C_i^r$, where $f_i^l, f_i^r \geq 0$. Moreover, differentiation of the kinematic constraints with respect to time and evaluation at zero-velocity stance, the velocities v_i can be replaced by the accelerations a_i in all contact mode's constraints. Table 4.2 summarizes these reformulations of the contact modes' constraints.

4.3.1 Formulation of the frictional dynamics

We now define our basic terminology, and formulate the dynamics of a planar rigid body $\mathcal{B}$ supported by two frictional contacts. Let $x_1, x_2 \in \mathbb{R}^2$ denote the positions of the contact points, and let $f_1, f_2 \in \mathbb{R}^2$ denote the contact forces. Let p_{ll} denote the intersection point of the left edges of the two frictions cones, let p_{rr} denote the

intersection point of the right edges of the two frictions cones, and let p_{nn} denote the intersection point of the two contact normals. The center-of-mass position of $\mathcal{B}$ is denoted $\boldsymbol{x}$. The mass of $\mathcal{B}$ is denoted m, and its moment of inertia is denoted I_c. Let ρ denote $\mathcal{B}$'s radius of gyration, satisfying $I_c = m\rho^2$. The body is subject to a net wrench of external force and torque denoted by (f_{ext}, τ_{ext}). Finally, let $a \in I\!R^2$ and $\alpha \in I\!R$ denote the linear and angular acceleration of $\mathcal{B}$'s body frame located at its center of mass. The equations of motion of $\mathcal{B}$ under the influence of an external wrench and two contact forces are:

$$\begin{aligned} ma &= f_1 + f_2 + f_{ext} \\ m\rho^2\alpha &= (\boldsymbol{x} - x_1)^T J f_1 + (\boldsymbol{x} - x_2)^T J f_2 + \tau_{ext}, \end{aligned} \qquad \text{where } J = \begin{bmatrix} 0 & -1 \\ 1 & 0 \end{bmatrix}. \tag{4.2}$$

The possible contact modes of $\mathcal{B}$ are encoded by two-letter words from the alphabet $\{S, F, R, L\}$, describing the interaction at each of the two contacts. Assuming a contact mode adds four equality constraints in f_i and a_i for $i = 1, 2$ as detailed in Table 4.3. The contact accelerations a_i are related to (a, α) via the rigid-body relation

$$a_i = a + J(x_i - \boldsymbol{x})\alpha. \tag{4.3}$$

Using this relation, the contact mode constraints augmented with the equation of motion (4.1) give a linear system in the unknowns $\{f_1, f_2, a, \alpha\}$. This system is generically full rank, and its unique solution is the instantaneous dynamic solution associated with a specific contact mode, which is a function of $\mathcal{B}$'s center of mass $\boldsymbol{x}$. Substituting the dynamic solution into the contact mode's inequality constraints (with v_i replaced by a_i in the kinematic constraints) gives inequalities in $\boldsymbol{x}$, which define the contact mode's *feasibility region*, which is the region of center-of-mass locations where this particular mode is feasible.

4.3.2 Feasibility regions of contact modes

We now explicitly formulate the center-of-mass feasibility regions of all possible contact modes for a two-contact frictional equilibrium stance of $\mathcal{B}$. For two contacts, there are four qualitatively different non-static contact modes, listed as follows. Contact mode SS of two-contact separation (i.e. free flying), contact mode FS of rolling and separation, contact mode RS of sliding and separation, and contact mode RR of simultaneous two-contact sliding. Each other contact mode is obtained from these four by exchanging the order of contacts or reversing the sliding direction. The corresponding feasibility regions of these contact modes are denoted $\mathcal{R}_{SS}, \mathcal{R}_{FS}, \mathcal{R}_{RS}$ and $\mathcal{R}_{RR}$ respectively.

Note that the contact mode FF of static equilibrium, is a special case in which the associated equality constraints are linearly dependent. Therefore, the static solution of is indeterminate. Nevertheless, the contact mode's inequality constraints still define the feasibility region $\mathcal{R}_{FF}$, which is precisely the feasible equilibrium region $\mathcal{R}(\boldsymbol{w})$ computed in Chapter 2 for planar stances.

The following lemma formulates the center-of-mass feasibility regions of the four non-static contact modes.

Lemma 4.3.1 ([76]) *Let $\mathcal{B}$ be supported by two frictional contacts at rest, and be subjected to an external wrench (f_{ext}, τ_{ext}). Then the feasibility regions of the non-static contact modes are given as follows.*

1. *The SS feasible region is a semi-infinite polygon bounded by two edges, given by* $\mathcal{R}_{SS}=\{\boldsymbol{x} : \rho^2 f_{ext} \cdot n_i - \tau_{ext}(\boldsymbol{x} - x_i) \cdot t_i \geq 0,\ i = 1, 2\}$.

2. *With x_1 chosen as frame origin, the FS feasible region is given by*

$$\mathcal{R}_{FS} = \big\{\boldsymbol{x} : \min_{i=1,2,3}\{T_i(\boldsymbol{x})\} \geq 0\big\},$$

where $T_1(\boldsymbol{x}) = \big(-J\boldsymbol{x}\tau_{ext} + (J\boldsymbol{x}\boldsymbol{x}^T J + \rho_o^2 I)f_{ext}\big) \cdot JC_1^l$, $T_2(\boldsymbol{x}) = \big(J\boldsymbol{x}\tau_{ext} - (J\boldsymbol{x}\boldsymbol{x}^T J + \rho_o^2 I)f_{ext}\big) \cdot JC_1^r$, *and* $T_3(x) = (\boldsymbol{x}^T J^T f_{ext} + \tau_{ext})(t_2 \cdot x_2)$, *where* $\rho_o^2 = \rho^2 + \|\boldsymbol{x}\|^2$, *and* I *is the* 2×2 *identity matrix.*

3. *With* x_1 *chosen as frame origin, The RS feasible region* $\mathcal{R}_{RS}$ *is the union of two sets,* $\mathcal{R}_{RS} = \mathcal{R}_{RS}^1 \cup \mathcal{R}_{RS}^2$, *given by*

$$\begin{aligned}\mathcal{R}_{RS}^1 &= \big\{\boldsymbol{x} : \min_{i=1,2,3,4}\{W_i(\boldsymbol{x})\} \geq 0\big\}\\ \mathcal{R}_{RS}^2 &= \big\{\boldsymbol{x} : \max_{i=1,2,3,4}\{W_i(\boldsymbol{x})\} \leq 0\big\},\end{aligned}$$

where $W_1(\boldsymbol{x}) = (t_1 \cdot \boldsymbol{x})\tau_{ext} - \rho^2(f_{ext} \cdot n_1)$, $W_2(\boldsymbol{x}) = \rho^2(n_1 \cdot C_1^l) - (t_1 \cdot \boldsymbol{x})\boldsymbol{x}^T J^T C_1^l$, $W_3(\boldsymbol{x}) = (n_1 \cdot \boldsymbol{x})W_0(\boldsymbol{x}) + \big((t_1 \cdot C_1^l)W_1(\boldsymbol{x}) + (t_1 \cdot f_{ext})W_2(\boldsymbol{x})\big)$, *and* $W_4(\boldsymbol{x}) = t_2 \cdot (\boldsymbol{x} - x_2)W_0(\boldsymbol{x}) + \big((n_2 \cdot C_1^l)W_1(\boldsymbol{x}) + (n_2 \cdot f_{ext})W_2(\boldsymbol{x})\big)$, *where* $W_0(\boldsymbol{x}) = (n_1 \cdot f_{ext})\boldsymbol{x}^T J^T C_1^l + (n_1 \cdot C_1^l)\tau_{ext}$.

4. *With* p_{ll} *chosen as frame origin, The RR feasible region* $\mathcal{R}_{RR}$ *is the union of two sets,* $\mathcal{R}_{RR} = \mathcal{R}_{RR}^1 \cup \mathcal{R}_{RR}^2$, *given by*

$$\begin{aligned}\mathcal{R}_{RR}^1 &= \big\{\boldsymbol{x} : \min_{i=1,2,3,4,5}\{Q_i(\boldsymbol{x})\} \geq 0\big\}\\ \mathcal{R}_{RR}^2 &= \big\{\boldsymbol{x} : \max_{i=1,2,3,4}\{Q_i(\boldsymbol{x})\} \leq 0\big\},\end{aligned}$$

where $Q_0(\boldsymbol{x}) = \boldsymbol{x}^T J^T f_{ext} + \tau_{ext}$, $Q_1 = (n_1 \cdot (p_{nn} - x_1))Q_0(\boldsymbol{x})$, $Q_2 = (n_2 \cdot (p_{nn} - x_2))Q_0(\boldsymbol{x})$, $Q_3(\boldsymbol{x}) = \boldsymbol{x}^T(\boldsymbol{x} - p_{nn}) + \rho^2 = \|\boldsymbol{x} - \frac{1}{2}p_{nn}\|^2 - \frac{1}{4}\|p_{nn}\|^2 + \rho^2)$, $Q_4(\boldsymbol{x}) = ((C_2^l \cdot (\boldsymbol{x} - p_{nn}))Q_0(\boldsymbol{x}) + (C_2^l \cdot Jf_{ext})Q_3(x))/(n_2 \cdot t_1)$, $Q_5(\boldsymbol{x}) = ((C_1^l \cdot (\boldsymbol{x} - p_{nn}))Q_0(\boldsymbol{x}) + (C_1^l \cdot Jf_{ext})Q_3(x))/(n_1 \cdot t_2)$

The proof of this lemma, which appears in appendix A, is based on applying the following two steps for each particular contact mode. First, substitute the contact mode's equality constraints into the equation of motion (4.2), and explicitly compute

the dynamic solution of $\{f_1, f_2, a, \alpha\}$ as a function of the center-of-mass position $\boldsymbol{x}$. Then, substitute the dynamic solution into the contact mode's inequality constraints, to obtain inequality constraints on $\boldsymbol{x}$, defining the contact mode's feasibility region. Note that the feasibility regions of all other non-static contact modes can be obtained from the regions listed in Lemma 4.3.1 by simply exchanging the indices or reversing the sliding directions.

4.3.3 Graphical examples

The following examples show the feasibility regions of contact modes, and demonstrate one of the fundamental problems of frictional dynamics, namely the *frictional dynamic ambiguity* phenomenon. This phenomenon occurs when the feasibility regions of two or more contact modes are overlapping. When the center of mass is located in the overlap region, the friction model under rigid body assumption fails to predict which of the contact mode will actually happen. In this work, we naturally focus on ambiguity of the static contact mode FF with other non-static contact mode. Such ambiguity results in *dynamic instability* of the particular equilibrium posture, as proven in the next section.

Fig. 4.3.3 shows the feasibility region of contact mode SS for $f_{ext} = f_g, \tau_{ext} \neq 0$, together with the corresponding feasible equilibrium region $\mathcal{R}_{FF}$, for two different stances with $\mu = 0.4$. The overlap region in Fig. 4.2b corresponds to dynamic ambiguity of these two contact modes. We can make two observations on the possible overlap of $\mathcal{R}_{SS}$ with $\mathcal{R}_{FF}$. As $|\tau_{ext}|$ approaches zero, $\mathcal{R}_{SS}$ moves away from the contacts toward infinity, until it vanishes at infinity when $\tau_{ext} = 0$. Let us assume that $f_{ext} = f_g$, in which case $\mathcal{R}_{FF}$ is a vertical strip. In the $\vee$-shaped terrain of Figure 4.2a, there exists an upper bound T such that for all $|\tau_{ext}| \leq T$ the region $\mathcal{R}_{SS}$

is disjoint from $\mathcal{R}_{FF}$. Consequently the entire equilibrium region is safe from both contacts breaking off in response to (f_{ext}, τ_{ext}). However, in the L-shaped terrain of Figure 4.2b, $\mathcal{R}_{FF}$ intersects $\mathcal{R}_{SS}$ for *any* non-zero τ_{ext}. Thus in general a portion of $\mathcal{R}_{FF}$ is dynamically ambiguous with respect to the SS mode.

Figure 4.3.3 shows the feasible equilibrium region $\mathcal{R}_{FF}$ for a two-contact stance under the nominal gravitational wrench $\boldsymbol{w} = (f_g, 0)$. The figure also plots, in shaded regions, the feasibility regions of contact modes FS, RS, and LS, associated with pure rolling, right sliding, and left sliding at x_1, and separation at x_2. Note that the portion of $\mathcal{R}_{FF}$ that lies outside the vertical strip bounded by the contacts suffers from frictional dynamic ambiguity of the static mode FF with one of the non-static contact modes FS,RS and LS. When the center-of-mass is positioned in this portion of $\mathcal{R}_{FF}$, $\mathcal{B}$ is highly sensitive to initial perturbations of rolling or sliding. Such scenarios suffer from frictional instability, as proven in section 4.4. Another interesting observation from Fig 4.3 is the fact that the regions $\mathcal{R}_{FS}$, $\mathcal{R}_{RS}$, and $\mathcal{R}_{LS}$ are neighboring, but not overlapping. In fact, the formulation of these region in Lemma 4.3.1 shows that at zero contact-velocity, the contact modes of right-sliding, pure rolling, and left-sliding at a particular contact are never ambiguous with respect to each other.

4.4 The Strong Equilibrium Criterion

In this section we address the problem of frictional dynamic ambiguity by applying the *strong equilibrium* condition, which was first defined by Trinkle et. al [84]. In the case of two-contact stances of a rigid body, this condition is used to compute the center-of-mass region satisfying strong equilibrium. We then prove that strong equilibrium is a necessary condition for frictional stability of equilibrium postures.

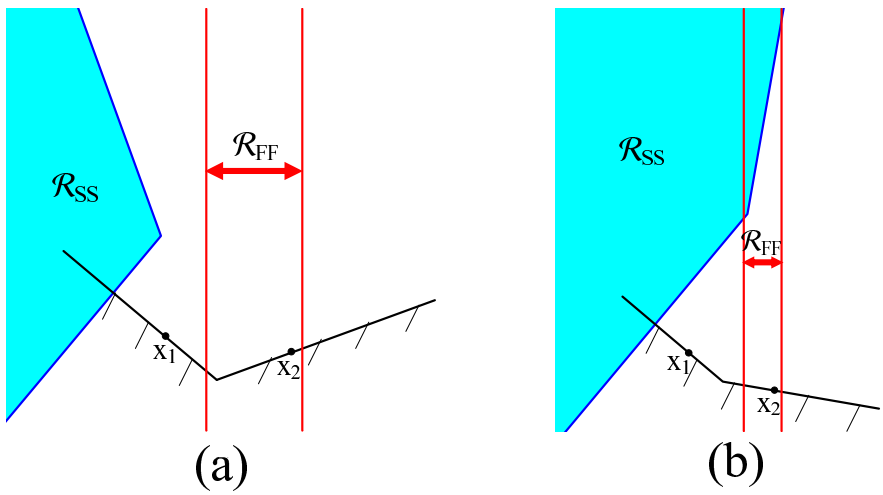

Figure 4.2: The feasible regions of modes FF and SS for two stances with $\mu = 0.4$

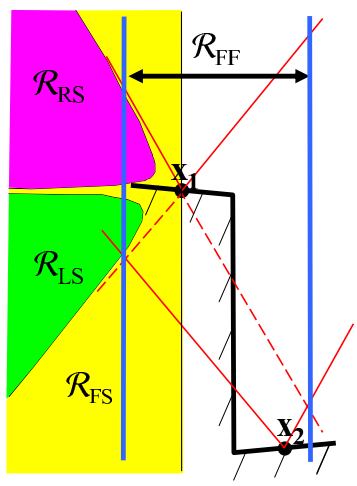

Figure 4.3: The feasible regions of modes FF, FS, RS and LS for a stances with $\mu = tan(30°)$

The definition of strong equilibrium is as follows. An equilibrium state of a mechanical system with frictional contact is a strong equilibrium, if all non-static contact modes are infeasible at the particular posture (with zero velocities). Since strong equilibrium posture is non-ambiguous with any other non-static contact mode, it is guaranteed that the only dynamically consistent motion of the system is static equilibrium.

4.4.1 Strong equilibrium in planar two-contact stances

We now apply the strong equilibrium condition for the reduced case of a planar rigid body $\mathcal{B}$ supported at an equilibrium stance by two frictional contacts. For a given external wrench $\boldsymbol{w} = (f_{ext}, \tau_{ext})$, we define the *strong equilibrium region*, denoted $\mathcal{R}(\boldsymbol{w})$ as the region center-of-mass positions $\boldsymbol{x}$ that satisfy the strong equilibrium condition. This region is computed by removing the feasibility regions of all non-static contact modes from the feasible equilibrium region $\mathcal{R}_{FF}(\boldsymbol{w})$. The following proposition summarizes the procedure for computing the strong equilibrium region for two contact stances.

Proposition 4.4.1 *Let $\mathcal{B}$ be supported by two frictional contacts and be subjected to an external wrench $\boldsymbol{w} = (f_{ext}, \tau_{ext})$. Then the strong equilibrium region for the stance, denoted $\mathcal{R}(\boldsymbol{w})$, is given by*

$$\mathcal{S}(\boldsymbol{w}) = \mathcal{R}_{FF} - (\mathcal{R}_{SS} \cup \mathcal{R}_{RR} \cup \mathcal{R}_{LL} \cup \mathcal{R}_{FS} \cup \mathcal{R}_{SF} \cup \mathcal{R}_{RS} \cup \mathcal{R}_{SR} \cup \mathcal{R}_{LS} \cup \mathcal{R}_{SL}), \quad (4.4)$$

where $\mathcal{R}_{LL}$ is obtained from $\mathcal{R}_{RR}$ by reversal of sliding direction, $\mathcal{R}_{SF}$ is obtained from $\mathcal{R}_{FS}$ by exchange of contact indices, and $\mathcal{R}_{LS}, \mathcal{R}_{SR}, \mathcal{R}_{SL}$ are obtained from $\mathcal{R}_{RS}$ by reversal of sliding direction or exchange of contact indices.

In the two-contact stance of Figure 4.3.3 with $\boldsymbol{w}_0 = (f_g, 0)$, the region $\mathcal{R}_{SS}$ is empty, and the regions $\mathcal{R}_{RR}$ and $\mathcal{R}_{LL}$ do not overlap $\mathcal{R}_{FF}$. However, after removing the

regions $\mathcal{R}_{FS}$,$\mathcal{R}_{RS}$,$\mathcal{R}_{LS}$, $\mathcal{R}_{SF}$,$\mathcal{R}_{SR}$,$\mathcal{R}_{SL}$, the strong equilibrium region $\mathcal{S}(\boldsymbol{w}_0)$ is the vertical strip spanned by the contacts x_1 and x_2.

4.4.2 Relation of strong equilibrium and frictional stability

We now show that strong equilibrium is a necessary component in achieving frictional stability. For the sake of simplicity, we assume that the terrain is *piecewise linear* in the vicinity of the contacts, and that each contact point is a sharp vertex of the contacting body, which is a fixed point with respect to the body. The following Theorem establishes the relationship between strong equilibrium and frictional stability.

Theorem 5 *Let a planar mechanical system with m frictional contacts be at an equilibrium configuration q_0 on a piecewise-linear terrain. Then a necessary condition for frictional stability of q_0 is that it is a strong equilibrium.*

Proof: Assume that the nominal configuration q_0 is not strong equilibrium. Therefore, there exists a non-static contact mode $MODE$, which is consistent under zero contact-velocities. The rest of this proof shows that under arbitrarily small velocity perturbations which are consistent with the contact mode $MODE$, the dynamic response $q(t)$ is not bounded within an arbitrarily small neighborhood of q_0.

The non-static contact mode $MODE$ contains at least one contact which is either separating or sliding. In the following, we assume that $MODE$ is associated with contact separation at the contact x_j for some j, while the second case of a sliding contact can be treated similarly. Let us define $z(q) = n_j \cdot (x_j(q) - x_j^o)$, where $x_j(q)$ is the location of the j-th contact point on the contacting body as a function of q, and $x_j^o = x_j(q_0)$ is the location of the contact point on the nominal configuration q_0. We now consider a perturbation of the form $q(0) = q_0$ and $\dot{q}(0) = \beta\eta$, where $\beta > 0$

and η is a nonzero velocity satisfying $\|\eta\|=1$, which is consistent with the kinematic constraints associated with the contact mode $MODE$. Under this perturbation, there exists a dynamic solution for accelerations and contact forces $\ddot{q} = \ddot{q}(q(t), \dot{q}(t))$, $f_i = f_i(q(t), \dot{q}(t))$, which is determined by the equations of motion (4.1) and the contact mode constraints in table 4.1. Differentiating $z(q)$ twice with respect to time and substituting the dynamic solution, the dynamics of $z(q)$ is given by $\ddot{z}(q, \dot{q}) = n_i \cdot (\dot{J}(q)\dot{q} + J_i(q)\ddot{q}(q, \dot{q}))$. Since the contact mode $MODE$ is consistent at $(q, \dot{q}) = (q_0, 0)$, there exists $a_0 > 0$ such that $\ddot{z}(q_0, 0) = a_0$. Since the dynamic solution is continuous in $(q, \dot{q})$, there exists a neighborhood defined by N_ϵ of $(q_0, 0)$, such that $\ddot{z}(q, \dot{q}) > \frac{a_0}{2}$ for all $(q, \dot{q}) \in N_\epsilon$. Define the flow $\Phi_t(q(0), \dot{q}(0))$ of the contact mode $MODE$ as the solution for $(q, \dot{q})$ at time t, satisfying the equations of motion (4.1) and the constraints of the contact mode $MODE$, with the initial conditions $q(0), \dot{q}(0)$. Since the flow Φ is continuous in $(q(0), \dot{q}(0))$ and in t, there exists $t_0 > 0$ such that the flow $\Phi_t(q_0, \beta\eta)$ is consistent with the contact mode $MODE$ and satisfies $\Phi_t(q_0, \beta\eta) \in N_\epsilon$ for all $0 < t < t_0$ and $0 < \beta < \frac{\epsilon}{2}$. Therefore, the dynamics of $z(t)$ under a initial conditions $(q_0, \beta\eta)$ such that $0 < \beta < \frac{\epsilon}{2}$ satisfies $\ddot{z}(t) > \frac{a_0}{2}$ for $t \in [0, t_0]$, and its initial conditions satisfy $z(0) = 0 \quad \dot{z}(0) \geq 0$. Hence $z(t_0)$ satisfies $z(t) > \frac{1}{4}a_0 t_0^2$ for $(q(0), \dot{q}(0)) = (q_0, \beta\eta)$ such that $0 < \beta < \frac{\epsilon}{2}$, and we can thus conclude that the solution $q(t_0)$ cannot be bounded within an arbitrarily small neighborhood of q_0 by setting β sufficiently small. $\square$

4.5 The Persistent Equilibrium Criterion

In this section we address the problem of dynamic inconsistency for mechanical systems with frictional sliding contacts. We present a new criterion, called the *persistent*

equilibrium condition, which guarantees that this inconsistency is avoided. Finally, we apply this criterion for a two-contact stance of a rigid body, and derive the *persistent equilibrium region*, which is the region of center-of-mass positions for which the persistent equilibrium condition is satisfied.

4.5.1 Frictional dynamic inconsistency and dynamic jamming

The rigid-body dynamics under Coulomb's friction assumption suffers from two major problems. The first problem is the dynamic ambiguity, which was already demonstrated in section 4.4, and can be avoided by applying the strong equilibrium condition. The second problem is the dynamic inconsistency, associated with frictional sliding. This problem was first discovered by Painlevé, with his famous example of a thin rod sliding on a plane (Fig. 4.4a). In this example, for some certain choices of the rod's physical parameters and geometry, there exist initial conditions corresponding to sliding of the rod, under which the contact mode of sliding is dynamically inconsistent, and no other contact mode is consistent. This paradoxical result, where no finite-force solution is feasible, has been recently resolved by a solution of impulsive forces, using the concept of *tangential impact* [117], (or "impact without collision" [28],[16]), in which the contact experiences an impulsive contact force, which causes a discontinuous velocity jump followed by contact separation.

Under initial conditions of nonzero sliding velocity v_i, the inconsistency of sliding occurs when the dynamic solution of the contact force f_i violates the constraint $f_i \cdot n_i \geq 0$. Since the instantaneous dynamics can be formulated as a square linear system in $(\ddot{q}, f_i)$, the dynamic solution of f_i is a fraction $f_i(q, \dot{q}) = F_{num}(q, \dot{q})/F_{den}(q)$, where $F_{den}(q)$ is the determinant of the linear system's matrix. When $F_{den}(q)$ approaches zero, the force f_i becomes unbounded. When $F_{den}(q)$ crosses zero, the sign of f_i

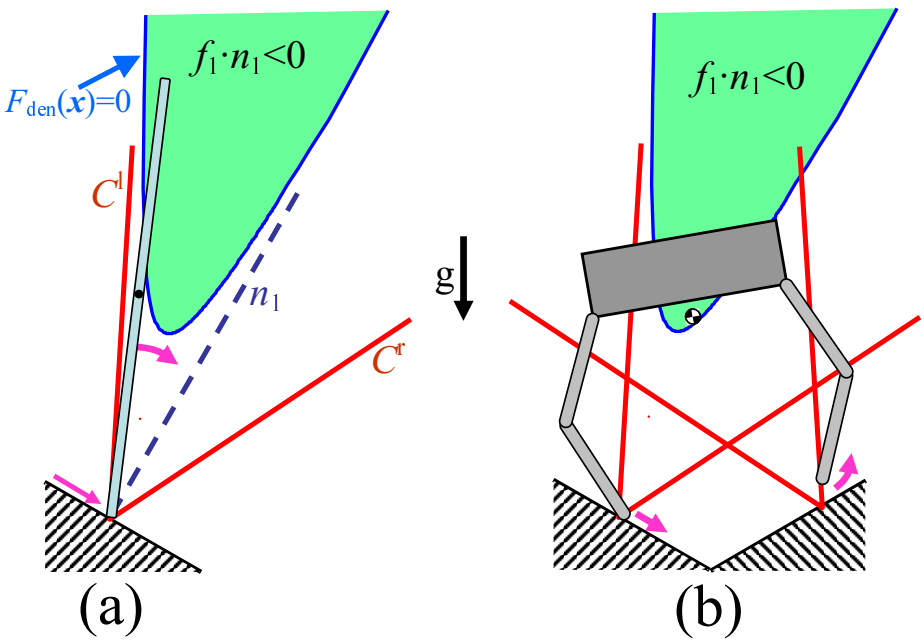

Figure 4.4: Center-of-mass region for sliding inconsistency

reverses, and sliding becomes inconsistent, and an tangential impact event occurs, followed by contact mode transition. This phenomenon, named *dynamic jamming*, was analyzed by Dupont et al. [24], and by Génot et al. [28].

We now formulate the dynamic inconsistency and dynamic jamming conditions in terms of center-of-mass location. In the case of a rigid body $\mathcal{B}$ with a variable center-of-mass $\boldsymbol{x}$ and a single right-sliding contact, the dynamic solution is identical to the RS contact mode presented in Lemma 4.3.1, since the contact force f_2 is zero. Choosing the contact x_1 as the frame origin, the denominator $F_{den}(q)$ is given by $F_{den} = (\boldsymbol{x} \cdot t_1)(\boldsymbol{x} \cdot C_1^l) - \rho^2 cos\gamma$, where ρ is $\mathcal{B}$'s radius of gyration and $\gamma = tan^{-1}(\mu)$. The curve $F_{den} = 0$ is a hyperbolic curve in $\boldsymbol{x}$, shown in Fig. 4.4a. If a sliding rod is given an initial sliding such that its center-of-mass crosses the curve $F_{den} = 0$, a dynamic jamming event occurs. This scenario was recently demonstrated experimentally by

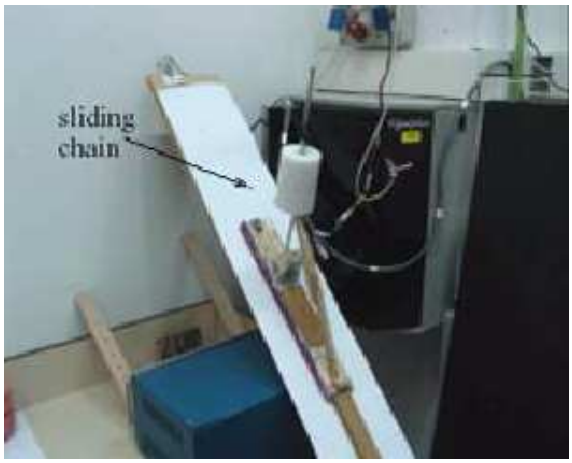

Figure 4.5: Experimental sliding rod system for demonstration of dynamic jamming

Meltz, Or and Rimon [67] on an experimental system mimicking Painlevé's rod (Fig 4.5). The sliding inconsistency and dynamic jamming may have a crucial effect on stability of equilibrium stance. In the example of Fig. 4.4b, a two-contact equilibrium stance of a rigid body is given a small perturbation such that one contact is sliding and the second is separating. Under a certain choice of physical parameters and center-of-mass position, the body may encounter a tangential impact event followed by a two-contact separation, which does not lead to the desired convergence to a nearby contact configuration. This example motivates the definition of persistent equilibrium condition.

4.5.2 The persistent equilibrium criterion

We now define the persistent equilibrium condition, which requires that both dynamic ambiguity and dynamic inconsistency are eliminated. The definition of persistent equilibrium is as follows. An equilibrium configuration of a mechanical system with frictional contact is a persistent equilibrium if it satisfies two conditions. First, is a

strong equilibrium configuration. Second, for each non-static contact that involves rolling or sliding at some contact x_j, the corresponding dynamic solution for the contact force mode f_j under zero velocities satisfies $f_j \cdot n_j > 0$.

The persistent equilibrium ensures that under a small perturbation that dictates a particular contact mode, this contact mode will govern the system's dynamics for a finite time, until either a separated contact is recovered, or a sliding contact becomes stationary. This result is summarized in the following theorem.

Theorem 6 *Let a planar mechanical system with m frictional contacts be at a persistent equilibrium configuration q_0 on a piecewise-linear terrain. Then there exists a sufficiently small neighborhood of position and velocity perturbations about equilibrium, under which the dictated contact mode persists for an arbitrarily small time $[0, t_0]$, such that on t_0 either a separated contact is recovered, or a sliding contact becomes stationary, while staying within an arbitrarily small neighborhood of q_0.*

Proof: Assume an initial perturbation $(q(0), \dot{q}(0))$ in a neighborhood N_ϵ of $(q_0, 0)$ that dictates a contact mode $MODE$. In the following, we choose a quantity $z(q)$, corresponding to either a tangential displacement, or a normal displacement of a particular contact point. We then show that under the dynamics governed by $MODE$, $\dot{z}(t)$ or $z(t)$ decreases to zero in finite time t_0, which can be made arbitrarily small by taking ϵ sufficiently small. Under the contact mode $MODE$, each contact point in is either rolling, sliding or separating. We shall defer the discussion of rolling contacts to the end of this proof. Thus, we are left with three possible cases. In the first case, all the contacts are separating. Since q_0 is strong equilibrium, $MODE$ is inconsistent at $(q, \dot{q}) = (q_0, 0)$. Thus, there exists a contact x_i such that its dynamic solution at $((q_0, 0)$ satisfies $a_i \cdot n_i < 0$. In such case, we choose $z(q) = n_i \cdot (x_i(q) - x_i^o)$, where

$x_i(q)$ is the location of the i-th contact point on the contacting body as a function of q, and $x_i^o = x_i(q_0)$ is the location of the contact point on the nominal configuration q_0. In the second case, some of the contacts are sliding. Without loss of generality, we assume right-sliding at all sliding contacts. Since q_0 is persistent equilibrium, the force constraints $f_j \cdot n_j > 0$ for all sliding contacts of $MODE$ are satisfied at $(q, \dot{q}) = (q_0, 0)$. However, q_0 is also strong equilibrium, hence $MODE$ is inconsistent at $(q, \dot{q}) = (q_0, 0)$. Thus, there exist either a separating contact x_i such that the dynamic solution at $(q_0, 0)$ satisfies $a_i \cdot n_i < 0$, or a sliding contact x_i such that the dynamic solution at $(q_0, 0)$ satisfies $a_i \cdot t_i < 0$. We choose $z(q)$ accordingly, as either $z(q) = n_i \cdot (x_i(q) - x_i^o)$ or $z(q) = n_i \cdot (x_i(q) - x_i^o)$.

Under the contact mode $MODE$, the dynamic solution for accelerations and contact forces $\ddot{q} = \ddot{q}(q(t), \dot{q}(t)),\ f_i = f_i(q(t), \dot{q}(t))$ is determined by the equations of motion (4.1) and the contact mode constraints of $MODE$ according to Table 4.1. Differentiating $z(q)$ twice with respect to time and substituting the dynamic solution gives the instantaneous acceleration $\ddot{z}(q, \dot{q})$. Due to the special choice of $z(q)$, at $(q, \dot{q}) = (q_0, 0)$ the acceleration satisfies $\ddot{z}(q_0, 0) = -a_0 < 0$. The dynamic solution is continuous in $(q, \dot{q})$ (note that the persistent equilibrium requirement guarantees that discontinuities due to dynamic jamming are avoided). Therefore, there exists a sufficiently small $\epsilon_0 > 0$ such that $\ddot{z}(q, \dot{q}) < -\frac{a_0}{2}$, and the force inequalities $f_i(q, \dot{q}) \cdot n_i > 0$ are satisfied at all sliding contacts x_i of $MODE$, for all $(q, \dot{q}) \in N_{\epsilon_0}$. Assume that $z(q)$ is the normal displacement of a separating contact. Therefore, the dynamics of $z(t)$ under the contact mode $MODE$ is required to reach zero within a given time t_0. Recall that the flow $\Phi_t(q(0), \dot{q}(0))$ of the contact mode $MODE$ is defined as the solution for $(q, \dot{q})$ at time t, satisfying the equations of motion (4.1) and the constraints of the contact mode $MODE$, with the initial conditions $q(0), \dot{q}(0)$. Using the continuity of Φ in

$(q(0), \dot{q}(0))$ and in t, there exist $t_1, \epsilon_1 > 0$ such that $\Phi_t(q(0), \dot{q}(0)) \in N_{\epsilon_0}$ for all times $0 \leq t \leq t_1$, and for all initial conditions $(q(0), \dot{q}(0)) \in N_{\epsilon_1}$ that are consistent with the contact mode $MODE$. Therefore, the dynamics of $z(t)$ satisfy $\ddot{z}(t) < -a_0/2$, and is bounded by $z(t) < z(0) + \dot{z}(0)t - a_0 t^2/4$ for all initial conditions $(q(0), \dot{q}(0)) \in N_{\epsilon_1}$, and for all $t \in [0, t_*]$, where $t_* = \min\{t_0, t_1\}$. Since $\dot{z}(0)$ is linear in $\dot{q}(0)$, there exists $\epsilon_2 > 0$, such that $|\dot{z}(0)| < a_0 t_*/8$ for all $(q(0), \dot{q}(0)) \in N_{\epsilon_2}$. Since $z(q_0) = 0$, there exists $\epsilon_3 > 0$ such that $|z(0)| < a_0 t_*^2/8$ for all $(q(0), \dot{q}(0)) \in N_{\epsilon_3}$. Under these condition, the time t at which $z(t)$ reaches zero is bounded by $t < (\dot{z}(0) + \sqrt{\dot{z}^2(0) + a_0 z(0)})/2a_0 < t^* \leq t_0$, for any initial conditions $(q(0), \dot{q}(0)) \in N_\epsilon$ which are consistent with $MODE$, where $\epsilon = \min\{\epsilon_1, \epsilon_2, \epsilon_3\}$.

If $z(q)$ is the tangential displacement of a sliding contact, the dynamics of $\dot{z}(t)$ under the contact mode $MODE$ is required to reach zero the time t_0. Using the ϵ-neighborhood defined above, $\dot{z}(t)$ is guaranteed to reach zero within the bounded time $t < t_*/2 < t_0$.

Finally, assume that the initial conditions dictate a contact mode $MODE$ that involves rolling at a contact x_j. Since q_0 is persistent equilibrium, $MODE$ is inconsistent at $(q, \dot{q}) = (q_0, 0)$, but its associated dynamic solution satisfies $f_j \cdot n_j > 0$. Thus, we are left with three possible reasons for the inconsistency of $MODE$ at $(q, \dot{q}) = (q_0, 0)$. The first reason is that there exists a separating contact x_i such that its dynamic solution at $((q_0, 0)$ satisfies $a_i \cdot n_i < 0$. In such case, we choose $z(q) = n_i \cdot (x_i(q) - x_i^o)$. The second reason, is that there exists a sliding contact x_i such that its dynamic solution at $((q_0, 0)$ violates the inequality regarding the sign of $a_i \cdot t_i$. In such case, we choose $z(q) = n_i \cdot (x_i(q) - x_i^o)$. The last possible reason for inconsistency of the contact mode $MODE$ involving rolling at x_j is that the dynamic solution for the contact force f_j violates the inequalities $\left|(f_j^t)\right| \leq \mu f_j^n$. In such case, it

can be shown that the contact mode obtained by replacing the rolling at x_j by either right-sliding or left-sliding at x_j, has a dynamic solution in which the force constraint $f_j \cdot n_j > 0$ and the kinematic constraint regarding the sign of $a_j \cdot t_j$ are both consistent at $(q, \dot{q}) = (q_0, 0)$. Therefore, the initial contact mode $MODE$ should be replaced accordingly.

4.5.3 Persistent equilibrium in planar two-contact stances

We now apply the persistent equilibrium condition for the reduced case of a planar rigid body $\mathcal{B}$ supported at an equilibrium stance by two frictional contacts. For a given external wrench $\boldsymbol{w} = (f_{ext}, \tau_{ext})$, we define the *persistent equilibrium region*, denoted $\mathcal{P}(\boldsymbol{w})$ as the region center-of-mass positions $\boldsymbol{x}$ that satisfy the persistent equilibrium condition. The procedure for computing the persistent equilibrium region is summarized as follows. First, for each non-static contact mode $MODE$, we compute its *persistency region*, denoted $\mathcal{R}'_{MODE}$, which is the region of center-of-mass locations for which the dynamic solution corresponding to $MODE$ with zero velocity under external wrench $\boldsymbol{w}$ satisfies $f_i \cdot n_i > 0$ for each contact point x_i which is sliding or rolling at the contact mode $MODE$. Using these definition and the definition of the strong equilibrium region $\mathcal{S}(\boldsymbol{w})$, the persistent equilibrium region is then given by

$$\mathcal{P}(\boldsymbol{w}) = \mathcal{S}(\boldsymbol{w}) \cap \mathcal{R}'_{RR} \cap \mathcal{R}'_{LL} \cap \mathcal{R}'_{FS} \cap \mathcal{R}'_{SF} \cap \mathcal{R}'_{RS'} \cap \mathcal{R}'_{SR} \cap \mathcal{R}'_{LS} \cap \mathcal{R}'_{SL}. \tag{4.5}$$

Graphical example: Figure 4.6 shows the feasible equilibrium region $\mathcal{R}_{FF}$ and the persistent equilibrium region $\mathcal{P}$ under the nominal gravitational wrench, for two identical symmetric stances with $\mu = 0.5$. The difference between the stances in Fig. 4.6a

and Fig. 4.6b is the mass distribution of $\mathcal{B}$, which is captured by the radius of gyration ρ. The dimensions of ρ are length units, and its true length relative to the stance's geometry is shown on both stances. The feasible equilibrium region $\mathcal{R}_{FF}$ is not affected by ρ, and is thus identical for both stances. However, the persistent equilibrium region is significantly affected by ρ, as follows. The hyperbolic curves which define the region $\mathcal{P}$ have fixed asymptotes, but their "sharpness" depends on ρ, such that they become "sharper" as ρ decreases, and a larger portion of $\mathcal{R}_{FF}$ is removed. The radius of gyration in the stance of Fig. 4.6a is twice as larger than in Fig. 4.6b, thus the persistent equilibrium region $\mathcal{P}$ in Fig. 4.6b is smaller than in Fig. 4.6a. This indicates that the persistent equilibrium region is large when ρ is large, i.e. when the mass is mostly distributed away from the center-of-mass. Note that as ρ approaches zero (i.e. the mass is concentrated near the center-of-mass), $\mathcal{P}$ does not necessarily become empty, and in the limiting case $\rho \rightarrow 0$ it can be easily computed as a polygonal region by accounting only for the asymptotes of the hyperbolic curves.

4.6 Possible Generalizations

This section sketches some possible generalizations of the concepts developed in this chapter. First, we discuss the generalization of strong and persistent equilibrium regions to multiple contacts. Next, we discuss the generalization of strong equilibrium region to guarantee robustness with respect to a given neighborhood of external wrenches neighborhood. Finally, we discuss the computation of dynamics and contact modes in 3D.

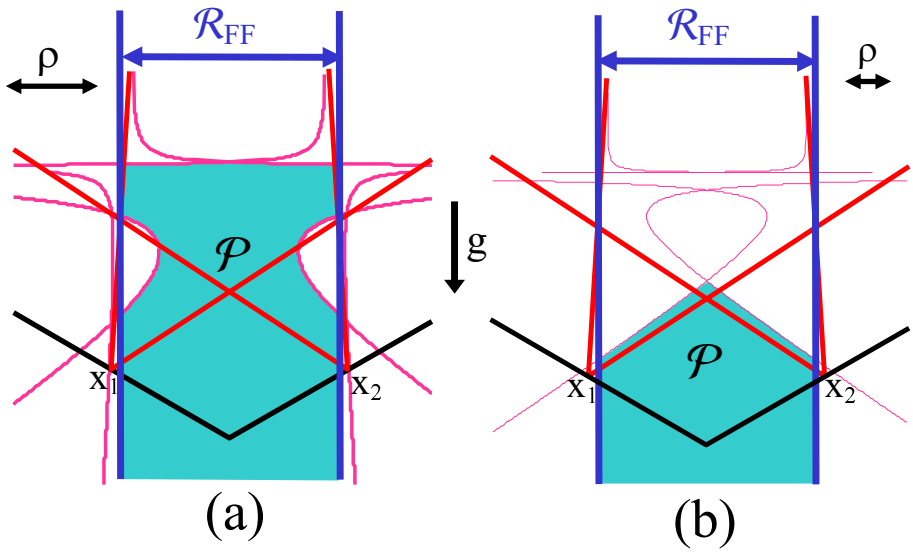

Figure 4.6: The persistent equilibrium region $\mathcal{P}(\boldsymbol{w}_o)$ for two identical stances with different radius of gyration ρ.

4.6.1 Strong and persistent equilibrium for multiple-contact stances

In order to compute the strong and persistent equilibrium regions for planar stances with k contacts, one first needs to enumerate all the possible non-static contact modes for k contacts. Given all these contact modes, one needs to compute the feasible region $\mathcal{R}_{MODE}$ and the persistent region $\mathcal{R}'_{MODE}$ for each contact mode $MODE$. Finally these regions are substituted in a straightforward extension of Eqs. (4.4) and (4.5) to obtain the strong and persistent equilibrium regions $\mathcal{S}$ and $\mathcal{P}$.

Enumeration of multiple contact non-static modes

Consider a k-contact stance of a rigid body $\mathcal{B}$. The non-static k-contact modes are k-letter words from the alphabet $\{S, F, R, L\}$. Although there are 4^k different

combinations, some of them represent contact modes which over-constrain the instantaneous motion of $\mathcal{B}$, and are therefore *kinematically infeasible*. For example, the 3-contact modes RRR and LLL are kinematically feasible only if the three contact normals intersect at a single point, which is a non-generic geometry. As a result, the kinematically feasible k-contact modes are represented by k-letter words where only two letters are allowed from the set $\{S, F, R, L\}$, and the rest $k-2$ letters must be S. Therefore, the total number of the non-static modes is bounded by $(4k)^2$, which is merely quadratic in k.

This principle also holds when enumerating the contact modes of a planar kinematic chain with n degrees of freedom and k frictional contacts. The contact modes are k-letter words from the alphabet $\{S, F, R, L\}$ such that $2n_F + n_R + n_L < n$, where n_F, n_R, n_L are the numer of occurences of the letters F, R, L respectively. Therefore, the numer of kinematically feasible contact modes is roughly exponential in $\min\{n, k\}$.

Construction of of non-static feasible regions

We now sketch the procedure for computing the non-static feasible regions in $k-$contact postures. Taking $k = 3$ as an example, the kinematically feasible contact modes are 3-letter words, which contain at least one S letter. Therefore we only need to consider the combinations SXX, XSX, XXS, where $X \in \{S, F, R, L\}$. Since S represents vanishing of a contact force, the associated dynamic solutions involve only *two* active contacts. Therefore, the feasible region of a 3-contact mode is simply the intersection of the feasible region of a 2-contact mode, as described in section 4.3, together with the inequality imposed by the additional S letter. For example, the feasible region of RSS mode is obtained by taking the RS region ignoring x_3, and then intersecting with the additional inequality $a_3 \cdot n_3 > 0$ after substituting the dynamic solution. For the general k-contact case, the feasible region of a $k-$contact mode is obtained

by taking the feasible region of the two active contacts, and then intersecting with additional inequalities of the form $a_i \cdot n_i > 0$. Finally, The computation of the strong equilibrium region now follows the same course as described in section 4.4, using $k-2$ additional constraints in each non-static mode.

When computing the k-contact persistent equilibrium region, one needs to compute the persistent region of each contact mode. However, the persistent region of a k-contact mode $MODE$ is identical to the persistent region of the two-contact mode obtained by ignoring all the separating contacts (S letter) of $MODE$. Therefore,extending the computation of persistent equilibrium region in Eq. (4.5) to multiple contact is straightforward.

4.6.2 Robustness of strong equilibrium region

Given a neighborhood $\mathcal{W}$ of external wrenches surrounding the nominal gravitational wrench, the robust strong equilibrium region, denoted $\mathcal{S}(\mathcal{W})$ is the center-of mass region that maintain strong equilibrium under any external wrench $\boldsymbol{w}$ from $\mathcal{W}$. Formally, this regions is defined as the intersection

$$\mathcal{S}(\boldsymbol{w}) = \cap_{\boldsymbol{w} \in \mathcal{W}} \mathcal{S}(\boldsymbol{w}) \ .$$

We now sketch the procedure for computing the robust strong equilibrium region $\mathcal{S}(\mathcal{W})$, which is detailed in [77],[76]. First, one needs to compute the $\mathcal{W}$-feasible region of each non-static contact modes. The $\mathcal{W}$-feasible region of a non-static contact modes $MODE$ is the union of the feasible region $\mathcal{R}_{MODE}(\boldsymbol{w})$ for all $\boldsymbol{w} \in \mathcal{W}$. The feasible region of $MODE$ is determined by inequalities in $\boldsymbol{x}$ and $\boldsymbol{w}$, which define a region in the composite space of $(\boldsymbol{x}, \boldsymbol{w})$. The $\mathcal{W}$-feasible region of $MODE$ is precisely the projection of this region onto the $\boldsymbol{x}$-plane. This projection is computed in [76]

by using standard techniques for identifying candidate silhouette curves (e.g. [19, p. 102]), which results in a planar arrangement of cells. Finally, $\mathcal{S}(\mathcal{W})$ is obtained by subtracting the $\mathcal{W}$-feasible of all contact modes from the robust equilibrium region $\mathcal{R}_{FF}(\mathcal{W})$, whose computation is detailed in chapter 2. A robust persistent equilibrium region $\mathcal{P}(\mathcal{W})$ of center-of-mass locations guaranteeing persistent equilibrium for any $\boldsymbol{w} \in \mathcal{W}$ can be computed by a similar procedure. However, this computation is not discussed further in this chapter.

4.6.3 Frictional dynamics in three dimensions

We now briefly discuss the dynamics of mechanical systems with frictional contacts in 3D. Let q denote the configuration of an n degrees-of-freedom mechanical system with k contacts in 3D. Recall that each contact x_i is assigned a frame (s_i, t_i, n_i) such that n_i is the contact normal and s_i, t_i are unit tangents to the contact. The system's equation of motion is given by Eq. (4.1), where the contact forces $f_i \in \mathbb{R}^3$ are constrained to lie within their quadratic friction cones $\mathcal{C}_i$, whose definition is given in Eq. (3.3) in Chapter 3. At a given instant, where $(q, \dot{q})$ are known, the dynamic solution for $\ddot{q}$ and contact forces f_i in (4.1) requires additional constraints associated with a chosen contact mode. There are only three possible interactions at a single contact in 3D, which are separation, rolling, and sliding. Coulomb's friction model states that contact force at a sliding contact point lies at the boundary of its friction cone. Furthermore, the direction of the contact force at a sliding contact point is determined such that the tangential component of the contact force opposes the tangential velocity at the corresponding contact point. This principle is known as *the maximum dissipation principle*, and in the 2D case it reduces to simply determining the sign of the force's tangential component. The kinematic and force constraints

for each contact mode in 3D are summarized in Table 4.3. A key observation is that each contact mode contribute *three* scalar equality constraints. Using the relation $v_i = J_i(q)\dot{q}$ and its time derivative, the equation of motion (4.1) augmented with the constraints of a particular k-contact mode give $n + 3k$ equations in the unknowns $\ddot{q}, f_i$. Note that in case of fixed (rolling) or separating contacts, the equations are *linear* in $\ddot{q}, f_i$. Consider now a k-contact mode associated with sliding at a contact x_i. If the given contact velocity v_i is nonzero, the direction u_i of the contact force f_i is uniquely determined by its two equality constraints, while only its magnitude λ_i is unknown. Since for a given u_i, λ_i appears linearly in the equation of motion and contact constraints, they can be reformulated as a linear system. However, when the instantaneous contact velocity v_i is zero, the situation is more complicated. The time-derivative of the constraint $(f_i - (n_i \cdot f_i)n_i)||v_i$ is a linear constraint in $\ddot{q}$ and f_i. Since the acceleration a_i is unknown, the direction of f_i is unknown. Thus, the constraint $f_i \in \mathsf{bdy}(\mathcal{C}_\mathsf{i})$ is *quadratic* in f_i. Recall that evaluation of strong equilibrium configurations require computation of the instantaneous dynamic solution associated with each contact mode *at zero velocity.* Thus, the dynamics associated with a k-contact mode with n_s sliding contacts gives a polynomial system of total degree 2^r in the unknowns $\ddot{q}, f_i$, posing major technical difficulties in computing the solution for large values of n_s. Moreover, unlike the planar case, a single contact mode that involves sliding can have multiple dynamic solutions. Under these observations, the strong equilibrium region cannot be formulated in closed form even for the minimal number of three contacts. However, approximate solutions can be obtained by replacing the friction cone boundaries by polyhedral facets, which "linearize" the dynamics of sliding contacts. This approach was used in [86] to formulate the dynamics as a linear complementarity problem. However, the implementation of this approach for

contact mode	**kinematic constraints**	**force constraints**
separation	$v_i \cdot n_i > 0$	$f_i = \vec{0}$
fixed (rolling)	$v_i = \vec{0}$	$f_i \in \mathcal{C}_i$
sliding	$v_i \cdot n_i = 0$	$f_i \in \mathsf{bdy}(\mathcal{C}_\mathsf{i})$ $(f_i - (n_i \cdot f_i)n_i) \| \| v_i$

Table 4.3: Contact modes at a single frictional contact in 3D.

approximating the center-of-mass strong and persistent equilibrium regions in 3D is still an open problem.

Chapter 5

Hybrid Dynamics of Planar Mechanical Contact Systems

This chapter analyzes the impulsive hybrid dynamics of planar mechanical contact systems. In particular, we focus on the case of a planar rigid body $\mathcal{B}$ supported by two frictional contacts. The structure of this chapter is as follows. Section 5.1 defines the basic terminology of impulsive hybrid dynamical systems, which combine phases of continuous motion with discrete events of collisions. We then use the classical example of a bouncing ball to demonstrate the phenomenon of *Zeno limit point* at which the system's dynamic solution converges to a contact configuration while experiencing an infinite sequence of collisions in finite time. In section 5.2 we analyze the dynamics of a rigid rod with two contact points on a horizontal floor. We show that there exists an open set of initial conditions for which the rod's dynamic solution is *bouncing motion* on a single contact, that converges a single-contact Zeno limit point. Section 5.4 analyzes the *clattering motion*, which is a dynamic solution involving an infinite sequence of alternating collisions at two contacts, that converges to a double-contact

Zeno limit point. We derive conditions on the systems's parameters guaranteeing that clattering motion is stable, and show that there exists an open set of initial conditions for which the systems' solution converges to clattering motion. Simulation results are shown in Section 5.5. Section 5.6 extends the analysis to symmetric equilibrium stances of a planar symmetric rigid body. Finally, Section 5.7 generalizes to the non-symmetric case, derives the general conditions for clattering stability, and provides a graphical example of the center-of-mass region of clattering stability in a two-contact frictional equilibrium stance.

5.1 Definition of Impulsive Hybrid Dynamical Systems

In this section we define the basic notation of *impulsive hybrid dynamical systems* for modelling planar multiple-contact mechanical systems. Then we define the notion of em dynamic solution for such systems. Finally, we analyze the classical example of a bouncing ball, and demonstrate the key concept of dynamic solution that converges to a *Zeno limit point*.

5.1.1 Basic terminology

Let Q denote the n-dimensional configuration space of a mechanical system with m contacts, and let $(q, \dot{q})$ denote the dynamical system's state, composed of the system's configuration and velocity. The contacts are represented by m unilateral constraints of the form $h_i(q) \geq 0$, where $h_i : Q \to I\!R$ are smooth functions. We assume that the sets defined by $\mathcal{S}_i = \{q : h_i(q) = 0\}$ are smooth manifolds. Finally, let $\mathcal{F}$ denote the

space of of *contact-free states* , defined by $\mathcal{F} = \{(q, \dot{q}) : h_i(q) > 0 \text{ for } i = 1 \dots k\}$. For contact-free states, the system's dynamics is governed by the equation of motion

$$M(q)\ddot{q} + B(q, \dot{q}) + G(q) = 0, \tag{5.1}$$

where $M(q)$ is the positive-definite inertia matrix, $B(q, \dot{q})$ is the vector of velocity-dependent generalized forces, and $G(q)$ is the vector of gravitational terms. When the system reaches a contact with a non-zero approach velocity, a collision occurs. This condition on the system's state can be formulated as $(q, \dot{q}) \in G_i$, where $G_i = \{(q, \dot{q}) : h_i(q) = 0 \text{ and } \dot{q} \cdot N_i(q) < 0\}$, for $i = 1 \dots m$, and $N_i(q) = \nabla_q h_i(q)$. The collision is modelled as a discrete event of discontinuous jump in the system's state. This jump is described by a set of *reset maps* $R_i : G_i \to TQ$, for $i = 1 \dots k$, that takes the system's pre-collision state $(q^-, \dot{q}^-)$ to a post-collision state $(q^+, \dot{q}^+ = R_i(q^-, \dot{q}^-)$. A hybrid system with unilateral constraints is fully defined by its contact-free equation of motion (5.1), its unilateral constraints $h_i(q)$ representing the contacts, and its reset maps R_i describing the interaction at collisions. A *dynamic solution* of an impulsive hybrid dynamical system for a given initial state $(q(0), \dot{q}(0))$ consists of a piecewise-smooth function $q(t)$ and an ordered set of collision times $\mathcal{T} = \{t_1, t_2, \dots\}$, which may be a finite of infinite set. Between collision times $t \in (t_j, t_{j+1})$, the system's state $(q(t), \dot{q}(t))$ satisfies the equation of free motion (5.1). At any collision time $t_j \in \mathcal{T}$, the system's state satisfies $(q(t_j), \dot{q}(t_j)) \in G_i$ for some $i \in \{1 \dots m\}$, corresponding to a collision at the i-th contact. At each collision time, a discontinuous jump in the system's state occurs, which is determined by the reset map as $(q(t_j^+), \dot{q}(t_j^+)) = R_i(q(t_j^-), \dot{q}(t_j^-))$. In application of mechanical systems with intermittent contact, the reset maps describe the effect of an instantaneous *impact* acting at the contacts.

5.1.2 Modelling impact in rigid-body collisions

We now briefly overview some basic notions of rigid body impact, which are used to define the reset maps. When two bodies collide, they interact during a short period of time, and the evolving contact forces are coupled with local deformations at the vicinity of the contacts, depending on the stiffness of the two bodies. When the stiffness of the bodies is high, they are commonly idealized as perfectly rigid, and the interaction during collision is lumped to an infinitesimally short period of time, as follows. The interacting contact forces are modelled as an impulsive force f_i acting at the contact point x_i. During the collision interaction, the contact force f_i is dominating over all other forces, and the equation of motion during the collision reduces to $M(q)\ddot{q} = J_i^T(q)f_i$, where J_i is the Jacobian matrix of the contact point's position x_i. Since the duration of collision is considered infinitesimally, f_i is modelled as an impulsive force, causing a discontinuous change in the velocity $\dot{q}$, while the configuration q is assumed to remain unchanged. The *impulse* is defined as $P_i = \int f_i dt$. The relation between the impulse and the velocity change $\Delta\dot{q}$ at a contact configuration q_0 is thus given by

$$M(q_0)\Delta\dot{q} = J_i^T(q_0)P_i. \tag{5.2}$$

Since the velocity of the contact point x_i satisfies $v_i = J\dot{q}$, the change in v_i due to the impact is given by $\Delta v_i = J_i(q_0)M(q_0)J_i^T(q_0)P_i$. Therefore, a physically realistic reset map R_i can be obtained by choosing a *collision law*, which defines a relation between the pre-collision contact velocity v_i and the impact P_i. In this work we will be using a simple collision law, based on *normal impact with normal restitution.* This collision law assumes that the impulse P_i acts at the contact point in the normal direction. The magnitude of the impulse is determined such that the change in the

normal velocity at the contact, defined by $v_i^n = \dot{q} \cdot N_i(q)$, satisfies $v_i^n(t^+) = -ev_i^n(t^-)$, where t^- and t^+ are, respectively, the pre-collision and post collision instants. This law uses a single scalar parameter, named *coefficient of normal restitution* $e \in [0, 1]$, representing the degree of energy dissipation during the collision. The corresponding reset maps R_i are formulated as ([1])

$$R_i(q, \dot{q}) = (q, A_i(q)\dot{q}), \text{ where } A_i(q) = I - \frac{1+e}{N_i(q)^T M^{-1}(q) N_i(q)} M^{-1}(q) N_i(q) N_i(q)^T, \tag{5.3}$$

and I is the $n \times n$ identity matrix. This law amounts to a linear relationship between the pre- and post- collision velocities, which is given by $\dot{q}_i(t^+) = A_i(q)\dot{q}(t^-)$, where q is the configuration at collision. Examples of more complicated collision laws that account for friction at the contacts can be found in [21],[117],[108]. In the rest of this work, we assume that $0 < e < 1$, and exclude the two limiting cases of perfectly plastic and perfectly elastic collisions.

5.1.3 Coordinate transformation and linearization

Suppose that we define an alternative set of coordinates, demoted q'. The equation of motion (5.1) and the collision law (5.3) can now be expressed in q' as follows. The velocities $\dot{q}$ and $\dot{q}'$ are related by the linear transformation $\dot{q}' = J(q)\dot{q}$, where $J(q) = \frac{\partial q'}{\partial q}$ denotes the Jacobian matrix. Differentiating this relation and substituting into the equation of motion (5.1) gives the equation of motion expressed in q':

$$\ddot{q}' - \dot{J}(q)J^{-1}(q)\dot{q}' + J(q)M^{-1}(q)(B(q, \dot{q}) + G(q)) = 0. \tag{5.4}$$

The reset maps (5.3) can now be expressed in $\dot{q}'$ as

$$\dot{q}'(t^+) = A_i'(q)\dot{q}'(t^-), \text{ where } A_i'(q) = J(q)A_i(q)J^{-1}(q),\ i = 1 \ldots m. \tag{5.5}$$

. Assuming now that the dynamic solution of the system stays in the neighborhood of a configuration q_0, the linearized equation of motion is given by

$$\ddot{q}' - \dot{J}(q_0)J^{-1}(q_0)\dot{q}' + J(q_0)M^{-1}(q_0)(B(q_0,\dot{q}) + G(q_0)) = 0, \tag{5.6}$$

and the linearized reset maps are given by $\dot{q}'(t^+) = A_i'(q_0)\dot{q}'(t^-)$.

5.1.4 The bouncing ball example and Zeno limit point

The classical example of a bouncing ball was widely explored in the literature (e.g. [2],[121],[112]) as an example of Zeno behavior in hybrid dynamical systems. Consider a ball modeled as a point mass m bouncing on a horizontal floor in planar gravitational field (Fig. 5.1(a)). The system's configuration is the position of the ball $q = (x, y)$. The contact-free dynamics of the system is given by

$$\begin{bmatrix} m & 0 \\ 0 & m \end{bmatrix} \begin{pmatrix} \ddot{x} \\ \ddot{y} \end{pmatrix} = \begin{pmatrix} 0 \\ -mg \end{pmatrix},$$

where $g > 0$ is the acceleration of gravity. The contact is represented by a single constraint $h_1(q) = y \geq 0$. Using the frictionless impact model with coefficient of normal restitution e, the reset map is given by $R_1(q, \dot{q}) = (q, (-e\dot{y}, \dot{x}))$. We now analyze the dynamic solution of the impulsive hybrid dynamical system of the bouncing ball, for given initial conditions $q(0) = (y_0, x_0)$ and $\dot{q}(0) = (v_{y0}, v_{x0})$. One of the most common techniques for analysis of hybrid dynamical systems is the *Poincaré Map* [34],[70], which is based on sampling the dynamic solution $q(t), \dot{q}(t)$ on specific times, which are naturally chosen as the collision times. The Poincaré Map induces a discrete-time dynamics, associated with the system's state at collision times. We now demonstrate the Poincaré Map technique on the classical bouncing ball example. Integrating the ball's equation of motion, the time of first collision with the floor can be computed

as $t_1 = \frac{v_{y0}+\sqrt{v_{y0}^2+2gy_0}}{g}$, with hitting velocity of $\dot{y}(t_1^-) = -\sqrt{v_{y0}^2 + 2gy_0}$. After the first collision, a new free-flight phase starts with the initial vertical velocity given by $\dot{y}(t_1^+) = -e\dot{y}(t_1^-))$, while the horizontal velocity v_x remains unchanged. Integrating the flight motion similarly for the next flight phases, it can be shown that the post-collision vertical velocity is governed by the discrete-time dynamic equation $\dot{y}(t_{k+1}^+) = e\dot{y}(t_k^+)$. The solution of this discrete system is given by $\dot{y}(t_k^+) = e^k\sqrt{v_{y0}^2 + 2gy_0}$. Hence for any $e < 1$ this discrete-time dynamics is stable, and the sequence of collision velocities asymptotically converges to zero. Furthermore, it can be shown that the bouncing is completed in finite time, as follows. Let us denote $\tau_k = t_k - t_{k-1}$ as the time difference between two consecutive collisions. Integrating the flight equation between two collisions, τ_k can be computed as $\tau_k = \frac{2\dot{y}(t_{k-1}^+)}{g}$. The total time of the collisions sequence is $t_\infty = t_1 + \sum_{k=1}^{\infty} \frac{2\dot{y}(t_k^+)}{g} = \frac{v_{y0}}{g} + \frac{1+e}{1-e}\frac{\sqrt{v_{y0}^2+2gy_0}}{g}$. This is precisely the *Zeno behavior*, describing a dynamic solution with infinite number of collisions, that is completed in finite time. The set $\{(q, \dot{q}) : h_1(q) = 0 \text{ and } \eta_1(q) \cdot \dot{q} = 0\}$ is denoted *a Zeno limit set*, to which the system's state converges in finite time t_∞, while recovering the contact. Note that the solution of the impulsive hybrid dynamical system is not defined past the Zeno time t_∞. However, physical consideration suggest that the system's solution should be concatenated with a solution of a constrained mechanical system that maintains the recovered contact, whose initial conditions are determined by the system's state at the Zeno time t_∞ [3]. In the bouncing ball example, note that the ball's horizontal motion is unaffected by the collisions. Thus, after the bouncing motion ceases and contact is recovered at $t = t_\infty$, the ball starts sliding horizontally with new initial conditions, given by $x(t_\infty) = x_0 + v_{x0}t_\infty$ and $\dot{x}(t_\infty) = v_{x0}$, while the contact is maintained.

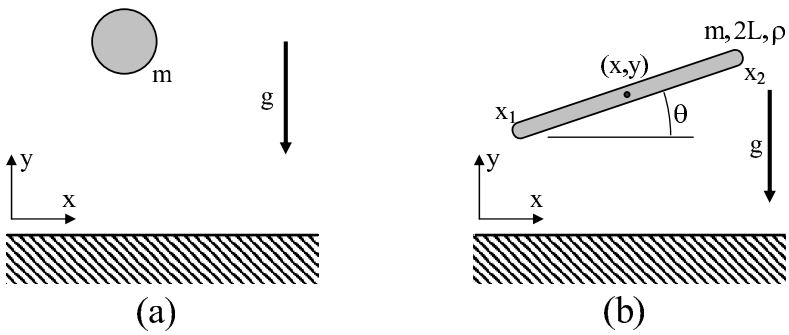

Figure 5.1: (a) The bouncing ball example (b) The symmetric horizontal rod example.

5.2 The Symmetric Horizontal Rod Example

In this section we analyze the planar example of a symmetric rod flying above a horizontal floor under gravity. First we formulate the rod's linearized equations of motion as an impulsive hybrid dynamical system. Then we show that the motion of the rod is governed by two qualitatively different modes. The first mode is the *bouncing motion*, at which the rod possesses an infinite sequence of collisions at a single contact. The second mode is the *clattering motion*, at which the rod possesses an infinite sequence of alternating collisions at both contacts.

5.2.1 Formulation of the linearized hybrid system

Consider a thin rigid rod on a horizontal floor in a planar gravitational field. The mass of the rod is m and its length is $2L$. The mass of the rod is distributed symmetrically about its center such that its moment of inertia is $m\rho^2$, where ρ is the *radius of gyration*. The configuration of the rod is given by $q = (x, y, \theta)$, where (x, y) is the position of the rod's center-of-mass, and θ is its angle about the horizontal direction

(Fig 5.1(b)). The rod's equation of free motion is given by

$$\begin{pmatrix} m & 0 & 0 \\ 0 & m & 0 \\ 0 & 0 & m\rho^2 \end{pmatrix} \begin{pmatrix} \ddot{x} \\ \ddot{y} \\ \ddot{\theta} \end{pmatrix} = \begin{pmatrix} 0 \\ -mg \\ 0 \end{pmatrix}. \tag{5.7}$$

We assume that the rod makes contact with the ground only by its two endpoints x_1 and x_2. The contact constraints are thus given by

$$h_1(q) = y - L\sin\theta \geq 0, \text{ and } h_2(q) = y + L\sin\theta \geq 0, \tag{5.8}$$

where h_i is the height of the endpoint $x_i, i = 1, 2$ above the floor (Fig. 5.1b). We now make a natural choice of an alternative coordinate set, given by $q' = (h_1, h_2, x)$, with its velocity denoted by $\dot{q}' = (v_1, v_2, v_x)$. The Jacobian matrix that satisfies the relation $\dot{q}' = J\dot{q}$ is given by

$$J = \begin{pmatrix} 0 & 1 & -L\cos\theta \\ 0 & 1 & L\cos\theta \\ 1 & 0 & 0 \end{pmatrix}.$$

At the configuration $q_0 = \vec{0}$ the rod lies horizontally on the floor. We assume that the rod's motion stays within a small neighborhood of q_0 such that the angle θ is small $|\theta| \ll 1$. The equation of motion (5.7) can now be expressed in q' as shown in (5.4), and linearized about q_0 as described in (5.6). The resulting linearized equation of motion expressed in q' is given by

$$\begin{pmatrix} \ddot{h}_1 \\ \ddot{h}_2 \\ \ddot{x} \end{pmatrix} = \begin{pmatrix} -g \\ -g \\ 0 \end{pmatrix}. \tag{5.9}$$

Note that the centripetal accelerations that depend on ω^2 vanish at $q = q_0$. The collision laws (5.3) can be expressed in $\dot{q}'$ as described in (5.5). Evaluation at $q = q_0$ gives the linearized collision laws

$$\dot{q}'(t^+) = A_i'\dot{q}'(t^-)\ ,\ i = 1, 2\ ,\ \text{where}$$
$$A_1' = \begin{pmatrix} -e & 0 & 0 \\ (1+e)\psi & 1 & 0 \\ 0 & 0 & 1 \end{pmatrix}, A_2' = \begin{pmatrix} 1 & (1+e)\psi & 0 \\ 0 & -e & 0 \\ 0 & 0 & 1 \end{pmatrix}, \text{and } \psi = \tfrac{L^2-\rho^2}{L^2+\rho^2}. \tag{5.10}$$

The nondimensional parameter ψ (denoted q in [30]) encompasses the mass distribution of the rod as follows. For $\psi = 1$ the rod's mass is concentrated at its center. For $\psi = 0.5$ the rod's mass is uniformly distributed. For $\psi = 0$ the rod's mass is concentrated at its endpoints. In the following analysis we show that the pair (e, ψ) has a crucial influence on the motion of the rod. Moreover, we show that the motion of the rod is dominated by two qualitatively different modes, namely, the bouncing motion and the clattering motion. For simplicity, we assume that at $t = 0$, the rod starts from rest $\dot{q}(0) = \vec{0}$, and is given a small perturbation in its initial configuration $q(0)$.

5.3 Bouncing Motion of the Rod

The bouncing motion occurs when the rod possesses an infinite (Zeno) sequence of collisions at one of its endpoints while the other endpoint remains contact-free. We now analyze the linearized dynamics of bouncing and derive conditions on the initial states that converge to bouncing motion. Assume that the rod possesses bouncing motion at x_1, and consider the motion of $h_1(t)$. The equation of free motion for h_1 is $\ddot{h}_1 = -g$. At a collision time t_k the reset map (5.10) implies that $v_1(t_k^+) = -ev_1(t_k^-)$.

Therefore, the motion of $h_1(t)$ is identical to the motion of a bouncing ball, and results in a Zeno sequence that depends only on the initial conditions $h_1(0), v_1(0)$. However, in order to guarantee that bouncing at x_1 will actually occur, the rod's other endpoint x_2 must not establish contact during the whole bouncing time. The motion of the second endpoint $h_2(t)$ is coupled with the motion of $h_1(t)$, and depends on initial conditions and on the non-dimensional parameters (e, ψ). The following theorem establishes the conditions on the systems's initial configuration for which bouncing will occur, converging to a single-contact Zeno limit point.

Theorem 7 *Consider the linearized hybrid dynamics of the horizontal rod, with the initial configuration* $q'(0) = (h_{10}, h_{20}, x_0)$, $\dot{q}'(0) = \vec{0}$, *such that* $h_{10} < h_{20}$. *Then the dynamic solution corresponds to bouncing motion on* x_1 *and converges to a single-contact Zeno limit point if and only if the initial configuration satisfies the condition given by*

$$h_{20} \geq \left(1 + \frac{4e(1+\psi)}{(1-e)^2}\right) h_{10} \tag{5.11}$$

It is important to note here that the Zeno limit point corresponds to recovering a single contact, but *it is not a equilibrium point of the physical system.* This means that at $t = t_\infty$ the rod has nonzero velocity, and may even have nonzero sliding velocity at the recovered contact. Note, too, that when $h_{10} > h_{20}$, the condition for bouncing on x_2 to a Zeno limit point can be similarly obtained by exchanging the indices in (5.11).

Proof: Assuming that $h_{10} < h_{20}$, the rod first collides with x_1 at time $t_1 = \sqrt{2h_{10}/g}$. When bouncing on x_1, the solution of $v_1(t)$ is identical to the bouncing ball motion, and is given by $v_1(t_k^+) = v_0 e^k$, where $v_0 = \sqrt{2gh_{10}}$. The time-difference between two consecutive collisions is given by $\tau_k = t_k - t_{k-1} = \frac{2v_1(t_{k-1}^+)}{g}$. We now

analyze the motion of the second endpoint x_2. After the first collision with x_1, the velocity of x_2 is given by $v_2(t_1^+) = -(\psi(1+e)+1)v_0$. At the following collisions, v_2 satisfies

$$v_2(t_{k+1}^+) = v_2(t_{k+1}^-) + \psi(1+e)v_1(t_{k+1}^-) = v_2(t_k^+) - g\tau_{k+1} - \psi(1+e)v_1(t_k^+)$$

The sequence of velocities v_2 is thus formulated by

$$v_2(t_k^+) = v_2(t_1^+) - \sum_{j=1}^{k-1}(2+(1+e)\psi)v_1(t_j^+) = -\left(1+(1+e)\psi + (2+(1+e)\psi)\frac{e}{1-e}(1-e^{k-1})\right)v_0.$$

At the first collision time the height h_2 is given by $h_2(t_1) = h_{20} - h_{10}$. At the following collision times, h_2 satisfies

$$h_2(t_{k+1}) = h_2(t_k) + v_2(t_k^+)\tau_{k+1} - \tfrac{1}{2}g\tau_{k+1}^2 = h_2(t_k) + \tfrac{2}{g}v_1(t_k^+)\left(v_2(t_k^+) - v_1(t_k^+)\right).$$

The sequence of h_2 at collision times is thus formulated by

$$h_2(t_k) = h_2(t_1) + \tfrac{2}{g}\sum_{j=1}^{k-1} v_1(t_j^+)\left(v_2(t_j^+) - v_1(t_j^+)\right) = h_{20} + \left(4\frac{e^k(1+e) - e^{2k} - e}{(1-e)^2}(1+\psi) - 1\right)h_{10}.$$

The bouncing motion on x_1 is completed without colliding at x_2 if the limit value of h_2 satisfies $h_2(t_\infty) \geq 0$, which is the condition given in (5.11). □

Consider now the plane of initial conditions (h_{10}, h_{20}), where only its first quadrant $h_{10}, h_{20} \geq 0$ is physically permissible. Theorem 7 can be interpreted graphically as definition of regions in (h_{10}, h_{20}) plane for which the solution of the rod's hybrid system corresponds to bouncing motion on a single contact that converges to a Zeno limit point. These regions are the planar sectors formulated in (5.11) with possible exchange of indices, and are illustrated in Figure 5.2. Note that when the initial conditions lie outside of these regions, the dynamic solution involves collisions at both contacts, whose analysis is more difficult. In the next section we focus on the

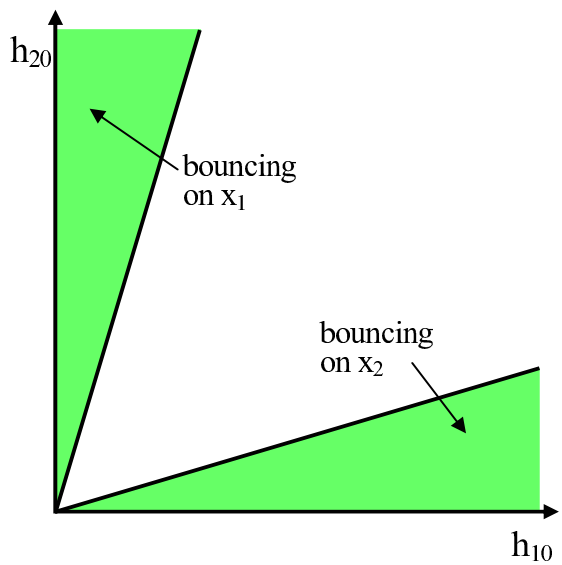

Figure 5.2: The plane of initial conditions (h_{10}, h_{20}), with the regions that correspond to bouncing motions (shaded).

special case of *clattering motion*, on which the rod possesses an infinite sequence of alternating collisions at both contacts.

5.4 Clattering Motion of the Rod

The clattering motion occurs when the rod possesses an infinite sequence of alternating collisions at both contacts. When analyzing the clattering motions, two different conditions must be checked:

1. Clattering persistence - the alternating order of collisions is maintained during the whole sequence of collisions.

2. Clattering convergence - the solution converges to a Zeno limit point at which the two contacts are recovered in finite time.

Clattering motion is then termed as *stable clattering* if both conditions, of persistence and convergence, are met. Our analysis of clattering motion is strongly based on works by Goyal et. al. [30],[31]. We start by reviewing the analysis of Goyal, which derives conditions for stability of clattering motion under the simplifying assumption of *zero gravity*. Then we extend Goyal's assumption, analyze the dynamics of clattering with nonzero gravity, and derive general conditions on clattering stability. Finally, we derive condition on the initial configuration for which the rod will enter clattering mode and converge to a two-contact Zeno limit point.

5.4.1 Clattering motion with zero gravity

We now review Goyal's analysis of clattering motion under the simplifying assumption of zero gravity. Under this assumption, during the free-flight phase formulated in (5.9) the velocities $\dot{q}'(t)$ remain constant, and change only at the instants of collisions. Thus the rod's linearized dynamics is governed only by the impact equations, and can be formulated as a discrete-time linear system in the post-collision velocities, as follows. Let us define $\boldsymbol{v}_k = [v_1(t_k^+)\ v_2(t_k^+) v_x(t_k^+)]^T$ for $k > 0$, where by convention, we denote $\boldsymbol{v}_0 = [v_1(t_1^-)\ v_2(t_1^-)\ v_x(t_1^-)]^T$. Without loss of generality, we further assume that the collisions at endpoint x_1 occur on times t_k for odd k, and collisions at x_2 occur on times t_k for even k. Using the reset maps (5.10) the discrete-time dynamics of $\boldsymbol{v}_k$ is formulated as:

$$\boldsymbol{v}_{k+1} = \begin{cases} A_1' \boldsymbol{v}_k & k \text{ is odd} \\ A_2' \boldsymbol{v}_k & k \text{ is even.} \end{cases} \tag{5.12}$$

Due to symmetry, A_1' and A_2' satisfy the relation

$$A_1' = PA_2'P \text{ and } A_2' = PA_1'P, \text{ where } P = \begin{pmatrix} 0 & 1 & 0 \\ 1 & 0 & 0 \\ 0 & 0 & 1 \end{pmatrix}.$$

Note that the matrix P acts as an "index exchange operator" that corresponds to interchanging the rod's endpoints. The discrete-time solution of (5.12) is given by

$$\boldsymbol{v}_k = \begin{cases} P(PA_1')^k \boldsymbol{v}_0 & k \text{ is odd} \\ (PA_1')^k \boldsymbol{v}_0 & k \text{ is even.} \end{cases} \tag{5.13}$$

The stability of clattering motion is thus dominated by the eigenvalues of the matrix PA_1', which are given by

$$\lambda_{1,2} = \frac{\psi(1+e) \pm \sqrt{\psi^2(1+e)^2 - 4e}}{2}, \ \lambda_3 = 1. \tag{5.14}$$

In the classical stability theory of linear systems, a linear discrete system is asymptotically stable if all its corresponding eigenvalues satisfy $|\lambda_i| < 1$. Therefore, the third eigenvalue $\lambda_3 = 1$ indicates that the pre-linearized system might be unstable. However, the eigenvector corresponding to λ_3 is $[0\ 0\ 1]^T$, which is associated with the evolution of v_x. It can be shown that the motion of v_1 and v_2 is completely uncoupled from the motion of v_x, even when considering the pre-linearized dynamics with nonzero gravity. The physical reason for this uncoupling is that gravity during the flight phases, as well as the impulsive forces at frictionless collisions, are perpendicular to the horizontal direction of v_x, which remains constant during the motion. The motion of v_1 and v_2 is thus characterized only by a subsystem of (5.12), associated with the eigenvalues $\lambda_{1,2}$, which are given in (5.14) as a function of the two nondimensional parameters (e, ψ). It can be shown that for $e, \psi \in (0, 1)$, the eigenvalues automatically satisfy $|\lambda_{1,2}| < 1$, thus clattering convergence is guaranteed. In the absence of

gravity, the condition for clattering persistence reduces to the requirement that after a collision at one endpoint, the velocity of the opposing endpoint is negative. This condition can be formulated as

$$\begin{aligned} v_2(t_k^+) &< 0 \qquad k \text{ is odd} \\ v_2(t_k^+) &< 0 \qquad k \text{ is even.} \end{aligned}$$

Goyal et. al. have shown that this condition is met for all $k > 0$ iff the eigenvalues $\lambda_{1,2}$ are positive real scalars. This is Goyal's condition for clattering stability in the absence of gravity, which is formulated in terms of the parameters (e, ψ) as

$$\psi > \frac{2\sqrt{e}}{1+e} \quad . \tag{5.15}$$

5.4.2 Clattering motion with nonzero gravity

We now formulate the Poincaré map of clattering with nonzero gravity as a nonlinear discrete-time dynamical system. Instead of using the indices $\{1, 2\}$, we will use the alternating indices $\{a, b\}$, where a is the index of the rod's colliding endpoint, and b is the index of the free-flying endpoint at time t_k. Thus, assuming that collisions at x_1 occur on times t_k with odd k, one gets that $a = 1, b = 2$ for odd k and $a = 2, b = 1$ for even k. Let us denote $v_{ak} = v_a(t_k^+), v_{bk} = v_b(t_k^+), h_{ak} = h_a(t_k^+), h_{bk} = h_b(t_k^+)$. Note that by definition, $h_{ak} = 0$ for all k. After a collision at x_a on time t_k, integrating the linearized dynamics (5.9) for the free-flight phase gives $h_i(\tau) = h_{ik} + v_{ik}\tau - g\tau^2/2$ for $i = 1, 2$, where $\tau = t - t_k$. The time to the next collision at the endpoint x_b is thus given by $\tau_{bk} = (v_{bk} + \sqrt{v_{bk}^2 + 2gh_{bk}})/g$. The next collision time is thus given by $t_{k+1} = t_k + \tau_{bk}$, and the pre-collision velocities are $v_i(t_{k+1}^-) = v_{ik} - g\tau_{bk}$ for $i = 1, 2$. The post-collision velocities at time t_{k+1}^+ are determined in terms of the pre-collision velocities according to the linearized reset maps (5.10). Finally, interchanging the

indices a and b at time t_{k+1}^{+} completes a full cycle of the discrete-time system, and the Poincaré map of clattering motion is then given by

$$\begin{aligned}
v_{a,k+1} &= e\sqrt{v_{bk}^2 + 2gh_{bk}} \\
v_{b,k+1} &= v_{ak} - v_{bk} - (\psi(1+e)+1)\sqrt{v_{bk}^2 + 2gh_{bk}} \\
h_{a,k+1} &= 0 \\
h_{b,k+1} &= v_{ak}\tau_{bk} - g\tau_{bk}^2/2 \text{ , where } \tau_{bk} = (v_{bk} + \sqrt{v_{bk}^2 + 2gh_{bk}})/g.
\end{aligned} \tag{5.16}$$

The condition for clattering persistence (i.e. maintain the alternating order of the collisions) is $\tau_{bk} < \tau_{ak}$ for all k, where $\tau_{ak} = 2v_{ak}/g$ is the time to a repeating collision at x_a after its collision on time t_k. The persistence condition can be formulated as

$$\eta_k < 1 \text{ for all } k \geq 1, \text{ where } \eta_k = \frac{v_{bk} + \sqrt{v_{bk}^2 + 2gh_{bk}}}{2v_{ak}}. \tag{5.17}$$

Note that (5.16) is a nonlinear discrete-time dynamics, whose right-hand side is *not differentiable* at $v_{ak} = v_{bk} = h_{ak} = h_{bk} = 0$, which is our point of interest. Therefore, its stability properties cannot be checked by conventional linearization. In order to cope with this difficulty, we will generalize Goyal's assumption, as follows. Let us define the ratio $\epsilon_k = 2gh_{bk}/v_{bk}^2$, and assume that it satisfies $\epsilon_k \ll 1$ for all k. Moreover, we assume that $\epsilon_k \to 0$ as $k \to \infty$. The physical meaning of this assumption is that on collision times t_k, the height h_{bk} of the free-flying endpoint x_b is sufficiently small compared to its approach velocity v_{bk}, such that the change in the velocities v_a, v_b during the flight phase due to gravity is negligible (Note that Goyal's assumption of zero gravity implies that $\epsilon_k = 0$ for all k). Using the definition of ϵ_k, the Poincaré map

(5.16) can be rewritten as

$$\begin{aligned}
v_{a,k+1} &= -ev_{bk}\sqrt{1+\epsilon_k} \\
v_{b,k+1} &= v_{ak} + \psi(1+e)v_{bk} + (\psi(1+e)+1)(\sqrt{1+\epsilon_k}-1)v_{bk} \\
h_{a,k+1} &= 0 \\
h_{b,k+1} &= v_{ak}\tau_{bk} - g\tau_{bk}^2/2 \text{ , where } \tau_{bk} = \tfrac{h_{bk}}{|v_{bk}|}\cdot\tfrac{2(\sqrt{1+\epsilon_k}-1)}{\epsilon_k},
\end{aligned} \tag{5.18}$$

and the discrete-time evolution of ϵ_k is given by

$$\epsilon_{k+1} = \frac{|v_{bk}|v_{ak}}{|v_{b,k+1}|^2}\left(2(\sqrt{1+\epsilon_k}-1) - (\sqrt{1+\epsilon_k}-1)^2\right). \tag{5.19}$$

In order to examine the validity of our assumption, we now formulate the dynamics assuming that $\epsilon_k \ll 1$, and check if the discrete-time evolution of ϵ_k implies that it converges to zero. Let $\bar{v}_{ik}, \bar{h}_{ik}$ denote the dynamic solution of v_{ik}, h_{ik} in (5.18) for $k \geq 1, i = 1, 2$, assuming that $\epsilon_k \ll 1$. Assigning $\epsilon_k \to 0$ in (5.18), the dynamics of $\bar{v}_{ik}, \bar{h}_{ik}$ is given by

$$\begin{aligned}
\bar{v}_{a,k+1} &= -e\bar{v}_{bk} \\
\bar{v}_{b,k+1} &= \bar{v}_{ak} + \psi(1+e)\bar{v}_{bk} \\
\bar{h}_{a,k+1} &= 0 \\
\bar{h}_{b,k+1} &= \bar{v}_{ak}\bar{\tau}_{bk} \text{ , where } \bar{\tau}_{bk} = \bar{h}_{bk}/|\bar{v}_{bk}|.
\end{aligned} \tag{5.20}$$

Using first-order Taylor series expansion of (5.19) about $\epsilon_k = 0$, the linearized dynamics of ϵ_k is given by

$$\bar{\epsilon}_{k+1} = \frac{|\bar{v}_{bk}|\bar{v}_{ak}}{|\bar{v}_{b,k+1}|^2}\,\bar{\epsilon}_k = e\,\frac{|\bar{v}_{bk}|\cdot|\bar{v}_{b,k-1}|}{|\bar{v}_{b,k+1}|^2}\,\bar{\epsilon}_k, \tag{5.21}$$

where $\bar{\epsilon}_k$ is defined as $\bar{\epsilon}_k = 2g\bar{h}_{bk}/\bar{v}_{bk}^2$. Note that the dynamics of $\bar{v}_{ak}, \bar{v}_{bk}$ is identical to the dynamics in (5.12) under Goyal's assumption of zero gravity. Therefore, their dynamic solution is similar, and can be formulated as

$$\bar{v}_{ak} = a_1\lambda_1^k + a_2\lambda_2^k \;\;,\;\; \bar{v}_{bk} = b_1\lambda_1^k + b_2\lambda_2^k, \tag{5.22}$$

where $a_1, a_2, b_1, b_2 \in I\!R$ are determined by initial conditions, and λ_1, λ_2 are the eigenvalues given in (5.14). Assuming that $\lambda_{1,2}$ satisfy Goyal's stability condition (5.15), they are positive real numbers, hence we choose them such that $\lambda_2 > \lambda_1$. Since the initial conditions, which are the pre-collision velocities at t_1^- satisfy $\bar{v}_{b0} < 0, \bar{v}_{a0} \leq 0$, it can be shown that $b_1 > 0$ and $b_2 < 0$. Substituting (5.22) into (5.21), the dynamics of $\bar{\epsilon}_k$ can be rewritten as

$$\bar{\epsilon}_{k+1} = \frac{e}{\lambda_2^3}\left(1-\alpha_k\right)\left(1-\beta_k\right)\bar{\epsilon}_k \text{ , where } \alpha_k = -\frac{b_1\lambda_1^k(\lambda_2-\lambda_1)}{b_1\lambda_1^{k+1}+b_2\lambda_2^{k+1}} \text{ and } \beta_k = -\frac{b_1\lambda_1^{k-1}(\lambda_2^2-\lambda_1^2)}{b_1\lambda_1^{k+1}+b_2\lambda_2^{k+1}} \text{ .} \tag{5.23}$$

It can be shown that $0 < \alpha_k, \beta_k < 1$ for all k, and that $\alpha_k, \beta_k \to 0$ as $k \to \infty$. This implies that $\bar{\epsilon}_k$ converges asymptotically to zero if and only if $e < \lambda_2^3$. This is a necessary condition for validity of the assumption $\epsilon_k \to 0$, which can be formulated in terms of the parameters (e, ψ) as

$$\psi > \frac{e^{1/3}+e^{2/3}}{1+e}. \tag{5.24}$$

Note that this condition is more restrictive than the condition given in (5.15) for clattering stability with zero gravity. In the following, we show that the condition given in (5.24) is also a sufficient condition for asymptotic convergence of ϵ_k to zero from any initial value of ϵ_1, and for clattering stability. The proof will be based on comparing the solution of the dynamical system (5.18) and the solution of the dynamical system (5.20), when both systems start from the same initial conditions at $k=1$. The following Lemmas give the relations between the solutions of these two systems.

Lemma 5.4.1 *Let h_{ik}, v_{ik} be the solution of the dynamical system (5.18), and let $\bar{h}_{ik}, \bar{v}_{ik}$ be the solution of the dynamical system (5.20) for $k \geq 1$ and $i \in \{a, b\}$, such*

that the initial conditions satisfy $\bar{h}_{a1}=h_{a1}=0, \bar{h}_{b1}=h_{b1}>0, \bar{v}_{a1}=v_{a1}\geq 0, \bar{v}_{b1}=v_{b1}<0$. *Then the following inequalities hold for all* $k\geq 1$*:*

1. $\frac{v_{ak}}{|v_{bk}|} \leq \frac{\bar{v}_{ak}}{|\bar{v}_{bk}|}$

2. $v_{ak} \geq \bar{v}_{ak} > 0$ *and* $v_{bk} \leq \bar{v}_{bk} < 0$

3. $\psi(1+e)|v_{bk}| - v_{ak} \geq \psi(1+e)|\bar{v}_{bk}| - \bar{v}_{ak}$

4. $\left|\frac{v_{bk}}{v_{b,k+1}}\right| \leq \left|\frac{\bar{v}_{bk}}{\bar{v}_{b,k+1}}\right|$

5. $\frac{v_{ak}}{|v_{b,k+1}|} \leq \frac{\bar{v}_{ak}}{|\bar{v}_{b,k+1}|}$

6. $\frac{v_{ak}}{|v_{a,k+1}|} \leq \frac{\bar{v}_{ak}}{|\bar{v}_{a,k+1}|}$

Proof: Since inequalities 1 to 6 are satisfied as equalities at $k=1$, we assume that they are satisfied for $k=n$, and prove, by induction, that they are satisfied for $k=n+1$.

1. This condition can be rewritten as $v_{ak}|\bar{v}_{bk}| - \bar{v}_{ak}|v_{bk} \leq 0$. Assigning $k=n+1$ and substituting the dynamics in (5.18) and (5.20) gives

$$\begin{aligned} v_{a,n+1}|\bar{v}_{b,n+1}| - \bar{v}_{a,n+1}|v_{b,n+1} &= e|v_{bn}|\sqrt{1+\epsilon_n}(\bar{v}_{bn} - \psi(1+e)\bar{v}_{an}) \\ &\quad -e|\bar{v}_{bn}|\left(|v_{bn}|(\psi(1+e) + (\psi(1+e)+1)(\sqrt{1+\epsilon_n}-1)) - v_{ak}\right) \\ &= -e(\sqrt{1+\epsilon_n}-1)|v_{bn}|(\bar{v}an + |\bar{v}_{bn}|) + e(v_{an}|\bar{v}_{bn}| - \bar{v}_{an}|v_{bn}), \end{aligned}$$

   which is negative, according to the induction hypothesis.

2. Recall that according to the analysis of Goyal et al. [30], the solution of (5.20) satisfies $\bar{v}_{ak} > 0$ and $\bar{v}_{bk} < 0$ for all $k\geq 1$. Let us define $\Delta_{an} = v_{an} - \bar{v}_{an}, \Delta_{bn} = v_{bn} - \bar{v}_{bn}$. By the induction hypothesis, inequality 2 implies that $\Delta_{an} \geq 0$ and

$\Delta_{bn} \leq 0$, and inequality 3 implies that $\Delta_{an} + \psi(1+e)\Delta_{bn} \leq 0$. Substituting the dynamics in (5.18) and (5.20), we now formulate $\Delta_{a,n+1}$ and $\Delta_{b,n+1}$:

$$\Delta_{a,n+1} = v_{a,n+1} - \bar{v}_{a,n+1} = -e\Delta_{bn} - e(\sqrt{1+\epsilon_n} - 1)v_{bn}$$
$$\Delta_{b,n+1} = v_{b,n+1} - \bar{v}_{b,n+1} = \Delta_{an} + \psi(1+e)\Delta_{bn} + (\psi(1+e)+1)(\sqrt{1+\epsilon_n} - 1)v_{bn},$$

and the induction hypothesis implies that $\Delta_{a,n+1} \geq 0$ and $\Delta_{b,n+1} \leq 0$.

3. This inequality stems directly (without induction) from inequalities 1 and 2, as follows. Let us define $\alpha = v_{ak}/\bar{v}_{ak}$ for some k. Then inequality 1 implies that $|v_{bk}| \geq \alpha|\bar{v}_{bk}|$, and inequality 2 implies that $\alpha \geq 1$. Therefore, one gets

$$\psi(1+e)|v_{bk}| - v_{ak} \geq \alpha(\psi(1+e)|\bar{v}_{bk}| - \bar{v}_{ak}) \geq \psi(1+e)|\bar{v}_{bk}| - \bar{v}_{ak}.$$

4. Under the induction hypothesis, we now prove that $|\bar{v}_{b,n+1}|\cdot|v_{bn}| - |v_{b,n+1}|\cdot|\bar{v}_{bn}| \leq 0$. Using the definitions of Δ_{an} and Δ_{bn}, inequality 1 implies that

$$\Delta_{an}|\bar{v}_{bn}| - |\Delta_{bn}|v_{an} \geq 0. \tag{5.25}$$

Using the dynamics (5.18) and (5.20) gives

$$|\bar{v}_{b,n+1}| \cdot |v_{bn}| - |v_{b,n+1}| \cdot |\bar{v}_{bn}| = |\Delta_{bn}| \cdot |\bar{v}_{b,n+1}| - |\Delta_{b,n+1}| \cdot |\bar{v}_{bn}|$$
$$= |\Delta_{bn}|(\psi(1+e)|\bar{v}_{bn}| - \bar{v}_{an}) - |\bar{v}_{bn}|(|\Delta_{bn}|\psi(1+e) + |v_{bn}|(\psi(1+e)+1)(\sqrt{1+\epsilon_n} - 1) - \Delta_{an})$$
$$= \Delta_{an}|\bar{v}_{bn}| - |\Delta_{bn}|v_{an} - |\bar{v}_{bn}| \cdot |v_{bn}|(\psi(1+e)+1)(\sqrt{1+\epsilon_n} - 1),$$

which, according to (5.25), is non-positive.

5. Under the induction hypothesis, we now prove that $|\bar{v}_{b,n+1}|\cdot v_{an} - |v_{b,n+1}|\cdot\bar{v}_{an} \leq 0$. Using the dynamics (5.18) and (5.20) gives

$$|\bar{v}_{b,n+1}| \cdot v_{an} - |v_{b,n+1}| \cdot \bar{v}_{an} = |\bar{v}_{b,n+1}| \cdot \Delta_{an} - |\Delta_{b,n+1}| \cdot \bar{v}_{an}$$
$$= \psi(1+e)(\Delta_{an}|\bar{v}_{bn}| - |\Delta_{bn}|v_{an}) - \bar{v}_{an} \cdot |v_{bn}|(\psi(1+e)+1)(\sqrt{1+\epsilon_n} - 1),$$

which, according to (5.25), is non-positive.

6. Under the induction hypothesis, we now prove that $\bar{v}_{a,n+1}v_{an} - v_{a,n+1}\bar{v}_{an} \leq 0$. Using the dynamics (5.18) and (5.20) gives

$$\begin{aligned}\bar{v}_{a,n+1}v_{an} - v_{a,n+1}\bar{v}_{an} &= \bar{v}_{a,n+1}\Delta_{an} - \Delta_{a,n+1}\bar{v}_{an} \\ &= e(\Delta_{an}|\bar{v}_{bn}| - |\Delta_{bn}|v_{an} - (\sqrt{1+\epsilon_n} - 1)|v_{bn}|),\end{aligned}$$

which, according to (5.25), is non-positive.

□

The following lemma asserts that under the condition (5.24), clattering motion with gravity maintains persistence, and converges to a two-contact Zeno limit point faster than clattering motion with zero gravity.

Lemma 5.4.2 *Let h_{ik}, v_{ik} be the solution of the dynamical system (5.18), and let $\bar{h}_{ik}, \bar{v}_{ik}$ be the solution of the dynamical system (5.20) for $k \geq 1$ and $i \in \{a, b\}$, such that the initial conditions satisfy $\bar{h}_{a1} = h_{a1} = 0, \bar{h}_{b1} = h_{b1} > 0, \bar{v}_{a1} = v_{a1} \geq 0, \bar{v}_{b1} = v_{b1} < 0$. Then under the condition (5.24), the following inequalities hold:*

1. *$\bar{h}_{bk} \leq h_{bk}$ for all $k \geq 1$*
2. *$\bar{\tau}_{bk} \leq \tau_{bk}$ for all $k \geq 1$*
3. *ϵ_k decreases to zero monotonously with k*
4. *η_k decreases to zero monotonously with k*

Proof:

1. Using the dynamics (5.18) and (5.20), inequality 1 of Lemma 5.4.1 and the fact that $\epsilon_k \geq 0$ for all k imply that

$$\frac{h_{b,k+1}}{h_{bk}} \geq \frac{v_{ak}}{|v_{bk}|} \geq \frac{\bar{v}_{ak}}{|\bar{v}_{bk}|} = \frac{\bar{h}_{b,k+1}}{\bar{h}_{bk}}.$$

Since the initial conditions are $h_{b1} = \bar{h}_{b1}$, one gets $h_{bk} = \bar{h}_{bk}$ for all $k \geq 1$.

2. Using the dynamics (5.18) and (5.20), the inequalities $h_{bk} \leq \bar{h}_{bk}, |v_{bk}| \geq |\bar{v}_{bk}|$ and the fact that $\epsilon_k \geq 0$ for all k imply that

$$\tau_{bk} = \frac{h_{bk}}{|v_{bk}|} \cdot \frac{2(\sqrt{1+\epsilon_k} - 1)}{\epsilon_k} \geq \frac{\bar{h}_{bk}}{|\bar{v}_{bk}|} = \bar{\tau}_{bk}.$$

3. Condition (5.24) guarantees that $\bar{\epsilon}_k$ decreases monotonously to zero. Using the dynamics of ϵ_k given in (5.19), the inequalities in Lemma 5.4.1 and the fact that $\epsilon_k \geq 0$ for all k imply that

$$\frac{\epsilon_{k+1}}{\epsilon_k} \leq \frac{|v_{bk}|v_{ak}}{|v_{b,k+1}|^2} \leq \frac{|\bar{v}_{bk}|\bar{v}_{ak}}{|\bar{v}_{b,k+1}|^2} = \frac{\bar{\epsilon}_{k+1}}{\bar{\epsilon}_k} < 1.$$

Thus, ϵ_k also decreases monotonously to zero.

4. The definition of η_k is given in (5.17). Using the expression of ϵ_{k+1} in (5.19) and the inequalities in Lemma 5.4.1, one gets

$$\frac{\eta_{k+1}}{\eta_k} = \frac{|v_{b,k+1}|v_{ak}}{|v_{bk}|v_{a,k+1}} \cdot \frac{\sqrt{1+\epsilon_{k+1}}-1}{(\sqrt{1+\epsilon_k}-1)\epsilon_{k+1}} \cdot \epsilon_{k+1}$$

$$\leq \frac{|v_{b,k+1}|v_{ak}}{|v_{bk}|v_{a,k+1}} \cdot \frac{\sqrt{1+\epsilon_{k+1}}-1}{(\sqrt{1+\epsilon_k}-1)\epsilon_{k+1}} \cdot \frac{|v_{bk}|v_{ak}}{|v_{b,k+1}|^2} \cdot 2(\sqrt{1+\epsilon_k} - 1)$$

$$= \frac{|v_{b,k+1}|v_{ak}}{|v_{bk}|v_{a,k+1}} \cdot 2\frac{\sqrt{1+\epsilon_{k+1}}-1}{\epsilon_{k+1}} \leq \frac{v_{ak}^2}{v_{a,k+1}|v_{b,k+1}|} \leq \frac{\bar{v}_{ak}^2}{\bar{v}_{a,k+1}|\bar{v}_{b,k+1}|} \quad .$$

Assigning the dynamics (5.20) and its solution (5.22) gives

$$\frac{\bar{v}_{ak}^2}{\bar{v}_{a,k+1}|\bar{v}_{b,k+1}|} = e\frac{|\bar{v}_{b,k-1}^2|}{\bar{v}_{bk}|\bar{v}_{b,k+1}|} = \frac{e}{\lambda_2^3}\left(1-\alpha_{k-1}\right)\left(1-\beta_k\right),$$

where $\alpha_k, \beta_k \in (0,1)$ are defined in (5.23). Therefore, condition (5.24) implies that $\eta_{k+1}/\eta_k < e/\lambda_2^3 < 1$ for all k, and thus η_k decreases monotonously to zero.

□

The following theorem uses the results in Lemmas 5.4.1 and 5.4.1 to establish the conditions on the initial configuration for which clattering motion evolves, and converges to a two-contact Zeno limit point.

Theorem 8 *Consider the linearized hybrid dynamics of the horizontal rod, with the initial configuration* $q'(0) = (h_{10}, h_{20}, x_0)$, $\dot{q}'(0) = \vec{0}$, *such that* $h_{10} < h_{20}$. *Assume that the parameters* (e, ψ) *satisfy the condition (5.24). Then if the initial configuration satisfies*

$$h_{10} < h_{20} < (1 + 4e(1+e)(1+\psi))\, h_{10}, \tag{5.26}$$

then the dynamic solution corresponds to clattering motion that converges to a two-contact Zeno limit point in finite time t_∞, *which is bounded by*

$$t_\infty < \left(1 + \frac{2e(1+e)}{(1+\psi(1+e))(1-\psi)}\right)\sqrt{\tfrac{2h_{10}}{g}}. \tag{5.27}$$

Moreover, if the initial configuration satisfies

$$(1 + 4e(1+e)(1+\psi))\, h_{10} < h_{20} < \left(1 + \frac{4e(1+\psi)}{(1-e)^2}\right) h_{10}, \tag{5.28}$$

then the dynamic solution starts with a finite sequence of collisions at x_1, *followed by clattering motion that converges to a two-contact Zeno limit point in finite time.*

Note this theorem can be extended to include the case of $h_{10} > h_{20}$, by simply exchanging the indices in (5.26).

Proof: Assuming that the rod starts from rest, the first collision occurs at x_1 on time $t_1 = \sqrt{2h_{10}/g}$, and the post-collision velocities are given by $v_1(t_1^+) = egt_1$ and $v_2(t_1^+) = -(\psi(1+e)+1)gt_1$. The height h_2 at t_1 is $h_2(t_1) = h_{20} - h_{10}$. The

condition for onset of clattering motion is that the time to next collision at x_2 is less than the time for collision at x_1. This condition can formulated as $v_2(t_1^+) + \sqrt{v_2(t_1^+)^2 + 2gh_2(t_1)} < 2v_1(t_1^+)$. Substitution and simplification gives the inequality (5.26). This condition is equivalent to $\eta_1 < 1$. According to Lemmas 5.4.1 and 5.4.2, condition (5.24) guarantees that η_k is monotonously decreasing with k, and thus the clattering persistence condition $\eta_k < 1$ is maintained for all k. Since condition (5.15) is also satisfied, the zero-gravity solutions of $\bar{h}_{1k}, \bar{h}_{2k}$ converge to zero with k, and Lemma 5.4.2 implies that h_{1k}, h_{2k} also converge to zero with k, leading to a two-contact Zeno limit point. Moreover, since the flight times satisfy $\tau_{bk} \leq \tau_{bk}$ for all k, the upper bound on t_∞ can be computed based on the dynamics of the simplified system (5.20), as follows. Substituting the solution (5.22) into the dynamics (5.20) gives

$$\frac{\bar{\tau}_{b,k+1}}{\bar{\tau}_{b,k}} = \frac{\bar{v}_{ak}}{|\bar{v}b, k+1|} = e\frac{\bar{v}_{b,k-1}}{\bar{v}b, k+1} = \frac{e}{\lambda_2^2}\left(1 - \beta_k\right),$$

where λ_2 is the maximal eigenvalue defined in (5.14), and $\beta_k \in (0, 1)$ is defined in (5.23). Since the condition (5.15) implies that $e/\lg_2^2 < \psi^2 < 1$, $\bar{\tau}_{bk}$ is bounded by a geometric series given by $\bar{\tau}_{bk} \geq \bar{\tau}_1\psi^{2k-2}$. The total time of the nonzero-gravity clattering is thus bounded by the sum

$$t_\infty = t_1 + \sum_{k=1}^{\infty} \tau_{bk} \leq t_1 + \sum_{k=1}^{\infty} \bar{\tau}_{bk} \leq t_1 + \frac{\bar{\tau}_{b1}}{1 - \psi^2}.$$

Substituting $\bar{\tau}_{b1} = h_2(t_1)/|v_2(t_1^+)|$ and using the inequality in (5.26) yields the bound given in (5.27). Finally, when the initial configuration satisfies (5.28), $\eta_1 > 1$, and the dynamic solution starts with bouncing motion, having a sequence of collisions at x_1. However, since condition (5.11) of Theorem 7 is *not* satisfied, this sequence is finite, and there exists a finite n such that on time t_n the solution involves collision at x_2, thus satisfying $\eta_n < 1$. Therefore, according to lemma 5.4.2, once clattering

has started, η_k decreases monotonously to zero, and clattering motion persists until reaching a two-contact Zeno limit point in finite time. $\square$

We now revisit the plane of initial conditions (h_{10}, h_{20}). Under the condition of clattering stability (5.24), Theorems 7 and 8 impose a partition of the first quadrant $\{h_{10}, h_{20} > 0\}$ to regions associated with dynamical solutions of bouncing, clattering, and mixed motion of finite bouncing followed by clattering. These regions, which are the planar sectors defined by the inequalities (5.11) and (5.26), are shown in Fig. 5.3a. Note that there are three distinct lines in (h_{10}, h_{20}) plane, for which the solution of the hybrid dynamical system is not well-defined. The first line is $h_{10} = h_{20}$ (dotted line in Fig 5.3a, which corresponds to the rod starting exactly at horizontal angle. In this case, the two endpoints hit the ground at the same time, and at the rest of the solution is indeterminate. The two other lines, shown as dashed lines in Fig. 5.3a, are symmetric with respect to the first line, and are associated with the boundaries of the clattering region formulated in (5.26). When the initial conditions lie on one of these two lines, the first collision is well-defined, but at the second collision the rod hits the ground exactly at horizontal angle, making the rest of the solution indeterminate. A possible approach to overcome such indeterminacies, which is commonly used in computer simulations and is also physically justifiable, is to consider an arbitrary infinitesimal perturbation that drives the system's state away from the singular configuration. Equivalently, when two events of collisions occur simultaneously, one simply needs to choose and apply only one of them at random. Note that under this paradigm, a rod that meets the ground in horizontal position enters a *deadbeat clattering motion*, at which the velocities decay to zero by an infinite sequence of collisions occurring in zero time. (This scenario is termed *chattering Zeno* in [1].) Note

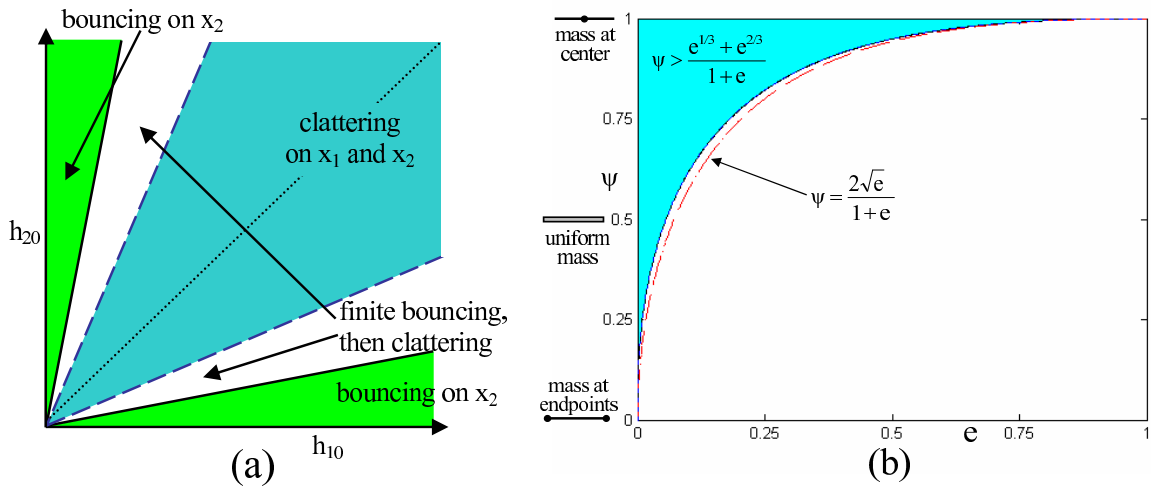

Figure 5.3: (a)Partition of the initial conditions plane into regions that correspond to different motions. (b)Clattering stability region in (e, ψ) plane.

that a similar situation of deadbeat clattering also occurs when both endpoints are initially in contact, and the rod is given and initial velocity perturbation such that one endpoint is given a colliding velocity. This scenario is of crucial importance when considering the switching between different contact modes, and will be discussed in the next chapter. We now provide a graphical interpretation for the clattering stability condition given in (5.24), and discuss its physical implications. This condition defines a region in (e, ψ) plane, which is the shaded region shown in Fig. 5.3b. The dashed line corresponds to the clattering stability condition under zero gravity, which is given in (5.15). Note that the condition (5.24) is more restrictive than the condition (5.24). The physical implication of (5.24), is as follows. First, clattering stability requires that the coefficient of restitution e is sufficiently small. Second, it requires that ψ is sufficiently large, meaning that the rod's mass is distributed such that most of the mass is concentrated close to the center-of-mass, and less mass is located in peripheral regions (i.e. the radius of gyration is sufficiently small).

5.5 Simulation Results of the Horizontal Rod

We now demonstrate the results by showing numerical simulations for the rod with representative initial conditions from each region in Fig. 5.3a. The simulations of clattering are executed for various values of (e, ψ) in order to validate the conditions for its clattering stability. The simulations were performed with the exact nonlinear model of the rod and contact constraints (5.7) and (5.8), using the nonlinear impact law (5.5). The simulations were executed in MATLAB workspace. In order to avoid numerical errors and imprecisions, we have simulated the equation of motion (5.7) expressed in the alternative coordinates $q' = (h_1, h_2, x)$, using the nonlinear transformation from q to q' as given in (5.4). The parameters of the rod were chosen as $m = 1Kg,\ L = 1m,\ g = 10m/s^2$ with the rod's mass being uniformly distributed, resulting in $I = mL^2/3$ and $\psi = 0.5$. Since the dynamic solution converge to a Zeno limit point, the simulations were terminated when the time-difference between collisions is less than 10^{-10} *sec*. According to condition (5.24) with $\psi = 0.5$, the coefficient of restitution must satisfy $e < 0.056$ for clattering stability. In the first two simulations the coefficient of restitution was taken as $e = 0.05$.

Simulation example 1: bouncing motion The condition for infinite sequence of bouncing for the chosen parameters is $h_{20} > 1.332h_{10}$. Fig. 5.4 shows the simulation results for initial conditions $h_{10} = 0.5$, $h_{20} = 0.75$. The discrete-time evolution of v_1 and v_2 is shown in Figs. 5.4a and 5.4b respectively, and converge to a Zeno limit point, where the contact at x_1 is recovered. At integer values of k, corresponding to impact times, the velocities show discontinuous jump, while between impact times the velocities are decelerating almost linearly. Since the rod bounces on x_1, the sequence $v_1(t_k)$ converges to zero, while the sequence $v_2(t_k)$ converges to a constant value of

$-5.36\ m/s$. Fig. 5.4c shows the discrete-time evolution of the rod's angle $\theta(t_k)$, which converges monotonically to a constant value of 1.34^o. Fig. 5.4d shows the collisions times t_k. For $k > 10$ the time difference between collision is less than 10^{-11} *sec*, and the simulation is stopped with t_k converging to 0.357 *sec*.

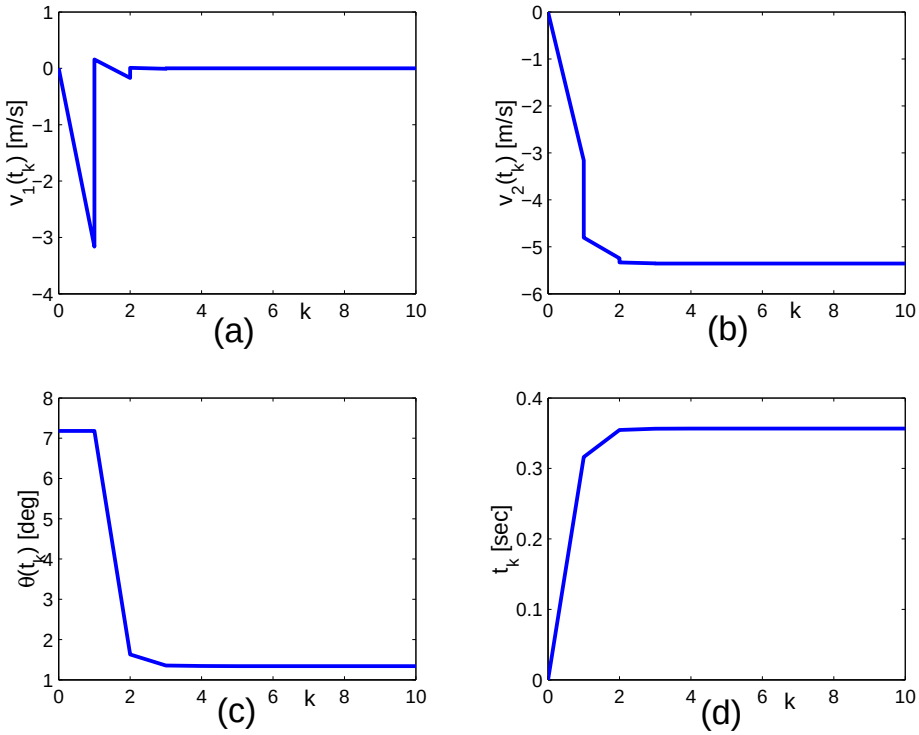

Figure 5.4: Simulation results of bouncing motion

Simulation example 2: clattering motion The condition for starting of clattering motion for the chosen parameters is $h_{10} < h_{20} < 1.315h_{10}$. Fig. 5.5 shows the simulation results for initial conditions $h_{10} = 0.5$, $h_{20} = 0.65$. Since the rod possesses a stable clattering motion, both sequences $v_1(t_k)$ and $v_2(t_k)$ converge to zero. Fig. 5.5c shows that the rod's angle $\theta(t_k)$ converges also to zero. Fig. 5.5d shows the discrete-time evolution of the sequence ϵ_k, which rapidly converges to zero as expected. collisions times t_k. For $k > 10$ the time difference between collision is less than 10^{-8} *sec*, and the simulation is stopped with t_k converging to 0.347 *sec*.

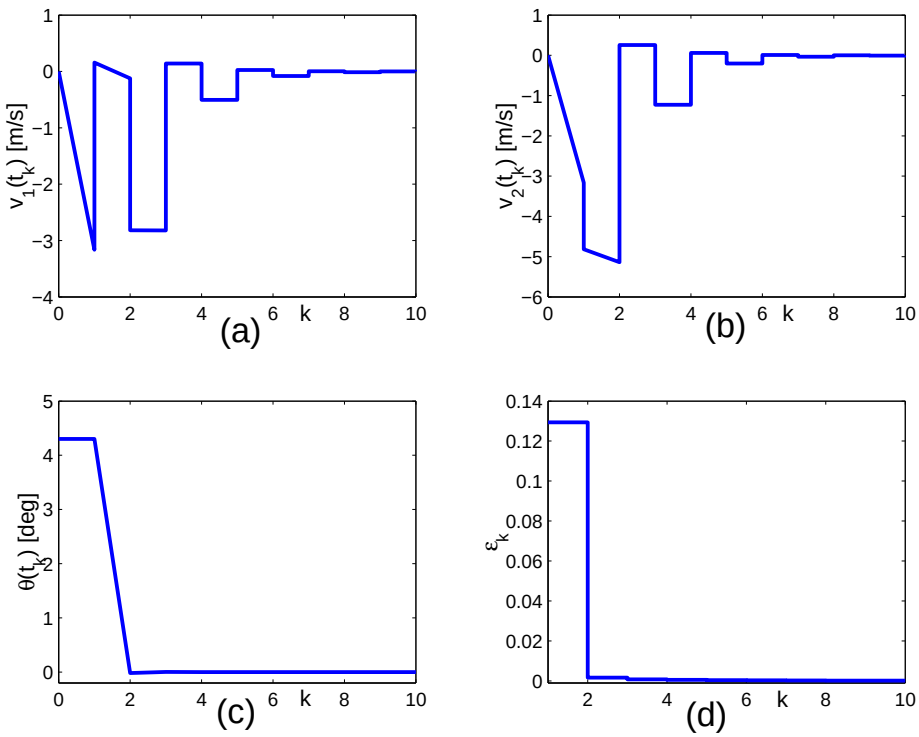

Figure 5.5: Simulation results of stable clattering motion

Simulation example 3: mixed bouncing-clattering motion According to the analysis of the linearized model, for the chosen parameters the region $1.315h_{10} < h_{20} <$

$1.332h_{10}$ is an intermediate region. Taking initial conditions within this region, the rod is expected to start bouncing on x_1, and then hit x_2 and switch to clattering motion, converging to a two-contact Zeno limit point. When simulating the exact nonlinear system, we have found out that the actual intermediate region for $h_{10} = 0.5$, is approximately $1.3569h_{10} \leq h_{20} \leq 1.3802h_{10}$. For such initial condition, the rod started with a small number of collisions at x_1, and then switched to clattering motion with v_1 and v_2. Figs. 5.6a and 5.6b show $v_1(t_k)$ and $v_2(t_k)$ respectively, for initial conditions $h_{10} = 0.5$, $h_{20} = 0.6901$. The collisions with x_1 are marked with '$\times$' and collisions with x_2 are marked with '$\circ$' on the figures. It can be seen that the rod starts with four collisions at x_1 and then switches to clattering motion. For $k > 15$ the time difference between collision is less than 10^{-15} *sec*, and the simulation is stopped with t_k converging to 0.354 *sec*.

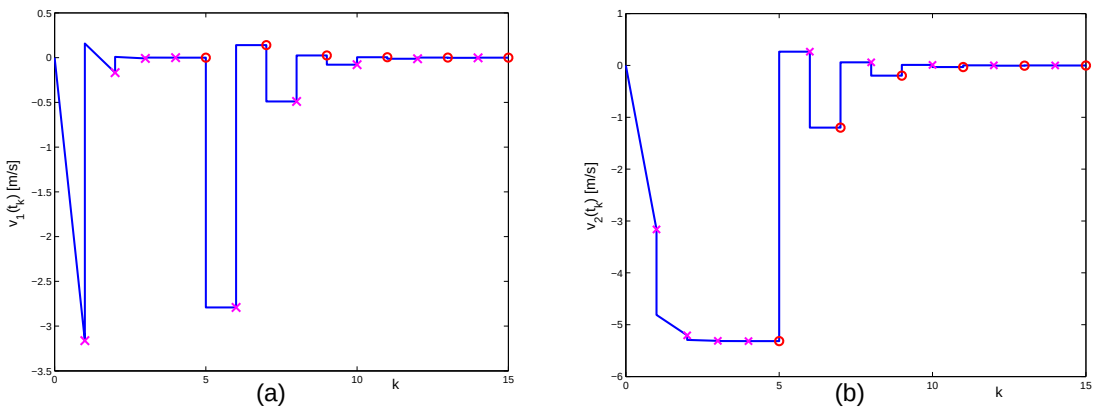

Figure 5.6: Simulation results of mixed bouncing-clattering motion

Simulation example 4: unstable clattering motion In the following simulation, the coefficient of restitution was taken as $e = 0.09$, which violates the clattering stability condition. The motion of the rod is then simulated for initial conditions

$h_{10} = 0.1$, and $h_{20} = 0.1582$. Figs. 5.7a and 5.7b show the resulting solution of $v_1(t_k)$ and $v_2(t_k)$ respectively. The collisions with x_1 are marked with '$\times$' and collisions with x_2 are marked with '$\circ$' on the figures. It can be seen that the rod starts with eight time steps of clattering, and then switches to bouncing on x_2 and converges to a one-contact Zeno limit point. For $k > 20$ the time difference between collision is less than 10^{-15} *sec*, and the simulation is stopped with t_k converging to 0.1668 *sec*. Trying different initial conditions, we have observed high sensitivity of the dynamic solution to small deviation in the initial conditions. For example, small deviation result in a dynamic solution of finite clattering followed by infinite bouncing on the other endpoint x_1.

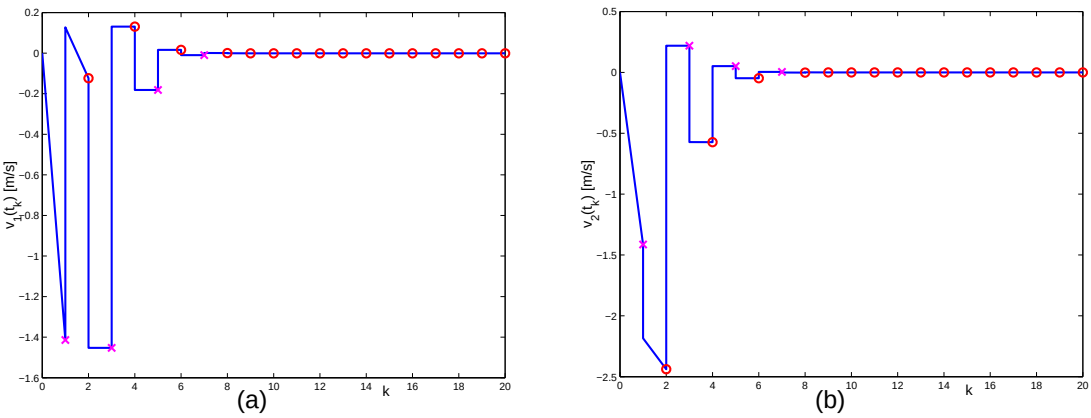

Figure 5.7: Simulation results of unstable clattering

5.6 Clattering Stability of a Symmetric Rigid Body

We now extend the results of the section 5.4, and investigate the case of a planar rigid body $\mathcal{B}$ with symmetric mass distribution on a symmetric terrain. The body is supported by a symmetric V-shaped terrain, with slope angles α with respect to

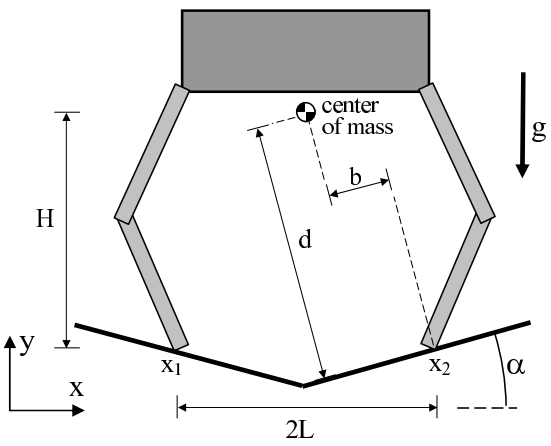

Figure 5.8: The symmetric rigid body on a symmetric terrain.

the horizontal direction (Fig. 5.8). It is assumed that $\mathcal{B}$ makes contact with the ground only at two vertices x_1 and x_2, which are fixed points with respect to $\mathcal{B}$. The configuration of $\mathcal{B}$ is $q = (x, y, \theta)$, where (x, y) is the position of $\mathcal{B}$'s center-of-mass and θ is the orientation of $\mathcal{B}$. At the configuration $q = \vec{0}$, $\mathcal{B}$ lies in an equilibrium posture with two contacts, which is symmetric with respect to the vertical axis (Fig. 5.8). At this posture, let $2L$ be the horizontal distance between the contacts, and let H denote the height of $\mathcal{B}$'s center-of-mass about the contacts. The mass of $\mathcal{B}$ is distributed symmetrically, and its moment of inertia is $I = m\rho^2$ where ρ is the radius of gyration. The equation of free motion expressed in q is identical to the rod's equation of motion (5.7). The contact constraints are given by

$$\begin{aligned} h_1(q) &= x \sin\alpha + y \cos\alpha - b \sin\theta + d(1 - \cos\theta) \geq 0 \\ h_2(q) &= -x \sin\alpha + y \cos\alpha + b \sin\theta + d(1 - \cos\theta) \geq 0, \end{aligned} \tag{5.29}$$

where $b = L\cos\alpha - H\sin\alpha$ and $d = H\cos\alpha + L\sin\alpha$ are the signed distances between $\mathcal{B}$'s center-of-mass and the contact point in the tangential and normal directions respectively (Fig. 5.8). Defining the alternative set of coordinates $q' = (h_1, h_2, \theta)$

with its velocity denoted by $\dot{q}' = (v_1, v_2, \omega)$, the equations of free motion can be expressed in q' by applying the coordinate transformation (5.4). Assuming that $\mathcal{B}$ maintains small angles $|\theta| \ll 1$ during its motion, the linearized equation of free motion expressed in q' are given by

$$\begin{pmatrix} \ddot{h}_1 \\ \ddot{h}_2 \\ \ddot{x} \end{pmatrix} = \begin{pmatrix} -g\cos\alpha + d\omega^2 \\ -g\cos\alpha + d\omega^2 \\ 0 \end{pmatrix}. \tag{5.30}$$

Assuming that the rod's velocities are kept sufficiently small during its motion, the ω^2-terms in (5.30), associated with centripetal accelerations, are negligible. Thus, the linearized equations of free motion reduce to those of the horizontal rod in (5.9). Using the impact law (5.3) and assigning the coordinate transformation (5.5) ,the linearized reset maps are expressed in q' as

$R'_i(q', \dot{q}') = (q', A'_i\dot{q}')$, $i = 1, 2$, where

$$A'_1 = \begin{pmatrix} -e & 0 & 0 \\ (1+e)\psi & 1 & 0 \\ (1+e)\varphi & 0 & 1 \end{pmatrix}, A'_2 = \begin{pmatrix} 1 & (1+e)\psi & 0 \\ 0 & -e & 0 \\ 0 & -(1+e)\varphi & 1 \end{pmatrix}, \ \varphi = \frac{b}{b^2+\rho^2}, \text{ and } \psi = \frac{b^2-\rho^2\cos(2\alpha)}{b^2+\rho^2}. \tag{5.31}$$

We now list a few observations about the relations between the hybrid dynamics of the symmetric body and the hybrid dynamics of the rod. First, note that the definition of the parameter ψ in (5.31) reduces to its previous definition in (5.10) when substituting $\alpha = 0,\ H = 0$. Second, note that A'_1 and A'_2 satisfy the relation

$$A'_1 = PA'_2P \text{ and } A'_2 = PA'_1P, \text{ where } P = \begin{pmatrix} 0 & 1 & 0 \\ 1 & 0 & 0 \\ 0 & 0 & -1 \end{pmatrix}.$$

The transformation matrix P represents a "reflection operator" about the vertical direction, which corresponds to interchanging the rod's endpoints and reversing the sign of the angular velocity ω. Finally, when analyzing the hybrid dynamics of the symmetric body, a key observation is that under the assumption of small angle and velocity, the dynamics of v_1 and v_2 in (5.30) and (5.31) is identical to the one given in (5.9) and (5.10) in the case of the horizontal rod. Therefore, Theorems 7 and 8, that characterize the conditions bouncing motion and for clattering stability, admit straightforward generalization to the case of the symmetric body, by using the new definition of ψ given in (5.31). However, there is one significant difference from the rod's case, which is the coupling between the velocities v_1, v_2 and the angular velocity ω, which is encompassed in the parameter φ in the impact dynamics (5.31). This coupling results in a drift in ω, and consequently in θ, during clattering and bouncing motion. Assuming that the clattering stability condition (5.24) is satisfied, and that the initial perturbation $q'(0)$ is sufficiently small, continuity considerations imply that the hybrid dynamics of h_1, h_2 and v_1, v_2 converges to a Zeno limit point with one or two recovered contacts. Due to the drift in ω and θ, they both converge to bounded limit values at the limit point.

5.6.1 Design of symmetric stances with clattering stability

The clattering stability criterion (5.24) is governed by the coefficient of restitution e and the nondimensional parameter ψ. For a given coefficient of restitution, this criterion dictates design limitations on the terrain's geometry and the mass distribution of $\mathcal{B}$. We now show examples in which the clattering stability criterion is applied for designing the parameters of two simple symmetric equilibrium postures.

Example 1: A uniform block on a flat terrain Consider a block of width W

and height H lying on a flat horizontal terrain (Fig. 5.9a). The mass distribution of the block is uniform, such that its radius of gyration is $\rho^2 = (L^2 + W^2)/3$. It is assumed that the block contacts the floor only at its two vertices. Using the clattering stability criterion (5.24) with ψ defined in (5.31) gives an upper bound on the ratio H/W guaranteeing clattering stability, as a function of the coefficient of restitution e. This condition is graphically illustrated in the parameter plane of $(e, H/W)$ as the clattering stability region depicted in Fig. 5.9b (shaded region). As e increases (less energy losses during collisions) the upper bound on permissible H/W ratio decreases. The maximum attainable value of e is 0.056, at which clattering stability maintains only for $H \rightarrow 0$. Note that at this case the block degenerates to a uniform thin rod, and that the same result of $e < 0.056$ was obtained in section 5.4 for the horizontal rod. For nearly plastic collisions $e \rightarrow 0$, the largest H/L ratio for which clattering stability can be obtained is $H/L = \sqrt{2}$, which is like the dimensions of an A4 paper. For higher values of H/L, the radius of gyration is too large (i.e. the mass is distributed away from the center-of-mass), and clattering stability cannot be attained for all e.

Example 2: A uniform rod on a symmetric V-shaped terrain Consider a rod of length L lying horizontally on a symmetric V-shaped terrain with slope angles α (Fig. 5.10a). The rod's mass is uniformly distributed, such that its radius of gyration is $\rho^2 = L^2/12$. Using the clattering stability criterion (5.24) with ψ defined in (5.31) gives a lower bound on the angle α guaranteeing clattering stability, as a function of the coefficient of restitution e. This condition is graphically illustrated in (e, α) plane as the clattering stability region depicted in Fig. 5.10b (shaded region). Note that for $e \in (0, 0.056)$, the rod possesses clattering stability for all α. As e increases, the permissible range of α is narrowed. On the other hand, when α increases, the permissible range of e is enlarged. The intuitive explanation for this fact is that when

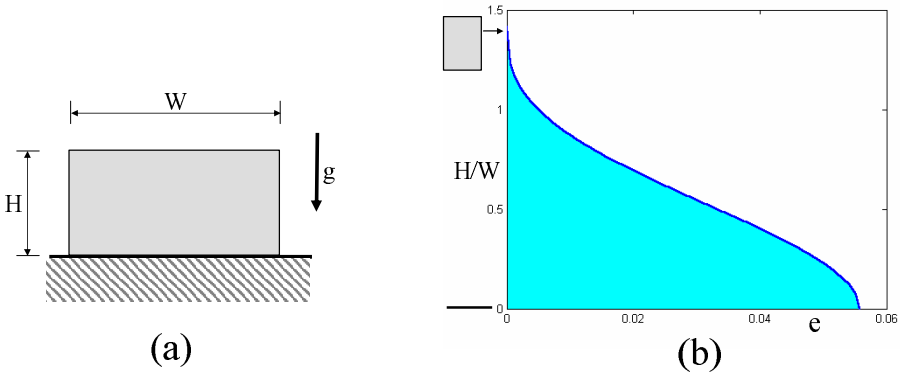

Figure 5.9: (a)A uniform block on a flat terrain (b)Clattering stability region in parameters' plane.

α is increased, an impulsive force at the endpoint x_1 has a larger component in the direction of the negative normal $-n_2$, which causes a larger negative change in v_2. Therefore, increasing α enhances the rod's clattering stability, as demonstrated in the following simulation example.

Simulation example: Stable clattering of a rod on a V-shaped terrain In simulation example 4 in the previous section we simulate the motion of a uniform rod on a horizontal plane with coefficient of restitution $e = 0.09$, and show that it results in unstable clattering motion. However, the stability region in Fig 5.10b indicates that when the horizontal terrain is replaced with a V-shaped terrain with $\alpha = 45^o$ and the same coefficient of restitution, clattering stability is achieved. The simulation results for a terrain with $\alpha = 45^o$ and $e = 0.09$, with initial conditions $h_{10} = 0.1, h_{20} = 0.1582$ and $\theta(0) = 0$ are shown if Fig. 5.11. Figs. 5.11a and 5.11b show the resulting motion of $v_1(t_k)$ and $v_2(t_k)$ respectively. The collisions with x_1 are marked with '$\times$' and collisions with x_2 are marked with '$\circ$' on the figures. Figures 5.11c and 5.11d show the resulting motion of $\theta(t_k)$ and $\omega(t_k)$ respectively. It can be seen that the rod is maintaining a stable clattering motion, and that $\theta(t_k)$ and $\omega(t_k)$

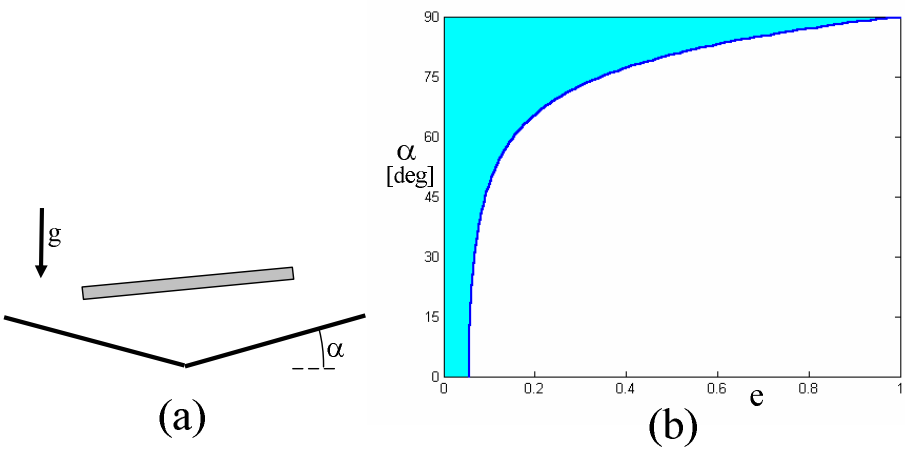

Figure 5.10: (a)A uniform rod on a V-shaped terrain (b)Clattering stability region in (e, α) plane.

both converge to nonzero constant values, as predicted by the theory.

5.7 Clattering Stability of a Non-Symmetric Rigid Body

This section considers the general case of a planar non-symmetric rigid body supported by two contacts on a general piecewise-linear terrain. The results are further extensions of the results in previous sections, and are sketched here without rigorous proofs. Consider a planar rigid body $\mathcal{B}$ with mass m and radius of gyration ρ. The configuration of $\mathcal{B}$ is $q = (r_c, \theta)$, where $r_c = (x, y)$ is the position of $\mathcal{B}$'s center-of-mass and θ is the orientation of a frame attached to $\mathcal{B}$, with respect to a fixed frame. At the nominal configuration $q = \vec{0}$, $\mathcal{B}$ lies in an equilibrium posture with two contacts, as shown if Fig. 5.12. It is assumed that contact is made only at the two vertices x_1 and x_2 of $\mathcal{B}$. Let r_i denote the vector from $\mathcal{B}$'s center-of-mass to the vertex x_i

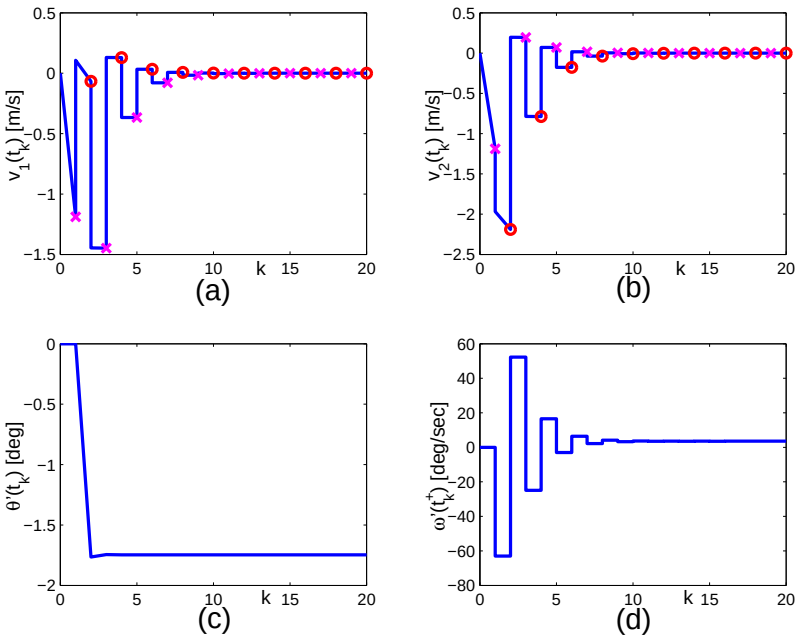

Figure 5.11: Simulation results of stable clattering of a uniform rod on a symmetric V-shaped terrain

for $i = 1, 2$, expressed in $\mathcal{B}$'s frame. The unit vector normal to the terrain at x_i is denoted n_i, and the unit vector tangent to the terrain at x_i is denoted t_i, such that (t_i, n_i) are right-handed pairs for $i = 1, 2$. It is assumed that the terrain satisfies the following requirements. First, we assume that the terrain is *piecewise linear* (i.e. it is linear in the vicinity of the contact points). Second, we assume that the terrain is *upward facing*, in the sense that $n_i \cdot \vec{g} < 0$ for $i = 1, 2$, where $\vec{g}$ is the vector of gravity acceleration. Finally, we assume that n_1 and n_2 are linearly independent (i.e. the two terrain segments are not parallel). Let us denote $g_i = n_i \cdot \vec{g}$ for $i = 1, 2$, and define the ratio $\Gamma = g_2/g_1$, which evaluates the terrain's asymmetry.

The equation of free motion of $\mathcal{B}$ expressed in q is identical to the rod's equation of

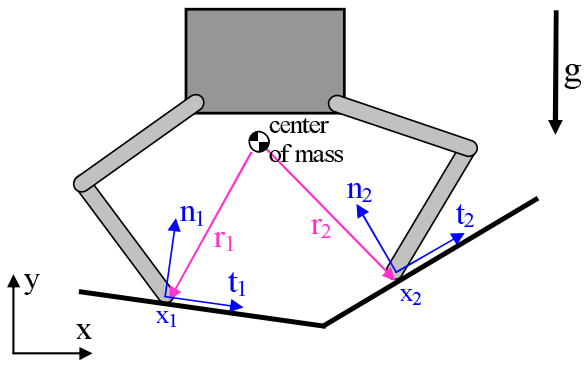

Figure 5.12: A non-symmetric rigid body on a general terrain.

motion (5.7). The contact constraints are given by

$$h_i = n_i \cdot (r_c + R(\theta) r_i) \geq 0 \text{ , where } R(\theta) = \begin{bmatrix} \cos\theta & -sin\theta \\ sin\theta & \cos\theta \end{bmatrix}. \tag{5.32}$$

Defining the alternative set of coordinates $q' = (h_1, h_2, \theta)$ with its velocity denoted by $\dot{q}' = (v_1, v_2, \omega)$, the Jacobian matrix satisfying $\dot{q}' = J\dot{q}$ is given by

$$J = \begin{pmatrix} n_1^T & b_1 \\ n_2^T & b_2 \\ 0 \quad 0 & 1 \end{pmatrix} \text{ , where } b_i = t_i \cdot r_i \text{ for } i = 1, 2. \tag{5.33}$$

Using the coordinate transformation 5.4 and assuming that $\mathcal{B}$ maintains small angles $|\theta| \ll 1$ during its motion, the linearized equation of free motion expressed in q' are given by

$$\begin{pmatrix} \ddot{h}_1 \\ \ddot{h}_2 \\ \ddot{x} \end{pmatrix} = \begin{pmatrix} g_1 + d_1\omega^2 \\ g_2 + d_2\omega^2 \\ 0 \end{pmatrix}, \tag{5.34}$$

where $d_i = -n_i \cdot r_i$ for $i = 1, 2$. Assuming that the rod's angular velocity ω is kept sufficiently small during motion, the centripetal accelerations in 5.34 are negligible,

and the linearized equations of free motion reduce to those of the horizontal rod in (5.9), with two distinct gravitational accelerations g_1, g_2 that reflect the terrain's asymmetry. Using the impact law (5.3) and assigning the coordinate transformation (5.5) ,the linearized reset maps are expressed in q' as

$$R_i'(q', \dot{q}') = (q', A_i'\dot{q}') \ , \ i = 1, 2 \ , \text{ where}$$

$$A_1' = \begin{pmatrix} -e & 0 & 0 \\ (1+e)\psi_1 & 1 & 0 \\ (1+e)\varphi_1 & 0 & 1 \end{pmatrix}, A_2' = \begin{pmatrix} 1 & (1+e)\psi & 0 \\ 0 & -e & 0 \\ 0 & (1+e)\varphi_2 & 1 \end{pmatrix} \ , \ \varphi_i = -\frac{b_i}{b_i^2+\rho^2}, \text{ and } \psi_i = -\frac{b_1 b_2 + (n_1 \cdot n_2)\rho^2}{b_i^2+\rho^2} \ . \tag{5.35}$$

The following two theorems generalize the results given in the previous sections for the horizontal rod and the symmetric postures. The first theorem, which is a generalization of Theorem 7, formulates the conditions for infinite bouncing on a single contact.

Theorem 9 *Consider the linearized hybrid dynamics of the nonsymmetric rigid body, with the initial configuration $q'(0) = (h_{10}, h_{20}, 0)$, $\dot{q}'(0) = \vec{0}$, such that $h_{20} > \Gamma h_{10}$. Then the dynamic solution corresponds to bouncing motion on x_1 and converges to a single-contact Zeno limit point if and only if the initial configuration satisfies the condition given by*

$$h_{20} \geq \left(\Gamma + \frac{4e(\Gamma + \psi_1)}{(1-e)^2}\right) h_{10}. \tag{5.36}$$

The proof of this theorem is similar to the proof of Theorem 7, with proper adaptations to account for the asymmetry, encompassed in the parameter Γ. The second theorem, which is a generalization of Theorem 8, summarizes the conditions for clattering stability.

Theorem 10 *Consider the linearized hybrid dynamics of the nonsymmetric rigid body, with the initial configuration* $q'(0) = (h_{10}, h_{20}, 0)$, $\dot{q}'(0) = \vec{0}$, *such that* $h_{20} > \Gamma h_{10}$. *Assume that the parameters* (e, ψ_1, ψ_2) *satisfy the conditions given by*

$$\psi_1 > 0,\ \psi_2 > 0,\ \textit{and}\ \sqrt{\psi_1\psi_2} > \frac{e^{1/3} + e^{2/3}}{1+e}. \tag{5.37}$$

Then if the initial configuration satisfies

$$h_{20} < (\Gamma + 4e(1+e)(\Gamma + \psi_1))\, h_{10}, \tag{5.38}$$

the dynamic solution corresponds to clattering motion that converges to a two-contact Zeno limit point in finite time. Moreover, if the initial configuration satisfies

$$(\Gamma + 4e(1+e)(\Gamma + \psi_1))\, h_{10} < h_{20} < \left(\Gamma + \frac{4e(\Gamma + \psi_1)}{(1-e)^2}\right) h_{10}, \tag{5.39}$$

then the dynamic solution starts with a finite sequence of collisions at x_1, *followed by clattering motion that converges to a two-contact Zeno limit point in finite time.*

Proof Sketch:

First, integrating the linearized dynamics 5.34 with $\omega = 0$, the first collision occurs at the endpoint x_1 if $h_20 > \Gamma h_{10}$. Formulating the times τ_1, τ_2 to the next collisions at x_1 and x_2 respectively, the inequality $\tau_2 < \tau_1$, which is the condition for onset of clattering, reduces to the condition 5.38.

Next, we formulate the dynamics of nonsymmetric clattering motion, under the assumption of zero gravity. This assumption implies that the velocities $\dot{q}'$ do not changed during the free motion phases, and are changed only at impact times. Let us define $\boldsymbol{v}_k = [v_1(t_k^+)\ v_2(t_k^+) v_x(t_k^+)]^T$ for $k > 0$, where by convention, we denote $\boldsymbol{v}_0 = [v_1(t_1^-)\ v_2(t_1^-)\ v_x(t_1^-)]^T$. Without loss of generality, we further assume that the collisions at endpoint x_1 occur on times t_k for odd k, and collisions at x_2 occur on

times t_k for even k. Using the reset maps (5.35) the discrete-time dynamics of $\boldsymbol{v}_k$ is given by

$$\boldsymbol{v}_{k+1} = \begin{cases} A_1' \boldsymbol{v}_k & k \text{ is even} \\ A_2' \boldsymbol{v}_k & k \text{ is odd.} \end{cases} \tag{5.40}$$

The discrete-time solution of 5.40 is given by

$$\boldsymbol{v}_k = \begin{cases} (A_1' A_2')^{\frac{k}{2}} \boldsymbol{v}_0 & k \text{ is even} \\ A_1' \left(A_1' A_2'\right)^{\frac{k-1}{2}} \boldsymbol{v}_0 & k \text{ is odd} \end{cases} \tag{5.41}$$

The stability properties of nonsymmetric clattering motion can be determined by the eigenvalues of $A_1' A_2'$, which are given by

$$\lambda_{1,2} = -e + \tfrac{1}{2}\left(\psi_1\psi_2(1+e)^2 \pm (1+e)\sqrt{\psi_1\psi_2(\psi_1\psi_2(1+e)^2 - 4e)}\right) \ , \ \lambda_3 = 1$$

Note that these eigenvalues are identical to the eigenvalues of $A_2' A_1'$, and that in the symmetric case where $\psi_1 = \psi_2$, they are the square of the eigenvalues given in 5.14, which are associated with a "half cycle" of the symmetric system. It can be shown that the eigenvalues $\lambda_{1,2}$ are associated with the discrete dynamics of v_1, v_2, and that clattering is stable if and only if these two eigenvalues are positive real numbers. This condition is captured by the inequalities

$$\psi_1 > 0, \ \psi_2 > 0, \text{ and } \sqrt{\psi_1\psi_2} > \frac{2\sqrt{e}}{1+e}.$$

We now formulate the dynamics of non-symmetric clattering motion with nonzero gravity. Using the indices $\{a, b\}$ and defining the ratio $\epsilon_k = 2g_b h_{bk}/v_{bk}^2$, the dynamics is identical to the Poincaré map given in 5.18, and the dynamics of ϵ_k is given by

$$\epsilon_{k+1} = \Gamma_k \frac{|v_{bk}| v_{ak}}{|v_{b,k+1}|^2} \left(2(\sqrt{1+\epsilon_k} - 1) - (\sqrt{1+\epsilon_k} - 1)^2\right),$$

where $\Gamma_k = \Gamma$ for even k, and $\Gamma_k = 1/\Gamma$ for odd k. The condition for clattering persistence is formulated as $\eta_k < 1$ for all $k \geq 1$, where $\eta_k = \Gamma_k(|v_{bk}|\sqrt{1+\epsilon_k})/(2v_{ak})$. Generalizing Lemma 5.4.1 and Lemma 5.4.2 to the non-symmetric case, it can be shown that

$$\frac{\epsilon_{k+2}}{\epsilon_k} \leq \frac{e^2}{\lambda_2^2} \text{ and } \frac{\eta_{k+2}}{\eta_k} \leq \frac{e^2}{\lambda_2^2} \text{ for all } k \geq 1,$$

where $\lambda_2 = -e + (\psi_1\psi_2(1+e)^2 + (1+e)\sqrt{\psi_1\psi_2(\psi_1\psi_2(1+e)^2 - 4e)})/2$. Therefore, the condition $\lambda_2 > e$ guarantees that ϵ_k and η_k converge asymptotically to zero, and clattering is stable. This condition is equivalent to the inequalities in 5.37. □

Graphical Example - center-of-mass region for clattering stability

This summarizing example considers an asymmetric planar rigid body $\mathcal{B}$ with a variable center-of-mass $\boldsymbol{x}$, and a given radius of gyration ρ. The body lies in a frictional equilibrium stance on a symmetric V-shaped terrain (Note that due to the variable center-of-mass, the stance is non-symmetric even though the terrain is symmetric). Our goal is to compute the region of center-of-mass locations achieving clattering stability. For a given radius of gyration, b_1 and b_2, defined in (5.33), are linear in $\boldsymbol{x}$. Thus, ψ_i, defined in (5.35) are fractions having numerators and denominators which are quadratic in $\boldsymbol{x}$. Thus, the clattering stability conditions in (5.37) define inequalities which are *quadratic and quartic* in $\boldsymbol{x}$. Fig. 5.13 shows two frictional equilibrium stances on a symmetric terrain with coefficient of friction $\mu = 0.5$ and coefficient of restitution $e = 0.1$. The difference between the stances in Fig. 5.13a and Fig. 5.13b is the value of the radius of gyration ρ. The dimensions of ρ are length units, and its true length relative to the stance's geometry is shown on both stances, showing that radius of gyration in the stance of Fig. 5.13a is twice as larger than in the stance of Fig. 5.13b. The clattering stability region, which is defined by the inequalities

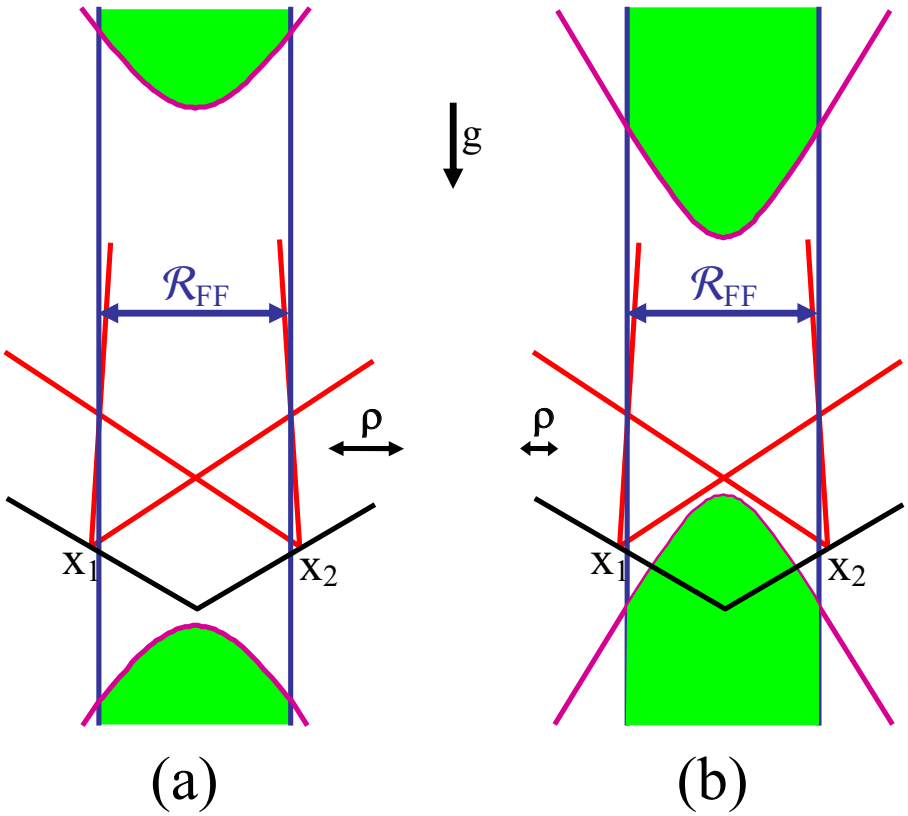

Figure 5.13: The clattering stability region of center-of-mass locations for two identical stances with different radius of gyration ρ.

in (5.37), is shown is a shaded region in both stances. This region is bounded by hyperbolic-like (yet, fourth order) curves, showing that the center-of-mass must be located either very high, or very low, with respect to the intersection point of the two contact normals. This clattering stability region is then intersected with the feasible equilibrium region $\mathcal{R}_{FF}$, which is an infinite vertical strip, and is identical in both stances. The example emphasizes the influence of the mass distribution of $\mathcal{B}$, encompassed by the radius of gyration ρ, on the clattering stability regions – concentrating the mass near the center-of-mass (i.e. decreasing ρ) enhances the clattering stability, and enlarges the clattering stability region.

Chapter 6

Frictional Stability of Two-Contact Stances

This chapter combines the results of all previous chapters, and presents sufficient conditions for frictional stability of two-contact frictional equilibrium stances of a planar rigid body $\mathcal{B}$ on a piecewise-linear terrain in planar gravitational field. The structure of this chapter is as follows. Section 6.1 defines the notion of completed dynamical system, which is the concatenation of the continuous and hybrid phases of the dynamics. Section 6.2 states the central result of sufficient conditions for frictional stability in planar two-contact stances. Finally, section 6.3 provides a procedure for computation of the center-of-mass region achieving stable equilibrium stances on a given terrain, and demonstrates with a graphical example.

6.1 The Completed Dynamical System

This section discusses the interrelations between the different phases of the frictional dynamics, which were analyzed in the previous chapters. Chapter 4 analyzed the continuous dynamics under a dictated contact mode, which persists until a separated contact recovers contact, and an impact event occurs. Chapter 5 analyzed the hybrid dynamics, composed of gravitational free flying interleaved by events of contact impact, which persists until reaching a Zeno limit point. One missing component for completely defining the dynamic response to a perturbation, is to determine what happens after a Zeno limit point. A recent work by Ames et al. [3] considers a Lagrangian hybrid dynamical system with a single constraint $h(q) \geq 0$. At a Zeno execution of the system, the dynamic solution converges to a limit point at a finite time t_∞, and satisfies $h(q(t_\infty)) = 0$ and $\dot{h}(q(t_\infty)) = 0$. Thus, it is argued in [3] that after the Zeno time t_∞, the hybrid dynamical systems *switches to a holonomically constrained dynamical system*, satisfying the constraint $h(q) \equiv 0$, with the initial conditions given by the Zeno limit point of the hybrid dynamical systems $q(t_\infty), \dot{q}(t_\infty)$. This concatenation of dynamical systems is termed *a completed hybrid system* in [3]. We now extend the concept of a completed hybrid system to the two-contact problem, and discuss its physical implications. The planar two-contact problem is formulated in Chapter 5 as a hybrid dynamical system involving two contact constraints $h_1(q), h_2(q) \geq 0$. Two types of Zeno executions for this system are analyzed, namely, the bouncing motion and the clattering motion. A Zeno execution of a bouncing motion converges to a point at which a single contact is re-established. Thus, the dynamics after a bouncing motion switches to a constrained dynamics involving a single sliding (or rolling) contact, which is precisely the dynamics associated with one of the

contact modes RS,FS, or LS. A Zeno execution of a clattering motion converges to a point at which two contacts are re-established simultaneously. Thus, the dynamics after a bouncing motion switches to a constrained dynamics involving a two sliding contacts, which is precisely the dynamics associated with one of the contact modes RR or LL.

Finally, the last component of the completed the dynamical system is as follows. Consider the constrained dynamics associated with sliding (or rolling) at a contact x_1, and separation at the other contact x_2 (contact modes RS,FS, or LS). This dynamics can either be dictated by particular initial conditions that satisfy the constraints, or it can evolve as a continuation after a Zeno limit point of bouncing motion. Under this dynamics, assume that at a given instant t_0, the free-flying contact x_2 is colliding. The impact at x_2 causes a discontinuous velocity jump, such that at t_0^+, the contact x_2 is given a separating velocity, pointing away from the contact, while the contact x_1 is given a colliding velocity, pointing towards the contact. Thus, a second collision at x_1 occurs, that reverses the normal components of the contact velocities, and so on. According to the analysis of clattering motion in Chapter 5, it can be easily shown that if the system's parameter satisfy the clattering stability conditions (5.37), this scenario results in an infinite sequence of collisions that converges to a Zeno limit point at which both contacts are re-established. This special scenario of clattering is termed *deadbeat clattering motion.* Two key features of deadbeat clattering motion are as follows. First, note that both contact points are in contact during the entire sequence of collisions, while only velocities are alternating. Second, note that there are no free-flight phases between collisions. Thus, according to the rigid body impact model, the whole infinite sequence of collisions occurs *in zero time.* (This special scenario of degenerate Zeno execution is termed *chattering Zeno* in [1].) Thus, the

deadbeat clattering can be viewed as a single event of non-smooth transition from a single-contact mode in $\{RS, LS, FS\}$ to a two-contact sliding mode in $\{RR, LL\}$.

6.2 Sufficient Conditions for Frictional Stability of Two-Contact Stances

This section states the key result of this research thesis, which combines all the results obtained in the previous chapters to derive a sufficient condition for frictional stability of two-contact stances of a planar rigid body. Recall that a frictional equilibrium posture q_0 of a mechanical contact system possesses frictional stability if for any sufficiently small position-and-velocity perturbation about q_0, the system's dynamic response recovers all contacts, and converges to a new equilibrium posture in an arbitrarily small neighborhood of q_0. Using the notion of completed dynamical system, the dynamic solution in response to a given initial condition is now defined as a composition of pieces of hybrid motion of clattering or bouncing that converges to a Zeno limit point, followed by pieces of continuous motion along contact modes. Using this completed dynamic solution, we can finally address the problem of frictional stability. The following theorem gives sufficient conditions for frictional stability of two-contact stances of a planar rigid body.

Theorem 11 *Let a planar rigid body $\mathcal{B}$ be at a frictional equilibrium configuration q_0 on a piecewise-linear terrain under gravity. Then q_0 possesses frictional stability if the following two conditions hold*

1. *q_0 is a persistent equilibrium configuration*

2. *q_0 possesses clattering stability*

Proof: The proof, which is not given here in full detail, is based on the fact that these two conditions induce a chronological order on the phases of the completed dynamical system in response to a perturbation. This chronological order, which is illustrated in the flowchart of Fig. 6.1, is as follows. Consider a small perturbation at which both contacts are separated, and the contact mode SS is initially dictated. According to Theorem 6, since q_0 is a persistent equilibrium configuration, the dynamic response reaches an event of collision at one contact in a finite time. Then, according to Theorems 9 and 10, under the clattering stability condition, the system enter a sequence of collisions, which converges either to a Zeno limit point of one-contact re-establishment via bouncing motion, or to a Zeno limit point of two-contact re-establishment via clattering motion. In the first case, after the Zeno time, the dynamic response switches to constrained dynamics with a single contact, say x_1, sliding or rolling. According to Theorem 6, under the persistent equilibrium condition, the dynamics may switch between sliding and rolling, but eventually the separated contact x_2 is colliding. At this point, a deadbeat clattering event of infinite collisions in zero time occurs, and the system switches to a mode of two-contact sliding. Finally, the persistent equilibrium condition implies that the two sliding contacts are decelerating, and come to a full stop simultaneously, in a new equilibrium posture. Note that in case of an initial perturbation that dictates a contact mode different from SS (free-flying), the process simply starts from an advanced phase in the flowchart of Fig. 6.1, and proceeds as described above. Note, too, that the completed dynamical system goes through a finite number of phases (at most six in the "longest" scenario - free flying; bouncing; one-contact roll/slide; deadbeat clattering; two-contact sliding; complete stop). Each phase occurs in finite time, and can be bounded within an arbitrarily small neighborhood of q_0, by setting its initial perturbation arbitrarily

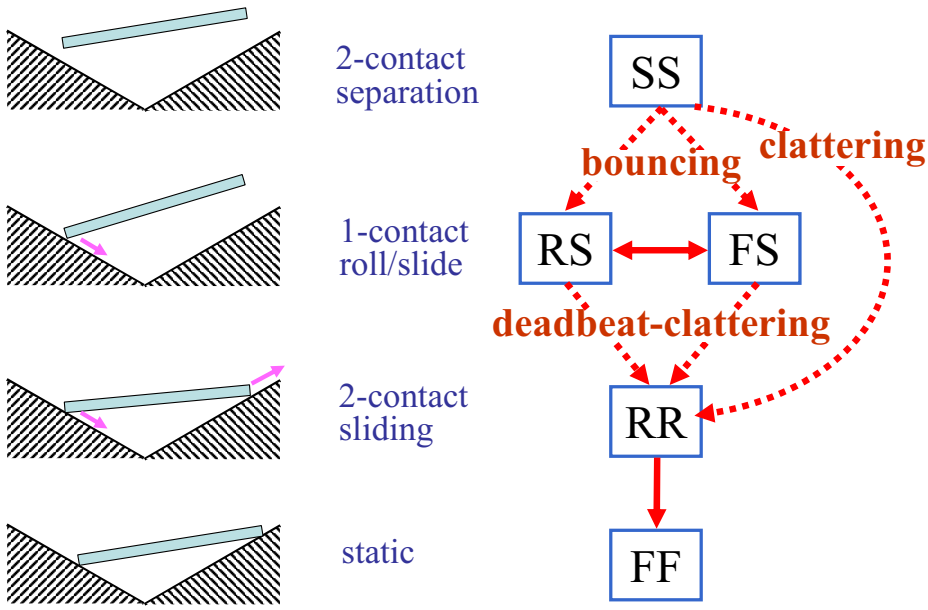

Figure 6.1: Flowchart of phases of the completed dynamical two-contact system under perturbation.

small. Therefore, by composing the bounds of each phase, and checking the finite set of all possible scenarios, one can explicitly derive a bound ϵ on the initial perturbation, such that the entire dynamic response stays within a δ-neighborhood of q_0 and reaches static equilibrium in finite time t_0, for any arbitrarily small δ and t_0. $\square$

6.3 The Center-of-Mass Region of Frictional Stability

This section summarizes the procedure for computing the center-of-mass region achieving a stable equilibrium stance of a planar rigid body $\mathcal{B}$ supported by given contacts on a piecewise linear terrain. We assume that the coefficient of friction μ, the coefficient of restitution e, as well as $\mathcal{B}$'s radius of gyration ρ, are all known. The procedure,

which is divided into three stages, is summarized in the following corollary.

Corollary 6.3.1 *Let $\mathcal{B}$ be a planar rigid body, with a radius of gyration ρ, a center-of-mass located at $\boldsymbol{x}$. Consider a stance on two given contact points a piecewise linear terrain with coefficient of friction μ and coefficient of restitution e. Then the region of center-of-mass locations $\boldsymbol{x}$ achieving an equilibrium stance with frictional stability is computed according to the following three steps.*

1. *Construct the feasible equilibrium region, which is the vertical strip whose computation is given in Chapter 2.*

2. *Enumerate all contact modes, compute their feasibility region and construct the persistent equilibrium region, whose computation is given in Chapter 4.*

3. *Construct the center-of-mass region guaranteeing clattering stability, as described in Chapter 5.*

4. *Finally, intersect all these regions, to obtain the the region of center-of-mass locations guaranteeing an equilibrium stance with frictional stability*

Graphical Example: The following graphical example shows the center-of-mass stable equilibrium region for two stances on a symmetric terrain with coefficient of friction $\mu = 0.5$ and coefficient of restitution $e = 0.1$. The difference between the two stances, shown in Fig. 6.2a and 6.2b, is the value of $\mathcal{B}$'s radius of gyration ρ, whose true length is shown on both stances. The feasible equilibrium region $\mathcal{R}_{FF}$, whose computation does not depend on ρ, is the vertical strip shown on both figures. The persistent equilibrium region for both stances was already computed in the graphical example of Fig. 4.6. The clattering stability region for both stances was already computed in the graphical example of Fig. 5.13. In this concluding example, the

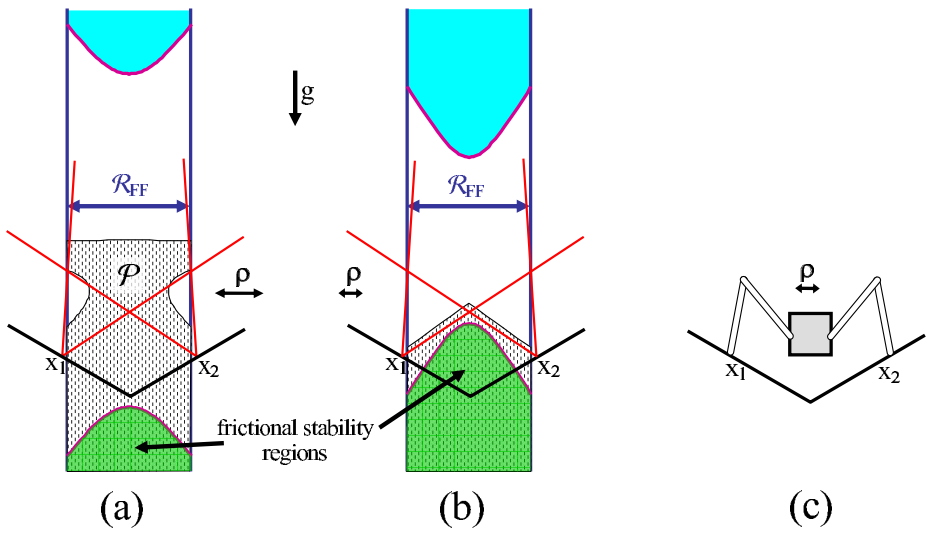

Figure 6.2: (a)-(b) Center-of-mass stable equilibrium regions for two stances with $\mu = 0.5$, $e = 0.1$, and different radii of gyration ρ, (c) Illustration of a stable equilibrium stance.

persistent equilibrium region for each stance is shown as a dotted region, and the clattering stability region for each stance is shown as a shaded region. The intersection region, which appears as a dark-shaded region, is the center-of-mass stable equilibrium region. Note that when designing a legged robot or a rigid body according to frictional stability considerations, there is a tradeoff regarding the mass distribution, or radius of gyration ρ, as follows. Decreasing the radius of gyration (i.e. concentrating the mass near the center-of-mass) enlarges the clattering stability region. On the other hand, with a small radius of gyration, the dynamics is more sensitive to frictional dynamic ambiguities and inconsistencies, and thus the persistent equilibrium region is smaller. In the stance of Fig. 6.2a, with a large radius of gyration, the persistent equilibrium region is large, but the clattering stability region is small, and the region of intersection is located under the terrain. Thus, stable equilibrium stances are not achievable in this case. In the stance of Fig. 6.2b, with ρ twice smaller, the

persistent equilibrium region is smaller, but the clattering stability region is larger, and the intersection region has a portion above the terrain, making stable equilibrium stances achievable. Finally, Fig. 6.2c shows an illustration of a two-legged mechanism (analyzed as a single rigid body) positioned in a stable equilibrium stance, by keeping the center-of-mass location sufficiently low. The small radius of gyration is achieved by taking a massive central body, with relatively thin limbs.

Chapter 7

Conclusion

This closing chapter concludes the results of this thesis, discusses their limitations, and sketches some possible directions of future research.

This thesis addressed the problem of identifying and computing stable equilibrium postures of multi-legged robots standing on rough terrain. Under the simplification of rigid-body paradigm and Coulomb's friction model, the center-of-mass region achieving feasible equilibrium was computed and geometrically characterized for two-dimensional and three-dimensional stances. The results were then extended to account for stance robustness with respect to a given neighborhood of disturbance wrenches, and to multiple contact points. Next, the dynamics of planar mechanical systems with frictional contacts was formulated using the concept of contact modes, and the notion of frictional stability was defined. The criterion of strong equilibrium, which eliminates dynamic ambiguity, and persistent equilibrium, which eliminates dynamic inconsistency and dynamic jamming, were then presented. These criteria were formulated in terms of mass distribution and center-of-mass locations, and their relationship with frictional stability was established. The hybrid dynamical system

of a rigid body undergoing sequential collisions at two contacts was then formulated, and the two motions of bouncing and clattering were analyzed . Using the Poincaré map technique, a novel criterion for clattering stability was derived. Finally, using the concept of completed dynamical system, the concluding result of this thesis states that persistent equilibrium augmented by clattering stability are sufficient conditions for frictional stability of planar two-contact stances. This result, which is formulated in terms of contact arrangement, coefficient of friction, coefficient of restitution, mass distribution and center-of-mass location, is graphically demonstrated as a permissible region for center-of-mass locations.

We now discuss the main limitations of the results in this thesis. First, aside from the computation of feasible equilibrium region in 3D (Chapter 3), the analysis of continuous and hybrid dynamics is limited to the planar case. Second, most of the results were derived under the simplification of rigid-body paradigm, and are not suitable for robotic systems with multiple links. Third, the analysis of hybrid dynamics and the concluding results of frictional stability are limited to two-contact stances. Fourth, the concluding theorem provides only *sufficient conditions* for frictional stability. Though the component of persistent equilibrium seems also necessary, the requirement of clattering stability might impose requirements that are too conservative. When clattering stability is not satisfied, the hybrid dynamics results in complex sequences of collisions at the two contacts, whose analysis is much more complicated. Analyzing these sequences and derivation of conditions for their convergence is a challenging open problem. Fifth, the results of frictional stability are *local*, and consider infinitesimally small perturbations. Global analysis such as robustness of stability and computation of basin of convergence are not discussed here. Finally, the impact model in the hybrid system assumes frictionless impact, and does not incorporate

some more complicated models of frictional impact, nor account for other effects such as elastic vibrations due to impact [46].

We now list some possible directions for future extension of this work. First, generalizing the analysis of clattering to three or more contacts seems naturally as the next step. A first component of such analysis might be checking the clattering motion involving all possible pairs of contacts, and then try to analyze more complex collisions sequences involving more than two contacts. Once this step is completed the second step would probably be generalization to three-dimensional stances, where the minimum number of contacts is three. Third, relaxing the rigid body assumption, the analysis of continuous and hybrid dynamics can be extended to account for robotic systems with multiple degrees-of-freedom and frictional contacts. Such analysis must incorporate for the control laws of the actuated joints into the dynamics, and may even result in synthesizing control laws that will improve the system's stability. Fourth, in order to account for uncertainties in the coefficient of friction and in the radius of gyration, some computational tools should be developed for conservative approximate computation of equilibrium stances that will guarantee stability under a given range of uncertainties. Finally, an additional generalization, which is the ultimate objective of this research, among others, is the development of a fully autonomous planning algorithm for stable legged locomotion on rough terrain, which will use all the basic tools developed in this thesis, and yet will meet computational efficiency requirements, in order to successfully handle complicated real-world scenarios.

Appendix A

Additional Proofs of Results

A.1 Proofs of results from Chapter 2

Proof of Proposition 2.1.1:

Let $\tilde{\mathcal{R}}(\boldsymbol{w}) = \mathsf{conv}\{\mathcal{R}_{ij}(\boldsymbol{w}),\ 1 \leq i, j \leq k\}$. First we show that $\tilde{\mathcal{R}}(\boldsymbol{w}) \subseteq \mathcal{R}(\boldsymbol{w})$, then we show that $\mathcal{R}(\boldsymbol{w}) \subseteq \tilde{\mathcal{R}}(\boldsymbol{w})$.

1. Let $x \in \tilde{\mathcal{R}}(\boldsymbol{w})$. Then there exist center-of-mass locations $x_{ij} \in \mathcal{R}_{ij}(\boldsymbol{w})$ and non-negative scalars λ_{ij} such that $x = \sum_{i,j} \lambda_{ij} x_{ij}$ where $\sum_{i,j} \lambda_{ij} = 1$. Consider now those (i, j) indices for which $\lambda_{ij} \neq 0$. Since $x_{ij} \in \mathcal{R}_{ij}(\boldsymbol{w})$, there exists a $2k$-vector $\boldsymbol{f}_{ij} \geq \vec{0}$ whose only non-zero components are associated with f_i and f_j, such that $\boldsymbol{f}_{ij}$ satisfies the equilibrium condition: $G_f \boldsymbol{f}_{ij} = -f_{ext}$ and $G_\tau \boldsymbol{f}_{ij} = -(x_{ij}^T J^T f_{ext} + \tau_{ext})$. If one chooses the contact forces as $\boldsymbol{f} = \sum_{i,j} \lambda_{ij} \boldsymbol{f}_{ij} \geq \vec{0}$, one gets

$$G_f \boldsymbol{f} = \textstyle\sum_{i,j} \lambda_{ij} G_f \boldsymbol{f}_{ij} = -\sum_{i,j} \lambda_{ij} f_{ext} = -f_{ext}$$
$$G_\tau \boldsymbol{f} = \textstyle\sum_{i,j} \lambda_{ij} G_\tau \boldsymbol{f}_{ij} = -\sum_{i,j} \lambda_{ij} (x_{ij}^T J^T f_{ext} + \tau_{ext}) = -(x^T J^T f_{ext} + \tau_{ext}).$$

Thus $\boldsymbol{f}$ satisfies the equilibrium condition (2.1) with center of mass at x. Hence $x \in \mathcal{R}(\boldsymbol{w})$.

2. Let $x \in \mathcal{R}(\boldsymbol{w})$. Let τ_{min} and τ_{max} be the solutions of the LP problems (2.3), and let $\boldsymbol{f}_{min}$ and $\boldsymbol{f}_{max}$ be the values of $\boldsymbol{f}$ corresponding to τ_{min} and τ_{max}. Since x lies in the strip $\mathcal{R}(\boldsymbol{w}) = \{x : \ \tau_{min} \leq x \cdot J^T f_{ext} + \tau_{ext} \leq \tau_{max}\}$, there exist two center-of-mass locations x_{min} and x_{max} on the edges of $\mathcal{R}(\boldsymbol{w})$ such that $x = \lambda x_{min} + (1-\lambda)x_{max}$ for some $\lambda \in [0, 1]$. Now recall that the extrema of a linear program always include a vertex of the constraints polytope. Let $\mathcal{P}$ denote the constraints polytope. According to (2.3), $\mathcal{P}$ is given by $\mathcal{P} = \{\boldsymbol{f} \in I\!R^{2k} : \quad G_f \boldsymbol{f} = -f_{ext}, \boldsymbol{f} \geq \vec{0}\}$. Thus $\mathcal{P}$ is defined by two equalities and $2k$ inequalities in $I\!R^{2k}$. Each vertex of $\mathcal{P}$ is an intersection of $2k$ facets of $\mathcal{P}$, hence it satisfies $2k$ equalities out of the $2k+2$ equations: $\boldsymbol{f} = \vec{0}$ and $G_f \boldsymbol{f}_v = -f_{ext}$. As a result, a vertex of $\mathcal{P}$ has at most two non-zero components. Since τ_{min} and τ_{max} are extrema of (2.3), $\boldsymbol{f}_{min}$ and $\boldsymbol{f}_{max}$ are vertices of $\mathcal{P}$. Focusing first on $\boldsymbol{f}_{min}$, it has at most two non-zero components, say i and j. It follows that $\boldsymbol{f}_{min}$ is generated only by two contact forces at x_i and x_j. But $\boldsymbol{f}_{min}$ corresponds to x_{min} and satisfies $G_f \boldsymbol{f}_{min} = -f_{ext}$ and $G_\tau \boldsymbol{f}_{min} = -\tau_{min} = -(x_{min}^T J^T f_{ext} + \tau_{ext})$. Therefore $x_{min} \in \mathcal{R}_{ij}(\boldsymbol{w})$. Using similar arguments for $\boldsymbol{f}_{max}$, there exist two indices m and n such that $x_{max} \in \mathcal{R}_{mn}(\boldsymbol{w})$. Finally, $x = \lambda x_{min} + (1 - \lambda)x_{max}$ and therefore $x \in \mathsf{conv}\{\mathcal{R}_{ij}(\boldsymbol{w}), \mathcal{R}_{mn}(\boldsymbol{w})\} \subseteq \tilde{\mathcal{R}}(\boldsymbol{w})$. $\square$

Proof of Corollary 2.1.2:

According to the proof of proposition 2.1.1, there exist at most four distinct contacts x_i, x_j, x_m, x_n such that $\mathcal{R}(\boldsymbol{w}) = \mathsf{conv}\{\mathcal{R}_{ij}(\boldsymbol{w}), \mathcal{R}_{mn}\}$. Hence the entire strip $\mathcal{R}(\boldsymbol{w})$ is determined by at most four contacts. $\square$

Proof of Theorem 2:

The wrenches parametrized by the vertices of $\mathcal{W} = [\kappa_1, \kappa_2] \times [\nu_1, \nu_2]$ are: $\boldsymbol{w}_{11} = (f_{ext}^1, \nu_1)$, $\boldsymbol{w}_{12} = (f_{ext}^1, \nu_2)$, $\boldsymbol{w}_{21} = (f_{ext}^2, \nu_1)$, $\boldsymbol{w}_{22} = (f_{ext}^2, \nu_2)$, where $f_{ext}^i = (\kappa_i, 1)$ for $i = 1, 2$. Let

$\overline{\mathcal{R}}(\mathcal{W})$ be the intersection of the feasible equilibrium strips associated with these four wrenches. We first show that $\overline{\mathcal{R}}(\mathcal{W})$ is the parallelogram of the theorem, then show that $\mathcal{R}(\mathcal{W}) = \overline{\mathcal{R}}(\mathcal{W})$. Using Theorem 1 with $\tau_{i,min}$ and $\tau_{i,max}$, the strips $\mathcal{R}(\boldsymbol{w}_{ij})$ are given by $\mathcal{R}(\boldsymbol{w}_{ij}) = \{x : \tau_{i,min} - \nu_j \leq x^T J f^i_{ext} \leq \tau_{i,max} - \nu_j\}$ for $1 \leq i, j \leq 2$. Since ν_j appears as a linear additive term in $\mathcal{R}(\boldsymbol{w}_{ij})$ and $\nu_1 \leq \nu_2$, the intersection $\overline{\mathcal{R}}(\mathcal{W})$ can be written as

$$\overline{\mathcal{R}}(\mathcal{W}) = \{x \in I\!R^2 : \tau_{i,min} - \nu_1 \leq x^T J f^i_{ext} \leq \tau_{i,max} - \nu_2 \ \text{ for } i = 1, 2\},$$

which is the parallelogram specified in the theorem. Next we prove that $\mathcal{R}(\mathcal{W}) = \overline{\mathcal{R}}(\mathcal{W})$ in two steps. First we show that $\mathcal{R}(\mathcal{W}) \subseteq \overline{\mathcal{R}}(\mathcal{W})$, then we show that $\overline{\mathcal{R}}(\mathcal{W}) \subseteq \mathcal{R}(\mathcal{W})$.

1. Let $x \in \mathcal{R}(\mathcal{W})$. Then by definition x lies in $\mathcal{R}(\boldsymbol{w})$ for all $\boldsymbol{w} \in \mathcal{W}$. In particular, x lies in $\mathcal{R}(\boldsymbol{w}_{ij})$ for $1 \leq i, j \leq 2$, which implies that $x \in \overline{\mathcal{R}}(\mathcal{W})$.

2. Let $x \in \overline{\mathcal{R}}(\mathcal{W})$. Then by definition x lies in $\mathcal{R}(\boldsymbol{w}_{ij})$ for $1 \leq i, j \leq 2$. Hence there exist $2k$-vectors $\boldsymbol{f}_{ij} \geq \vec{0}$ satisfying the equilibrium condition

$$\begin{aligned} G_f \boldsymbol{f}_{ij} &= -f^i_{ext} \\ G_\tau \boldsymbol{f}_{ij} &= -(x^T J^T f^i_{ext} + \nu_j) \end{aligned} \qquad \text{for } 1 \leq i, j \leq 2. \tag{A.1}$$

We now show that x lies in the individual strips $\mathcal{R}(\boldsymbol{w})$ for all $\boldsymbol{w}$ parametrized by $\mathcal{W}$. Any (p, q) in $\mathcal{W} = [\kappa_1, \kappa_2] \times [\nu_1, \nu_2]$ can be expressed as a convex combination of the four vertices:

$$\begin{pmatrix} p \\ q \end{pmatrix} = \lambda_{11} \begin{pmatrix} \kappa_1 \\ \nu_1 \end{pmatrix} + \lambda_{12} \begin{pmatrix} \kappa_1 \\ \nu_2 \end{pmatrix} + \lambda_{21} \begin{pmatrix} \kappa_2 \\ \nu_1 \end{pmatrix} + \lambda_{22} \begin{pmatrix} \kappa_2 \\ \nu_2 \end{pmatrix},$$

where $\lambda_{ij} \in [0, 1]$ and $\sum_{i,j} \lambda_{ij} = 1$ for $1 \leq i, j \leq 2$. Writing $\boldsymbol{w} = (f_{ext}, \tau_{ext})$ such that $f_{ext} = (p, 1)$ and $\tau_{ext} = q$, we have that $f_{ext} = (\lambda_{11} + \lambda_{12}) f^1_{ext} + (\lambda_{21} + \lambda_{22}) f^2_{ext}$ and

$\tau_{ext} = (\lambda_{11} + \lambda_{21})\nu_1 + (\lambda_{21} + \lambda_{22})\nu_2$. It follows that the vector of contact forces $\boldsymbol{f} = \sum_{i,j} \lambda_{ij} \boldsymbol{f}_{ij} \geq \vec{0}$ satisfies

$$\begin{aligned} G_f \boldsymbol{f} = & \sum_{i,j} \lambda_{ij} G_f \boldsymbol{f}_{ij} = -(\lambda_{11} + \lambda_{12}) f^1_{ext} - (\lambda_{21} + \lambda_{22}) f^2_{ext} = -f_{ext} \\ G_\tau \boldsymbol{f} = & \sum_{i,j} \lambda_{ij} G_\tau \boldsymbol{f}_{ij} = -x^T J^T \big((\lambda_{11} + \lambda_{12}) f^1_{ext} + (\lambda_{21} + \lambda_{22}) f^2_{ext}\big) \\ & -\big((\lambda_{11} + \lambda_{21})\nu_1 + (\lambda_{21} + \lambda_{22})\nu_2\big) = -(x^T J^T f_{ext} + \tau_{ext}). \end{aligned}$$

Thus $\boldsymbol{f}$ satisfies the equilibrium condition (2.5) for $\boldsymbol{w} = (f_{ext}, \tau_{ext})$ and center of mass at x. Hence $x \in \mathcal{R}(\boldsymbol{w})$. Since the above argument holds for all $\boldsymbol{w}$ parametrized by $\mathcal{W}$, we conclude that $x \in \mathcal{R}(\mathcal{W})$. □

A.2 Proofs of results from Chapter 3

Proof of Theorem 3:

1. Since each contact x_i satisfies $\boldsymbol{e} \in \mathcal{C}_i$, a vertical contact force $f_i = -f_g \in \mathcal{C}_i$ can balance the gravitational force when $\boldsymbol{x}$ lies on the vertical line through x_i, hence $x_i \in \mathcal{R}$. Since $\mathcal{R}$ is a convex vertical prism, it must contain the vertical prism spanned by the contacts, which is precisely Π.

2. We will show that for tame stances, any center-of-mass position that satisfies the equilibrium condition (3.1) must lie within Π. We will use the following definitions. Let l_{12} denote the line passing through x_1 and x_2, and let $\mathcal{B}_{12}$ denote the plane perpendicular to l_{12} that passes through x_3. Let $\mathcal{F}_{12}$ be a planar coordinate frame on $\mathcal{B}_{12}$. Let $\bar{f}_i$ and $\bar{f}_g$ denote the projections of the contact forces f_i and gravitational force f_g onto $\mathcal{B}_{12}$, expressed in the planar frame $\mathcal{F}_{12}$. Similarly, let $\bar{x}_i$ and $\bar{x}$ denote the projections of the contacts x_i and center-of-mass $\boldsymbol{x}$ onto $\mathcal{B}_{12}$, expressed in $\mathcal{F}_{12}$. Note that n_o lies in $\mathcal{B}_{12}$,

and is perpendicular to $\bar{x}_3 - \bar{x}_1$. Let $\bar{n}_o$ denote n_o expressed in the planar frame $\mathcal{F}_{12}$. Finally, let $J = \begin{bmatrix} 0 & -1 \\ 1 & 0 \end{bmatrix}$ be the planar 90° rotation matrix, and let $\sigma = \bar{n}_o^T J(\bar{x}_3 - \bar{x}_1)$. Since f_1 and f_2 generate zero torque about l_{12}, torque balance implies that the total torque generated by f_g and f_3 about l_{12} must sum to zero. This can be expressed in the planar frame $\mathcal{F}_{12}$ as $\bar{f}_g^T J(\bar{x} - \bar{x}_1) + \bar{f}_3^T J(\bar{x}_3 - \bar{x}_1) = 0$. Note that $J(\bar{x}_3 - \bar{x}_1) = \sigma \bar{n}_o$. Since the stance is tame, f_3 must satisfy $f_3 \cdot n_o = \bar{f}_3 \cdot \bar{n}_o > 0$. Therefore, the torque balance about l_{12} implies that $\mathsf{sgn}(\sigma)(\bar{f}_g^T J(\bar{x} - \bar{x}_1)) > 0$. The geometric implication of this inequality is that $\boldsymbol{x}$ must lie within a semi-infinite halfspace containing x_3, which is bounded by the vertical plane passing through x_1 and x_2. Repeating this argument with the other two possible permutations of contact indices, we conclude that $\boldsymbol{x}$ must lie within the vertical prism spanned by the contacts, which is precisely Π.

□

Proof of Lemma 3.4.2: The proof outline is as follows. For each type, we choose a set ψ of m parameters that parametrize the contact forces. A force f_i that lies in the interior of its friction cone is parametrized by its three components in $\mathbb{R}^3$. A nonzero force f_i that lies on the boundary of $\mathcal{C}_i$ is parametrized by the pair (c_i, ϕ_i) as shown in (3.12). Composing this parametrization with (3.11) defines a map $\chi : \mathbb{R}^m \to N$. A necessary condition for a wrench w to lie on a five-dimensional boundary cell of N, is that it is an image of a critical point of χ, on which the $6 \times m$ Jacobian matrix $\mathcal{J} = \frac{\partial \chi}{\partial \psi}$ has a rank of 5. We now validate this criticality condition for the three cases.

1. Two nonzero contact forces f_1 and f_2 are parametrized by their components.

The resulting 6×6 Jacobian matrix is given by

$$\mathcal{J} = \begin{pmatrix} I_{3\times 3} & I_{3\times 3} \\ [x_1\times] & [x_2\times] \end{pmatrix}.$$

It can be verified that the rank of $\mathcal{J}$ is automatically 5, as long as the contacts x_1 and x_2 do not coincide.

2. The contact force f_1 is parametrized by its three components in $I\!R^3$, while f_2 and f_3 are parametrized by $(c_2, \phi_2, c_3, \phi_3)$ as shown in (3.12). The resulting 6×7 Jacobian matrix of χ is given by

$$\mathcal{J} = \begin{pmatrix} I_{3\times 3} & u_2(\phi_2) & c_2 u_2'(\phi_2) & u_3(\phi_3) & c_3 u_3'(\phi_3) \\ [x_1\times] & [x_2\times]u_2(\phi_2) & c_2[x_2\times]u_2'(\phi_2) & [x_3\times]u_3(\phi_3) & c_3[x_3\times]u_3'(\phi_3) \end{pmatrix},$$

where $u_i'(\phi_i) = \cos(\phi_i)s_i - \sin(\phi_i)t_i$. Assume that $\mathsf{rank}(\mathcal{J}) = 5$. Therefore, there exists a vector $\Omega = (\omega, v) \in I\!R^6$ such that $\Omega^T\mathcal{J} = 0_{1\times 7}$. For convenience, let us locate the origin at x_1. Since the first three columns of $\mathcal{J}$ contain the identity matrix and a zero matrix, we get that $\omega = 0$. Therefore, v must satisfy $v^T[x_i\times]u_i = v^T[x_i\times]u_i' = 0$ for $i = 2, 3$, where the dependencies on ϕ_i are omitted for convenience. Since u_i and u_i' are two linearly independent vectors lying on the tangent plane $\mathcal{B}_i$, there exist scalars κ_i such that $\kappa_i u_i + (1-\kappa_i)u_i'$ is parallel to l_{i0} and l_i. Therefore, we get that $v^T[x_i\times]l_i = 0$, for $i = 2, 3$. Let us define $\tilde{v} = (v\cdot n_o)n_o$. Since x_i and l_i lie in $\mathcal{B}_o$, $[x_i\times]l_i$ is parallel to n_o. Therefore, we get $\tilde{v}^T[x_i\times]l_i = v^T[x_i\times]l_i = 0$. Scaling by $v\cdot n_o$ and relaxing the assumption $x_1 = 0$ gives the relation (3.13). The geometrical meaning of (3.13) is that the lines l_{20}, l_{30} generate zero torque about x_1, thus they must pass through x_1. Note that (3.13) gives two uncoupled scalar equations in ϕ_2 and ϕ_3, each having up to two isolated solutions. Therefore, type-2 critical forces are parametrized

by the five scalars (f_1, c_2, c_3), while ϕ_2 and ϕ_3 are fixed. It can be shown that the special case $n_o \cdot v = 0$ occurs when the tangent planes $\mathcal{B}_2(\phi_2)$ and $\mathcal{B}_3(\phi_3)$ intersect at a common line that lies within the base plane $\mathcal{B}_o$. Note that this non-generic geometric relation violates the assumption of a tame stance.

3. Three contact forces lying on the boundaries of $\mathcal{C}_i$ are parametrized by the six scalars $(c_1, c_2, c_3, \phi_1, \phi_2, \phi_3)$. The 6×6 Jacobian matrix of χ is then given by

$$\mathcal{J} = \begin{pmatrix} u_1(\phi_1) & c_1 u_1'(\phi_1) & u_2(\phi_2) & c_2 u_2'(\phi_2) & u_3(\phi_3) & c_3 u_3'(\phi_3) \\ [x_1\times]u_1(\phi_1) & c_1[x_1\times]u_1'(\phi_1) & [x_2\times]u_2(\phi_2) & c_2[x_2\times]u_2'(\phi_2) & [x_3\times]u_3(\phi_3) & c_3[x_3\times]u_3'(\phi_3) \end{pmatrix}, \tag{A.2}$$

where $u_i'(\phi_i) = \cos(\phi_i)s_i - \sin(\phi_i)t_i$. Assume that $\det(\mathcal{J}) = 0$. Hence there exists a vector $\Omega = (\omega, v) \in I\!R^6$ such that $\Omega^T \mathcal{J} = 0_{1\times 6}$. This implies that $\omega^T u_i + v^T[x_i\times]u_i = 0$ and $\omega^T u_i' + v^T[x_i\times]u_i' = 0$ for $i = 1, 2, 3$, where the dependencies on ϕ_i are omitted. Since u_i and u_i' both lie on the tangent plane $\mathcal{B}_i$, there exist scalars κ_i such that $\kappa_i u_i + (1-\kappa_i)u_i'$ are parallel to l_i. Therefore, using this weighted sum gives $\omega^T l_i + v^T[x_i\times]l_i = 0$ for $i = 1, 2, 3$. Let us define $\tilde{\omega} = E_o\omega$, and $\tilde{v} = (v \cdot n_o)n_o$. Since l_i lies in $\mathcal{B}_o$, we have that $\omega^T l_i = \tilde{\omega}^T l_i$. Furthermore, locating the origin on B_o, we have that $[x_i\times]l_i$ is parallel to n_o, hence $\tilde{v}^T[x_i\times]l_i = v^T[x_i\times]l_i$. Therefore, we conclude that $\tilde{\omega}^T l_i + \tilde{v}^T[x_i\times]l_i = 0$. This implies that the vector $\tilde{\Omega} = (s_o \cdot \omega, t_o \cdot \omega, n_o \cdot v)$ satisfies $\tilde{\Omega}^T \mathcal{M} = 0$, and the matrix $\mathcal{M}$ is singular, as stated in (3.14). The geometric meaning of (3.14) is that the three lines l_{i0} generate zero torque about n_o, hence they are either parallel or have a common intersection point in $\mathcal{B}_o$. It can be shown that the special case $s_o \cdot \omega = t_o \cdot \omega = n_o \cdot v = 0$ occurs when the tangent planes $\mathcal{B}_1, \mathcal{B}_2, \mathcal{B}_3$ intersect at a common line that lies within the base plane $\mathcal{B}_o$. Note that this non-generic geometric relation violates the assumption of a tame stance.

Finally, it can be verified that two forces lying within the interior of their friction cone and a third nonzero force on the boundary of its friction cone can be critical only in the non-generic situation where at least one friction cone is tangent to the base plane $\mathcal{B}_o$, thus violating the assumption of a tame stance. Therefore, no other type of critical contact forces exists. $\square$

A.3 Proofs of results from Chapter 4

Proof of Lemma 4.3.1:

1. Substitution of $f_1 = f_2 = \vec{0}$ into (4.2) gives the rigid-body acceleration $a = \frac{1}{m} f_{ext}$ and $\alpha = \tau_{ext}/m\rho^2$. Substituting for (a, α) and the rigid-body relation (4.3) into the inequality constraints $n_i \cdot a_i \geq 0$ gives the region $\mathcal{R}_{SS}$ defined in the lemma.

2. Substituting the constraint $a_1 = \vec{0}$ into the acceleration formula (4.3), gives $a = J(\boldsymbol{x} - x_1)\alpha$. Let the origin of the fixed reference frame be located at x_1, such that $x_1 = 0$. Substituting for a in the force-part of (4.2) and using the constraint $f_2 = \vec{0}$, we get $f_1 = mJ\boldsymbol{x}\alpha - f_{ext}$. Substituting in the moment-part of (4.2), we get $\boldsymbol{x}^T J(mJ\boldsymbol{x}\alpha - f_{ext}) + \tau_{ext} = I_c\alpha$. The solution for α and f_1 is thus given by

$$\begin{aligned} \alpha &= \tfrac{1}{m\rho_o^2}(\boldsymbol{x}^T J^T f_{ext} + \tau_{ext}) \\ f_1 &= -f_{ext} + \tfrac{1}{\rho_o^2}\big(J\boldsymbol{x}\tau_{ext} - J\boldsymbol{x}\boldsymbol{x}^T J f_{ext}\big). \end{aligned} \tag{A.3}$$

The inequality constraints $f_1^l, f_1^r \geq 0$ are equivalent to the inequalities $f_1 \cdot JC_1^r \geq 0$ and $f_1 \cdot JC_1^l \leq 0$. Substituting the solution for f_1 in (A.3) into these inequalities gives $T_1(\boldsymbol{x}), T_2(\boldsymbol{x}) \geq 0$. Finally, consider the inequality constraint $a_2 \cdot n_2 \geq 0$. Using the acceleration formula (4.3), $a_2 = -Jx_2\alpha$. Finally, substituting for a_2 and α in the inequality $a_2 \cdot n_2 \geq 0$ gives $T_3(\boldsymbol{x}) \geq 0$.

3. Substituting the equality constraints $f_1^r = 0, f_2 = \vec{0}$ in (4.2) gives the force part $ma = f_1^l C_1^l + f_{ext}$ and the moment-part $m\rho^2\alpha = (x_1 - \boldsymbol{x})^T J C_1^l f_1^l + \tau_{ext}$. Using the acceleration formula (4.3), the constraint $n_1 \cdot a_1 = 0$ gives $n_1 \cdot (a + J(x_1 - \boldsymbol{x})\alpha) = 0$, where $a = \frac{1}{m}(f_1^l C_1^l + f_{ext})$. Here, too, we select the origin of the fixed reference frame at x_1, such that $x_1 = 0$. Using the last two equations, the solution for f_1^l and α is given by

$$\begin{aligned} f_1^l &= \tfrac{1}{W_2(\boldsymbol{x})}\big((t_1 \cdot \boldsymbol{x})\tau_{ext} - \rho^2(f_{ext} \cdot n_1)\big) \\ \alpha &= \tfrac{1}{mW_2(\boldsymbol{x})}\big((n_1 \cdot f_{ext})\boldsymbol{x}^T J^T C_1^l + (n_1 \cdot C_1^l)\tau_{ext}\big), \end{aligned} \tag{A.4}$$

where $W_2(\boldsymbol{x}) = \rho^2(n_1 \cdot C_1^l) + (t_1 \cdot \boldsymbol{x})\boldsymbol{x}^T J^T C_1^l$. Let $W_1(\boldsymbol{x})$ be the numerator of f_1^l in (A.4). Then $f_1^l = W_1(\boldsymbol{x})/W_2(\boldsymbol{x})$, and the inequality constraint $f_1^l \geq 0$ is satisfied either by $W_1(\boldsymbol{x}) \geq 0$ and $W_2(\boldsymbol{x}) \geq 0$, or by $W_1(\boldsymbol{x}) \leq 0$ and $W_2(\boldsymbol{x}) \leq 0$.

Next consider the inequality constraint $t_1 \cdot a_1 \geq 0$. Let $W_0(\boldsymbol{x})$ be the numerator of α in (A.4). Substituting for a_1 in $t_1 \cdot a_1 \geq 0$ gives the inequality $\frac{1}{mW_2(\boldsymbol{x})}\big((n_1 \cdot \boldsymbol{x})W_0(\boldsymbol{x}) + \frac{1}{m}\big(t_1 \cdot (C_1^l W_1(\boldsymbol{x}) + f_{ext}W_2(\boldsymbol{x}))\big)\big) \geq 0$. Let $W_3(\boldsymbol{x})$ be the numerator of the resulting inequality, so that $t_1 \cdot a_1 = W_3(\boldsymbol{x})/W_2(\boldsymbol{x}) \geq 0$. In the case where $W_2(\boldsymbol{x}) \geq 0$, the inequality constraint becomes $W_3(\boldsymbol{x}) \geq 0$. In the case where $W_2(\boldsymbol{x}) \leq 0$, the inequality constraint becomes $W_3(\boldsymbol{x}) \leq 0$. Last consider the inequality constraint $n_2 \cdot a_2 \geq 0$. Using (4.3), $a_2 = a + J(\boldsymbol{x} - x_2)\alpha$. Substituting for a_2 in $n_2 \cdot a_2 \geq 0$ gives the inequality $\frac{1}{mW_2(\boldsymbol{x})}\big(t_2 \cdot (\boldsymbol{x} - x_2)W_0(\boldsymbol{x}) + \frac{1}{m}((n_2 \cdot C_1^l)W_1(\boldsymbol{x}) + (n_2 \cdot f_{ext})W_2(\boldsymbol{x}))\big) \geq 0$. Let $W_4(\boldsymbol{x})$ be the numerator of the inequality, so that $n_2 \cdot a_2 = W_4(\boldsymbol{x})/mW_2(\boldsymbol{x}) \geq 0$. In the case where $W_2(\boldsymbol{x}) \geq 0$, the inequality constraint becomes $W_4(\boldsymbol{x}) \geq 0$. In the case where $W_2(\boldsymbol{x}) \leq 0$, the inequality constraint becomes $W_4(\boldsymbol{x}) \leq 0$. Thus $\mathcal{R}_{RS} = \mathcal{R}_{RS}^1 \cup \mathcal{R}_{RS}^2$ such that $W_1(\boldsymbol{x}), W_2(\boldsymbol{x}), W_3(\boldsymbol{x}), W_4(\boldsymbol{x}) \geq 0$ for $\mathcal{R}_{RS}^1$, and $W_1(\boldsymbol{x}), W_2(\boldsymbol{x}), W_3(\boldsymbol{x}), W_4(\boldsymbol{x}) \leq 0$ for $\mathcal{R}_{RS}^2$.

4. In general terrain geometry, the contact normals are not parallel, and hence, in order to satisfy the simultaneous sliding along $+t_i$ at x_i, the body's instantaneous center of acceleration must lie at p_{nn} - the intersection point of the two contact normals. The accelerations at the contact points are given by $a_i = J(x_i - p_{nn})\alpha$ and the center-of-mass acceleration is given by $a = J(\boldsymbol{x} - p_{nn})\alpha$. Recall the definition of the point p_{ll} as the intersection of the left edges of the friction cones C_i^l. Let us define d_i as the signed distances of p_{ll} from x_i, such that $p_{ll} = x_i + d_i C_i^l$ for $i = 1, 2$. Let us chose a frame whose origin is located at p_{ll}, such that that $x_i = -d_i C_i^l$. The terms $x_i^T J C_i^l = -d_i (C_i^l)^T J C_i^l$ vanish, since J is skew-symmetric. The physical meaning is that contact forces along C_i^l generate zero torque about p_{ll}. Using the constraints $f_1^r = f_2^r = 0$, the equations of motion (4.2) reduce to

$$\begin{aligned} C_1^l f_1^l + C_2^l f_2^l + f_{ext} &= mJ(\boldsymbol{x} - p_{nn})\alpha \\ \boldsymbol{x}^T J(C_1^l f_1^l + C_2^l f_2^l) + \tau_{ext} &= m\rho^2\alpha \end{aligned} \tag{A.5}$$

Pre-multiplying the force equation by $\boldsymbol{x}^T J^T$ and adding to the torque equation, the solution for α is given by

$$\alpha = (\boldsymbol{x}^T J^T f_{ext} + \tau_{ext})/m(\boldsymbol{x}^T(\boldsymbol{x} - p_{nn}) + \rho^2) = Q_0(\boldsymbol{x})/mQ_3(\boldsymbol{x}). \tag{A.6}$$

The inequality constraints of acceleration are thus given by

$$a_i \cdot t_i = t_i^T J(x_i - p_{nn})\alpha = n_i \cdot (p_{nn} - x_i)\alpha > 0 \ \ , \ i = 1, 2. \tag{A.7}$$

Substituting the solution (A.6) for α, the inequalities (A.7) become $Q_1(\boldsymbol{x})/Q_3(\boldsymbol{x}) \geq 0$ and $Q_2(\boldsymbol{x})/Q_3(\boldsymbol{x}) \geq 0$. These inequalities are satisfied either by $Q_1(\boldsymbol{x}), Q_2(\boldsymbol{x}), Q_3(\boldsymbol{x}) \geq 0$ or by $Q_1(\boldsymbol{x}), Q_2(\boldsymbol{x}), Q_3(\boldsymbol{x}) \geq 0$.

Finally, multiplying the force part of (A.5) by JC_i^l for $i = 1, 2$, the solutions of f_1^l and f_2^l are given by

$$f_1^l = (mC_2^l \cdot (\boldsymbol{x} - p_{nn})\alpha + C_2^l \cdot Jf_{ext})/(C_2^l \cdot J^T C_1^l) = Q_4(\boldsymbol{x})/Q_3(\boldsymbol{x})$$

$$f_2^l = (mC_1^l \cdot (\boldsymbol{x} - p_{nn})\alpha + C_1^l \cdot Jf_{ext})/(C_1^l \cdot J^T C_2^l) = Q_5(\boldsymbol{x})/Q_3(\boldsymbol{x})$$

The force inequalities $f_1^l, f_2^l \geq 0$ are thus satisfied either by $Q_3(\boldsymbol{x}), Q_4(\boldsymbol{x}), Q_5(\boldsymbol{x}) \geq 0$ or by $Q_3(\boldsymbol{x}), Q_4(\boldsymbol{x}), Q_5(\boldsymbol{x}) \geq 0$.

Thus $\mathcal{R}_{RR} = \mathcal{R}_{RR}^1 \cup \mathcal{R}_{RR}^2$ such that $Q_1(\boldsymbol{x}), Q_2(\boldsymbol{x}), Q_3(\boldsymbol{x}), Q_4(\boldsymbol{x}), Q_5(\boldsymbol{x}) \geq 0$ for $\mathcal{R}_{RR}^1$, and $Q_1(\boldsymbol{x}), Q_2(\boldsymbol{x}), Q_3(\boldsymbol{x}), Q_4(\boldsymbol{x}), Q_5(\boldsymbol{x}) \leq 0$ for $\mathcal{R}_{RR}^2$.

Appendix B

Algorithm for Computing $\mathcal{R}$ for planar multiple-contact stances

We describe an algorithm for computing the feasible equilibrium strip of a k-contact stance such that $\mathcal{B}$ is subjected to the nominal gravitational wrench $\boldsymbol{w}_0 = (f_g, 0)$ (the algorithm is basically unchanged for a general external wrench). Let e denote the vertical upward direction in the two-dimensional environment, and let (s, t) denote the horizontal and vertical coordinates of the fixed world frame. For simplicity of the algorithm, we make a reasonable assumption that the friction cones are *upward pointing*, in the sense that $f_i \cdot e \geq 0$ for all $f_i \in \mathcal{C}_i$ and $i = 1 \ldots k$. The algorithm uses two lists $\mathcal{L}_1$ and $\mathcal{L}_2$ for the $2k$ directed lines aligned with the friction cones' edges. The lines pointing to the *left* of e are stored in $\mathcal{L}_1$, and the lines pointing to the *right* of e are stored in $\mathcal{L}_2$. It is worth noting that the two edges of a particular friction cone can be both left-pointing or right-pointing e.g., the edges of $\mathcal{C}_2$ in Figure B(a). The jth line has the form: $l_j = \{(s, t) : t = a_j s + b_j\}$, where (a_j, b_j) are the line's slope and t-axis intercept. Let $\mathcal{S}$ be the set of intersection points of lines in $\mathcal{L}_1$ with the

lines in $\mathcal{L}_2$. A key observation is that the edges of $\mathcal{R}(\boldsymbol{w}_0)$ are vertical lines that pass through the leftmost and rightmost points of $\mathcal{S}$. Hence the computation of $\mathcal{R}(\boldsymbol{w}_0)$ reduces to the computation of the leftmost and rightmost points of $\mathcal{S}$. We describe the portion of the algorithm which computes the rightmost point of $\mathcal{S}$.

The following discussion refers to the pseudo-code given below. In step 1.1 the algorithm computes a vertical line $l'(0)$ which lies on the right side of $\mathcal{S}$. The computation of this line is based on a trigonometric formula involving the slope and intercept of the lines in $\mathcal{L}_1$ and $\mathcal{L}_2$ [78]. The resulting line $l'(0)$ satisfies the following *separation condition.* Let p_1 denote the highest intersection point of the lines of $\mathcal{L}_1$ with $l'(0)$, and let p_2 denote the lowest intersection point of the lines of $\mathcal{L}_2$ with $l'(0)$. Then $l'(0)$ satisfies the condition that p_2 lies *above* p_1, a condition which implies that $l'(0)$ lies to the right of $\mathcal{S}$ (Figure B(a)). In step 1.2 the algorithm computes an initial vertical sweep line $l(0)$ which passes through a point of $\mathcal{S}$. While any point of $\mathcal{S}$ can be selected, the algorithm selects the intersection point of the highest right-pointing line with the lowest left-pointing line along $l'(0)$ as a good initial guess (Figure B(a)). Note that $l(0)$ typically does not satisfy the separation condition.

The ith iteration of the algorithm consists of three steps. In step 2.1 the algorithm sets a vertical line at the middle of the strip bounded by $l(i)$ and $l'(i)$. In step 2.2 the algorithm checks the separation condition along the middle line. If it is satisfied, the middle line lies to the right of $\mathcal{S}$ and $l'(i+1)$ moves to the middle line. In this case $l(i+1)$ moves to a new point of $\mathcal{S}$ which lies on the right side of $l(i)$. If the separation condition does not hold on the middle line, $l(i+1)$ moves to a point of $\mathcal{S}$ on the right side of the middle line while $l'(i+1) = l'(i)$. In step 2.3 the algorithm prunes the lists $\mathcal{L}_1$ and $\mathcal{L}_2$ according to their intersection pattern with the new sweep line. Any line in $\mathcal{L}_1$ whose intersection with $l(i+1)$ lies at or above p_2 does not contribute points

to $\mathcal{S}$ on the right side of $l(i+1)$. Hence this line is removed from $\mathcal{L}_1$. Similarly, any line in $\mathcal{L}_2$ whose intersection with $l(i+1)$ lies at or below p_1 is removed from $\mathcal{L}_2$. The algorithm terminates when $\mathcal{L}_1$ and $\mathcal{L}_2$ both become empty. This event occurs precisely when $l(i+1)$ passes through the rightmost point of $\mathcal{S}$. A pseudo-code of the algorithm follows.

Line Sweep Algorithm for Computing $\mathcal{R}(w_0)$

Data structures: Lists $\mathcal{L}_1$ and $\mathcal{L}_2$ containing indices of left and right pointing lines.

1. Initialization

1.1 Compute initial vertical line $l'(0)$ on the right side of $\mathcal{S}$:

Set $a^1_{min} = \min_{j\in\mathcal{L}_1} a_j$ and $a^1_{max} = \max_{j\in\mathcal{L}_1} a_j$.

Set $a^2_{min} = \min_{j\in\mathcal{L}_2} a_j$ and $a^2_{max} = \max_{j\in\mathcal{L}_2} a_j$.

Set $b^1_{max} = \max_{j\in\mathcal{L}_1} b_j$ and $b^2_{min} = \min_{j\in\mathcal{L}_2} b_j$.

Set $l'(0)$ at $s'(0) = \max\{\frac{b^1_{max}-b^2_{min}}{a^2_{min}-a^1_{max}}, \frac{b^1_{max}-b^2_{min}}{a^2_{max}-a^1_{min}}\}$.

1.2 Compute initial sweep line $l(0)$:

Set $j'_0 = \arg\max_{j\in\mathcal{L}_1}\{a_j s'(0) + b_j\}$ and $j_0 = \arg\min_{j\in\mathcal{L}_2}\{a_j s'(0) + b_j\}$.

Set $l(0)$ at $s(0) = \frac{b_{j'_0}-b_{j_0}}{a_{j_0}-a_{j'_0}}$.

1.3 Set $i = 0$.

2. Repeat:

2.1 Set middle line at $s_m = (s(0) + s'(0)/2$.

2.2 Check separation condition along middle line:

Set $t^1_{max} = \max_{j\in\mathcal{L}_1}\{a_j s_m + b_j\}$ and $t^2_{min} = \min_{j\in\mathcal{L}_2}\{a_j s_m + b_j\}$.

If $t^2_{min} \le t^1_{max}$ set $l(i+1)$ at $s(i+1) = s_m$. Goto step 2.3.

Otherwise set $l'(i+1)$ at s_m and $s(i+1) = s(i)$ (middle line lies on right side of $\mathcal{S}$).

2.3 Prune redundant lines from $\mathcal{L}_1$ and $\mathcal{L}_2$:

Set $t^1_{max} = \max_{j \in \mathcal{L}_1} a_j s(i{+}1) + b_j$ and $t^2_{min} = \min_{j \in \mathcal{L}_2} a_j s(i{+}1) + b_j$.

Remove from $\mathcal{L}_1$ any j such that $a_j s(i{+}1) + b_j \leq t^2_{min}$.

Remove from $\mathcal{L}_2$ any j such that $a_j s(i{+}1) + b_j \geq t^1_{max}$.

2.4 If $\mathcal{L}_1$ and $\mathcal{L}_2$ become empty, return $l(i{+}1)$ and STOP.

2.5 Move sweep line to a new point of S:

Set $j_0 = \arg\min_{j \in \mathcal{L}_2} \{a_j s(i{+}1) + b_j\}$.

Set $l(i{+}1)$ at $s(i{+}1) = \max_{j \in \mathcal{L}_1} \frac{b_j - b_{j_0}}{a_{j_0} - a_j}$.

2.6 Increment i.

End of repeat loop

The correctness and runtime of the algorithm is summarized in the following lemma. In the lemma, Δ is basically the maximal horizontal distance between the points of $\mathcal{S}$, while δ is bounded from below by the horizontal distance between the two rightmost points of $\mathcal{S}$ [78].

Lemma B.0.1 ([78]) *Let $\mathcal{B}$ be supported by k upward pointing frictional contacts and be subjected to the gravitational wrench $\boldsymbol{w}_0 = (f_g, 0)$. Then the sweep line algorithm computes the right edge of $\mathcal{R}(\boldsymbol{w}_0)$ in $O(k \cdot \min\{k, \log(\Delta/\delta)\})$ steps, where Δ is the initial search width and δ is the minimal search width.*

In worst case the algorithm runs in $O(k^2)$ steps, which is the same as a naive computation of all points in $\mathcal{S}$. However, the algorithm repeatedly prunes lines from $\mathcal{L}_1$ and $\mathcal{L}_2$ and is therefore more efficient than the naive computation. Moreover, in practical settings $\log(\Delta/\delta)$ is a small constant. For instance, let l_0 be the horizontal distance between x_1 and x_6 in the 6-contact stance of Figure B(b). Then $\Delta = 0.86 l_0$,

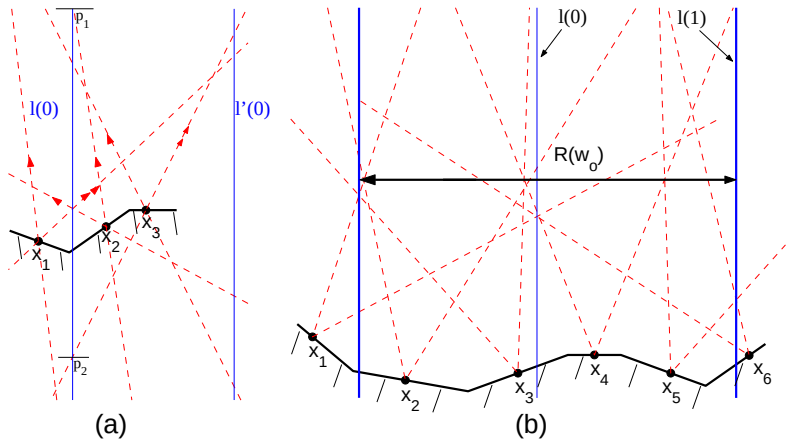

Figure B.1: (a) Illustration of the separation condition (right pointing lines are double arrowed). (b) Execution of the algorithm on a 6-contact stance.

$\delta = 0.06 l_0$, and consequently $\log(\Delta/\delta) = 3.85$. Thus $\min\{k, \log(\Delta/\delta)\} = \log(\Delta/\delta)$ in practice, and the time complexity of the algorithm is practically linear in k.

Execution Example: Consider the 6-contact stance shown in Figure B(b), with a coefficient of friction $\mu = 0.4$. An execution of the algorithm on this example yields the initial sweep line $l(0)$. After the first iteration the sweep line moves to $l(1)$. At this stage the lists $\mathcal{L}_1$ and $\mathcal{L}_2$ become empty and the algorithm terminates with $l(1)$ as the right edge of $\mathcal{R}(\boldsymbol{w}_0)$. Note that a naive computation would require inspection of $6^2 = 36$ intersection points.

Appendix C

Computation of Type-3 Boundary Curves

We now provide a numerical procedure for computing type-3 bounady curves. The condition for type-3 critical equilibrium forces is formulated as a single implicit polynomial, which can be solved numerically. The directions $(\phi_1, \phi_2\phi_3)$ of type-3 critical equilibrium forces form a one-dimensional manifold, which is the solution set of the two scalar equations given in (3.14). Recall that (s_o, t_o, n_o) is a right-handed frame such that n_o is normal to the base plane $\mathcal{B}_o$. Let us define another right-handed frame $(\hat{x}, \hat{y}, \hat{z})$, such that $\hat{z}$ is the upward vertical direction. Let us define the variables $\beta_i = \tan(\phi_i/2)$, which transform trigonometric expressions into algebraic expressions via the identities $sin(\phi_i) = \frac{2\beta_i}{1+\beta_i^2}$, $cos(\phi_i) = \frac{2\beta_i}{1+\beta_i^2}$. Substituting into (3.14) and multiplying by the numerators $1 + \beta_i^2$ gives

$$\det \begin{bmatrix} v_1(\beta_1) & v_2(\beta_2) & v_3(\beta_3) \end{bmatrix} = 0 \ , \ \det \begin{bmatrix} w_1(\beta_1) & w_2(\beta_2) & w_3(\beta_3) \end{bmatrix} = 0, \quad \text{(C.1)}$$

where

$$v_i(\beta_i) = \begin{pmatrix} v_{xi} \\ v_{yi} \\ v_{zi} \end{pmatrix} = \begin{pmatrix} a_{xi}\beta_i^2 + b_{xi}\beta_i + c_{xi} \\ a_{yi}\beta_i^2 + b_{yi}\beta_i + c_{yi} \\ a_{zi}\beta_i^2 + b_{zi}\beta_i + c_{zi} \end{pmatrix} \quad w_i(\beta_i) = \begin{pmatrix} w_{si} \\ w_{ti} \\ w_{ni} \end{pmatrix} = \begin{pmatrix} d_{si}\beta_i^2 + e_{si}\beta_i + f_{si} \\ d_{ti}\beta_i^2 + e_{ti}\beta_i + f_{ti} \\ d_{ni}\beta_i^2 + e_{ni}\beta_i + f_{ni} \end{pmatrix},$$

$$a_{xi} = \hat{x} \cdot (n_i - \mu s_i)\ ,\ b_{xi} = 2\mu\hat{x} \cdot t_i\ ,\ c_{xi} = \hat{x} \cdot (n_i + \mu s_i)\ ,$$

$$a_{yi} = \hat{y} \cdot (n_i - \mu s_i)\ ,\ b_{yi} = 2\mu\hat{y} \cdot t_i\ ,\ c_{yi} = \hat{y} \cdot (n_i + \mu s_i)\ ,$$

$$a_{zi} = \hat{z} \cdot x_i \times (n_i - \mu s_i)\ ,\ b_{zi} = 2\mu\hat{z} \cdot x_i \times t_i\ ,\ c_{zi} = \hat{z} \cdot x_i \times (n_i + \mu s_i)\ ,$$

$$d_{si} = s_o^T R_{90} M_i (n_i - \mu s_i)\ ,\ e_{si} = 2\mu s_o^T R_{90} M_i t_i\ ,\ f_{si} = s_o^T R_{90} M_i (n_i + \mu s_i)\ ,$$

$$d_{ti} = t_o^T R_{90} M_i (n_i - \mu s_i)\ ,\ e_{ti} = 2\mu t_o^T R_{90} M_i t_i\ ,\ f_{ti} = t_o^T R_{90} M_i (n_i + \mu s_i)\ ,$$

$$d_{si} = n_o^T R_{90} M_i [s_i\times](n_i - \mu s_i)\ ,\ e_{si} = 2\mu n_o^T R_{90} M_i [s_i\times] t_i\ ,\ f_{si} = n_o^T R_{90} M_i [s_i\times](n_i + \mu s_i)\ ,$$

$$R_{90} = I + [n_o\times]\ ,\ \text{and}\ M_i = I - (1+\mu^2) n_i n_i^T\ ,\ \text{for}\ i = 1, 2, 3.$$

Our goal is now to eliminate β_1 from the two equations (C.1) and get a single polynomial in β_2 and β_3. For any particular choice of β_3, this polynomial can be numerically solved for all real roots of β_2, and then β_1 can be found by solving an additional quadratic equations. For convenience, let us locate the origin at x_1, which implies that $v_{z1} = w_{s1} = 0$. Assuming that a particular value for β_3 is chosen, the terms $v_{x3}, v_{y3}, v_{z3}, w_{s3}, v_{t3}, v_{n3}$ are known scalars. The two equations in (C.1) can now be rewritten as

$$\begin{aligned} &h_2\beta_1^2 + h_1\beta_1 + h_0 = 0\ ,\ q_2\beta_1^2 + q_1\beta + q_0 = 0, \\ &\text{where } h_i = h_{i2}\beta_2^2 + h_{i1}\beta_2 + h_{i0}\ ,\ q_i = q_{i2}\beta_2^2 + q_{i1}\beta_2 + q_{i0}\ ,\ \text{for } i = 0, 1, 2 \\ &\text{and the coefficients } h_{ij} \text{ and } q_{ij} \text{ for } i, j \in \{0, 1, 2\} \text{ are listed in Table C.} \end{aligned} \tag{C.2}$$

Using dialytic elimination methods [95], β_1 can be eliminated from the two equations in (C.1) by computing its resultant, given by

$$\Delta = (h_2 q_0 - q_2 h_0)^2 + (h_2 q_1 - h_1 q_2)(h_0 q_1 - q_0 h_1).$$

$h_{00} = c_{y1}v_{x3}c_{z2} + c_{x1}v_{z3}c_{y2} - c_{y1}v_{z3}c_{x2} - c_{x1}v_{y3}c_{z2}$	$h_{01} = c_{x1}v_{z3}b_{y2} - c_{x1}v_{y3}b_{z2} - c_{y1}v_{z3}b_{x2} + c_{y1}v_{x3}b_{z2}$
$h_{02} = c_{x1}v_{z3}a_{y2} - c_{x1}v_{y3}a_{z2} - c_{y1}v_{z3}a_{x2} + c_{y1}v_{x3}a_{z2}$	$h_{10} = b_{x1}v_{z3}c_{y2} - b_{x1}v_{y3}c_{z2} - b_{y1}v_{z3}c_{x2} + b_{y1}v_{x3}c_{z2}$
$h_{11} = b_{x1}v_{z3}b_{y2} - b_{x1}v_{y3}b_{z2} - b_{y1}v_{z3}b_{x2} + b_{y1}v_{x3}b_{z2}$	$h_{12} = b_{x1}v_{z3}a_{y2} - b_{x1}v_{y3}a_{z2} - b_{y1}v_{z3}a_{x2} + b_{y1}v_{x3}a_{z2}$
$h_{20} = a_{x1}v_{z3}c_{y2} - a_{x1}v_{y3}c_{z2} - a_{y1}v_{z3}c_{x2} + a_{y1}v_{x3}c_{z2}$	$h_{21} = a_{x1}v_{z3}b_{y2} - a_{x1}v_{y3}b_{z2} - a_{y1}v_{z3}b_{x2} + a_{y1}v_{x3}b_{z2}$
$h_{22} = a_{x1}v_{z3}a_{y2} - a_{x1}v_{y3}a_{z2} - a_{y1}v_{z3}a_{x2} + a_{y1}v_{x3}a_{z2}$	$q_{00} = -f_{t1}w_{n3}f_{s2} + f_{t1}w_{s3}f_{n2} + f_{s1}w_{n3}f_{t2} - f_{s1}w_{t3}f_{n2}$
$q_{01} = f_{s1}w_{n3}e_{t2} - f_{s1}w_{t3}e_{n2} - f_{t1}w_{n3}e_{s2} + f_{t1}w_{s3}e_{n2}$	$q_{02} = f_{s1}w_{n3}d_{t2} - f_{s1}w_{t3}d_{n2} - f_{t1}w_{n3}d_{s2} + f_{t1}w_{s3}d_{n2}$
$q_{10} = e_{s1}w_{n3}f_{t2} - e_{s1}w_{t3}f_{n2} - e_{t1}w_{n3}f_{s2} + e_{t1}w_{s3}f_{n2}$	$q_{11} = e_{s1}w_{n3}e_{t2} - e_{s1}w_{t3}e_{n2} - e_{t1}w_{n3}e_{s2} + e_{t1}w_{s3}e_{n2}$
$q_{12} = e_{s1}w_{n3}d_{t2} - e_{s1}w_{t3}d_{n2} - e_{t1}w_{n3}d_{s2} + e_{t1}w_{s3}d_{n2}$	$q_{20} = d_{s1}w_{n3}f_{t2} - d_{s1}w_{t3}f_{n2} - d_{t1}w_{n3}f_{s2} + d_{t1}w_{s3}f_{n2}$
$q_{21} = d_{s1}w_{n3}e_{t2} - d_{s1}w_{t3}e_{n2} - d_{t1}w_{n3}e_{s2} + d_{t1}w_{s3}e_{n2}$	$q_{22} = d_{s1}w_{n3}d_{t2} - d_{s1}w_{t3}d_{n2} - d_{t1}w_{n3}d_{s2} + d_{t1}w_{s3}d_{n2}$

Table C.1: The coefficients h_{ij} and q_{ij} in Eq. (C.1)

$$p_0 = (h_{20}q_{00} - q_{20}h_{00})^2 + (h_{20}q_{10} - h_{10}q_{20})(h_{00}q_{10} - q_{00}h_{10})$$

$$p_1 = 2(h_{20}q_{00} - q_{20}h_{00})(-q_{20}h_{01} - q_{21}h_{00} + h_{20}q_{01} + h_{21}q_{00}) + (h_{20}q_{10} - h_{10}q_{20})(-q_{00}h_{11} - q_{01}h_{10} + h_{00}q_{11} + h_{01}q_{10}) + (-h_{10}q_{21} - h_{11}q_{20} + h_{20}q_{11} + h_{21}q_{10})(h_{00}q_{10} - q_{00}h_{10})$$

$$p_2 = 2(h_{20}q_{00} - q_{20}h_{00})(-q_{20}h_{02} - q_{21}h_{01} - q_{22}h_{00} + h_{20}q_{02} + h_{21}q_{01} + h_{22}q_{00}) + (-q_{20}h_{01} - q_{21}h_{00} + h_{20}q_{01} + h_{21}q_{00})^2 + (h_{20}q_{10} - h_{10}q_{20})(-q_{00}h_{12} - q_{01}h_{11} - q_{02}h_{10} + h_{00}q_{12} + h_{01}q_{11} + h_{02}q_{10}) + (-h_{10}q_{21} - h_{11}q_{20} + h_{20}q_{11} + h_{21}q_{10})\cdot (-q_{00}h_{11} - q_{01}h_{10} + h_{00}q_{11} + h_{01}q_{10}) + (-h_{10}q_{22} - h_{11}q_{21} - h_{12}q_{20} + h_{20}q_{12} + h_{21}q_{11} + h_{22}q_{10})(h_{00}q_{10} - q_{00}h_{10})$$

$$p_3 = 2(h_{20}q_{00} - q_{20}h_{00})(-q_{21}h_{02} - q_{22}h_{01} + h_{21}q_{02} + h_{22}q_{01}) + 2(-q_{20}h_{01} - q_{21}h_{00} + h_{20}q_{01} + h_{21}q_{00})\cdot (-q_{20}h_{02} - q_{21}h_{01} - q_{22}h_{00} + h_{20}q_{02} + h_{21}q_{01} + h_{22}q_{00}) + (h_{20}q_{10} - h_{10}q_{20})(-q_{01}h_{12} - q_{02}h_{11} + h_{01}q_{12} + h_{02}q_{11}) + (-h_{10}q_{21} - h_{11}q_{20} + h_{20}q_{11} + h_{21}q_{10})(-q_{00}h_{12} - q_{01}h_{11} - q_{02}h_{10} + h_{00}q_{12} + h_{01}q_{11} + h_{02}q_{10}) + (-h_{10}q_{22} - h_{11}q_{21} - h_{12}q_{20} + h_{20}q_{12} + h_{21}q_{11} + h_{22}q_{10})(-q_{00}h_{11} - q_{01}h_{10} + h_{00}q_{11} + h_{01}q_{10}) + (-h_{11}q_{22} - h_{12}q_{21} + h_{21}q_{12} + h_{22}q_{11})(h_{00}q_{10} - q_{00}h_{10})$$

$$p_4 = 2(h_{20}q_{00} - q_{20}h_{00})(h_{22}q_{02} - q_{22}h_{02}) + 2(-q_{20}h_{01} - q_{21}h_{00} + h_{20}q_{01} + h_{21}q_{00})(-q_{21}h_{02} - q_{22}h_{01} + h_{21}q_{02} + h_{22}q_{01}) + (-q_{20}h_{02} - q_{21}h_{01} - q_{22}h_{00} + h_{20}q_{02} + h_{21}q_{01} + h_{22}q_{00})^2 + (h_{20}q_{10} - h_{10}q_{20})(h_{02}q_{12} - q_{02}h_{12}) + (-h_{10}q_{21} - h_{11}q_{20} + h_{20}q_{11} + h_{21}q_{10})\cdot (-q_{01}h_{12} - q_{02}h_{11} + h_{01}q_{12} + h_{02}q_{11}) + (h_{22}q_{12} - h_{12}q_{22})(h_{00}q_{10} - q_{00}h_{10}) + (-h_{10}q_{22} - h_{11}q_{21} - h_{12}q_{20} + h_{20}q_{12} + h_{21}q_{11} + h_{22}q_{10})\cdot (-q_{00}h_{12} - q_{01}h_{11} - q_{02}h_{10} + h_{00}q_{12} + h_{01}q_{11} + h_{02}q_{10}) + (-h_{11}q_{22} - h_{12}q_{21} + h_{21}q_{12} + h_{22}q_{11})(-q_{00}h_{11} - q_{01}h_{10} + h_{00}q_{11} + h_{01}q_{10})$$

$$p_5 = 2(-q_{20}h_{01} - q_{21}h_{00} + h_{20}q_{01} + h_{21}q_{00})(h_{22}q_{02} - q_{22}h_{02}) + 2(-q_{20}h_{02} - q_{21}h_{01} - q_{22}h_{00} + h_{20}q_{02} + h_{21}q_{01} + h_{22}q_{00})\cdot (-q_{21}h_{02} - q_{22}h_{01} + h_{21}q_{02} + h_{22}q_{01}) + (-h_{10}q_{21} - h_{11}q_{20} + h_{20}q_{11} + h_{21}q_{10})(h_{02}q_{12} - q_{02}h_{12}) + (-h_{10}q_{22} - h_{11}q_{21} - h_{12}q_{20} + h_{20}q_{12} + h_{21}q_{11} + h_{22}q_{10})(-q_{01}h_{12} - q_{02}h_{11} + h_{01}q_{12} + h_{02}q_{11}) + (-h_{11}q_{22} - h_{12}q_{21} + h_{21}q_{12} + h_{22}q_{11})\cdot (-q_{00}h_{12} - q_{01}h_{11} - q_{02}h_{10} + h_{00}q_{12} + h_{01}q_{11} + h_{02}q_{10}) + (h_{22}q_{12} - h_{12}q_{22})(-q_{00}h_{11} - q_{01}h_{10} + h_{00}q_{11} + h_{01}q_{10})$$

$$p_6 = 2(-q_{20}h_{02} - q_{21}h_{01} - q_{22}h_{00} + h_{20}q_{02} + h_{21}q_{01} + h_{22}q_{00})(h_{22}q_{02} - q_{22}h_{02}) + (-q_{21}h_{02} - q_{22}h_{01} + h_{21}q_{02} + h_{22}q_{01})^2 + ((-h_{10}q_{22} - h_{11}q_{21} - h_{12}q_{20} + h_{20}q_{12} + h_{21}q_{11} + h_{22}q_{10})(h_{02}q_{12} - q_{02}h_{12}) + (-h_{11}q_{22} - h_{12}q_{21} + h_{21}q_{12} + h_{22}q_{11})\cdot (-q_{01}h_{12} - q_{02}h_{11} + h_{01}q_{12} + h_{02}q_{11}) + (h_{22}q_{12} - h_{12}q_{22})(-q_{00}h_{12} - q_{01}h_{11} - q_{02}h_{10} + h_{00}q_{12} + h_{01}q_{11} + h_{02}q_{10})$$

$$p_7 = 2(-q_{21}h_{02} - q_{22}h_{01} + h_{21}q_{02} + h_{22}q_{01})(h_{22}q_{02} - q_{22}h_{02}) + (-h_{11}q_{22} - h_{12}q_{21} + h_{21}q_{12} + h_{22}q_{11})(h_{02}q_{12} - q_{02}h_{12}) + (h_{22}q_{12} - h_{12}q_{22})(-q_{01}h_{12} - q_{02}h_{11} + h_{01}q_{12} + h_{02}q_{11})$$

$$p_8 = (h_{22}q_{02} - q_{22}h_{02})^2 + (h_{22}q_{12} - h_{12}q_{22})(h_{02}q_{12} - q_{02}h_{12})$$

Table C.2: The coefficients p_i in Eq. (C.3)

This results in an eight-degree polynomial in β_2

$$\Delta = p_8\beta_2^8 + p_7\beta_2^7 + p_6\beta_2^6 + p_5\beta_2^5 + p_4\beta_2^4 + p_3\beta_2^3 + p_2\beta_2^2 + p_1 + \beta_2 + p_0 \,, \qquad \text{(C.3)}$$

where the coefficients p_i are given in Table C. For a given value of β_3, the real roots of this polynomial can be computed numerically. The value of the eliminated unknown β_1 can now be computed by solving one of the quadratic equations in (C.1). Note that since some of the resulting roots are artificial solutions which do not solve the original system, all real solutions must be checked, and those who do not satisfy both equations in (C.1) simultaneously should be ruled out.

References

[1] A. D. Ames, A. Abate, and S. Sastry. Sufficient conditions for the existence of Zeno behavior. In *IEEE Conference on Decision and Control and European Control Conference (CDC-ECC'05)*, Seville, Spain, December 2005.

[2] A. D. Ames, P. Tabuada, and S. Sastry. On the stability of Zeno equilibria. In *Hybrid Systems: Computation and Control*, Santa Barbara, CA, 2006.

[3] A. D. Ames, H. Zheng, R. Gregg, and S. Sastry. Is there life after Zeno? taking executions past the breaking (Zeno) point. In *American Control Conference(ACC'06),*, Minneapolis, MN, 2006.

[4] M. Anitescu and F. A. Potra. Formulating dynamic multi-rigid-body contact problems with friction as solvable linear complementarity problems. *Nonlinear Dynamics*, 14:231–247, 1997.

[5] C. L. Bajaj and M-S. Kim. Convex hulls of objects bounded by algebraic curves. *Algorithmica*, 6(4):533–553, 1991.

[6] D. J. Balkcom, E. J. Gottlieb, and J. C. Trinkle. A sensorless insertion strategy for rigid planar parts. In *IEEE Int. Conf. on Robotics and Automation*, pages 882–887, 2002.

[7] D. J. Balkcom and J. C. Trinkle. Computing wrench cones for planar rigid body contact tasks. *Int. J. of Robotics Research*, 21(12):1053 – 1066, 2002.

[8] D. Baraff. Issues in computing contact forces for non-penetrating rigid bodies. *Algorithmica*, 10:292–352, October 1993.

[9] A. Bicchi. On the closure properties of robotic grasping. *The Int. J. of Robotics Research*, 14(4):319–334, 1995.

[10] A. Bicchi. Hands for dexterous manipulation and robust grasping: A difficult road toward simplicity. *IEEE Trans. on Robotics and Automation*, 16(6):652–662, 2000.

[11] J.-D. Boissonnat, O. Devillers, L. Donati, and F. P. Preparata. Motion planning for spider robots. In *IEEE Int. Conf. on Robotics and Automation*, pages 2321–2326, 1992.

[12] R.M. Brach. *Mechanical Impact Dynamics*. John Wiley, New York, 1991.

[13] T. Bretl. Motion planning of multi-limbed robots subject to equilibrium constraints: The free-climbing robot problem. *Int. Journal of Robotics Research*, 25(4):317–342, Apr 2006.

[14] T. Bretl and S. Lall. A fast and adaptive test of static equilibrium for legged robots. In *IEEE Int. Conf. on Robotics and Automation*, pages 1109 – 1116, 2006.

[15] T. Bretl, S. Rock, and J.C. Latombe. Motion planning for a three-limbed climbing robot in vertical natural terrain. In *IEEE Int. Conf. on Robotics and Automation*, pages 2946– 2953, 2003.

[16] B. Brogliato. *Nonsmooth Mechanics: Models, Dynamics and Control.* Springer-Verlag, London, 1999.

[17] N. Brook, M. Shoham, and J. Dayan. Grasping and walking finger manipulation of objects using a four-fingered hand. *Ann. CIRP*, 42(1):5–8, 1993.

[18] R. C. Brost. *Analysis and Planning of Planar Manipulation Tasks.* PhD thesis, CMU, 1991.

[19] J. F. Canny. *The complexity of robot motion planning.* MIT Press, Cambridge, MA, 1988.

[20] A. Chatterjee. *Rigid Body Collisions: Some General Considerations, New Collision Laws, and Some Experimental Data.* PhD thesis, Cornell Univ., 1997.

[21] A. Chatterjee and A. Ruina. A new algebraic rigid body collision law based on impulse space considerations. *Journal of Applied Mechanics*, 65(4):939–951, 1998.

[22] A. Dandurand. The rigidity of compound spatial grid. *Structural Topology*, 10:41–56, 1984.

[23] P. E. Dupont. The effect of Coulomb friction on the existence and uniqueness of the forward dynamics problem. In *IEEE Int. Conf. on Robotics and Automation*, pages 1442–1447, 1992.

[24] P. E. Dupont and S. P. Yamajako. Jamming and wedging in constrained rigid-body dynamics. In *IEEE Int. Conf. on Robotics and Automation*, pages 2349–2354, 1994.

[25] M. A. Erdmann. On a representation of friction in configuration space. *The Int. J. of Robotics Research*, 13(3):240–271, 1994.

[26] M. A. Erdmann. An exploration of nonprehensile two-palm manipulation. *The Int. J. of Robotics Research*, 17(5):485–503, 1998.

[27] F. Fen, M. Shoham, and R. Longman. Lyapunov stability of force-controlled grasps with a multifingered hand. *Int. J. of Robotics Research*, 15(2):137–154, 1996.

[28] F. Génot and B. Brogliato. New results on painlevé paradoxes. *European J. of Mechanics– A/Solids*.

[29] A. Ghasempoor and N. Sepehri. A measure of machine stability for moving base manipulators. In *IEEE Int. Conf. on Robotics and Automation*, pages 2249–2254, 1995.

[30] S. Goyal, J. M. Papadopoulos, and P. A. Sullivan. The dynamics of clattering I: Equation of motion and examples. *ASME J. of Dynamic Systems, Measurement, and Control*, 120:83–93, 1998.

[31] S. Goyal, J. M. Papadopoulos, and P. A. Sullivan. The dynamics of clattering II: Global results and shock protection. *ASME J. of Dynamic Systems, Measurement, and Control*, 120:94–102, 1998.

[32] W. C. Graustein. *Introduction to Higher Geometry.* Macmillan, New York, 1930.

[33] A. Greenfield, A. Rizzi, and H. Choset. Dynamic ambiguities in frictional rigid-body systems with application to climbing via bracing. In *IEEE Int. Conf. on Robotics and Automation*, pages 1959–1964, 2005.

[34] J. Guckenheimer and P. Holmes. *Nonlinear Oscillations, Dynamical Systems, and Bifurcations of Vector Fields.* Springer-Verlag, New York, 1983.

[35] K. Harada S. Kajita K. Kaneko F. Kanehiro K. Fujiwara H. Hirukawa, S. Hattori and M. Morisawa. A universal stability criterion of the foot contact of legged robots - adios ZMP. In *IEEE Int. Conf. on Robotics and Automation*, pages 1976–1983, 2006.

[36] S. Kajita K. Harada K. Kaneko F. Kanehiro K. Fujiwara M. Morisawa H. Hirukawa, S. Hattori and S. Nakaoka. A pattern generator of humanoid robots on a rough terrain. In *IEEE Int. Conf. on Robotics and Automation*, pages 2181–2187, 2007.

[37] W. M. Haddad, V. Chellaboina, and S. G. Nersesov. *Impulsive and Hybrid Dynamical Systems: Stability, Dissipativity, and Control.* Princeton Univ. Press, New Jersey, 2006.

[38] Li Han, J.c. Trinkle, and Z.X. Li. Grasp analysis as linear matrix inequality problems. *IEEE Trans. on Robotics and Automation*, 16(6):663–674, 2000.

[39] F. Hao and J.M. McCarthy. Conditions for line-based singularities in spatial platform manipulators. *J. of Robotic Systems*, 15(1), 1998.

[40] K. Harada, S. Kajita, K K. Kaneko, and H. Hirukawa. ZMP analysis for arm/leg coordination. In *IEEE/RSJ Conf. on Intelligent Robots and Systems (IROS)*, pages 75–81, 2003.

[41] M. Heymann, F. Lin, G. Meyer, and S. Resmerita. Analysis of Zeno behaviors in hybrid systems. *IEEE Trans. on Automatic Control*, 50:376–383, 2004.

[42] K. Hirai, M. Hirose, Y. Haikawa, and T. Takenaka. The development of Honda humanoid robot. In *IEEE Int. Conf. on Robotics and Automation*, pages 1321–1326, 1998.

[43] J. N. Hooker. Logical inference and polyhedral projection. In *Computer Science Logic, 5th Workshop, CSL '91, Proceedings*, pages 184–200, 1991.

[44] W. S. Howard and V. Kumar. On the stability of grasped objects. *IEEE Trans. on Robotics and Automation*, 12(6):904–917, 1996.

[45] K. H. Hunt. *Kinematic Geometry of Mechanisms*. Clarendon, Oxford, England, 1978.

[46] Y. Hurmuzlu. An energy based coefficient of restitution for planar impacts of slender bars with massive external surfaces. *ASME Journal of Applied Mechanics*, 65(4):952–961, 1998.

[47] T. Huynh, C. Lassez, and J-L. Lassez. Practical issues on the projection of polyhedral sets. *Ann. Math. Artif. Intell.*, 6(4):295–315, 1992.

[48] A. Isidori. *Nonlinear Control Systems: An Introduction*, volume 72 of *Lecture Notes in Control and Information Science*. Springer-Verlag, New York, 1985.

[49] Yan-Bin Jia. On the convex hulls of parametric plane curve. Technical report, www.cs.iastate.edu/ jia.

[50] K. L. Johnson. *Contact Mechanics*. Cambridge University Press, 1985.

[51] J. R. Kerr and B. Roth. Analysis of multi-fingered hands. *The International Journal of Robotics Research*, 4(4), Winter 1986.

[52] H. K. Khalil. *Nonlinear Systems*. Prentice Hall, 3rd edition, 2001.

[53] P. R. Kraus, V. Kumar, and P. Dupont. Analysis of frictional contact models for dynamic simulation. In *IEEE Int. Conf. on Robotics and Automation*, pages 2822–2827, 1998.

[54] D. J. Kriegman. Capture regions of curved 3D objects. In *IEEE Int. Conf. on Robotics and Automation*, pages 595–601, 1994.

[55] J. Kuffner, K. Nishiwaki, S. Kagami, M. Inaba, and H. Inoue. Motion planning for humanoid robots under obstacle and dynamic balance constraints. In *IEEE Int. Conf. on Robotics and Automation*, pages 692–698, 2001.

[56] G. F. Liu, J. Li, and Z. X. Li. Coordinated manipulation of objects by multifingered robotic hand in contact space and active joint space. In *IEEE Int. Conf. on Robotics and Automation*, pages 3743–3748, 2002.

[57] P. Lotstedt. Coulomb friction in two-dimensional rigid body systems. *Zeitschrift fur Angewandte Mathematik und Mechanik*, 61:605–615, 1981.

[58] K. M. Lynch and M. T. Mason. Stable pushing: Mechanics, controllability, and planning. *The Int. J. of Robotics Research*, 15(6):533–556, 1996.

[59] A. Madhani and S. Dubowsky. Motion planning of mobile multi-limb robotic systems subject to force and friction constraints. In *IEEE Int. Conf. on Robotics and Automation*, pages 233–239, 1992.

[60] M. P. Mann and Z. Shiller. Dynamic stability of off-road vehicles: a geometric approach. In *Proceedings of IEEE International Conference on Robotics and Automation*, pages 3705 – 3710, 2006.

[61] M. T. Mason. Two graphical methods for planar contact problems. In *IEEE/RSJ Conf. on Intelligent Robots and Systems (IROS)*, pages 443–448, 1991.

[62] M. T. Mason. *Mechanics of Robotic Manipulation*. MIT Press, Cambridge, MA, 2001.

[63] M. T. Mason and Y. Wang. On the inconsistency of rigid-body frictional planar mechanics. In *IEEE Int. Conf. on Robotics and Automation*, pages 524–528, 1988.

[64] R. Mason, J. W. Burdick, and E. Rimon. Stable poses of 3-dimensional objects. In *IEEE Int. Conf. on Robotics and Automation*, pages 391–398, 1997.

[65] R.B. McGhee and A.A. Frank. On the stability properties of quadruped creeping gaits. *Mathematical Biosciences*, 3(3–4):331–351, 1968.

[66] L. Meirovitch. *Introduction to Dynamics and Control*. John Wiley, 2001.

[67] D. Meltz, Y. Or, and E. Rimon. Experimental verification and graphical characterization of dynamic jamming in frictional rigid-body mechanics. In *Proceedings of the 2007 IEEE International Conference on Robotics and Automation*, (to appear).

[68] J.-P. Merlet. Singular configurations of parallel manipulators and Grassmann geometry. *Int. J. of Robotics Research*, 8(5), 1989.

[69] K. Mirza and D. E. Orin. General formulation for force distribution in power grasps. In *IEEE Int. Conf. on Robotics and Automation*, pages 880–887, 1994.

[70] S. Nersesov, V. Chellaboina, and W. Haddad. A generalization of Poincaré's theorem to hybrid and impulsive dynamical systems. *Int. J. Hybrid Systems*, 2:35–51, 2002.

[71] W. Neubauer. Spider-like robot that climbs vertically in ducts or pipes. In *IEEE/RSJ/GI International Conference on Intelligent Robots and Systems*, pages 2:1178–1185, 1994.

[72] V.-D. Nguyen. Constructing force-closure grasps. *The Int. J. of Robotics Research*, 7(3):3–16, 1988.

[73] V.-D. Nguyen. Constructing stable grasps. *The Int. Journal of Robotics Research*, 8(1):27–37, 1988.

[74] T. Omata and K. Tsukagoshi abd O. Mori. Whole quadruped manipulation. In *IEEE Int. Conf. on Robotics and Automation*, pages 2028–2033, 2002.

[75] T. Omata and K. Nagata. Rigid body analysis of the indeterminate grasp force in power grasps. *IEEE Trans. on Robotics and Automation*, 16(1):46–54, 2000.

[76] Y. Or and E. Rimon. Robust multiple-contact postures in a two-dimensional gravitational field. Tech. report, Dept. of Mechanical Engineering, Technion, http://robots.technion.ac.il/publications, October 2003.

[77] Y. Or and E. Rimon. Robust multiple contact postures in a two-dimensional gravitational field. In *IEEE Int. Conf. on Robotics and Automation*, pages 4783–4788, 2004.

[78] Y. Or and E. Rimon. Computation and graphic characterization of robust multiple-contact postures in gravitational environments. Tech. report, Dept. of Mechanical Engineering, Technion, http://robots.technion.ac.il/publications, 2005.

[79] Y. Or and E. Rimon. Computation of multiple-contact frictional equilibrium postures in three-dimensional gravitational environments. Tech. report, Dept. of Mechanical Engineering, Technion, http://robots.technion.ac.il/publications, September 2005.

[80] Y. Or and E. Rimon. Computation and graphical characterization of robust multiple- contact postures in two-dimensional gravitational environments. *Int. Journal of Robotics Research*, 2006.

[81] Y. Or and E. Rimon. Computing 3-legged equilibrium stances in three-dimensional gravitational environments. In *IEEE Int. Conf. on Robotics and Automation*, pages 1984 – 1989, 2006.

[82] Y. Or and E. Rimon. New results on computing frictional equilibrium stances in three-dimensional gravitational environments. Tech. report, Dept. of Mechanical Engineering, Technion, http://robots.technion.ac.il/publications, August 2006.

[83] P. Painlevé. Sur les lois du frottement de glissement. *Comptes Rendus De L'Acadamie Des Sciences*, (121):112–115, 1895.

[84] J. S. Pang and J. C. Trinkle. Stability characterizations of fixtured rigid bodies with Coulomb friction. In *IEEE Int. Conf. on Robotics and Automation*, pages 361–368, 2000.

[85] J. S. Pang and J. C. Trinkle. Stability characterizations of rigid body contact problems with Coulomb friction. *Zeitschrift fur Angewandte Mathematik und Mechanik*, 80(10):643–663, 2000.

[86] J.S. Pang and J.C. Trinkle. Complementarity formulations and existence of solutions of dynamic multi-rigid-body contact problems with Coulomb friction. *Mathematical Programming*, 74, 1996.

[87] E. Papadopoulos and D. Rey. A new measure of tipover stability margin for mobile manipulators. In *IEEE Int. Conf. on Robotics and Automation*, pages 3111–3116, 1996.

[88] F. Pfeiffer, T. Rossmann, N. Bolotnik, F. Chernousko, and G. Kostin. Simulation and optimization of regular motions of a tube-crawling robot. *Multibody System Dynamics*, 5:159–184, 2001.

[89] J. Ponce, D. Stam, and B. Faverjon. On computing force-closure grasps of curved two-dimensional objects. *The International Journal of Robotics Research*, 12(3):263–273, June 1993.

[90] J. Ponce, S. Sullivan, A. Sudsang, J.-D. Boissonnat, and J.-P. Merlet. On computing four-finger equilibrium and force-closure grasps of polyhedral objects. *The Int. Journal of Robotics Research*, 16(1):11–35, February 1997.

[91] V. T. Rajan, R. Burridge, and J. T. Schwartz. Dynamics of rigid body in frictional contact with rigid walls. In *IEEE Int. Conf. on Robotics and Automation*, pages 671–677, 1987.

[92] O. Reiner. Stability of spider-like robots in two-dimensional gravitational environments. Master's thesis, Dept. of Mechanical Engineering, Technion, Haifa, Israel, 2007 (to appear).

[93] E. Rimon, S. Shoval, and A. Shapiro. Design of a spider robot for motion with quasistatic force constraints. *Autonomous Robots*, pages 279–296, 2001.

[94] T. Roassmann and F. Pfeiffer. Control and design of a pipe crawling robot. In *13th World Congress of Automatic Control*, San Francisco, USA, 1996.

[95] G. Salmon. *Lessons Introductory to the Modern Higher Algebra.* Chelsea Publishing Co., New York, 1964.

[96] U. Saranli, M. Buehler, and D.E. Koditschek. Rhex: A simple and highly mobile hexapod robot. *Int. J. of Robotics Research*, 20(7):616 – 631, 2001.

[97] J. Savall, A. Avello, and L. Briones. Two compact robots for remote inspection of hazardous areas in nuclear power plants. In *Proceedings of IEEE International Conference on Robotics and Automation*, pages 1993–1998, 1999.

[98] T. Schlegl, M. Buss, T. Omata, and G. Schmidt. Fast dextrous regrasping with optimal contact forces and contact sensor-based impedance control. In *IEEE Int. Conf. on Robotics and Automation*, pages 103–108, 2001.

[99] A. Shapiro. *Design and Control of an Autonomous Spider-Like Robot for motion in 2D Tunnels Environments.* PhD thesis, Dept. of Mechanical Engineering, Technion, Haifa, Israel, Oct 2003.

[100] A. Shapiro and E. Rimon. PCG: a foothold selection algorithm for spider robot locomotion in 2D tunnels. In *IEEE Int. Conf. on Robotics and Automation*, pages 2966–2972, 2003.

[101] A. Shapiro, E. Rimon, and J. W. Burdick. Passive force closure and its computation in compliant-rigid grasps. In *IEEE/RSJ Conf. on Intelligent Robots and Systems (IROS)*, pages 1769–1775, 2001.

[102] J. Shen and J.S. Pang. Linear complementarity systems: Zeno states. *SIAM J. on Control and Optimization*, 44(3):1040–1066, 2005.

[103] N. Simaan and M. Shoham. Singularity analysis of a class of composite serial in-parallel robots. *IEEE Transactions on Robotics and Automation*, 7(3):301–311, OJune 2001.

[104] M. W. Spong and M. Vidyasager. *Robot Dynamics and Control*. John Wiley, New York, 1989.

[105] D. E. Stewart and J. C. Trinkle. An implicit time-stepping scheme for rigid body dynamics with inelastic collisions and Coulomb friction. *Int. J. of Numerical Methods in Engineering*, 39:2673–2691, 1996.

[106] D.E. Stewart. Rigid-body dynamics with friction and impact. *SIAM Review*, 41(1):3–39, 2000.

[107] T. J. Stone, D. S. Cook, and B. L. Luk. Robug iii - the design of an eight legged teleoperated walking and climbing robot for disordered hazardous environments. *Mechanical Incorporated Engineer*, 7(2):37–41, 1995.

[108] W. J. Stronge. *Impact Mechanics*. Cambridge University Press, Cambridge, UK, 1979.

[109] J. C. Trinkle, , A. O. Farahat, and P. F. Stiller. First-order stability cells of active multi-rigid-body systems. *IEEE Trans. on Robotics and Automation*, 11(4):545–557, 1995.

[110] J. C. Trinkle, A. O. Farahat, and P. F. Stiller. Second-order stability cells of a frictionless rigid body grasped by rigid fingers. In *IEEE Int. Conf. on Robotics and Automation*, pages 2815–2821, 1994.

[111] L.-W. Tsai and A. P. Morgan. Solving the kinematics of the most general six- and five-degree-of-freedom manipulators by continuation methods. *ASME J. Mech. Trans. Automat. Des.*, 107:189–200, 1985.

[112] A. van der Schaft and H. Schumacher. *An Introduction to Hybrid Dynamical Systems*. Lecture Notes in Control and Information Sciences 251, Springer-Verlag, 2000.

[113] M. Vukobratovic and B. Borovac. Zero moment point — thirty five years of its life. *Int. J. of Humanoid Robotics*, 1(1):157–173, 2004.

[114] M. Vukobratovic, A.A. Frank, and D. Juricic. On the stability of biped locomotion. In *IEEE Trans Biomed Eng*, volume 17, pages 25–36, 1970.

[115] M. Y. Wang. A full-kinematics model of fixtures for precision locating applications. In *IEEE/RSJ Int. Conf. on Intelligent Robots and Systems (IROS)*, pages 1135–1140, 2001.

[116] Y. Wang. Dynamic modeling and stability analysis of mechanical systems with time-varying topologies. *ASME J. of mechanical design*, 155(4):808–816, 1993.

[117] Y. Wang and M. T. Mason. Two-dimensional rigid body collisions with friction. *J. of Applied Mechanics*, 10:292–352, 1993.

[118] J. J. Xu, G. F. Liu, and Z. X. Li. On quality functions for grasp synthesis and fixture planning. In *IEEE Int. Conf. on Robotics and Automation*, pages 333–338, 2004.

[119] Y. Yokokohji, S. Nomoto, and T. Yoshikawa. Static evaluation of humanoid robot postures constrained to the surrounding environment through their limbs. In *IEEE Int. Conf. on Robotics and Automation*, pages 1856–1863, 2002.

[120] T. Yoshikawa. Passive and active closure by constraining mechanisms. *J. of Dynamic Systems, Measurement, and Control*, 121 (3-4):418–424, 1999.

[121] J. Zhang, K. H. Johansson, J. Lygeros, and S. Sastry. Zeno hybrid systems. *Int. J. Robust and Nonlinear Control*, 1(2):435–451, 2001.

תנוחות שיווי משקל חיכוכי של רובוטים ניידים - חישוב, אפיון גיאומטרי, וניתוח יציבות

יזהר אור

תנוחות שיווי משקל חיכוכי של רובוטים ניידים - חישוב, אפיון גיאומטרי, וניתוח יציבות

חיבור על מחקר

לשם מילוי חלקי של הדרישות לקבלת תואר
דוקטור לפילוסופיה

יזהר אור

הוגש לסנט הטכניון — מכון טכנולוגי לישראל

תמוז תשס"ז חיפה יולי 2007

חיבור על מחקר נעשה בהדרכת פרופסור אילון רימון

בפקולטה להנדסת מכונות

הכרת תודה

ראשית, ברצוני להודות לפרופ' אילון רימון על עזרתו והנחייתו המסורה בכל שלבי המחקר.

תודות לכל אנשי צוות המרכז למערכות ייצור ורובוטיקה בטכניון על סיועם ועל בניית מערכות הניסוי.

בנוסף, הנני מודה לפקולטה להנדסת מכונות בטכניון, שהיתה ביתי השני במשך עשר השנים האחרונות.

ולסיום, תודה לכל בני משפחתי האהובה על תמיכתם ועידודם לאורך כל הדרך.

אני מודה לטכניון, מלגת נאמן, קרן המילואים של הטכניון ולמלגת לבציון (מאת ות"ת) על התמיכה הכספית הנדיבה בהשתלמותי

עבודה זו מוקדשת באהבה למשפחתי היקרה.

תקציר

מזה זמן רב מפתחים בעולם רובוטים בעלי רגליים להליכה אוטונומית. רובוטים בעלי רגליים הינם בעלי תכונות עבירות טובות יותר מרכבים עם גלגלים או זחלים, ויכולים לבצע תנועה גם בשטחים קשים בעלי טופוגרפיה לא אחידה. לרובוטים הולכים שימושים אפשריים מגוונים, ביניהם שימוש למטרות סריקה חילוץ והצלה באיזורים מוכי אסון כגון חורבות בתים לאחר פיגוע או רעידת אדמה, שימוש לצורך עבודות תחזוקה בתחנות חלל בסביבה חסרת כבידה, שימושים צבאיים כגון נשיאת משאות כבדים בשטח סבוך או סריקה של יעד מבוצר ללא סיכון חיי אדם, ועוד. דוגמאות ידועות של מספר סוגי רובוטים בעלי רגליים הקיימים כיום הינם רובוטים דמויי אדם (Humanoids), רובוטים בעלי ארבע רגליים ליישומים צבאיים ולמשחקים, רובוט תלת רגלי לטיפוס על קיר אנכי, וכן רובוט בעל שש-רגליים שנבנה על סמך השראה מעולם החרקים והתיקנים.

הליכה רובוטית אוטונומית מצריכה פיתוח אלגוריתמים לתכנון התנועה תוך התחשבות בתנאי השטח המשתנים ובתכונות הרובוט. בניגוד לתנועה בשטחים פשוטים, כגון משטחים אחידים או גרמי מדרגות, על מנת לנוע באופן בטוח בשטח קשה יש לנוע בצורה קוואזיסטטית, בה הרובוט נמצא במצב שווי משקל סטטי בכל רגע במהלך התנועה. תכנון הליכה קוואזיסטטית מצריך פיתוח תיאוריה שיטתית לאפיון וחישוב תנוחות שיווי משקל, שיקיימו גם דרישות נוספות כגון עמידות בפני כוחות חיצוניים ויציבות דינמית ביחס להפרה של מצב שווי המשקל.

עבודות מחקר קודמות פיתחו כלים לתכנון תנועה המבוססת על אחיזות קיבוע יציבות, בהן

הרובוט מקבע את עצמו באמצעות אחיזה בקירות מנוגדים, ומנצל את כוחות החיכוך כדי להניע את הגוף המרכזי ולהניף רגל חופשית לאחיזת קיבוע חדשה. בתנועת הליכה בשטח קשה, בדרך כלל אין אפשרות להשתמש באחיזות קיבוע, ולכן בחירת תנוחות שווי משקל תלויה במיקום נכון של מרכז הכובד של הרובוט ביחס למיקומי כפות הרגליים. בנוסף לדרישת שיווי המשקל והעמידות בפני כוחות חיצוניים, יש לבחור תנוחות בעלות יציבות דינמית. יציבות דינמית של תנוחת שיווי משקל נקבעת ע"פ התגובה הדינמית של הר-ובוט להפרות קטנות ממצב שיווי המשקל, שעשויות לכלול גם החלקות, גלגולים וניתוקים בנקודות המגע. תנוחת שיווי משקל הינה יציבה דינמית מקומית באם הדינמיקה של הר-ובוט בתגובה להפרה מבטיחה חזרה למגע ולמצב שווי משקל בסביבה קרובה של התנוחה המקורית.

מטרת עבודת מחקר זו הינה פיתוח תיאוריה שיטתית לאפיון וחישוב תנוחות שיווי משקל בעלות יציבות דינמית ועמידות לכוחות חיצוניים, עבור רובוט מרובה רגליים הנע בשטח קשה בנוכחות חיכוך. כאשר מתייחסים לרובוט כגוף קשיח בעל מרכז כובד משתנה ומגעים קבועים, הבעיה מפושטת למציאת איזור מותר למיקום מרכז הכובד עבור נקודות מגע נתונות, כך שיתקיימו אילוצי שווי המשקל, העמידות והיציבות הדינמית.

העבודה מחולקת לחמישה חלקים. בחלק הראשון מוצג חישוב ואפיון גיאומטרי של תנוחות שיווי משקל חיכוכי בשדה כבידה מישורי תחת הנחת חיכוך קולון (Coulomb). עבור שתי נקודות מגע נתונות, מוצג קריטריון לבנייה גרפית של איזור מרכז הכובד המבטיח שווי משקל. עבור מספר כללי של מגעים, הבעיה מנוסחת כבעיית תכנות ליניארי (Linear Programming), ובנוסף, מוצג אלגוריתם יעיל המשתמש בשיטות גיאומטריה חישובית לחישוב האיזור המותר למיקום מרכז הכובד. בהמשך הפרק, האנליזה מורחבת גם לחישוב איזור מרכז הכובד עמידות (Robustness) של שווי המשקל ביחס לסביבה נתונה של כוחות ומומנטים של הפרעה חיצונית, ומוצגות תוצאות ניסוי של בחינת עמידות תנוחות שיווי מש-קל של מכניזם מישורי דו-רגלי ביחס לכוח הפרעה, תוך השוואה לתוצאות התיאורטיות.

בחלק השני מוצג חישוב ואפיון גיאומטרי של תנוחות שיווי משקל חיכוכי בשדה כבידה

תלת-מימדי. בעיית חישוב איזור מיקום מרכז הכובד המבטיח שיווי משקל עם שלוש נקו-דות מגע חיכוכי מנוסחת כבעיה של הטלת איזור חמש מימדי למישור דו-מימדי, וכן כבעייה של חיתוך בין קונוס קמור שש-מימדי למישור אפיני דו-מימדי במרחב הכוחות והמומנטים. בעיית ההטלה נפתרת בעזרת קירוב פוליהדרלי של אילוצי החיכוך ושימוש בשיטות סט-נדרטיות להטלה של פוליהדרון קמור ממימד גבוה למימד נמוך יותר. בעיית החיתוך נפתרת באופן מדויק בעזרת שימוש בשיטות של גיאומטריה דיפרנציאלית וגיאומטריה של קווים (Line Geometry), ומתקבל ניסוח מלא ואפיון גיאומטרי של כל תאי השפה של איזור שווי המשקל. בהמשך מוצגת השוואה לקריטריון הקלאסי של Support Polygon Principle עבור תנוחות בסביבה שטוחה, והרחבה של התוצאות למספר כללי של נקודות מגע במרחב, ול-הבטחת עמידות ביחס לכוחות ומומנטים חיצוניים. בנוסף, מוצגות תוצאות ניסוי של מיפוי איזור שווי המשקל עבור מכניזם תלת רגלי עם מרכז כובד משתנה, תוך השוואה לתוצאות התיאורטיות.

בחלק השלישי מוגדרת בעיית היציבות הדינמית של תנוחות שיווי משקל חיכוכי בתגובה להפרות ביחס למצב שיווי המשקל, הכוללות החלקות, גלגולים וניתוקים בנקודות המגע. מוצג ניסוח של הדינמיקה של מערכות מכניות מישוריות עם אילוצי חיכוך במגעים. שלוש תופעות הייחודיות לסוג כזה של מערכות הינן ריבוי פתרונות (Dynamic Ambiguity), אי-קיום של פתרונות (Dynamic Inconsistency), וקפיצה בלתי-חלקה של הפתרון הדינמי (Dynamic Jamming). תופעות אלו מודגמות ומנוסחות כאילוצים על איזורי מיקום מרכז הכובד. לאחר מכן מוגדר קריטריון "שיווי משקל חזק" (Strong Equilibrium) שנועד למנוע מצב של ריבוי פתרונות דינמיים, ומוצגת הוכחה לכך שקריטריון זה הוא למעשה תנאי הכרחי ליציבות דינמית של תנוחות שיווי משקל חיכוכי. בנוסף, מוגדר גם קריטריון של "שיווי משקל מתמיד" (Persistent Equilibrium), שנועד למנוע מצב של אי-קיום או אי-חלקות של הפתרון הדינמי. קיום שני קריטריונים אלו מבטיחים כי בהינתן הפרה קטנה ממצב שיווי המשקל, הכוללת ניתוקים ו/או החלקות במגעים, התגובה הדינמית תגרום לעצירת החלקה או לחידוש מגע תוך זמן סופי, שהינן תופעות רצויות להבטחת יציבות

דינמית.

חידוש המגע כולל אירוע של התנגשות, שבו המתקף (Impact) של כוח המגע גורם לק-פיצה בלתי רציפה במהירות, ודורש ניתוח הדינמיקה של מערכות עם התנגשויות במגעים. החלק הרביעי של העבודה עוסק בניתוח את התגובה הדינמית של גוף מישורי העובר התנ-גשויות בשתי נקודות מגע, תוך שימוש בהכללה של עקרון מקדם התקומה (Coefficient of Restitution). משוואות התנועה של הגוף מנוסחות כמערכת היברידית עם אימפולסים (Impulsive Hybrid Dynamical Systems). תופעה ייחודית למערכות מסוג כזה הינו "פתרון זנון" (Zeno Solution), בו המערכת מבצעת מספר אינסופי של התנגשויות תוך זמן סופי, ומתכנסת למצב של חידוש המגע בנקודה אחת או שתיים. ניתוח התכנסות הפתרון הדינ-מי של המערכת נעשה תוך שימוש בשיטה של מיפוי פואנקרה (Poincaré Map) שממיר את הבעייה לבעיית יציבות של מערכת דינמית לא ליניארית בזמן בדיד תחת אילוצים. בהמשך מוצג קריטריון חדשני הנקרא "יציבות הנקישות" (Clattering Stability), המבטיח התכנסות של המערכת לפתרון זנון של חידוש המגע בנקודה אחת או בשתיים. הקריטריון מנוסח כאילוצים על מיקום מרכז הכובד ופילוג המסה של הגוף, כתלות במקדם התקומה ובגיאומטריה של משטחי המגע. המסקנות התיאורטיות בחלק זה מודגמות באמצעות ביצ-וע סימולציה דינמית נומרית של המערכת ההיברידות עם אירועי אימפקט על גבי מחשב, עבור מספר תרחישים שונים.

בחלק החמישי והמסכם, מאוחדות תוצאות כל הפרקים הקודמים, ומוכחת הטענה כי קיום תנאי שיווי המשקל החזק והמתמיד, יחד עם תנאי יציבות הנקישות, הינם תנאים מספיקים להבטחת היציבות הדינמית של תנוחות שיווי משקל של גוף קשיח מישורי על שני מגעים חיכוכיים. בהמשך מובאות דוגמאות של איזורי מיקום מרכז כובד המבטיחים יציבות דינמית של תנוחות שיווי משקל במישור, וכן דיון על השפעת פרמטרים פיסיקליים של המערכת על היציבות. לסיום, מפורטים מספר כיוונים אפשריים להמשך המחקר ולהכללה של התוצאות.